

FLUCTUATIONS OF ENERGY DEPOSITED IN BIOLOGICAL TARGETS BY IONIZING RADIATION

Paweł Olko

**Institute of Medicine, KFA Jülich, FRG
Institute of Nuclear Physics, Kraków, Poland**

Ph.D. Dissertation

Submitted to the Institute of Nuclear Physics, Kraków, Poland

December 1989

**The work described in this thesis has been performed at the
Institute of Medicine,
KFA Jülich, FRG**

Fluctuations of Energy Deposited in Biological Targets by Ionizing Radiation.

P. OLKO

ABSTRACT

This work deals with energy deposition by photons and ions in biological targets (as cell nucleus or DNA) which is of significance for radiation biology and radiation protection. Microdosimetric distributions in small spherical sites are calculated and applied to interpret biological action of ionizing radiation.

A method is developed to calculate microdosimetric distributions for photons, which is based on calculations of photon induced secondary electron spectra in water vapour and Monte Carlo simulations of corresponding electron tracks. Microdosimetric distributions are calculated for photons of energies from 0.3 to 300 keV and target sizes from a few nanometer to 2 μm . Results of calculations are in good agreement with the available experimental data. Based on the results of track structure simulations for ions, an analytical recipe is developed to calculate microdosimetric distributions for protons and alpha particles. This recipe includes the straggling of the energy deposition and the energy deposited by delta-electrons to the sensitive sites. Parameters of the recipe are calculated for particle energies from 0.3 to 10 MeV/amu and for targets down to 1 nm.

The calculated microdosimetric distributions are applied to unfold biological response functions, BRF. BRF for DNA double strand breaks was derived and used as an universal function to calculate the frequency of these lesions induced in mammalian cells in other biological experiments. It was shown that the correlation exists between the frequency of induced DNA breaks and cellular effects. BRF's calculated for cellular end-points are used to discuss the Quality Factor issue. The results of unfolding do not support the ICRU-40 proposal to modify present regulations of Quality Factor. It is shown that the structure of the presently available radiobiological data leads to uncertain conclusions on radiation quality for lineal energies below 10 keV/ μm and above 200 keV/ μm . It is therefore recommended to perform radiobiological experiments with more than one low-LET radiation and with several radiations in the saturation region.

Fluktacje energii deponowanej przez promieniowanie jonizujące w mikroskopowych strukturach biologicznych

P. OLKO

STRESZCZENIE

Prezentowana praca traktuje o depozycji energii fotonów i jonów w ważnych dla radiobiologii i ochrony radiologicznej mikroskopowych strukturach biologicznych o wielkościach odpowiadających jądro komórki i DNA. Rozkłady mikrodozymetryczne obliczone w tych strukturach użyte zostały do wyjaśniania działania promieniowania jonizującego na materię ożywioną.

Opracowano metodę obliczania rozkładów mikrodozymetrycznych indukowanych przez foton wykorzystując symulację Monte Carlo śladów elektronów wtórnych w parze wodnej. Rozkłady te zostały obliczone dla fotonów o energiach od 300 eV do 300 keV i dla targetów o średnicach od kilku nanometrów do 2 μm . Rezultaty obliczeń dobrze zgadzają się z dostępnymi danymi eksperymentalnymi. Bazując na rezultatach symulacji struktury śladu jonów opracowano analityczny przepis na obliczanie rozkładów mikrodozymetrycznych dla protonów i cząstek alfa. Przepis ten uwzględnia w widmach mikrodozymetrycznych fluktuacje w stratach energii przy przechodzeniu przez target oraz energię deponowaną przez elektryny delta. Parametry tego przepisu podano dla cząstek o energiach od 0.3 do 10 MeV/nukleon i dla targetów od 1 do 1000 nm.

Obliczone rozkłady mikrodozymetryczne zastosowano do dekonwolucji funkcji odpowiedzi biologicznych. Analiza przeprowadzona dla uszkodzeń DNA pokazała istnienie korelacji między częstością indukowania uszkodzeń DNA i częstością występowania efektów komórkowych. Wyniki dekonwolucji przeprowadzonych dla efektów komórkowych użyte zostały do dyskusji problemu współczynnika jakości promieniowania. Prezentowane wyniki nie potwierdzają propozycji Międzynarodowego Komitetu Jednostek i Pomiarów Radiacyjnych ICRU [Raport Nr 40] mających na celu modyfikację obecnie przyjętych współczynników jakości. Pokazano, że struktura obecnie dostępnych danych radiobiologicznych prowadzi do niepewnych wniosków dotyczących funkcji jakości promieniowania dla energii liniowych poniżej 10 keV/ μm i powyżej 200 keV/ μm . W związku z tym zaleca się, aby doświadczenia radiobiologiczne służące wyznaczaniu QF były wykonywane z użyciem więcej niż jednego promieniowania o niskiej gęstości jonizacji i szeregu promieniowań w obszarze saturacji efektu.

LIST OF CONTENTS

Abstract	3
Streszczenie	4
List of contents	5
1. INTRODUCTION	8
1.1. General	8
1.2. Review	9
1.3. Scope of work	10
1.4. Delimitations	10
2. RADIATION INTERACTION WITH BIOLOGICAL MATTER AND PARTICLE TRACKS	11
2.1. Photon interactions	11
2.1.1. Photoelectric effect	11
2.1.2. Compton effect	13
2.1.3. Photon cross sections	14
2.2. Charged particles interactions in matter	15
2.3. Principles of Monte Carlo simulations of charged particle tracks	17
2.3.1. Electron track structure code Moca-8	18
2.3.2. Ion track structure code Moca-14	18
2.3.3. Delimitations of the MOCA programs for use in radiation biology	23
3. REVIEW OF TOPICS DISCUSSED IN THIS WORK	24
3.1. The limits for application the macroscopic parameters to describe radiation action	24
3.1.1. Absorbed dose	24
3.1.2. Linear Energy Transfer	26
3.2. Microdosimetric quantities and distributions	28
3.2.1. Quantities	28
3.2.2. Distributions	28
3.3. Measurements of energy deposition distributions	31
3.3.1. Principle of simulation of a sensitive volume	31
3.3.2. Proportional counters measurements of microdosimetric distributions	33
3.4. Calculations of microdosimetric distributions	34
3.4.1. Principles of calculations using track structure simulation	34
3.4.2. Review of calculations for photons	35
3.4.3. Review of calculations for ions	36
3.5. Microdosimetry and radiation biology	37
3.5.1. Sensitive sites in biological cells	38

3.5.2. Radiation induced biological effects	38
3.5.3. Quantitative description of radiation induced lesions	39
3.5.4. Review of radiobiological experiments with heavy ions and photons	42
3.6. Biological Response Function, an alternative approach to biological action of radiation	44
3.6.1. Concept of a response function for biological targets	44
3.6.2. Survey of unfolding methods	45
3.6.3. Response functions in radiobiology- a review	47
3.7. Microdosimetry and radiation protection	50
3.7.1. Microdosimetric concept of low dose and low dose rate	50
3.7.2. Quality factors in radiation protection	51
3.7.3. Proposals for new radiation protection regulations	52
4. EVALUATION AND INTERPRETATION OF ENERGY DEPOSITION FOR PHOTONS	53
4.1. Method of calculation microdosimetric distributions for photons	53
4.1.1. Calculation of secondary electron spectra in water	53
4.1.2. Simulation of electron tracks in water vapour and scoring microdosimetric distributions	55
4.1.3. Method of approximation of microdosimetric distributions for TE targets	57
4.2. Results of calculations and discussion	58
4.2.1. Calculation of fractions of dose due to Compton and photoelectrons in TE gases	58
4.2.2. Comparison of calculated and measured with walled KFA TEPC microdosimetric distribution	61
4.2.3. Comparison of calculated and measured with wall-less TEPC microdosimetric distributions	62
4.2.4. Microdosimetric distributions for nanometer targets	65
4.2.5. Limitations of the method	68
5. EVALUATION AND INTERPRETATION OF ENERGY DEPOSITION FOR IONS	72
5.1. Principles of ions energy deposition in a sensitive site	72
5.1.1. Ion and delta-event microdosimetric distribution	72
5.1.2. Straggling of energy deposition in small targets	73
5.2. Formulation of the analytical approach	74
5.2.1. Ion events	74
5.2.2. Delta-ray events	77
5.2.3. Total distribution of ionization $f_1(j)$	77
5.2.4. Method of scoring ionization distributions	79
5.3. Results and discussion	80
5.3.1. Parameters of analytical approach	80
5.3.2. Microdosimetric distributions	83
5.3.3. Investigation of limits of MOCA-14	85

6.	DETERMINATION OF BIOLOGICAL RESPONSE FUNCTION	93
6.1.	Method of calculation	93
6.1.1.	Choise of unfolding method	93
6.1.2.	Modifications of SAND-II	95
6.1.3.	Testing of the code	96
6.2.	Results of unfolding and discussion	96
6.2.1.	Biological Response Functions for DNA double strand breaks and their implications for radiobiology	96
6.2.2.	Biological Response Functions for cellular effects and their implications for radiation protection	100
7.	SUMMARY AND CONCLUSIONS	105
APPENDIXES		107
A.1	Measurements and calculations of radial dose distributions	107
A.2	Method of calculation of radial dose distributions from heavy ion tracks	108
B.1	Evaluation of initial slopes of dose-response curves	109
C.1	Exemplary calculation with the analytical recipe	116
C.2	Parameters of the analytical recipe to calculate microdosimetric distributions for protons and alpha particles	117
C.3	Parameters of the analytical recipe to calculate microdosimetric distributions for radiations used in radiobiological experiments	120
D.1	Testing the SAND-II unfolding algorithm	121
REFERENCES		127
ACKNOWLEDGEMENTS		137

1. INTRODUCTION

1.1. GENERAL

Energy of ionizing radiation is imparted to the irradiated media in a non-uniform manner, being concentrated along the tracks of charged particles. In addition, biological matter is not uniformly sensitive for radiation. In a biological cell, which is the smallest independent constituent of living organisms, only some organelles (cell nucleus and the DNA structures covered in it) are sensitive to radiation. Due to these two factors, the energy deposited to the sensitive biological sites fluctuates. In the irradiated tissue one can always find a fraction of cells which received much higher energy deposition events than the average, but also a lot of targets which did not experience energy deposition at all.

The fluctuations clearly depend on the type of radiation. When a densely ionizing radiation is considered, it produces tracks with a high ionization density. In that case the spatial fluctuations of energy deposition are larger than in the case of more uniformly distributed tracks from e.g. Co-60 gamma rays. In fact, it is observed in radiobiology that a densely ionizing radiation produces higher effects at these same average doses. This different effectiveness of ionizing radiations is referred to as radiation quality.

The fluctuations also depend on the target size. In general, the smaller the target the lower the probability of hitting the target and the greater are the differences in energy deposited in affected and unaffected sensitive volumes.

The study of fluctuation of energy deposition is the main objective of microdosimetry. There are two aspects of these investigations. The first, is to gain a better understanding of underlying mechanisms of radiation damage. It is clear that dose alone, as an average parameter, cannot describe the highly non-uniform pattern of radiation action in biological systems. The second one, not less important, is to apply these concepts and corresponding experimental techniques to the radiation protection. By using measurements of energy distributions in sites of dimensions comparable with biological targets, it is possible to measure radiation quality in an unknown radiation field.

For these purposes, microdosimetric experimental techniques were developed based on microdosimetric proportional counters [Rossi & Rosenzweig, 1955], [Glass & Gross, 1972], [Booz et al., 1981], [Schmitz et al., 1985]. In these counters, tissue-equivalent gases at low pressures are applied. An ionizing particle crossing the counter sensitive volume should experience comparable interactions as if it were traversing the biological target. Due to technical reasons, it is not possible to simulate volumes much smaller than 1 μm .

The distributions of energy deposition in nanometer targets are required to investigate the radiation action on the molecular level. At present, these distributions can only be assessed with computational methods.

1.2. REVIEW

There are at least three factors which contribute to the fluctuations in energy deposited to the sensitive volume. Firstly, charged particles intersect targets with different chord lengths. If only that factor is taken into account, energy deposition in the site can be approximated by calculating chord length distribution and assuming, e.g., continuous energy loss of the charged particle along the given chord (Continuous Slowing Down Approximation). This approach has been used in analytical calculations of energy deposited in sites of micrometer dimensions, e.g., due to neutron action [Caswell, 1966], [Coppola & Booz, 1975], [Morsttin et al., 1985] leading to a good agreement with measurements. The second reason of fluctuations is the discrete manner in which radiation interacts with matter. The fluctuations in the number and the type of primary radiation interactions is called straggling of energy loss. The distributions of energy loss can be calculated analytically [Vavilov, 1957]. The straggling of energy loss was also introduced to the neutron Monte Carlo calculation [Coppola & Booz, 1973]. However, not all energy transferred to the medium by the primary radiation interactions is deposited in the vicinity of the interaction point. The delta-electrons can transport energy away from the primary charged particle interaction point. This is the third contribution to the non-uniform pattern of energy deposited in the small biological targets.

When only the first geometrical factor is taken into account there is, in principle, no change in the description of energy deposition with a decreasing site size. Two other factors play a predominant role when the target size is of the same order of magnitude (or smaller) than the distance between the two primary interactions and/or than the range of delta-rays. For typical radiations encountered in the experimental radiobiology the straggling and the delta-ray transport should be taken into account when target sizes are smaller than, say 1 μm [Kellerer & Chmelevsky, 1975a]. At present, the only chance to account for both effects in nanometer targets offer track structure calculations.

Two types of radiation are of particular interest for radiobiology. Ions are applied to investigate radiation effects in a wide range of LET and under well-defined physical conditions. Photons are used in radiobiological experiments to normalize effects from high-LET radiations and to test radiobiological models (soft X-rays).

Some exemplary calculations were performed in order to assess distributions in nanometer sites for ions by using track structure calculations [Kellerer & Chmelevsky, 1975b], [Wilson & Paretzke, 1981]. However, these works comprise only a limited number of examples and the results cannot be used to perform calculations for the particular radiation modalities used in biological experiments. Also, no analytical method is available to generate realistic distributions for demanded ion and target parameters. The analytical model of Wilson [Wilson et al., 1988] enables one to calculate ionization distributions produced by protons in spherical sites. This model does not take into account energy deposited by ions passing outside the sensitive site (so-called touchers). Photon data is even more fragmentary. Some results for nanometer sites are available, but they are scarce and presented in the form only related to classical microdosimetric spectra [Goodhead & Brenner, 1983], [Oda & Iwanami, 1985].

Required microdosimetric distributions can be applied to unfold biological response functions which are of interest for radiobiology and radiation protection [Kellerer & Rossi, 1972], [Varma & Bond 1982], [Feinendegen et al., 1985]. It was recognized, that it is possible to find a function which expresses the probability of effect versus energy deposited in the target. Such response functions for cellular effects, based on energy distributions in micrometer sites, were unfolded for many radiobiological end-points [Zaider & Brenner, 1985], [Morsttin et al., 1989]. No similar unfolding was done for

DNA damage, e.g., for double strand breaks due to the lack of adequate microdosimetric distributions.

Results of such an unfolding, performed on a micrometer scale [Zaider & Brenner, 1985] for chromosome aberrations in human lymphocytes [Edwards et al., 1980a,b], were used to support a new concept of the Quality Factor [ICRU 40]. However, the particular quality function suggested at ICRU-40 creates great controversies [Kellerer & Hahn, 1988], [Morstyn et al., 1989].

1.3. SCOPE OF WORK

The purpose of this work is to calculate microdosimetric distributions in targets of micrometer and nanometer diameters after photon and ion irradiations, and to show how these distributions can be utilized in radiation protection and radiobiology.

This goal is achieved in two steps. First, energy deposition in spherical targets is studied with the help of Monte Carlo programs simulating the structure of tracks of electrons and ions. Then, the examples are given by applying calculated spectra to analyze radiobiological experiments by unfolding biological response functions.

Chapters 2 and 3 introduce the concepts used in this work. Calculations and interpretations of microdosimetric distributions are presented in Chapter 4 for photons. Energy deposition to the targets due to the ion action is investigated in Chapter 5. Chapter 6 concerns the unfolding of Biological Response Functions, based on previously calculated microdosimetric spectra, and applying these functions to the ongoing discussion on the Quality Factor issue.

1.4. DELIMITATIONS

Results presented in this work are limited to calculations only. No experiments were performed. The measured microdosimetric distributions used for comparisons were taken from the literature.

The basic tools used to calculate microdosimetric distributions were track structure Monte Carlo programs MOCA-8 and MOCA-14 (authors: H.G. Paretzke, GSF Muenchen and W.E. Wilson, PNL, USA). These programs calculate tracks of electrons and ions in water vapour because a fairly complete set of ionization and excitation cross sections exists only for that biologically relevant medium. Results of calculations were then rescaled into the medium of unit density. Throughout this work, the biological targets are assumed to be spherical in shape. No attempt was made to incorporate other possible shapes of these targets.

Neutrons are not considered in this work. In biomedical applications neutrons are frequently used to irradiate thick tissues, mainly *in vivo*, because of high penetration. Investigations with ions and soft X-rays constitute a separate class of experiments, because with these radiations usually only a single layer of specially cultured cells can be irradiated with the required uniformity. Also, neutrons act through their charged secondaries and secondary photons. Therefore, if energy spectrum of these secondaries in tissue is known, it should in principle be possible to reproduce it via the ion and photon calculations presented here. However, this difficult task is beyond the scope of the present work.

2. RADIATION INTERACTIONS WITH BIOLOGICAL MATTER AND PARTICLE TRACKS

Ionizing radiation interacts with atoms and molecules producing ionizations and excitations. Radiation interactions with biological matter initiate a long chain of processes leading to biological effects in living organisms. In this chapter the most important features of photon (Ch.2.1) and charged particle (Ch.2.2) interactions are presented. The particular attention is paid to describe physical processes which are of importance for biological matter. In the last paragraph (Ch.2.3) the manner is shown how to numerically simulate charged particle tracks.

2.1. PHOTON INTERACTIONS

The probability and type of photon interactions in matter are determined by the photon energy and by the atomic composition of the medium. Chemical structure of the absorber will not be taken into account in this work because effects of chemical bindings on interaction cross sections for photons of energies above 0.3 keV can usually be ignored [Hubbel, 1982]. In the energy range from 0.3 keV to 1250 keV and in biological matter composed mainly of hydrogen, carbon, nitrogen and oxygen, four main types of photon interactions take place: photoelectric effect, Compton scattering (incoherent), Raleigh scattering (coherent), and pair production.

Raleigh scattering is an elastic deflection of a photon on a tightly bound electron. This process does not contribute to energy deposition in matter, in the sense that the whole atom takes part in conserving momentum and therefore the kinetic energy of the atom, after experiencing Raleigh scattering, is minimal.

The threshold energy of electromagnetic radiation for pair production in the Coulomb field of nucleus is about 1.02 MeV. The contribution of pair production to the mass absorption coefficient for the highest photon energy considered in this work (1.3 MeV gamma rays from Co-60) and for carbon ($Z=6$) is less than 0.1% [Hubbell, 1969]. Therefore, in what follows, this kind of photon interaction will not be considered. Here, interactions which mainly contribute to energy deposition processes are photoeffect (below 100 keV) and Compton scattering.

2.1.1 Photoelectric effect

The photoelectric effect is the most important interaction of low-energy photons in biological matter. In this interaction the incident photon energy $h\nu$ is totally absorbed by a tightly bound inner shell atomic electron of binding energy E_b . The electron leaves the atom with kinetic energy T equal to:

$$T = h\nu - E_b \quad (2.1)$$

The atom assists in conserving momentum in this collision but it carries negligible kinetic energy due to the larger difference between the masses of the atom and of the photoelectron. For example, for an oxygen atom and 10 keV photon, this energy does not exceed 0.4 eV.

The direction of photoelectron emission depends on the initial photon energy. For photon energies below 100 keV, the angle between the direction of the incident photon and the photoelectron is broadly distributed between 0° and 180°; for very energetic photons in the MeV region, photoelectrons are emitted predominantly in the forward direction [Davisson & Evans, 1952]. The angular correlation of photoelectrons with regard to incident photon direction appears not to be of great importance for biological effects, because biological targets are usually randomly oriented.

The probability of photoelectric effect (per atom) increases with atomic number, Z, and decreases with photon energy, $h\nu$. For photons below 100 keV this interaction cross section per atom, $_{\text{a}}\tau$, can be approximated by the following expression

$$_{\text{a}}\tau \sim \frac{Z^4}{(h\nu)^3} \quad (2.2)$$

The corresponding cross section per unit mass, τ/ρ is called the mass attenuation coefficient for photoeffect

$$\tau/\rho \sim Z \ _{\text{a}}\tau \quad (2.3)$$

These equations do not show the complications arising from the binding energy of electrons. If the photon energy just above the binding energy of an orbital electron and then decreases, the cross section first increases and then rapidly decreases below the shell binding energy. For low Z elements, which are the main constituents of biological matter, this effect can be seen only for soft X-rays, because K-absorption edges for carbon, nitrogen and oxygen all lie below 1 keV. This is demonstrated in Fig.2.1 [Hummer, 1984] which shows the mass absorption coefficient (see Ch.2.1.3) for the cell nucleus as a function of incident photon energy. The cell nucleus was assumed to be composed (by weight) of 10.6%, 9% C, 3.2% N, 74.1% O, 2.6% P and 0.4% S. The corresponding K-absorption edges for carbon (0.28 keV), nitrogen (0.4 keV), oxygen (0.53 keV) and phosphorus (2.14 keV) can be identified in this figure.

Photoelectron emission leads to an inner shell vacancy and leaves the atom in an excited state. In the de-excitation process, this vacancy is filled by an electron from a higher (less bound) shell. The energy released in this process can be transported outside the atom by a fluorescence photon or by an Auger electron. These are competing phenomena. The probability of emitting a fluorescence X-ray from a given shell K, L, ..., is called the fluorescence yield, Y_K , Y_L , ..., respectively. For the K-shell Y_K is negligible up to $Z=10$, and then increases up to 0.5 for $Z=32$ [Lederer & Shirley, 1979]. Y_L is negligible below $Z=30$. Thus, as concerns photoeffect in biological matter, Auger electron emission is considered to be the predominating mode of atomic deexcitation.

An example of a photoeffect energy balance is given below. If the threshold energy for producing a K-shell vacancy is E_{bK} , the photoelectron's energy, T_P , is:

$$T_P = h\nu - E_{bK} \quad (2.4)$$

Assume that after the photon interacts with an atom a K-shell vacancy is produced, filled with an electron from the L-shell (binding energy E_{bL}) and that the atom is deexcited due to emission of an Auger electron. The kinetic energy T_A of the Auger electron is then

$$T_A = (E_{bK} - E_{bL}) - E_{bL} \quad (2.5)$$

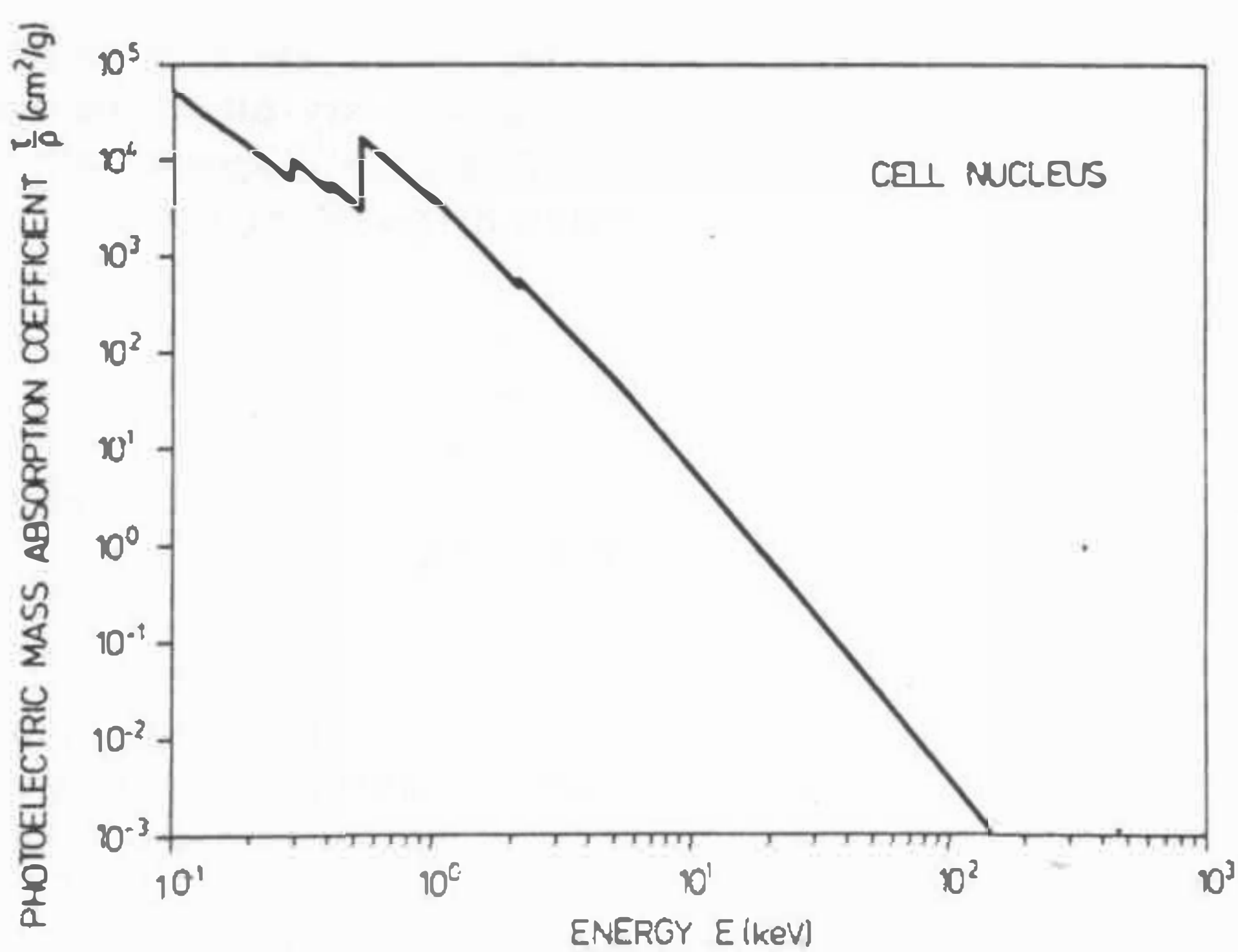


Fig.2.1 Photoelectric mass absorption coefficient for a cell nucleus as a function of the incident photon energy (from [Hamm, 1983])

if emission took place from the L-shell. Now the atom has two vacancies on the L-shell which can be filled by electrons from higher shells. This cascade process continues until all vacancies are placed on the outermost shells. For example, in an oxygen atom the threshold energy for producing a K-shell vacancy is 532 eV, while the average L-shell binding energy is about 12 eV [Lederer & Shirley, 1979]. This gives, from Eq.2.5, an average energy of the Auger electron of 508 eV. Of course, in case of oxygen atom, no cascade process will occur, as the L-shell is the outermost one.

2.1.2. Compton effect

Compton effect is a process of photon scattering by an unbound and stationary electron. Assumptions concerning electron state are not very rigorous and photon scattering on weakly bounded electrons in atoms is still described well enough by equations derived for a free electron. The greatest deviations from this situation are expected for high Z elements and low energy photons, but this is a region where photoeffect dominates and the contribution to energy deposition from Compton electrons is small. For biological matter (low Z) the region where Compton effect is important lies between 20 keV and 30 MeV.

From the principles of momentum and energy conservation it is possible to calculate the kinematic relationship between the energies of the incident photon, $h\nu$, and of the scattered electron, E:

$$E = \frac{h\nu \alpha}{1 + \alpha(1 - \cos\theta)} \quad (2.6)$$

where $\alpha = h\nu/mc^2$ and θ is the scattering angle of the electron relative to the direction of the incident photon. The photon can never give away all of its energy in a collision with a free electron. The maximum energy of Compton electron, E_{Ce} , (Compton edge) is reached when the incident photon is backscattered ($\theta=180^\circ$).

$$E_{Ce} = \frac{h\nu \alpha}{1 + 2\alpha} \quad (2.7)$$

E_{Ce} approaches $h\nu - 0.2555$ MeV for $h\nu \gg 0.511$ MeV.

The probability for Compton scattering was first calculated by Thompson and later improved by [Klein & Nishina, 1928] using Dirac's relativistic theory of the electron. The differential cross section for the free electron having recoil energy between E and $E + dE$, is [Evans, 1955]:

$$\frac{d_e \sigma}{dE} = \frac{p r_0^2}{\alpha^2 mc^2} \left[2 + \left(\frac{E}{h\nu - E} \right)^2 \left[\frac{1}{\alpha^2} + \frac{h\nu - E}{h\nu} - \frac{2(h\nu - E)}{\alpha E} \right] \right] \quad (2.8)$$

where $r_0 = 2.18 \cdot 10^{-15}$ m is the classical electron radius
 $mc^2 = 511$ keV is the electron rest energy
 E is the kinetic energy of Compton electron, and
 $h\nu$ is the photon energy

This cross section is averaged over all scattering angles θ . Using these equations it is possible to calculate initial energies of electrons generated in the medium by photons of a given energy spectrum. Angular distributions of Compton electrons are of less importance for understanding radiation action in biological targets, and will not be discussed here.

2.1.3. Photon cross sections

If a monoenergetic and parallel beam of N_0 photons crosses perpendicularly an absorber of thickness x , the number of transmitted photons N_x is given by:

$$N_x = N_0 e^{-\mu x} \quad (2.8)$$

where μ is the linear attenuation coefficient, expressed per unit length of absorber. It is more convenient to use the mass attenuation coefficient μ/ρ_0 which is independent of the physical state of the absorber and is expressed in units of $m^2 kg^{-1}$. The total mass attenuation coefficient is defined as the sum of contributions from different kinds of interactions:

$$\frac{\mu}{\rho_0} = \frac{\tau}{\rho_0} + \frac{\sigma_c}{\rho_0} \quad (2.9)$$

where

τ/ρ_0 is the photoelectric mass attenuation coefficient, and
 σ_c/ρ_0 is the Compton mass attenuation coefficient

The total mass attenuation coefficient, μ/ρ_0 , determines the probability of removing a photon from the primary beam but not the probability of depositing the photon's energy in the absorber. This latter effect is quantitatively described by a mass absorption coefficient which relates the incident photon energy converted to electron kinetic energy. For low Z each photoelectric interaction results in almost total absorption of the incident photon energy. Thus the mass attenuation coefficient, τ/ρ_0 , and mass absorption coefficient, τ_a/ρ_0 , are approximately equal for low Z elements. In the Compton effect only a fraction of the photon energy is transferred to secondary electrons. The attenuation cross section, σ_c/ρ_0 , equal to:

$$\frac{\sigma_c}{\rho_0} = \frac{\sigma_a}{\rho_0} + \frac{\sigma_s}{\rho_0} \quad (2.10)$$

is a sum of the from mass absorption coefficient, σ_a/ρ_0 , and scattering mass attenuation coefficient, σ_s/ρ_0 . The first contribution is related to the actual photon energy lost to the absorber and the second to photons being scattered out of the primary beam. The total mass absorption coefficient, μ_a , is then equal to:

$$\frac{\mu_a}{\rho_0} = \frac{\tau_a}{\rho_0} + \frac{\sigma_a}{\rho_0} \quad (2.11)$$

2.2. PRINCIPLES OF CHARGED PARTICLES INTERACTIONS IN MATTER

Fast charged particles lose their energy in a different way than photons do. Photons undergo one or more "catastrophic" interactions in which they radically loose their energy and produce fast electrons. Instead, charged particles are surrounded by their Coulomb field and act on atoms or molecules in a large number of interactions producing excitations and ionizations.

The complexity of charged particles interactions with matter implicates various ways of classification of these phenomena. Firstly, one can distinguish elastic and nonelastic collisions. To energy deposition contribute only nonelastic collisions. Elastic collisions become important for low energy electrons (below 200 eV). These collisions influence the pattern of energy deposition by allowing electron to diffuse at the end of its track.

Another classification can be done with regard to impact parameter of an interaction. When a charged particle passes an atom at a distance much larger than the atom dimensions then particle's electric field affects the atom as a whole. These "soft" collisions lead mainly to excitations or ionizations and the energy transfer to the atom is of order of a few eV. Soft collisions are the most frequent types of interactions. When the impact parameter is comparable with dimensions of the atom a "hard" (knock-on, binary encounter) collision is more probable. In such the interaction an atomic electron can be ejected from the atom with a high kinetic energy. The maximum energy E_{max} that can be transferred from a charged particle of mass M with kinetic energy E_i to a free electron of mass m_0 in a single collision can be calculated from the classical principle of momentum conservation:

$$E_{\max} = \frac{4 M m_0}{(M + m_0)^2} E_i \quad (2.12a)$$

For collision between 2 electrons the E_{\max} can be, at maximum

$$E_{\max} = 0.5 E_i \quad (2.12b)$$

because of indistinguishability of incident and ejected electrons.

When the impact parameter is much smaller than the atomic radius then charged particles (mainly electrons) can interact with the external nuclear field. In most cases the electron is elastically scattered. The electron can also take part in an inelastic collision leading to emission of an photon (Bremsstrahlung). This happens rarely for low-Z atoms constituting biological matter and low energy electrons. E.g. for 100 keV electrons energy loss in water due to Bremsstrahlung contributes to the total stopping power in 0.1%. Probability of the effect increases with increasing Z and increasing energy of electrons. The last class of interactions are nuclear interactions produced by energetic heavy charged particles. They however occur for much higher ion energies (at least 100 MeV for protons) as compared to those considered in this work (10 MeV protons).

An average information on density of collisions experienced by a particle is given by the collisional stopping power (see Ch.3.1.2). The stopping power dE/dx of the medium can be calculated with some analytical formulas e.g. with Bethe formula for heavy ions [Bethe, 1933]

$$\frac{dE}{dx} = 4\pi r_0^2 m c^2 \frac{z^2}{\beta^2} \frac{Z}{A} \left[\ln \frac{2mc^2\beta^2}{1 - \beta^2} - \beta^2 - \frac{\ln I}{Z} - \frac{C}{2} - \frac{\delta}{2} \right] \quad (2.13)$$

where r_0 is the Bohr radius ($5.3 \cdot 10^{-11} \text{ m}$), m mass of projectile and z is its charge, β is equal v/c , I is a mean excitation potential, Z and A are average atomic and mass numbers of atoms constituting medium, C/Z shell corrections [Bichsel, 1968] and δ is a density effect correction. On the other hand the stopping power, dE/dx can be calculated as the sum of all single energy loss processes [Paratzke, 1987]. The comparison of this sum energy loss with Eq.2.13 can be used as a consistency check for a set of ionization and excitation cross sections applied in track structure simulations.

The Eq.2.13 does not hold for low energy ions because at low velocities ions charge is reduced (on the average) due to picking up electrons from a medium. To account for these processes the effective charge, z^* , was introduced. The effective charge can be calculated as

$$z^{*2} = \frac{S_i}{S_p} \quad (2.14)$$

where S_p and S_i are stopping powers of proton and of an ion having the same velocity β . The most known semiempirical expression on effective charge was derived from analysis of heavy ions tracks in nuclear emulsion [Barkas, 1953].

$$z^* = z [1 - \exp(-125\sqrt{E_{\max}/1022 \text{ keV}}) z^{-2/3}] \quad (2.15)$$

where the E_{\max} is calculated with Eq.2.12a.

The reciprocal of collision stopping power is proportional to the expectation value of distance between two succeeding collisions called a mean free path, λ . This quantity is of basic importance for simulation of charge particle tracks.

2.3. PRINCIPLES OF MONTE CARLO SIMULATIONS OF CHARGED PARTICLES

The spatial pattern of energy deposition, with possible detailed specification of every interaction (coordinates, type of interaction, energies and angles of particles involved, etc.) is called a charged particle track. Such a track can be mathematically simulated when a sufficient set of cross sections is available. This simulation is done with Monte Carlo techniques, event by event.

A charged particle of energy E , emitted from the point of origin in a given direction, will undergo collisions with assumed probability density

$$p(s) = 1/\lambda e^{-\lambda s} \quad (2.16a)$$

where

- λ - mean free path
- s - distance to the next collision

The actual distance to the next interaction, s_r , can be randomly chosen according to the distribution given by Eq.2.16a. This can be practically performed e.g. by selection a random number, r , ($0 < r < 1$) and applying the function [Carter & Coyne, 1975]

$$s_r = -\lambda \ln r \quad (2.16b)$$

When the interaction point is reached, a decision is taken whether an elastic or nonelastic collision take place. In the elastic collision no energy is deposited to the medium. The primary particle is only scattered and is moving with the unchanged energy E . In a nonelastic collision the particles loses part of its energy, E_1 , and is moving with new energy $E' = E - E_1$. Energy lost depends on the type of interaction. Energy deposited in the point of interaction, E_d , is defined as energy lost minus kinetic energies of secondary particles (e.g. secondary electrons and Auger electrons) released from the molecule.

$$E_d = E_1 - \sum E_i \quad (2.17)$$

After each interaction the actual directions of primary and secondary particles are determinated basing on a double differential cross sections.

2.3.1. Electron Monte Carlo track structure code Moca-8

MOCA-8 was developed in the Institute for Radiation Protection, GSF, Neuherberg by Dr. H.G. Paretzke. The program traces an electron of given start energy E_0 in water vapour (3-D space) and stores information about all interactions until the electron is completely stopped.

The collision electron mean free path, used in the program, were derived from summing up the contributions from all single cross sections for ionizations and excitations and were checked for consistency with formula for electron stopping power given by ICRU-16 [1976].

5 types of ionizations of water molecule are considered: one inner shell ionization (hard-collision) and 4 outer shell ionizations in glancing collisions from the shell $1b_1$, $3a_1$, $1b_2$, $2a_1$. The ionized shell is selected according to the partial oscillator strength distribution for all ionizations and excitations processes in water vapor [Paretzke, 1987]. When an excitation take place one of the 12 types of excitations of water molecule is selected and energy loss of these events is recorded.

In the case of ionizing collision, angular deflection of primary electron is calculated from the classical Rutherford cross section. Emission angle of secondary electrons of energies exceeding 200 eV is set on 90° to primary electron, between 50 eV and 200 eV is based on semiempirical fit to Opal et al. [1972] data and below 50 eV is isotropic. In case of excitations no angular deflection is assumed.

When a secondary electron is created, an actual position, energy and direction of primary electron is stored and the secondary electron is traced. This is continued until the secondary electron is completely slowed down and then the primary is considered. When an electron is slowed down below a limiting energy of 8 eV, the rest (subexcitation) energy is deposited in one quantum according to the assumed free path distribution.

An example of application of MOCA-8 is shown in Figs.2.2. Figs.2 a, b, and c show an example of the track structure from the electrons of a typical disintegration of I-125 in water vapor. The point of disintegration is indicated by a plus sign. Fig.2.2a presents the whole track whereas Figs.2.2b and c show expanded view of the central part. Total energy of 11.4 keV was released in form of electron kinetic energy.

2.3.2. Ion track structure code Moca-14

This program was developed in the Institute for Radiation Protection, GSF, Neuherberg by Dr. H.G. Paretzke and in the Pacific Northwest Laboratory, Richland, USA by Dr. W.E. Wilson. The program traces an electron of given start energy E_0 in water vapour (3-D space) and stores information about all interactions until the electron is completely stopped.

Moca-14 is a code for the generation heavy-ion tracks. The program follows the history of an ion of energy E_0 and all its secondary electrons. Elastic scattering of the ion is not considered i.e. the ion is moving along the z-axis without changing its direction.

The ion travels through the medium with the constant energy i.e. it is assumed that even after experiencing an interaction with energy loss E_1 ion conserve its energy E_0 . This type of simulations is called a track-segment regime because only a short segment of the

track is simulated in which total energy lost by the ion is small in comparison to the ion energy.

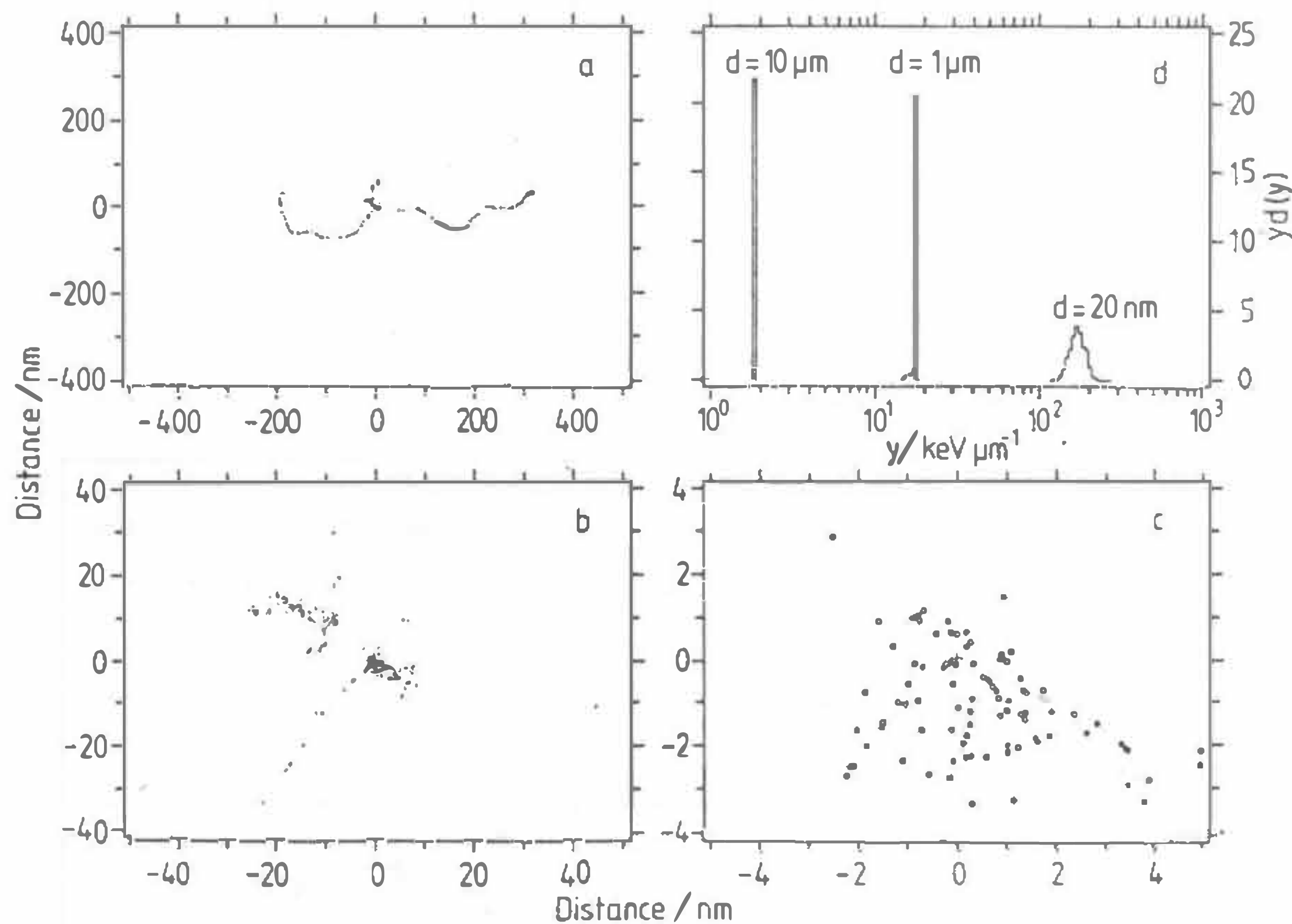


Fig.2.2 Two-dimensional presentation of 3D track structure from electrons of a typical disintegration of I-125 in water vapor. Total energy of electrons $E=11.4$ keV. The sign "+" indicates the point of disintegration. Open circles denote excitations, closed ionizations. (after [Booz et al. 1987])

All energy-deposition events caused directly by the ion have no radial extension i.e. lie directly on the ion axis. For a 0.8 MeV proton about 50 % of all ionizations are created on the track axis. The others ionizations are produced by delta-electrons ejected from the ion axis. The secondary spectrum of these delta-electrons is separately calculated and read by the program in the input data. The spectrum of electrons ejected from the water vapour is calculated from the analytical model of [Miller et al., 1985] that uses photoabsorption and ion impact ionization data to evaluate the coefficients in Bethe's asymptotic cross section for inelastic scattering of high velocity ions. This formula was fitted to the experimental cross sections for 0.5 to 4.2 MeV protons but the author [Wilson, 1988] recommend to use it also for higher proton energies up to 10 MeV. The secondary electrons are traced with the electron track structure code MOCA-8, which is the subroutine in the MOCA-14.

There is practically no experimental data available on excitations in water vapor produced directly by protons. In the MOCA-14 simulation of excitations processes is performed by considering cross section corresponding to the cross sections for electrons of equivalent velocity [Wilson & Miller, 1984]

No special formula for stopping power was built-in to the program, stopping power (and in consequence a mean free path) is considered as a sum of partial cross sections for ionizations and excitations. In Fig.2.3 [Olko et al., 1989] the deviations of the resulting

stopping power from values recommended by ICRU-36 in TE and ICRU-16 in water are shown. In the energy range from 0.2 to 1 MeV the results of Moca-14 match very good the values compiled in ICRU-16. For energies above 3 MeV Moca-14 underestimates the stopping power up to 6%.

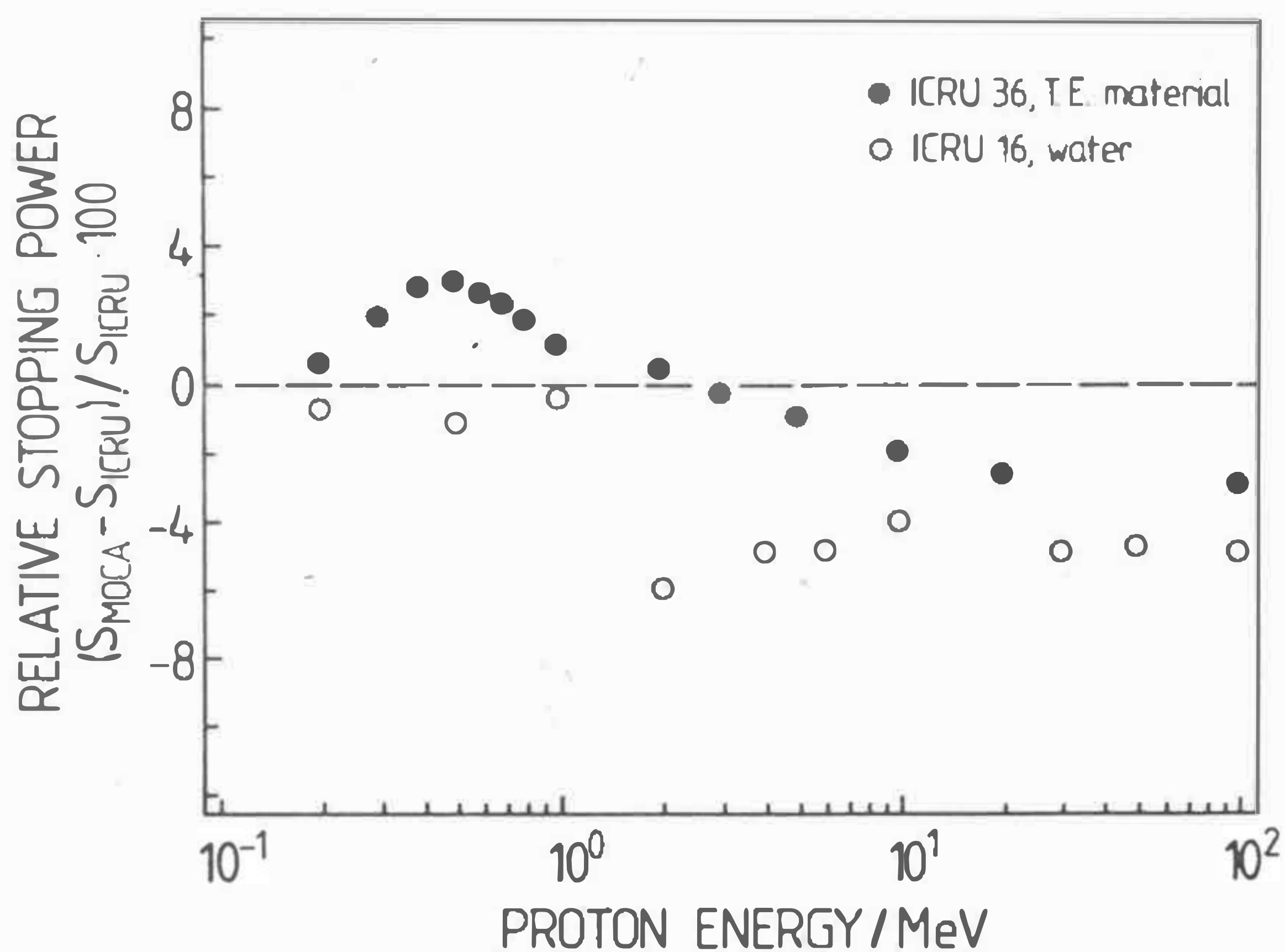


Fig.2.3

Relative stopping power of protons in water vapor as calculated with MOCA-14 and compared with data for TE material (ICRU 36) and water (ICRU 16) [Olko et al., 1989].

The program enables to simulate tracks for ions heavier than proton by multiplying the total interaction cross section by the squared effective charge [Barkas, 1953]. This changes the total collision free path and therefore the total frequency of events. In other words, an heavy ion track is obtained from a proton track by compressing the proton track along the z-axis by the factor z^{*2} . This is demonstrated in Fig. 2.4 where examples of charged particle tracks for proton, Li-6 and C-12 having equal velocities are plotted. Only ionization events are depicted. It is shown that delta-electrons have approximately this same energy spectrum (range) for ions of different Z and identical velocities.

Protons tracks of energies from 0.3 to 10 MeV are presented in Fig.2.5. With increasing proton energy increases the range of delta electrons and decreases the density of ionization on the proton axis.

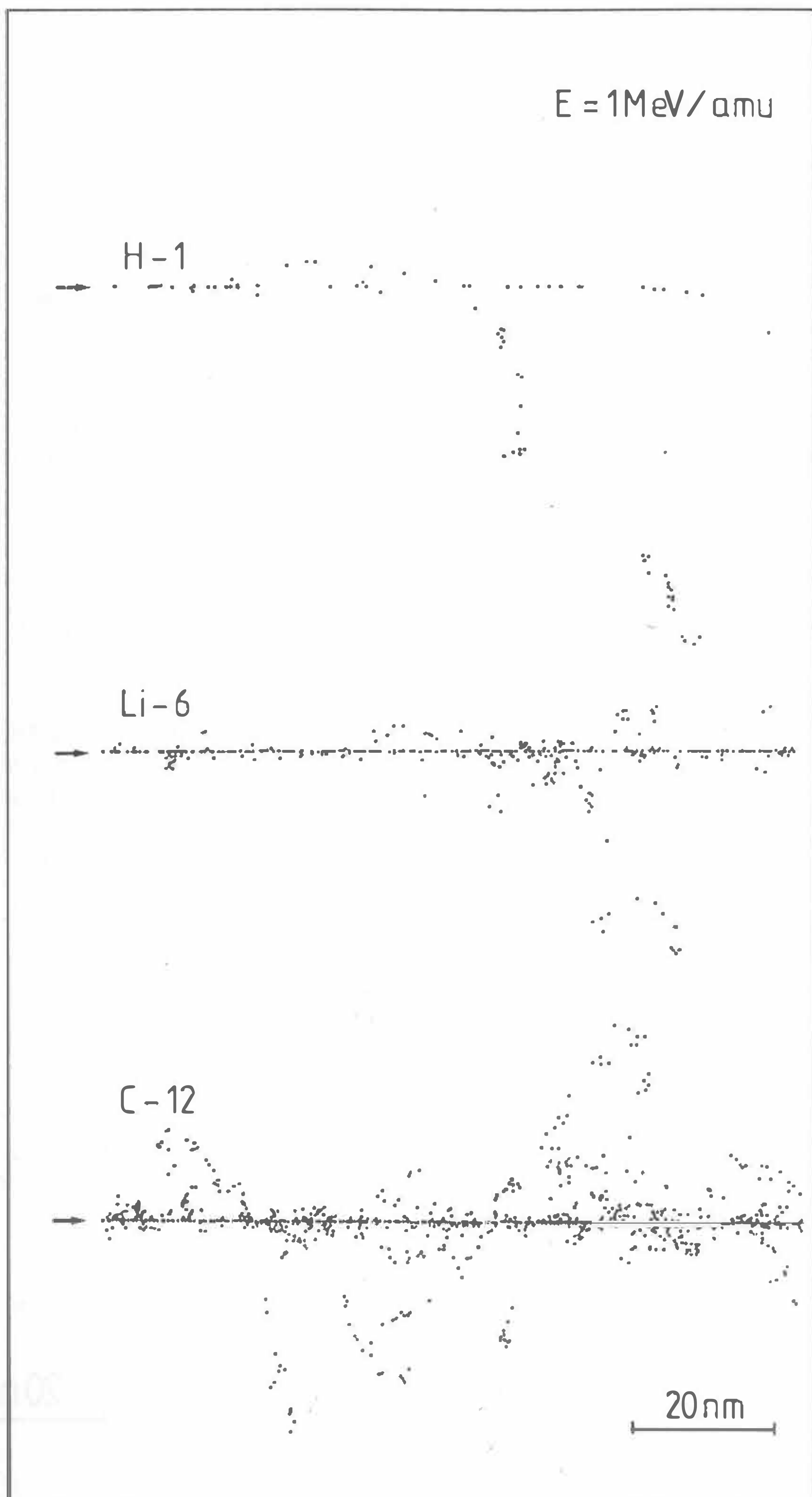


Fig.2.4

Two dimensional presentation of 3D fragments (100 nm in length) of hydrogen, lithium and carbon ions of energies 1 MeV/amu in water vapor scaled from distances in dilute gases to unit density material. Points represent position of ionizations. Calculations were performed with track structure code MOCA-14.

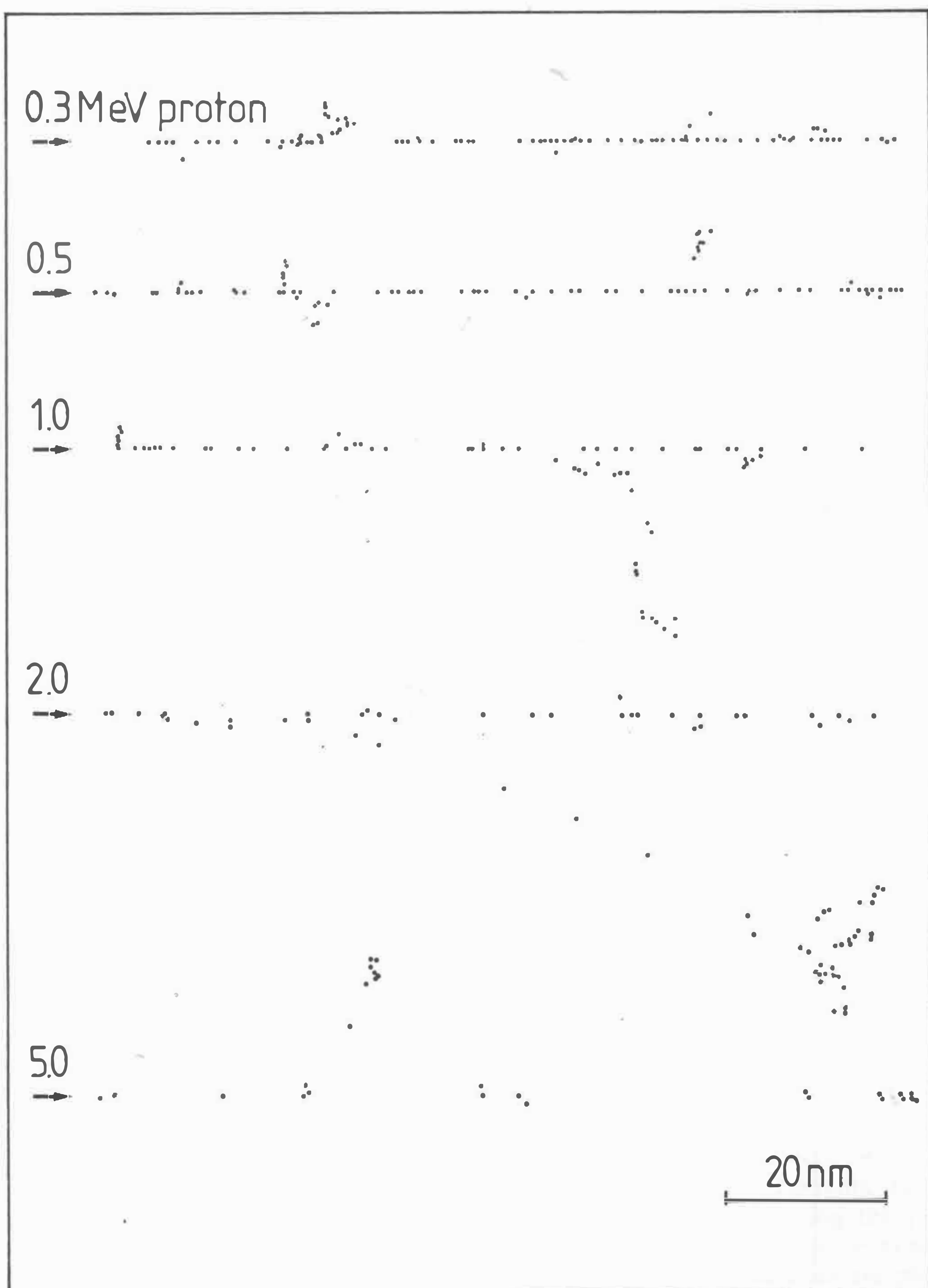


Fig.2.5 Two dimensional presentation of 3D fragments of proton tracks in water vapour scaled from distances in dilute gases to unit density material.

2.3.3. Delimitations of the MOCA programs for use in radiation biology

Delimitations of the MOCA programs for use in radiation biology result from two main reasons:

- inability of the programs to simulate charge particle tracks in real biological media
- limited energy range available for the programs: 20 eV to 100 keV for electrons and 0.3 to 10 MeV for ions.

Tracks are calculated for water vapour because cross sections available for water vapour constitute the most complete set of biologically relevant data. Tracks are just scaled to unit density water. From one side the particular interactions (especially excitations) which take place in a real tissue can be quite different than those considered in the program. On the other hand no special type among these excitations was found to be of particular importance for radiation action besides to contributing to local energy deposition. This fact can justify the present approach.

The highest energy limit of the MOCA-14 is too low to analyse radiobiological experiments with very energetic heavy ions produced by the new generation of accelerators (BEVALAC, UNILAC). The lowest energy range (about 0.3 MeV) does not let for calculations of the end of ion tracks (so-called stoppers, see Ch.3.4). The latter limit is not significant when track-segment experiments are performed but are important when neutron action is considered. The energy limits of the MOCA-8 programs unable to calculate energy deposition distribution for photons of energies exceeding about 250 keV.

3. REVIEW OF TOPICS DISCUSSED IN THIS WORK

This chapter introduces to the main problems concerned in the work and reviews literature dealing with these topics. First (Ch.3.1), the reasons are shown, why macroscopic parameters are not able to predict effects in small biological sites. Then, the alternative stochastic quantities are defined which are related to energy deposition in targets (Ch.3.2). These distributions of energy deposition can, in principle, be simulated experimentally. However, due to technical reasons such simulations are limited to site diameters not much smaller than 1 μm (Ch.3.3). The distributions of energy deposited in smaller targets can be calculated using track structure calculations. However, no calculations were performed which can be directly applied to analyze most of radiobiological experiments, especially for low simulated diameters. Section Ch.3.5 introduces to problems concerning radiation action in living organisms. In Ch.3.6 a concept of Biological Response Function is discussed. Its implication for radiation protection are presented in the Ch.3.7.

3.1. LIMITS FOR THE APPLICATION OF MACROSCOPIC PARAMETERS TO DESCRIBE RADIATION ACTION

It is one of the goals of radiobiology and radiation protection to find an adequate, measurable, physical parameter of ionizing radiation which would be useful to predict biological effects induced by the radiation. Two of such parameters have been in the past of particular importance and still are in common use: the absorbed dose, D, and the Linear Energy Transfer, LET.

3.1.1. Absorbed dose

Absorbed dose is related to the amount of energy imparted to the given mass. The energy imparted, ϵ , by ionizing radiation to the matter in a volume is

$$\epsilon = R_{in} - R_{out} + \sum Q_i \quad (3.1)$$

R_{in} - the sum of the energies (excluding rest energies) of all those charged and uncharged ionizing particles which enter the volume (radiant energy incident on the volume)

R_{out} - the radiant energy emerging from the volume

$\sum Q_i$ - the sum of all changes of the rest mass energy of nuclei and elementary particles in any nuclear transformations which occur in the volume.

The absorbed dose, D, is the limit $\bar{\epsilon}$ by m for $m \rightarrow 0$, where $\bar{\epsilon}$ is the mean energy imparted by ionizing radiation to matter of mass m .

$$D = \lim_{m \rightarrow 0} \frac{d\bar{\epsilon}}{dm} \quad (3.2)$$

The unit of absorbed dose is gray (Gy). According to the definition, absorbed dose is a macroscopic average, related to a mathematical point.

In Fig.3.1 are presented schematically three populations of cells in which three different doses of photons from a Co-60 source are absorbed. The wavy lines represent photons and the short lines crossing the cells represent tracks consisting of ionizations and excitations produced by Compton electrons. At the highest dose of 0.3 Gy every cell is traversed many times and the energy deposition pattern is rather uniform. After a dose of 3 mGy, each cell is traversed, on the average, only once. In reality, hits are independent of each other and, statistically, of about 37% of cells do not experience any events. After a dose of 0.3 mGy energy is deposited in only 10% of cells exposed. But even one were to select from the whole population only cells affected, the amount of energy deposited in these cells would vary from cell to cell. These fluctuations of energy deposition in cell-representing targets, resulting from the discrete manner in which energy is deposited and from the small target dimensions (in relation to the distance between two separate tracks), is called the straggling of energy deposition.

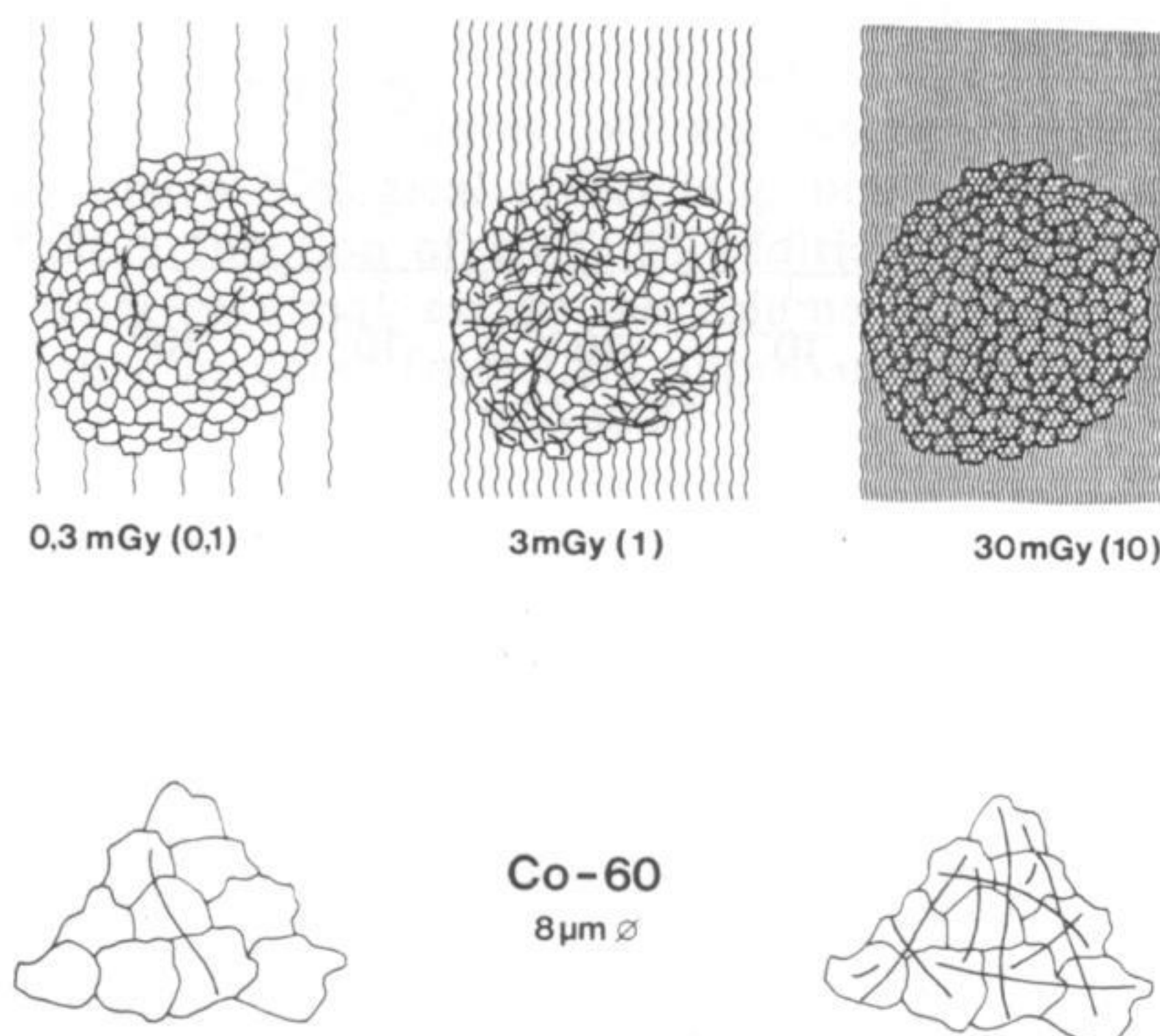


Fig.3.1 *Schematic presentation of aggregates of target volumes (8 μm diameter) in Co-60 gamma radiation fields. Top row: schematic presentation of electron tracks after doses of 0.3, 3 and 30 mGy. Bottom row: enlarged view of some target volumes [Booz & Feinendegen, 1988]*

In Fig.3.2 the relation between the macroscopic dose, D , and the elemental dose¹⁾, δ , experienced by cell nuclei irradiated with Co-60 is plotted. The small dots denote doses δ in single nuclei when a tissue receives a given macroscopic dose, D . For doses greater

¹⁾ Elemental dose is a specific energy (see Ch.3.2.1) in a target volume of 8 μm diameter. 8 μm corresponds to the diameter of the average mammalian cell nucleus.

than 0.1 Gy the microscopic doses do not fluctuate very much, points being situated on the line $D = \delta$. With decreasing dose the distribution of microscopic dose in affected targets becomes independent of dose and only the fraction of cell nuclei "hit", F , (broken line) decreases. This is the low-dose region at which the amount of energy deposited in a single target is not longer correlated with macroscopic dose but depends only on the type of radiation and on the size of the target.

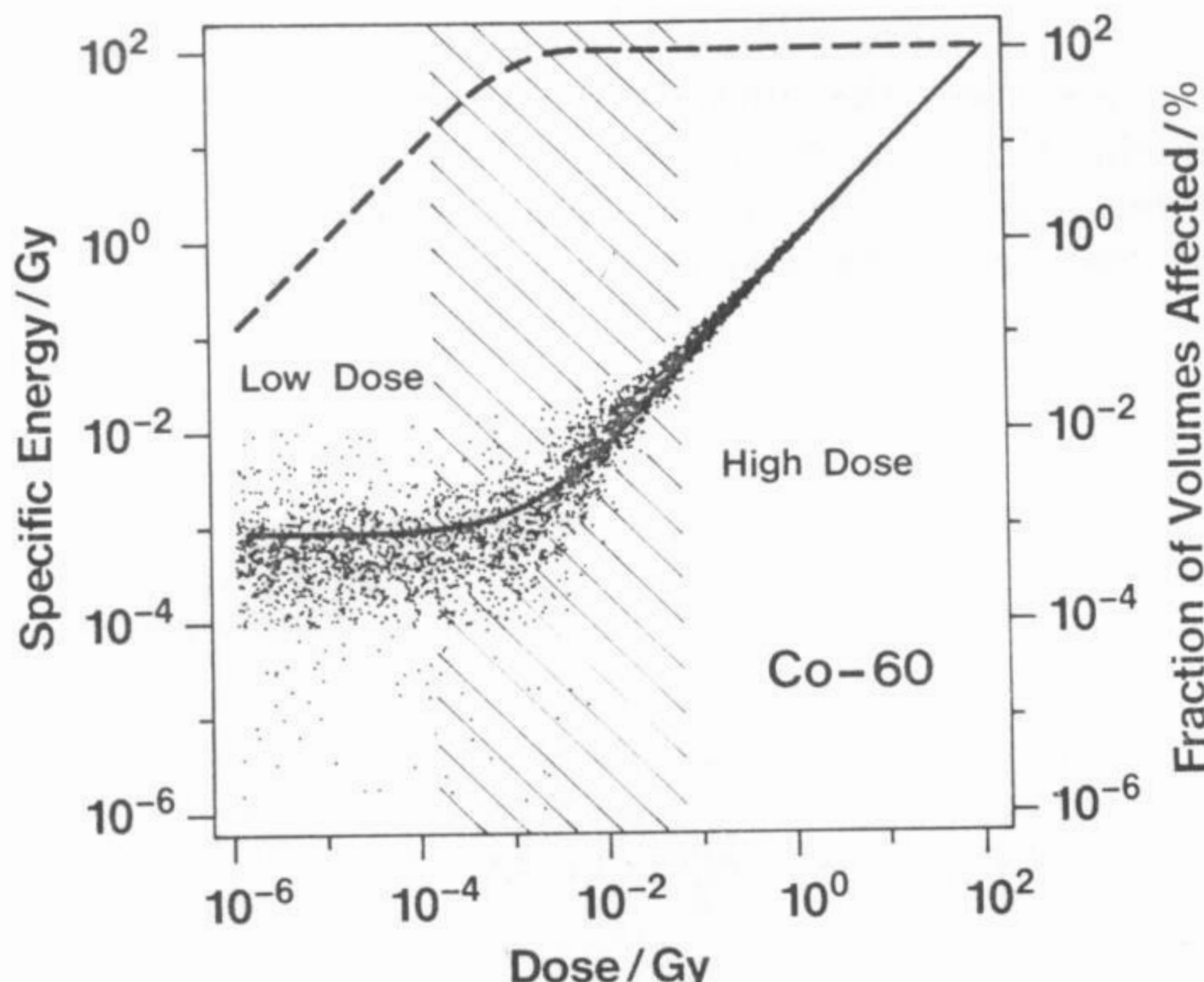


Fig.3.2

Mean specific energy in affected targets (solid line, left ordinate) and fraction of targets affected (dashed line, right ordinate) as a function of absorbed dose for Co-60 gamma-rays. Each dot represents one casual value of z according to the $d(z)$ distribution. The hatched area is the transitional region between low and high doses [Booz & Feinendegen, 1988].

The limits of applicability of absorbed dose in models of radiation action result from discrete picture of radiation interactions and small (in comparison to density of tracks) dimensions of targets. Cells do not respond simply to the average energy density. For "low doses" an average, macroscopic parameter "absorbed dose" cannot account for fluctuations in energy deposition and does not describe a risk for a single, hit cell.

3.1.2 Linear Energy Transfer

Linear Energy Transfer [ICRU 33, 1980] or restricted linear collision stopping power, L_{Δ} , for charged particles is the quotient of dE by dl

$$L_{\Delta} = \frac{dE}{dl} \quad (3.3)$$

where dE is the mean energy loss by a charged particle in traversing a distance dl due to those collisions with electrons in which the energy loss is less than Δ . Δ equal to ∞ indicates that all collisions with electrons have been included and the L_∞ is called unrestricted LET (collisional stopping power). Common units are keV/ μm .

The LET concept has been widely used in radiation protection and in radiobiology. There are however some basic limitations of this concept connected with the fact that a macroscopic, average parameter is not able to describe required microscopic properties of energy deposition. The most important are:

- the LET for a given particle and specified energy is an arithmetic mean energy which a large number of such particles would transfer per unit path length. Thus, LET is not able to account for fluctuations in energy loss among identical particles. The statistical fluctuations occurs because number and types of primary interactions with atoms in the medium are stochastic quantities (straggling of energy loss) [Vavilov, 1957];
- two particles can have this same LET but completely different delta-ray spectra due to differences in charge and velocities. For example, the LET of 0.5 MeV proton in ICRU tissue is 42 keV/ μm [ICRU 36, 1983] and is approximately equal to LET of 10 MeV/amu Li⁺³ ions. However, the maximum range of delta-electrons ejected by the proton is 140 nm whereas for the latter about 8 μm . This implicates that a biological effect (e.g. biological cross section, see Ch.3.5) cannot be a unique function of LET. In addition, when energy in a small target is considered, delta-rays may escape the volume of interest and energy deposition can be smaller than assumed from LET approximation;
- the range of a charge particle can be limited with regard to dimensions of the volume of interest. A slow ion can be totally stopped in a volume of interest and a real energy deposited in a volume will be smaller then calculated with assumption of a constant LET;
- LET does not consider the length of the track relative to a finite target structure. In other words, when a target is hit the energy imparted to the volume depends not only on LET but on the actual particle chord length as well.

Kellerer and Chmelevsky [1975a] and Leuthold and Burger [1985] formulated criteria for applicability of LET when energy deposition in 1 nm to 10 μm targets are considered. They took into account the limitations described above. According to these criteria, LET can properly describe ions and electrons energy deposition only in particular region of particles energy and target diameter. E.g. straggling and delta-ray escape must be taken into account for 1 μm sites for protons faster than 10 MeV whereas for 0.1 μm targets for 2 MeV protons. For describing energy deposition in smaller targets as e.g. in DNA structures LET concept should not be used.

3.2. MICRODOSIMETRIC QUANTITIES AND DISTRIBUTIONS

It was shown in the previous section that average, macroscopic parameters have limited possibilities to explain radiation action. This section deals with quantities and distributions relevant to stochastic action of ionizing radiation in small targets.

3.2.1. Quantities.

The basic quantity used in microdosimetry is called energy imparted to the matter in a volume, ϵ (Eq.3.1). The quotient of energy imparted, ϵ , and the mass of the volume, m , is called specific energy, z ,

$$z = \frac{\epsilon}{m} \quad (3.4)$$

The unit of z is the joule per kilogram (gray).

When energy imparted, ϵ , is divided by the mean chord length of the volume¹⁾, \bar{l} , the resulting quantity is called lineal energy, y .

$$y = \frac{\epsilon}{\bar{l}} \quad (3.5)$$

The most commonly used unit of y is keV/ μm .

ϵ is a stochastic quantity. Also specific energy, z , and lineal energy, y , related to ϵ by constant factors, are stochastic quantities. The relation between z and y for a sphere of unit density is following

$$z [\text{Gy}] = 0.204 \frac{y [\text{keV}/\mu\text{m}]}{d^2 [\mu\text{m}]} \quad (3.6)$$

Instead of energy imparted to the volume one can also consider the number of ionizations in the volume of interest, j .

3.2.2. Distributions

ϵ , j , z , y are stochastic quantities. It is useful to consider the corresponding probability distributions. The following distributions are used in microdosimetry:

a) distribution function $F(y)$

The value of $F(y)$ is the probability that lineal energy is less or equal to y

¹⁾ Mean chord length of the convex body having volume V and surface S is $\bar{l} = 4V/S$. For the sphere, $\bar{l} = 2/3 d$, where d -sphere diameter.

b) probability density $f(y)$ (lineal energy frequency distribution) is defined

$$f(y) = \frac{dF(y)}{dy} \quad (3.7)$$

The first moment of $f(y)$ is called frequency-mean lineal energy, \bar{y}_F .

c) dose distribution $D(y)$

The value of $D(y)$ is the probability that absorbed dose is delivered with lineal energies less or equal to y .

d) dose probability density (lineal energy dose distribution) $d(y)$ is

$$d(y) = \frac{dD(y)}{dy} \quad (3.8)$$

The first moment of $d(y)$ is called dose-mean lineal energy, \bar{y}_D .

The relation between $d(y)$ and $f(y)$ is

$$d(y) = \frac{y}{\bar{y}_F} f(y) \quad (3.9)$$

Similar definitions and averages can be defined for energy imparted, ϵ , number of ionizations, j , and specific energy, z .

In Fig.3.3 the difference between the frequency and dose distributions is schematically explained. A population of 11 sites were crossed by an ion leading to producing ionizations in 6 sites. Only the affected sites are considered. Two of the sites get one ionization per site, the next two 2 ionizations and the last two sites 3 ionizations per site. Frequency distribution of ionization is being constant (the left distribution). The distribution from the right side shows the dose distribution of ionizations corresponding to the pattern of energy deposited. One ionization events contribute in 1/6 to total dose, two ionization events in 1/3 and three in 1/2 to total dose.

All energy deposition processes which take place in the volume due to action of a single one particle track are called an event. The energy imparted to the volume may come from one or from more events (tracks). Microdosimetric distributions which consider only energy deposition due to single-events are called single-event distributions and are denoted with the subscript 1, e.g. $f_1(y)$.

A single-event distribution is independent of the absorbed dose, as exemplified in Fig.3.2. When the energy deposition distribution in a target population is calculated, only those targets are considered which are affected. With decreasing dose the fraction of hit targets decreases but the pattern of energy deposition in affected targets is not changing. Multi-event distributions $f(z; D)$ are dose dependent. These distributions can be calculated from a single-event distribution by folding procedure [Kellerer, 1968]

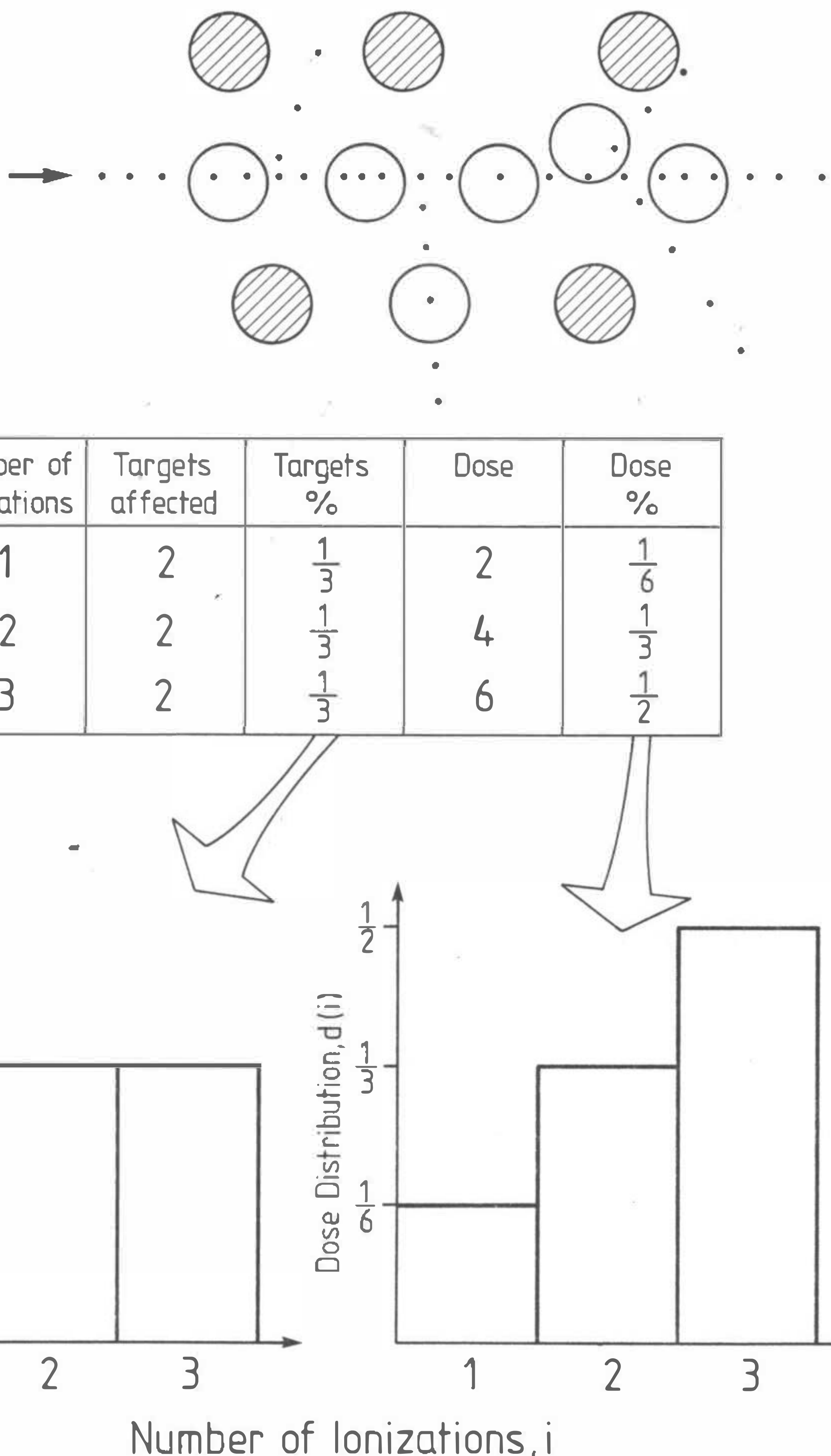


Fig.3.3

Schematic explanation of differences between the frequency and dose microdosimetric distributions. For more explanation see text.

For low doses, namely $D/\bar{z}_F \ll 1$, this relation can be written

$$f(z; D) = \frac{D}{\bar{z}_F} f_1(z) \quad (3.10)$$

Radial dose distributions offer another approach to describe the nonuniformity in energy deposited by heavy charged particles. These distributions found important applications in radiobiology in the so-called Katz model [Katz et al., 1971]. Radial dose $D(r)$ is the average energy imparted to a cylindrical volume having radii r and $r + dr$ divided by the mass of the cylinder.

Radial dose is not a stochastic quantity and is not directly correlated with energy deposition in a site. It is however possible to approximate microdosimetric distributions by stochastic sampling of radial dose distributions. The quality of the approximation increases when the maximal range of delta-rays is getting smaller in comparison with the site size [Varma & Zaider, 1989]

3.3. MEASUREMENTS OF ENERGY DEPOSITION DISTRIBUTIONS

3.3.1. Principles of simulation of a sensitive volume with proportional counters and their limitations.

It is actually not possible to build a solid detector¹⁾ of unit density and of micrometer (or smaller) dimensions which can measure distributions of energy deposition. It is however possible to use a large volume filled with a low density gas in which a charged particle will experience identical energy loss as in micrometer volume of unit density.

When the S is a mass stopping power, ρ_0 density and l is the actual chord length this leads to the following relation

$$S_g \rho_{0g} l_g = S_t \rho_{0t} l_t \quad (3.11)$$

where subscript g corresponds to the gas and t to the tissue. Assuming identical mass stopping powers $S_g = S_t$ and site diameters $l_t = 1 \mu\text{m}$ and $l_g = 30 \text{ mm}$ the required density of the gas in the counter is 0.033 kg/m^3 .

First microdosimetric proportional counter working with this principle was developed by [Rossi & Rosenzweig, 1955]. This solid wall spherical counter consisted of a tissue-equivalent conducting chamber (cathode) and the central collecting wire (anode), which was electrically biased from the anode. In order to assure a cylindrical electric field around the anode an additional helical electrode was used. A wall-less counter (Fig.3.4a) was introduced to microdosimetric measurements in order to avoid so-called wall-effects i.e. a distortion of the secondary particle spectrum due to presence of the solid interface

¹⁾ A prototype of the first semiconducting microdosimetric counter was built by [Orlic, 1989]. However, due to calibration problems, results of measurements had not been yet presented in terms of energy deposition distributions.

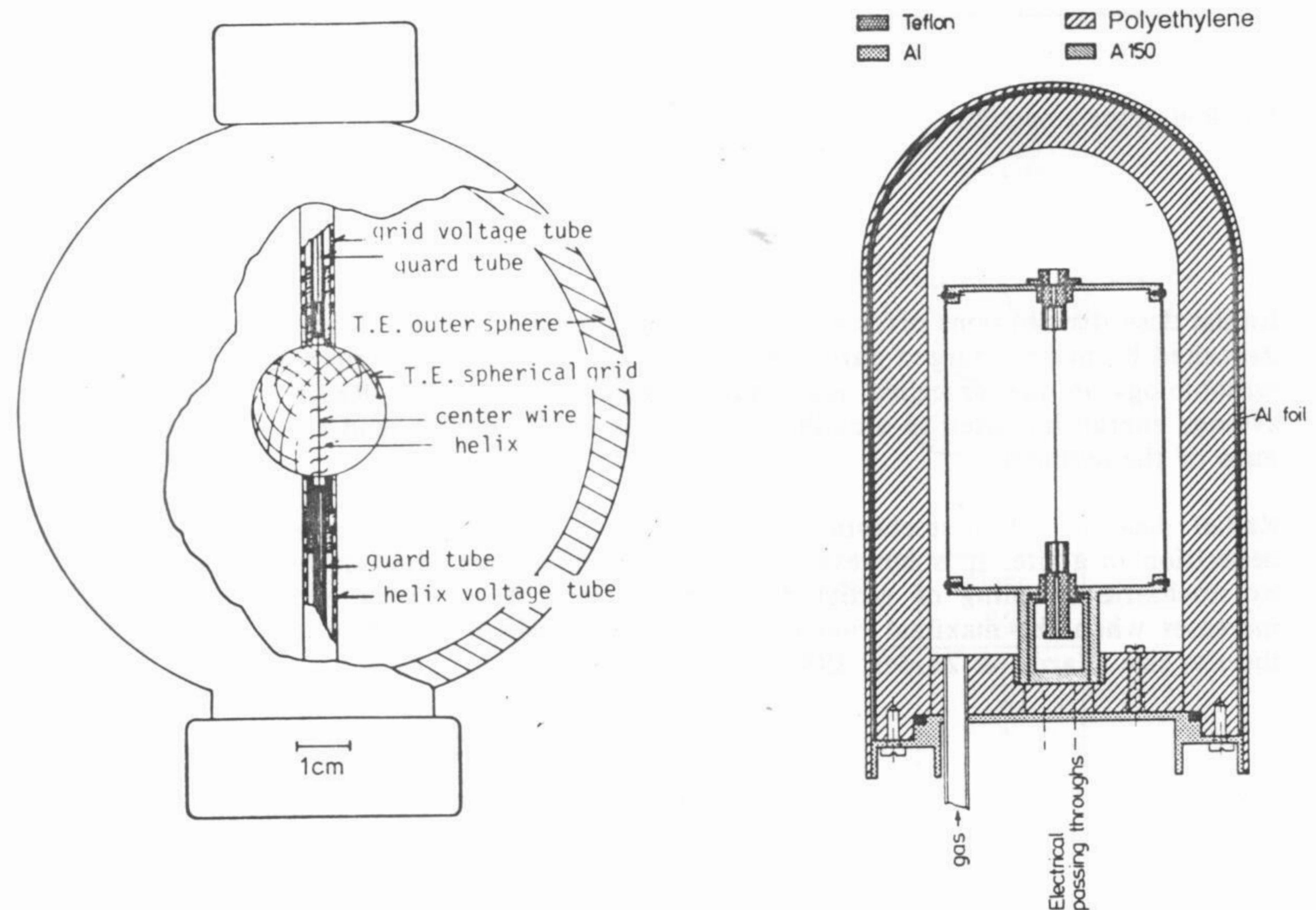


Fig.3.4

Examples of microdosimetric proportional counters:

- a) *A wall-less grid counter mounted inside of a spherical tissue-equivalent plastic shell. This construction is used to minimize the influence of solid walls.*
- b) *A walled, KFA Tissue Equivalent Proportional Counter. The thin inside wall is to assure the charge particles equilibrium in the sensitive volume. The thick outside wall is to simulate measurements in conditions (10 mm depth in 30 cm ICRU sphere) required by radiation protection regulations.*

surrounding the sensitive volume. Borders of the sensitive volume in a wall-less counter are usually delineated by a grid built from a conducting, TE plastic. A structure of the grid is usually transparent for radiation in about 90%. The grid (a sensitive volume) is positioned in a solid shell of dimensions large enough to establish radiation equilibrium in the sensitive volume.

A disadvantage of spherical counters is the necessity of using a helix to correct electrical field distribution around the anode because the helix introduces additional uncertainties in measurements [Bednarek et al., 1988]. Therefore, the conventional cylindrical proportional counters are now more likely applied in practical applications e.g. as radiation protection monitors. Cylindrical walled KFA counter is shown in Fig.3.4b. The quadratic cylinder is used which has the same mean chord length as sphere of identical diameter. The thin, inside wall from TE A-150 conducting plastic is to assure the equilibrium of secondary particles in detecting gas. The thick outside wall is used to simulate the measurements on the certain depth in the human body [Schmitz et al., 1985]

A number of primary ionizations in the sensitive volume is approximately proportional to the energy deposited to the volume by a single track. Pulse heights, which are assumed to be directly proportional to the number of ionizations, are stored in a multichannel analyzer and after calibration are presented as a frequency distribution of lineal energy or more frequently are recalculated on dose distributions.

It is, however, not yet possible to accurately simulate, with a proportional counter, a sensitive volume smaller than $0.25 \mu\text{m}$. The limit arises from the fact that, for such low pressures of the gas, the multiplication region around the anode wire becomes comparable with the dimensions of the counter. In that case, pulse heights are not any more proportional to the primary number of ionizations.

There are some experimental techniques which try to overcome these difficulties and measure energy deposition in nanometer volumes as initial recombination method [Sullivan & Zielczyński, 1976] or "ion counter" method [Pszona, 1976]. Most recently [Kliauga, 1989] demonstrated preliminary, qualitative results of measurements of microdosimetric distributions produced by 14 MeV neutrons in counter with 5 nm simulated diameter. Even if some new experimental techniques give some promising results they still are under development.

3.3.2. Proportional counter measurements of microdosimetric distributions.

A large set of microdosimetric distributions were measured in the last 30 years. However, not many experiments were performed for one counter with different photon energies and for various simulated diameters. Such measurements enable to study the structure of microdosimetric distributions with regard to parameters of radiation and the counter.

The most complete set of measurements were done by Kliauga and Dvorak [1978] with the wall-less tissue equivalent Rossi counter shown in Fig.3.4a. They measured distributions for 6 simulated diameters from $0.25 \mu\text{m}$ to $8 \mu\text{m}$, using for each diameter 8 photon energies from 12 to 1250 keV. It was demonstrated that a shape of microdosimetric distributions is sensitive to the primary photon energy and the simulated site size. They observed that with increasing photon energy increase variances of the distributions. Some irregularities for energies between 40 and 150 keV were attributed to the transition from photoeffect to Compton effect. The influence of these effects on \bar{y}_F and \bar{y}_D were investigated by a simple approximation of electron tracks with straight lines.

[Schmitz et al., 1989] studied response of a walled KFA Tissue Equivalent Proportional Counter in semi-monoenergetic photon fields. In these measurements, performed with simulated diameter of $2 \mu\text{m}$, 16 photon spectra of average energies of 6.5, 9, 12, 17, 26, 33, 48, 65, 83, 100, 118, 161, 205, 248, 661 and 1250 keV were used. It was demonstrated that for the transition region between the photo and Compton effect (20-150 keV) the shapes of distributions are irregularly related to photons energy. E.g. the distribution for 17 keV and 118 keV photons were almost identical. For 33 keV a double peak was observed, which could not be explained with any available method [Schmitz, 1988].

These type of effects are difficult to be investigated with proportional counters because this experimental technique give no insight into the measured distributions. In addition no calculations of photon induced microdosimetric distributions are available which would help in understanding of measured distributions.

Measurements of ion-induced microdosimetric distributions are more difficult than those for photons due to the lower penetration of ions. For these purposes only wall-less counters with thin windows can be applied. Only a few measurements are available.

First measurements of energy deposition distributions from a broad beam of 5.3 MeV alpha particles and for the simulated diameter of 1.04 μm were reported by Glass and Braby [1969]. They observed a triangular microdosimetric distribution slightly distorted by straggling of energy loss and by contribution of delta-electrons ejected by ions passing outside the sensitive volume. Gross and co-workers [1970] measured frequency distributions of lineal energy, $f(y)$ for ^{241}Am alpha-particle source and simulated diameters 0.5 to 2 μm . They also observed contribution from delta-events (touchers) to energy deposition in a target which increased with decreasing simulated target diameter. In later experiments Gross and Rodgers [1972] used narrow pencil beams of 1.7 and 4 MeV protons to investigate energy deposition in 0.18 to 1.0 μm diameter targets as a function of the impact parameter¹⁾. They also evaluated the percent of dose to the target from touchers, which was slightly lower than those calculated theoretically [Kellerer, 1971].

The same counter was used by Kliauga and Rossi [1976] to measure impact parameter-dependent energy deposition in a 1 μm site for 10 MeV protons, 40 MeV Li^{3+} and 23 MeV protons. They observed that for impact parameters $b>1$ events in the target were 9 times more frequent for Li^{3+} ions than for 10 MeV protons. This finding was consistent with the Z^2 dependence for the production of delta-rays.

Recently, Meiting and co-workers [1988] reported measurements of microdosimetric distributions for high-energy heavy ions (600 MeV/amu). The proportional counter used in the experiments was surrounded by a larger gas chamber in order to avoid "wall-effects" and to provide equilibrium conditions for delta-rays from 600 MeV/amu ions. Microdosimetric distributions were measured for several impact parameters ("pencil-beam" irradiation) and then integrated over the impact parameter in order to obtain microdosimetric distributions $f(z)$. It was shown, that even for targets as large as 1.3 μm 78% of events are produced by delta-rays. It was also stated that the frequency-mean specific energy, \bar{z}_F , for delta-rays which occur at large distances from the ion path, exceeds the calculated radial dose distribution by two orders of magnitude. This comparison suggests the inadequacy of radial dose distributions in the description of energy deposition in a site distant from the ion path.

3.4. CALCULATIONS OF MICRODOSIMETRIC DISTRIBUTIONS

3.4.1. Principles of calculation using track structure simulations

A charged particle track contains information on the coordinates of all ionizations and excitations (transfer points) produced in the medium by the charged particle. The procedure of calculating a microdosimetric distribution from the track is called scoring in this work.

The most straightforward scoring is done by sampling with constant probability throughout the medium. Assume that the track consist from M transfer points T_i , with

¹⁾ The impact parameter, b , is the ratio x/r where x is the distance from the center of a target and r is the target radius.

$i=1, \dots, M$. One use a Monte Carlo technique to generate randomly N points in the medium. Each point is the center of a sampling sphere. The energy deposits in the i -th sphere ϵ_i , ($i=1, \dots, N$) is calculated and ϵ_i are stored in a histogram. Resulting distribution is a frequency distribution of energy deposition, $f_i(\epsilon)$. A disadvantage of the technique is that for sampling with a small diameter one may obtain many sampling points with zero energy deposit which are not relevant to a single-event distribution.

These difficulties are avoided in a sampling over individual transfer points [Kellerer & Chmielevsky, 1975b]. In this sampling technique one selects randomly a transfer point ϵ_i with selection probability proportional to ϵ_i . Then the center of a sampling sphere is randomly selected in the distance from point "i" not exceeding the sphere diameter. The energy deposited in the sampling sphere is stored and lead to dose distribution of energy deposited $d(\epsilon)$ because the selection probability is proportional to the value of ϵ_i . In this scoring technique no zero events are possible because to the energy deposition in a sphere "i" contributes at least one transfer point with energy ϵ_i . For other specific methods of scoring of microdosimetric distributions see [Chmielevsky and Kellerer, 1977], [Charlton et al., 1985].

It is useful to consider different classes of particle tracks with regard to their position to the sensitive volume. In the Fig.3.5 these classes of particles are schematically shown. For more information see ICRU-36 [1983].

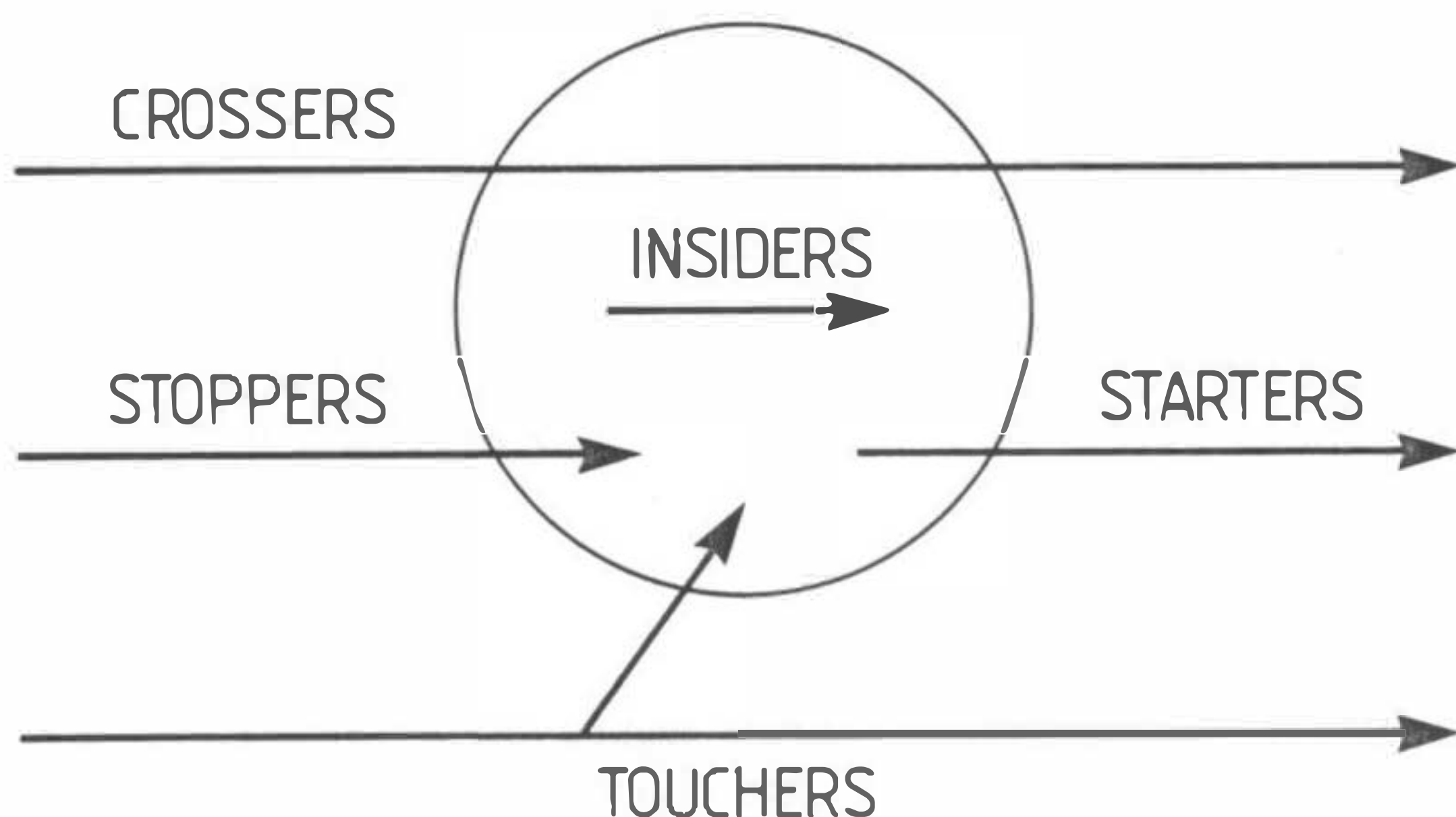


Fig.3.5 Classification of particle tracks with regard to their position to the sensitive volume: insiders, starters, crossers, stoppers and touchers.

3.4.2. Review of calculations for photons

Goodhead and Thacker [1977] used a simple analytical method to approximate distribution in a small targets for soft X-rays. In this method an electron track was assumed to be a segment of a line. Probability of interception of the track with a spherical target was investigated with methods of geometrical probability. Different analytical calculations in nanometer sites were performed by Odo and Iwanami [1984],

who calculated frequency distributions of the number of primary events in nanometer targets, induced by C-60, 7 MeV electrons and tritium electrons in water. Goodhead and Brenner [1983] calculated energy deposition in the nanometer targets using track structure calculation. They apply the computer code Phoel-2 [Turner et al., 1980] to calculate spectra of secondary electrons in water vapor and corresponding tracks of electrons with the program MOCA-7B. The calculations were performed for targets from 1 to 20 nm and for X-rays of energies 0.3, 1.5 keV and 250 kVp. Results were reported in terms of probability of deposition in the target of energies greater than an assumed threshold.

Unfortunately, in the above works the computed quantities were not presented in a form used typically in microdosimetry (e.g. as functions of lineal energy, y), nor were the calculations extended to sites of micrometer dimensions, which made direct comparison with experiment impossible. No evaluations were available which could assess energy deposition in nanometer sites and at the same time be verifiable in micrometer region, against the available measurements with tissue equivalent proportional counters.

3.4.3. Review of calculations for ions.

Together with experimental techniques, several numerical approaches were developed. Many efforts were directed towards assessing energy deposition in nanometer targets, for which measurements are not yet possible.

The most important group of methods for calculating microdosimetric distributions is based on Monte Carlo track structure simulations. A detailed description of the Monte Carlo program used in this work (MOCA-14) is given in Ch.2.3.2.

The first complete calculations of microdosimetric distributions for ions were performed by Kellerer and Chmelevsky [1975b]. They developed convenient statistical methods to extract microdosimetric information from simulated tracks. Tracks of H^+ , He^{+2} and C^{+6} ions generated by an early version of the MOCA-3 program prepared by Paretzke [1973] were used. It was shown that for nanometer-size targets straggling of energy deposited is considerable and triangular distributions cannot be used to approximate the stochastic of energy deposition in spherical targets from heavy ions.

A new code, MOCA-13, was significantly improved by implementing a new model of ion-ejected secondary electron spectra and by modification of electron transport [Wilson & Paretzke, 1980]. Microdosimetric distributions were calculated for different impact parameters in order to simulate narrow beam experiments, however, no comparisons with measurements were made. An improved version of the MOCA program (MOCA-14) was used to build a semi-theoretical model for energy deposition from protons in spherical sites of diameters in the range from 1 to 1000 nm [Wilson et al., 1988]. This model describes energy deposition from protons of energies between 0.25 to 20 MeV. The model is applicable only for crossers i.e. for events with impact parameters $b < 1$ but does not take into account touchers which for simulated sites of some nanometers can deliver even more than 50% of the total dose.

Quantities of interest in radiobiology, such as lineal energy distributions and radial dose distributions, were also calculated with another track structure code PROTON [Brenner & Zaider, 1984]. Authors showed that these quantities, especially at the nanometer level, appear to be sensitive to cross section data used in the track structure code and to the

approach used in calculations e.g. inclusion or exclusion of excitations when microdosimetric distributions are scored from tracks.

In summary, it is worth to stressing that neither measurements nor calculations yield a complete set of microdosimetric distributions (energies, ions, site diameters) which could be readily applied in radiobiological calculations. It is however clear that in the evaluation of such data for sites of nanometer-sizes, straggling of energy loss and delta-ray transport must be taken into account.

3.5. MICRodosimetry AND RADIATION BIOLOGY

This section contains an introduction to the problem of radiation action in living organisms and shows the connections between radiation biology and radiation protection. In Ch.3.5.1 biological sensitive sites and their dimensions are described. In Ch.3.5.2 some basic radiation-induced biological effects are presented. The next section (Ch.3.5.3) discusses radiation effects qualitatively and shows how different radiobiological models extrapolate from the region of high dose to the low-dose region, relevant for radiation protection.

3.5.1. Sensitive sites in biological cells

The purpose of this section is to present a spatial organization and dimensions of biological cells with the special emphasis on the DNA. This presentation should give a review of potential target diameters.

The smallest physiologically independent constituents of biological systems are biological cells. A typical mammalian cell has a mass of 1 ng and is separated from the outside environment by a cell membrane. The cell membrane covers cytoplasm, which constitutes an environment for some structures in the cells called organelles. The biggest and the most important organelles is a cell nucleus. The cell nucleus is separated from the cytoplasm by a nuclear membrane. The most important component of the cell nucleus are molecules of the deoxyribonucleic acid DNA which are coding genetical information of the cell.

Radiobiological experiments indicate that the biological matter is not uniformly sensitive for radiation. Cytoplasm is very resistant for radiation and even high doses do not affect physiological processes going on there [Davies & Evans, 1966]. Almost exclusively, all effects on the cell as mutations or cell death are produced by interactions with a cell nucleus.

The primary structure of DNA molecule is a polymer strand build of 4 types of nucleotides. A nucleotid has three components: piramidine base, sugar and phosphate. The strand is formed by binding a sugar unit from one nucleotid with a phosphate of the next nucleotide, this phosphate is connected to the sugar of the next nucleotide etc. This sugar-phosphate backbone form right handed helix with diameter of 2 nm [Kornberg, 1985]. Two strands of DNA are usually wounded around each other building a DNA double helix [Watson & Crick, 1953]. These two chains are connected by hydrogen bonds between the bases. Each full turn of the helix has a length of 3.4 nm. A typical length of the DNA molecule is large (some millimeters) in order to code genetical information about the cell.

A DNA molecule does not usually occur unbounded in the cell nucleus. It is associated with proteins called histons creating more stable but complicated spatial secondary structures. First, a two turns of the DNA double helix are wrapped around a complex of histons building a nucleosome. The diameter of nucleosome is of about 10 nm. At the next level of organization strings of nucleosomes appear to wind up into a solenoid to form a fiber, 20-35 nm thick. Only during the cell division (mitosis) the fiber forms a next order structure called chromosome, but for the most time of cell life (interphase) the nucleosome fiber fills randomly the cell nucleus. This structure of the DNA is schematically presented in Fig.3.6.

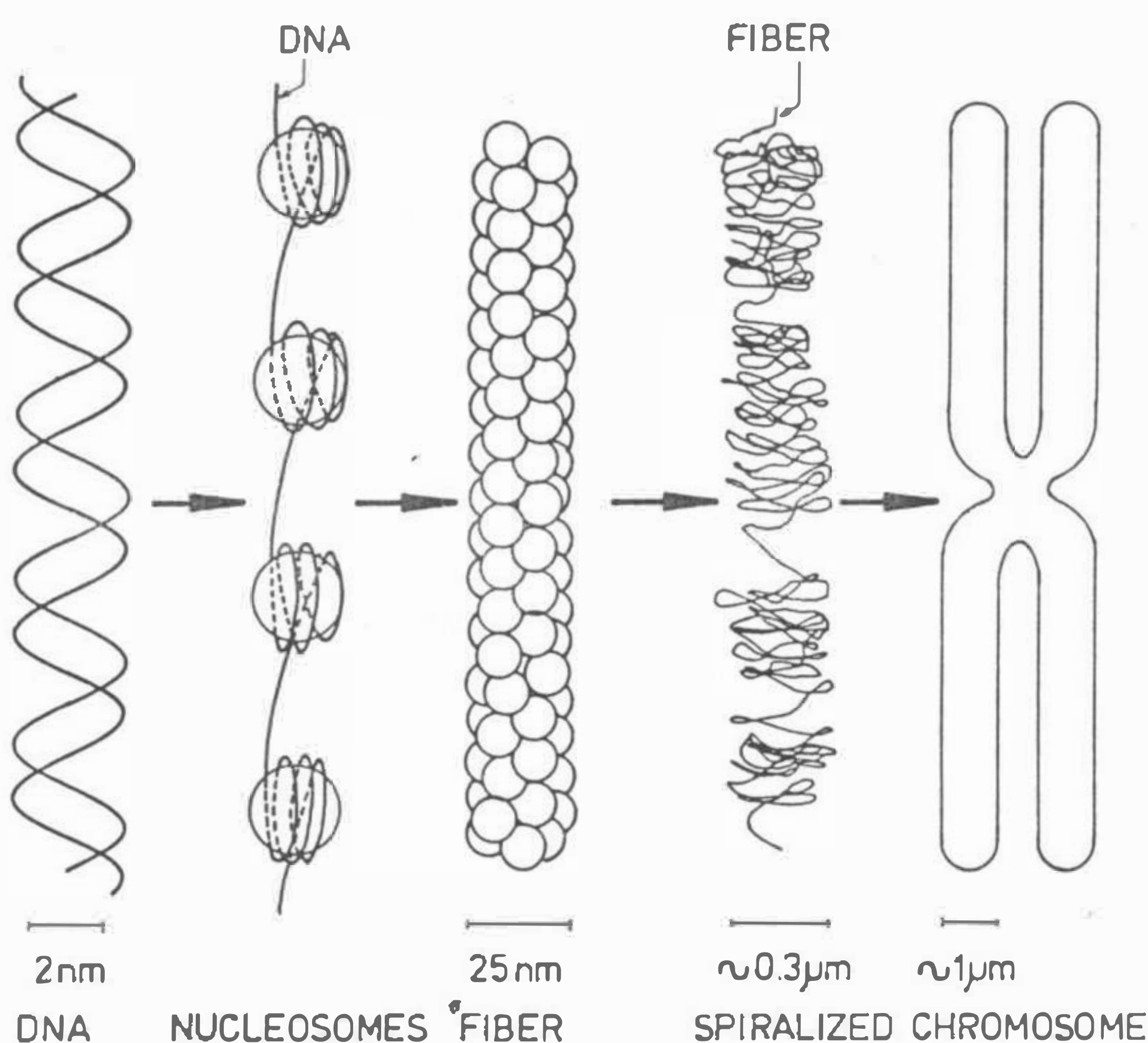


Fig.3.6 A schematic representation of how the very long DNA double helix molecule is spatially organized to create the visible chromosome at mitosis (after [Chadwick & Leenhouts, 1981])

3.5.2. Radiation induced biological effects

Energy imparted by ionizing radiations is usually very small in comparison with the amounts of energy used by man in typical activities. An absorbed energy of 4 joules per kilogram can increase the temperature of an irradiated object by 0.001 K at maximum of (assuming that no exothermic chemical reactions take place) and is not even detectable by human senses. For human beings, this "small" absorbed dose of 4 Gy has very serious consequences, leading mainly to death! The reason for this enormous efficiency of ionizing radiation is that it deposits energy in very concentrated portions, producing ionizations and excitations in atoms and molecules.

Living organisms are organized hierarchically: atoms and simple molecules, polymolecules (DNA, RNA, proteins), cells, tissues, organs, organisms. Radiation action occurs at the level of atoms and molecules but this molecular damage only initiates a long chain of

physico-chemical, chemical and biological processes leading to alterations having serious consequences for the whole organism [Booz & Feinendegen, 1987]. Genetic changes or cancer induction, which are of interest for radiation protection, are supposed to be developed from lesions in single cells caused by physical (radiation), chemical or biological (viral) agents. Biological cells are the smallest metabolically independent constituents of the human body. Therefore, to understand radiation effects in the human being one has to understand the radiation effects in cells.

There is increasing evidence that defects in the DNA molecule can change the genetic code of the cell, leading to mutations, or can hinder mitosis, leading to cell death. Two types of DNA damage are considered. Firstly, one of the four types of nucleotide bases can be affected, this type of lesion being called base damage. Secondly, a DNA sugar-phosphate backbone (DNA strand) can be disrupted. When one of the complementary chains is broken up, this lesion is called a single strand break, when both - a double strand break. The base damage alteration seems to be of minor importance for inducing biologically important lesions [Swinehart & Cerutti, 1975], [Chadwick & Leenhouts, 1981]. The most important lesions of DNA are strand breaks and only these types of DNA lesions will be further considered.

Chromosomes are structures in an eucariotic cell which are visible in a light microscope during the cell division. There are strong indications that every chromosome consists of a single, continuous double-helix DNA molecule. This DNA molecule is mechanically stabilized by folding with histons complex secondary structures. A diploid human cell contains 46 chromosomes, each of the size of a few micrometers. Structural changes in chromosomes observed before DNA replication (when single chromatid is seen) are called chromosome aberrations. After chromosome replication, two identical sister chromatids are present. Changes in this structure are called chromatid aberrations. Measurements of frequency of chromosome aberrations in human cells can inform *a posteriori* of absorbed dose (so-called biological dosimetry e.g. after nuclear accidents).

Somatic mutation is defined as a change in a genetic information in a somatic cell which is copied to the next generation of cell in mitotic division. Somatic mutations are classified as point-mutations, when alteration is associated with only one gene or as chromosome mutations, when changes take place in several genes. These type of lesions are considered as particularly relevant for studying radiation carcinogenesis.

Cell survival is the most common end-point studied in radiobiology. Cells plated on glass and irradiated, divide and form colonies. If this process does not occur after irradiation, the cell is considered to be inactivated (cell death).

3.5.3. Quantitative description of radiation induced lesions

Dose is a physical parameter most frequently used in radiobiology. Results of radiobiological experiments are usually presented in terms of dose-response curves i.e. survival, frequency of mutations etc. are plotted against dose.

Typical dose-response curves are shown on the Fig.3.7. These types of curves are called survival curves because they represent the fraction of organisms, S, which survived after irradiation with a given dose, D. Heavy ion survival curves usually demonstrate, in the linear-logarithmic coordinate system, a linear dependence on dose. Most frequently X-ray survival curves exhibit a significant quadratic component (shouldered curve).

Survival curves are usually fitted by formulas involving exponential functions because cell killing reduces the number of cells in the responding population of cells. The number of mutations, chromosome aberrations, or DNA strand breaks are plotted in linear scales because in the interesting dose range these effects are far away from saturation and the number of lesions is proportional to the dose.

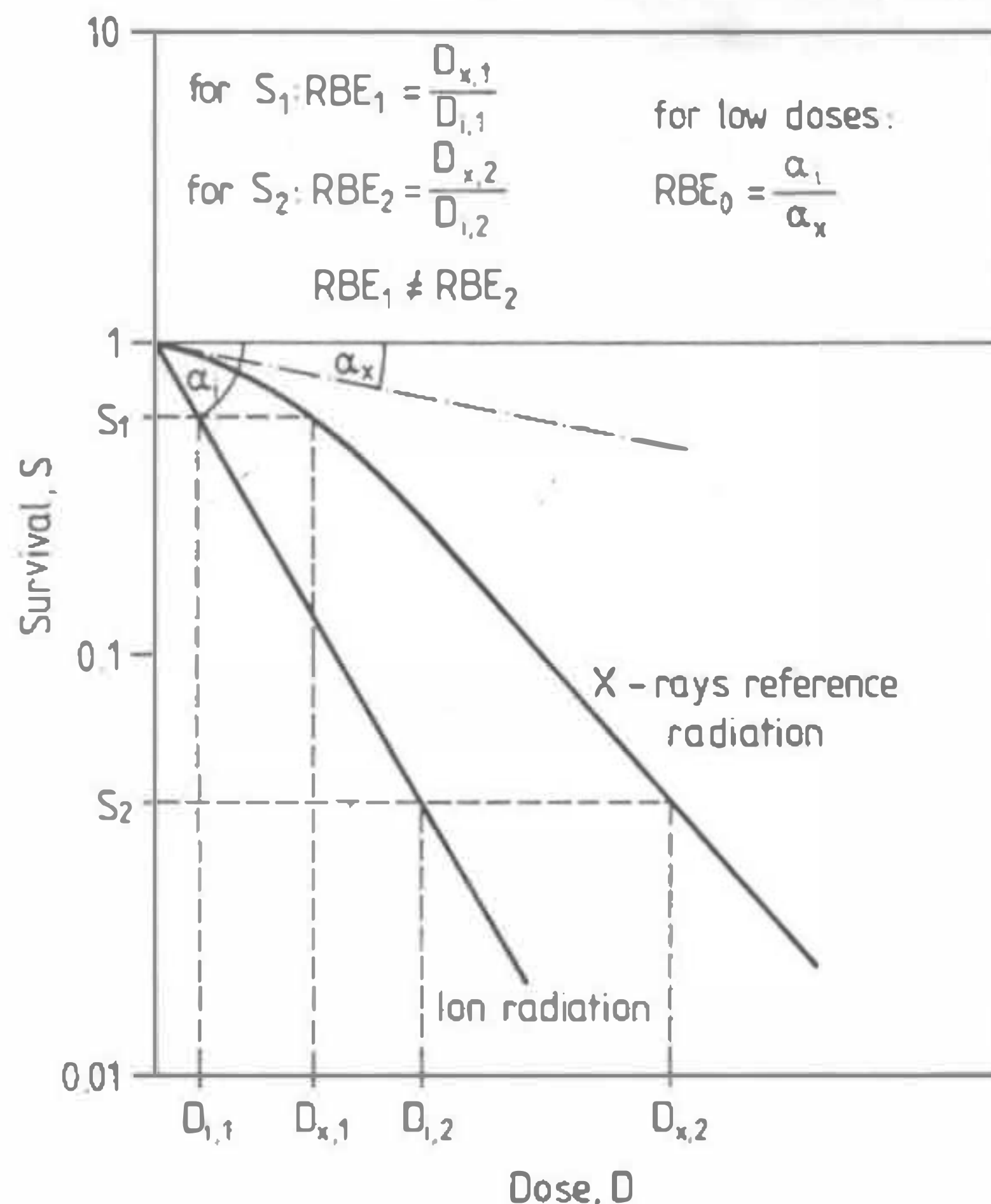


Fig.3.7

Diagram explaining definitions of Biological Effectiveness. The tangents α_x and α_i represent the initial slopes of typical X-rays and high-LET survivals curves. It is demonstrated that the RBE depends on the survival level chosen for analyzes.

In order to compare effects produced by different radiations the Relative Biological Effectiveness, RBE, is defined as the ratio of doses from a standard radiation, D_x , and from the investigated radiation, D_i , which produce an identical biological effect:

$$RBE = \frac{D_x}{D_i} \quad (3.12)$$

X-rays (250 kVp) or gamma-rays (Ba-137m, Co-60) are usually used as standard radiation. As it is depicted on Fig.2.8, RBE is a dose-dependent parameter i.e. for two different survival levels, S_1 and S_2 , RBE_1 is not equal to RBE_2 . RBE is also dependent on dose rate, fractionation, sensitizers or radioprotectors, presence of oxygen etc. It is clear, that RBE alone does not characterize sufficiently differences in action of two types of radiations on a given biological system.

Radiobiological experiments with cultured cells are performed at doses, which are much higher than those applicable to radiation protection. The initial slope of a dose-response

curve, α , (for $D=0$) is believed to be relevant for radiation protection. The corresponding "low dose" RBE₀ is defined as:

$$\text{RBE}_0 = \frac{\alpha_i}{\alpha_x} \quad (3.13)$$

In experiments with heavy ions results are often reported in terms of biological cross section, sigma, which is related to α

$$\sigma = \alpha L \rho_0 \quad (3.14)$$

where L is Linear Energy Transfer, ρ_0 is a medium density. σ has dimensions of μm^2 and is sometimes identified with the geometrical cross-sectional area of the cell nucleus, sensitive to radiation action [Lea, 1956].

The term "low dose" has a different meaning in radiation protection and in radiobiology. In radiation protection the current annual limit for intake, ingestion and external irradiation for workers is set at the level 50 mSv/year [ICRP, 1977]. A typical value for environmental exposure varies from 1 to 3 mSv/year [UNSCEAR, 1988]. Direct observation of biological effects produced in the human body by such small doses is not possible in practice. In radiobiology, the lowest X-ray doses used to investigate mutations or survival in cultured mammalian cells are about 0.5 Gy and results of experiments for these doses show a high experimental error.

In order to use results of radiobiological experiments for radiation protection purposes, e.g. for establishing the effectiveness of different types of radiation, one has to extrapolate the high dose data to the low dose region. This can be done on the ground of several radiobiological models. Each model leads to the specific type of equation for dose-response curves. One of the criterion for the model validity is its capability to predict (fit) parameters of this equation.

Most of the existing models [Kellerer & Rossi, 1972], [Chadwick & Leenhouts, 1981] exhibit the linear term in the dose-response curves i.e. for very low doses, effect is linearly proportional to dose. Therefore, the first derivative of the survival curve S=S(D) for D=0 is finite, disregarding the type of survival curve.

In the Katz approach [Katz et al., 1971] the multitarget model is used to fit survival curves after photon irradiations. Photons survival curves exhibit mostly shoulders and the corresponding fits result in the value of free parameter m greater than one. This gives a zero initial slope for survival, therefore the low-dose RBE is equal to infinity. Such a conclusion excludes the use of Quality Factor (see Ch.3.7) because the quality of radiation is dependent not only on the LET of radiation but on dose as well. The Katz's model is controversial in that it assumes vanishing initial slope in dose-response curves for low LET radiations. In fact, experimental points on dose-response curves are usually measured with such high standard deviations that it is not possible to prove or to disprove models on this base only. However, the statistical analysis performed by Morstyn [Morstyn et al., 1989] has shown that dose-response curves for mutation and inactivation of mammalian cells with X-rays and heavy ions can be fitted with polynomials covering the linear term with usually higher significance than without that term.

3.5.4. Review of radiobiological experiments with heavy ions and photons.

This review is limited only to experiments with heavy ions and soft X-rays. It is worth noting that absolute results of radiobiological experiments performed even on the same biological system but in different laboratories cannot be readily compared. Many factors in experiments with cultured cells are difficult to control e.g. plating efficiency. Therefore radiation quality should be analyzed basing on data coming from a single experiment but with as many radiation modalities as possible.

DNA breakage experiments

In the last 3 decades a large amount of experimental data concerning DNA breaks was accumulated [Guenther & Schultz, 1983], mostly for low-LET radiations and neutrons. Few DNA breakage measurements, performed at one laboratory with several radiation modalities, have been made for the high-LET region.

Christensen and co-workers [1972] used Φ X-174 bacteriophage, a replicative form of DNA, to investigate DNA breaks for 8 radiation modalities in the LET range between 0.3 to 2000 keV/ μ m. This form of virus DNA is relatively small (molecular weight $m = 3.5$ MDaltons), circular and double-stranded. The absolute measured number of DNA dsb varied between 0.9 and $6.1 \cdot 10^{-12} \text{ Gy}^{-1} \text{ Dalton}^{-1}$.

Ritter and co-workers [1977] investigated the frequency of non-rejoined DNA breaks induced by ions in the LET range from 9.4 to 1953 keV/ μ m in Chinese hamster V79 S171 cells. Non-rejoined breaks are those DNA breaks which do not rejoin after 8 hours of post-irradiation incubation in 37°C. The authors suggested that these lesions could be identified with not repaired double strand breaks. It was stated that the relative efficiency of this lesion, highest for LET of about 150 keV/ μ m, is in a good agreement with cell killing efficiency for T-1 human kidney cells [Todd, 1967].

It is also of interest to investigate DNA breaks due to low energetic photons because there is experimental evidence of high biological efficiency of soft X-rays [Cox et al. 1977b]. Experiments of [Frankenberg et al., 1986] on yeast cells have indicated that the frequency of DNA dsb per unit dose increases with decreasing photon energy.

The relative number of DNA double strand breaks for low and high-LET particles is similar in measurements performed with different cells and in different laboratories but the absolute values e.g. for low-LET, varying by one order of magnitude. This demonstrates not only differences in biology but also the range of experimental errors.

In vivo DNA breakage measurements with sucrose gradient sedimentation method require doses to mammalian cells greater than 10 Gy. The dose-response curves obtained for these doses usually show a linear dependence on dose [Guenther & Schultz, 1983]. One exception was the experiment of Dugle et al. [1976] with V79 Chinese hamster cells, indicating a quadratic dose relationship for the induction of dsb or unrepaired single strand breaks, similar to the quadratic relationship for survival curve. With neutral elution method it was possible to decrease doses to 1 Gy [Radford, 1986] and therefore investigate dose-response curves for DNA dsb in mammalian cells simultaneously with corresponding survival curves for these cells. The relative elution, which is expected to be linearly proportional to the frequency of strand breaks [Radford & Hodgson, 1985], showed an identical quadratic dependence on dose as the corresponding survival curves. It was suggested by the author that this is a direct confirmation that DNA dsb is a lethal lesion.

Survival, cell mutations, chromosome aberrations

These type of lesions are often scored together in one single experiment in order to investigate correlations between different end-points.

First survival curves for ion radiations and cultured human cells (T-1 kidney cells) were obtained by Barendsen et al. [1960]. These experiments were continued for ions over an extended range of LET (from 5.6 to 140 keV/ μ m) [Barendsen et al., 1963] Sigmoidal survival was found for 250 kVp X-rays, and exponential survival curves for densely-ionizing alpha particles. The RBE was found to increase from about 10 keV/ μ m and to saturate at about 100 keV/ μ m, reaching 7.0 at 80% survival level. A similar tendency was found by Deering and Race [1962] with HeLa cells and with lithium, carbon and oxygen ions of LET up to 350 keV/ μ m.

Skarsgard et al. [1967] investigated chromatid exchanges, abnormal metaphases and survival in CH₂B₂ cells irradiated with ions in LET range between 19 and 1950 keV/ μ m. It was shown that RBE curves went through a maximum at LET around somewhat about 100 keV/ μ m for all three end-points, but absolute values of RBE's varied with regard to levels of effect chosen for comparison.

Todd [1967] extended the LET range of experiments with T-1 kidney cells to 2000 keV/ μ m using 11 different radiation modalities. He confirmed the peak in the RBE curve around 220 keV/ μ m, reaching 6 for 80% survival level. Two X-ray radiations (250 and 50 kVp) were used, showing that no significant difference was observed in survival for these low-LET modalities. This work was continued on different cell lines [Todd, 1975] (human kidney T-1 cells, Chinese hamster M3-1 cells, human liver Chang cells) showing that the measured biological cross sections are for high-LET particles (above 500 keV/ μ m) matched the measured geometrical cross section of the cell nucleus.

Extended measurements of mutation and inactivation of human fibroblasts HF19 and Chinese hamster cells V79 by ions up to 470 keV/ μ m (9 ion energies plus 250 kVp X-rays) were performed by Cox and colleagues [1977a]. Their results were reported as initial slopes of dose response curves fitted with linear (HF19 human cells) or linear-quadratic functions (V79 Chinese hamster cells). The maximum RBE₀ was found to be about 4.0 for survival and 7.1 for mutation in HF19 (90 keV/ μ m) and, correspondingly, 9.0 and 18 for V79 cells.

In the last decade new types of accelerators become available for radiobiological experiments (BEVALAC at Lawrence Berkely Laboratory, UNILAC at the GSI Darmstadt). These devices enable one to perform experiments with very heavy ions and up to energies of 20 MeV/amu [Kraft et al., 1988]. This energy range and cross sections for very heavy ions are not yet available for track structure simulations and will be not discussed here. Such energetic ions of interest to radiation protection only in some rare cases, e.g. in space flights.

The presented experimental data for heavy ions demonstrate that the RBE for the studied biological end-points is usually below 10 and only for some end points (mutations in V79 cells) approaches 20. The RBE peaks are reported to occur at LET values between 90 and 200 keV/ μ m. The QF function used in radiation protection lies above the reported RBE values.

3.6. BIOLOGICAL RESPONSE FUNCTION, AN ALTERNATIVE APPROACH TO BIOLOGICAL RADIATION ACTION

It is difficult to build a mechanistic model in radiobiology. The number of unknown parameters which can affect radiation action is so high that it is impossible to account for all them. The concept of biological response function is built on another philosophy. No assumptions about mechanisms are made. It is only assumed that the probability of biological effect depends on the energy deposited in a sensitive target. This assumption is equivalent to the statement that for a given biological system and for a given endpoint there exists a function which relates energy deposited in the target to the probability of the effect. This function will be called here the Biological Response Function, BRF. In Bond and Varma [1982] approach this function is termed Hit Size Effectiveness Function, HSEF.

3.6.1. Concept of a response function for biological targets.

It is assumed in microdosimetry that any biological effect of ionizing radiation is a consequence of local energy deposition in a sensitive target. This assumption is formally expressed by the following equation [Kellerer, 1968]:

$$E(D) = \int f(z; D) \epsilon(z) dz \quad (3.15)$$

where $E(D)$ denotes the average effect induced by a given dose D , $f(z; D)$ is the probability of depositing in the target a value of specific energy z while in the whole tissue the macroscopic dose D is absorbed (See Ch.3.2). $\epsilon(z)$ is a function expressing the non-normalized probability of effect after depositing specific energy z in the target. The assumption that $\epsilon(z)$ is independent on radiation (i.e. on $f(z; D)$) is in fact a critical issue for the applicability of microdosimetric spectra for quantifying radiobiological effects [Morstyn et al., 1989]. For the low-dose region ($D/\bar{z}_F \ll 1$) Eq.3.15 asymptotically approaches [Zaider & Brenner, 1985]

$$E(D)/D = (1/\bar{z}_F) \int f_1(z) \epsilon(z) dz \quad (3.16)$$

$f_1(z)$ is the single-event microdosimetric distribution and \bar{z}_F is the first moment of this distribution. The term on the left side of Eq.3.16 expresses the effect per unit dose. For dose approaching zero, this is just equal to the initial slope of dose-effect curves, α .

Results (observables) α of a typical radiobiological experiment are the mean values which reflect an average response of individual cells in a large population affected by very different energy deposition events. A direct measurement of $\epsilon(z)$ is not possible. It is difficult to act on biological matter with the required precision in order to investigate the biological response after a given specific energy deposited in selected parts of the cell. It is, however, possible to recover the efficiency $\epsilon(z)$ by unfolding this information from experiments with several radiation modalities but concerning this same end point. This leads to a set of equations:

$$\alpha_i = (1/\bar{z}_{Fi}) \int f_{1i}(z) \epsilon(z) dz ; i=1, \dots, N \quad (3.17)$$

where N is the number of radiation modalities. As z and y differ only by a multiplication factor one can write [Morstyn et al., 1989]:

$$\alpha_i = (\sigma_\epsilon / \bar{y}_{Fi}) \int f_{1i}(y) R(y) dy ; i=1, \dots, N \quad (3.18)$$

$R(y)$ is a normalized (to one) probability function. σ_ϵ can be interpreted as a maximal probability for producing a given type of effect.

Substituting

$$\alpha_i' = \frac{\alpha_i \bar{y}_{F_i}}{\sigma_\epsilon} \quad (3.19)$$

one gets from 3.18

$$\alpha_i' = \int f_{1i}(y) R(y) dy ; i=1, \dots, N \quad (3.20)$$

3.6.2. Survey of unfolding methods

In this paragraph a review of methods is given which can be used to solve Eqs.3.18 or Eqs.3.20. This set of equations is a degenerate case of the Fredholm integral equation of the first kind. The process of evaluating the function $R(y)$ from Eq.3.20 is called unfolding.

In most cases this system of equations is undefined and does not have a unique solution since a finite number of discrete observables α_i' cannot, in general, define a continuous function $R(y)$. Therefore, in an unfolding procedure some assumptions as to the expected response function should be applied e.g. non-negativity, continuity, smoothness, monotony, etc. in order to obtain biologically relevant results. As values of α_i' are known with a certain experimental error, ϵ_i , Eq.3.20 can be rewritten in the following form:

$$\alpha_i' + \epsilon_i = \int f_{1i}(y) R(y) dy ; i=1, \dots, N \quad (3.21a)$$

or, for numerical evaluations:

$$\alpha_i' + \epsilon_i = \sum_{j=1}^N f_{ij} R_j ; i=1, \dots, N \quad (3.21b)$$

where f_{ij} is the value of $f_{1i}(y)$ for y_j and R_j is the response function for the y_j times the width of the corresponding lineal energy bin. Due to the above mentioned assumptions on the behavior of the response function ("prior knowledge") the system can become overdetermined which justifies looking for approximate solutions, e.g. in the least squares sense.

Unfolding criteria

Be α_i^0 an effect calculated for a particular response function R_j^0 :

$$\alpha_i^0 = \sum_{j=1}^N f_j R_j^0 ; i=1, \dots, N \quad (3.22)$$

Minimizing of the following quantity Q_1

$$Q_1 = \left[\frac{\alpha_1 - \alpha_1^0}{\alpha_1^0} \right]^2 \quad (3.23a)$$

can be the criterion for finding the best response function [Cross & Ing, 1985]. If the required solution is expected to be a smooth function, then the following quantity is minimized:

$$Q_2 = \sum_j (R_{j-1} - 2R_j + R_{j+1})^2 ; \quad dy=\text{const} \quad (3.23b)$$

The expression in brackets is equal to zero if three succeeding values of a discretely represented response function R_j are "ideally smoothed" i.e. are situated on a straight line. Q_1 or Q_2 used alone, or a combination of these parameters, can be used to test the quality of unfolding:

$$Q = w_1 Q_1 + w_2 Q_2 \quad (3.23c)$$

where w_1 , w_2 are appropriate weighting factors.

Over the last 30 years a number of numerical unfolding methods in neutron spectroscopy were published, extensively tested and compared [Routti & Sandberg, 1985], [Cross & Ing, 1985]. Some of these methods are also applicable in radiobiology.

Unfolding by a parametric representation of the response function

In this method of unfolding, the response function $R(y)$ is represented as a function, $F(y)$, of a known formula (or possibly as a sum of such functions) but with a finite number, K , of unknown parameters, p_j .

$$R(y) = F(y; p_1, p_2, \dots, p_j, \dots, p_K) \quad (3.24)$$

Unfolding is performed by determining such a set of parameters, p_K , which best satisfies e.g. Eq.3.23. The advantage of this method is that it allows one to select the best solution by comparing their statistical significance [Morsttin et al, 1989] (the number, M , of observables, α_i , must be higher than the number, K , of free parameters of the response function).

Unfolding with discrete intervals.

This is a broad group of numerical methods based on evaluating $R(y)$ from Eq.3.21b. Two types of methods are of particular interest.

In the least-squares method requiring matrix inversion, the response function is determined by solving the matrix equation Eq.3.21b in a least-square sense [Zaider & Brenner, 1985]. This can be continued iteratively until a satisfactory solution is obtained. The advantage of this method is that the covariance matrix corresponding to the unfolded function gives some information on the error involved. This method, however, does not exclude negative solutions and tends to oscillate. Therefore, for practical

calculations, some additional assumptions (called regularizations) such as smoothness, non-negativity, etc., are used.

In iterative methods, a guess response function R^0 is iteratively modified until an acceptable fitting error, e.g. Q_1 , is reached. The most widely used computer code for iterative unfolding is SAND-II [McElroy et. al., 1967]. The schematic algorithm of the code SAND-II is presented in Fig.3.8. The deconvolution process starts by setting up an initial guess function R^0 . With this response function effects a_{ij}^0 are calculated for all radiation modalities and compared with experimental values α_i . If the quality of the fit is not good enough (e.g. if Q_1 is greater than the assumed limit) then the response function must be corrected.

For each lineal energy bin 'j' and for each radiation modality 'i', the ratio, w_{ij}^0 , of the partial to the total calculated effect is evaluated. These ratios are used as weighting factors to compute correction factors f_j^0 .

The factor f_j^0 affected most is that from those radiation modalities "i" for which the product, a_{ij}^0 , of the microdosimetric distribution and of the iteratively improved response function, is the largest. This implies low reliability of the response function in those parts of the lineal energy range which are poorly covered by microdosimetric distributions. The exponent and logarithm in the correction algorithm are applied in order to accelerate convergence of the solution in cases of large differences between the initial guess and the required response function. The iteration process is stopped if the assumed condition (e.g. given by Eq.3.23a) is fulfilled or if the number of iterations exceeds a fixed limit.

A disadvantage of the discrete interval methods is its difficult error analysis. The number of radiation modalities used to investigate a given end-point does not usually exceed 10 and is much smaller than the number of discrete intervals which is chosen between 10 and 20 per decade. Eq.3.21 is therefore undefined and has not a unique solution. Therefore, only with the prior knowledge significance analysis can be performed. Even if an error band of the response function is known the quantitative comparison of two solutions depends on initial guesses, types of regularizations, etc.

3.6.3. Response functions in radiobiology - a review.

Since late 50'th it has been already clear for scientific community that dose alone is not the relevant parameter to explain radiation action and it became necessary to introduce formalism which was able to account for radiation quality [Rossi, 1968], [Kellerer & Rossi, 1972], [ICRU-36, 1983]. First *explicite* analysis of biological experiments by unfolding of response functions was performed by Bond and Varma [1982]. The authors assumed that exists a function which represents the probability of an all-or-none effect as a function of hit size (i.e. size of energy deposition events). This function describing the efficiency of particular events (hits) was termed the Hit-Size Effectiveness Function. In the further part of this work the terms Hit-Size Effectiveness Function and Biological Response Function will be used interchangeably.

The evaluation of the Hit Size Effectiveness Function, HSEF by Varma and Bond [1982] was performed for pink mutations in Tradescantia induced by X-rays and monoenergetic neutrons. Measured microdosimetric distributions for a simulated diameter of 1 μm were used in these calculations. A 4-parameter function was used. The parameters of this function were fitted by trial and error to obtain agreement between

ALGORITHM FOR SAND-II

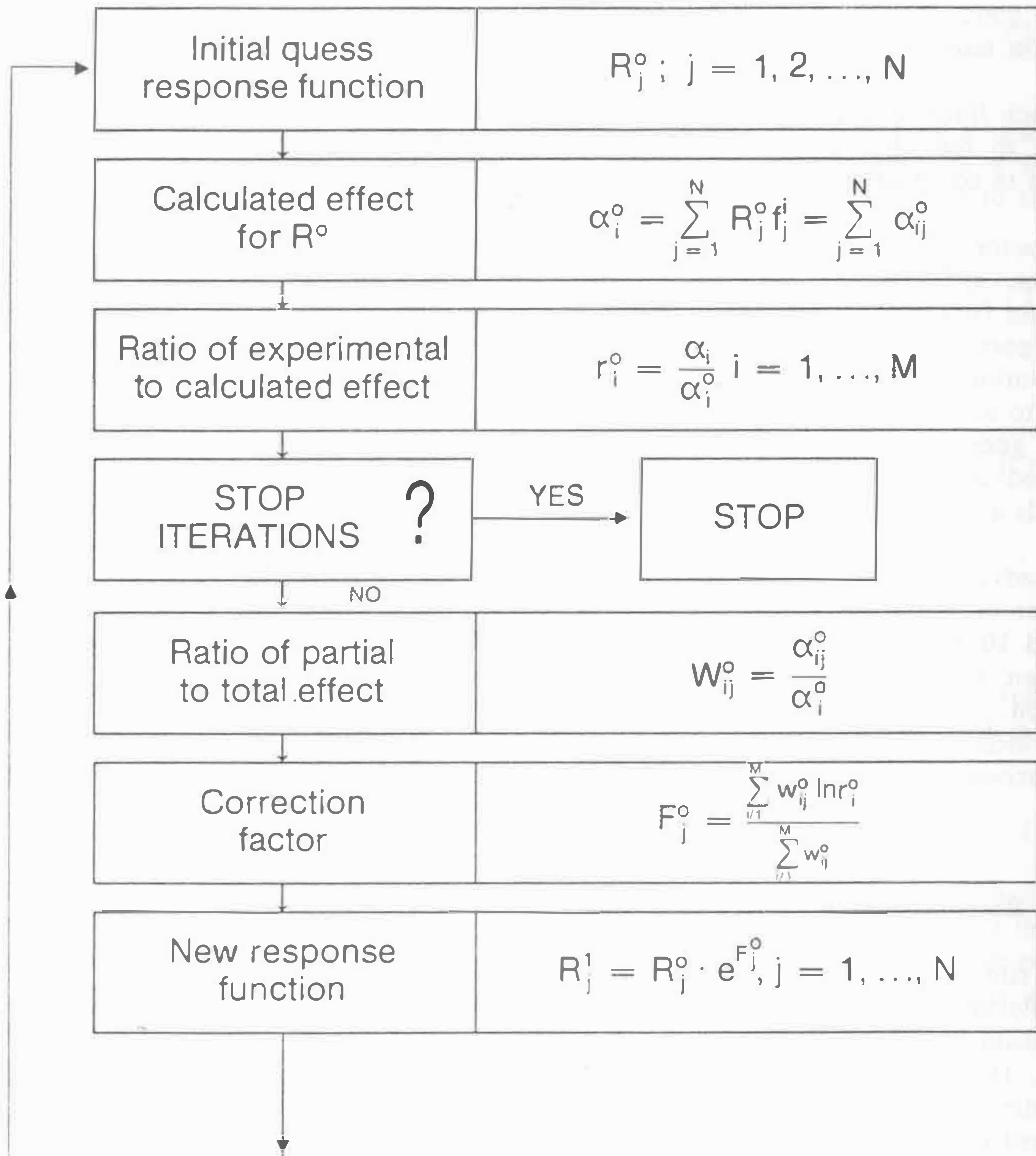


Fig.3.8 The algorithm of the program SAND-II used to iterative unfolding of unknown response function R .

input and calculated RBE's within a factor of 2. The evaluated HSEF had a threshold at $y=0.4 \text{ keV}/\mu\text{m}$ and increased rapidly ("step-wise") at $y=76 \text{ keV}/\mu\text{m}$. The disadvantage of this calculation was the lack of information about the statistical significance of this deconvoluted function.

A probabilistic approach to obtain HSEF was developed by Morsttin et al. [1989]. He applied the parametric unfolding to Eq.3.21. The guess functions $F(y)$ (Eq.3.24) was expressed as a sum of integral Gaussian and/or Poissonian functions or, alternatively, the so-called "saturated polynomials"

$$F(y) = 1 - \exp(\sum_i a_i y^i) \quad (3.25)$$

Number and values of parameters of these functions were searched in order to achieve the highest statistical significance of the solution. The statistical significance of each fit was evaluated taking into account the degrees of freedom of the solved equation, which is related to the number of different experiments N minus number of fitted parameters, M . The existence of a hypothetical threshold (response equal to zero for energy deposition events below a certain limit) was included in these investigations. Results have confirmed the existence of a step-like $P(y)$ relation for Tradescantia pink mutations but similar steps were not obtained for other end-points. No statistically significant threshold was found for any of the endpoints studied. For low y values (below, say 5 $\text{keV}/\mu\text{m}$) no significant overlinearity increase of response function was found to suggest any change of the QF for low-LET radiations.

The possibility of a new formulation of quality factors in terms of a response function scaled in lineal energy was suggested by Zaider and Brenner [1985, 1986]. Denoting

$$\epsilon(z) = q(z) z \quad (3.26)$$

and having in mind Eq.3.10 and that z and y differ only by a constant, one can write

$$q = \int q(y) d(y) dy \quad (3.27)$$

where $q(y)$ is called a Specific Quality Function and $d(y)$ is dose lineal energy distribution. With $q(y)$ known one can calculate average values q , for any radiation whose microdosimetric distribution $d(y)$ is known.

Zaider and Brenner evaluated Specific Quality Functions for chromosome aberrations in human lymphocytes [1985] and mutations in human fibroblasts [1986] using unfolding in the least square sense. The least squares method allowed them to control the error of the unfolded function which was expressed by a covariance matrix. It was shown that the uncertainties of the response function (square-roots of diagonal elements of covariance matrix) were highest for regions of y which were poorly covered by a microdosimetric distributions. In the case of unfolding of experiments with chromosome aberrations in human lymphocytes [Edwards et al., 1980a,b] it was found that the unfolded response function was most uncertain for y below 3 $\text{keV}/\mu\text{m}$ and above 130 $\text{keV}/\mu\text{m}$. The results of this unfolding had been later used by ICRU [ICRU-40, 1986] to suggest a new type of quality factors (see Ch.3.7).

3.7. MICRODOSIMETRY AND RADIATION PROTECTION

It has been already mentioned in Ch.3.1 that the absorbed dose alone is not a good parameter to describe radiation risk. For low doses, dose determinates only the frequency of hitting the targets but in addition quality of the hit is to be considered which depends exclusively on the type of radiation used.

This philosophy is of particular interest for radiation protection because radiation protection deals usually with small doses and small dose rates. In Ch.3.7.1 the microdosimetric definitions of low dose and low dose rates will be given. In Ch.3.7.2 radiation quality will be introduced. In the last Ch.3.7.3 proposals for a new regulations of Quality Factor will be presented and discussed.

3.7.1. Microdosimetric concept of low dose and low dose rate.

The terms low dose and low dose rates are often used arbitrary. For studying DNA breaks in mammalian cells the dose of 1 Gy from Co-60 gamma-rays is still a low dose. For radiation protection low doses are considered as doses not much exceeding natural background e.g. 1 mSv/year.

Microdosimetry provides some rules which are helpful to distinguish low and high doses. In general, low dose is considered as the dose at which a sensitive site is affected at maximum one times. Cell hits are statistically independent and it is possible that even for very low doses targets are hit two or more times. Therefore, the criterion is used that 90 % of cells which are affected must be hit by only one energy deposition event. This leads to condition that [ICRU-36, 1983]

$$D \leq 0.2 \bar{z}_F \quad (3.28)$$

In this case, about 18% of sensitive volumes experience one event and about 2% more than one. The border of low dose for Co-60, is equal to (for 8 μm volume) are depicted in Fig.3.2.

Present radiation protection regulations does not take into account the influence of dose rate on a biological damage. Some radiobiological data show a significant dependence on dose rate due to repair taking place in the biological systems [Pohlit & Heyder, 1981]. Generally, the smaller dose rate, the greater probability of system to be repaired. If a target receives hits with a constant rate, an equilibrium exists between the production and the repair of injuries. The dose rate, D^* , can be considered as small when [Feinendegen et al., 1985]

$$D^* \tau < 0.1 \bar{z}_D \quad (3.29)$$

where \bar{z}_D is a mean dose lineal energy in the cell nucleus and τ is the mean repair time. For $\tau = 90$ min (assumed from experiments with blood cells) the low dose rate is 170 $\mu\text{Gy}/\text{h}$ for Co-60 and 14 mGy/h for 14 MeV neutrons. In fact in most radiation fields, which are of interest for radiation protection, the average time between two events in a sensitive site is much higher then the mean repair time, τ , and therefore dose rate parameter is irrelevant.

3.7.2. Quality Factors in radiation protection.

Dose alone is not able to account for risk in biological systems. Thus, it was necessary to introduce in radiation protection a parameter which can characterize an average risk for human being from the given type of radiation. This parameter is called quality factor, Q. [NCRP, 1954], [ICRP, 1966, 1977]. The quantity correlated to the quality factor is called dose equivalent, H [ICRU, 1980]

$$H = Q \cdot N \cdot D \quad (3.30)$$

where Q is the quality factor, N is a product of other modifying factors (at present set to 1) and D is the absorbed dose in tissue at the point of interest. The unit of dose equivalent is the sievert (Sv) and $1 \text{ Sv} = 1 \text{ J/kg}$.

Quality factor does not represent the RBE for a given biological effect. It is a legal regulation, which is based on analyses of RBE's for many biological end points.

In spite of limitations listed in Ch.3.1, the quality factor is expressed as a function of L_∞ (Fig.3.9). For low-LET radiations as gamma or X-rays the Q is equal to one i.e. dose equivalent is numerically equal to the measured dose. The maximal Q is equal 20 for L_∞ exceeding 175 keV/ μm . It is a rare situation that a radiation field is composed from mono-LET particles. For a distribution of LET the mean quality factor is defined as

$$Q = \int Q(L_\infty) \cdot d(L_\infty) \cdot dL_\infty \quad (3.31)$$

where $d(L_\infty)$ is a dose distribution of L_∞ . $Q(L_\infty)$ has been specified in ICRP [1977]. If the radiation modality is unknown, simple rules used in radiation protection say that Q for low LET radiation is 1, for fast neutrons 10 and alpha particles 20.

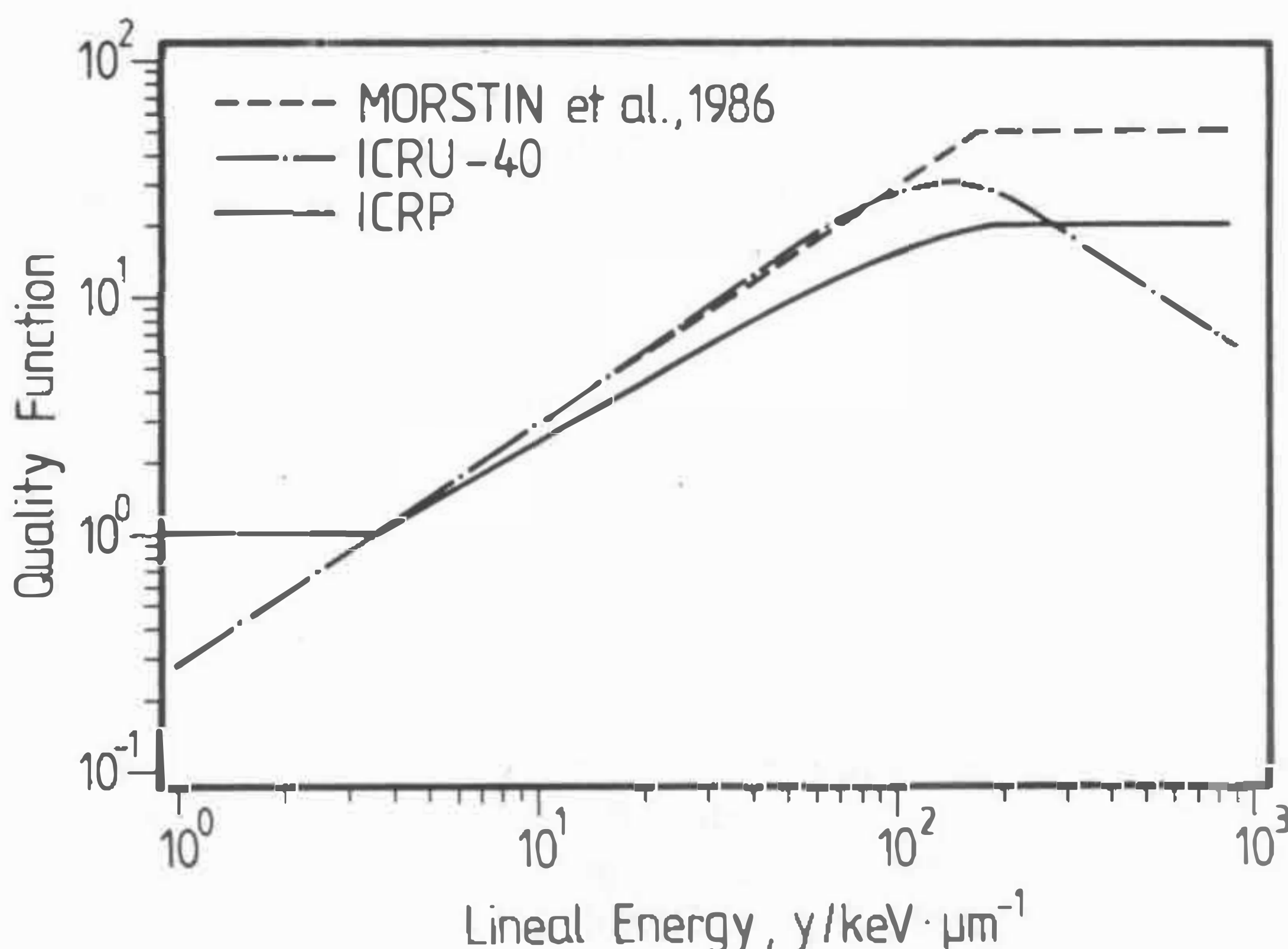


Fig.3.9 Quality factor as a function of LET (lineal energy, y). The dashed line - the function suggested by ICRU-40. MDB - the function proposed by Morstин et al. [1985] and ICRP actual definition of Quality Factor [ICRP, 1977]

The principal problem with practical applications of this definition is that there is no method for accurate determination of $d(L_\infty)$ or a mean L_∞ in an unknown radiation field. The $d(L_\infty)$ can be derived in an approximate way from measurements of lineal energy distributions [Rossi, 1968]. The difference between lineal energy and L_∞ is small only for large site diameters and ions producing short delta-rays.

3.7.3. Proposals for new radiation quality regulations

The complexity of radiation action in biological matter on one hand and the necessity of simple rules in radiation protection on the other hand make any definition of radiation quality difficult. Thus it should not be surprising that the simple rules used presently to calculate dose equivalent are being discussed since many years.

Firstly, dose equivalent (or quality factors) are independent of dose, whereas the adherents of Katz model [Katz et al., 1971] indicate that RBE can increase (to infinity) with dose (going to zero). However, for low dose region it cannot be checked experimentally. In addition, such modifications would unacceptable complicate the radiation protection philosophy.

Secondly, the absolute values of quality factors [ICRP, 1977] are called in question. It was proposed to increase Q to about 20-50 for neutrons with preserving the Q dependence on L_∞ [Morsttin et al., 1986]. These proposals were based on recent reassessments of estimates of radiation levels in nuclear explosion sites and on radiobiological experiments [ICRP, 1985].

The other proposals of quality factors are based on microdosimetric principles. Quality factor is there a function of the microdosimetric quantity, lineal energy. This is done because it is believed that energy imparted to small volumes is more fundamental for radiation risk than L_∞ . The second argument is pragmatic: lineal energy distributions are easily measurable with proportional counters. A mean quality factor for a given radiation field is calculated by folding a quality function with a microdosimetric distribution. This was suggested by Zaider and Brenner [1985] (see Ch.3.6) and formally proposed by a task group of ICRU and ICRP [ICRU-40, 1986]. However, the particular function proposed

$$q(y) = (a_1/y) [1 - \exp(-a_2y^2 - a_3y^3)] \quad (3.32)$$

with the coefficients:

$$\begin{aligned} a_1 &= 5510 \text{ keV } \mu\text{m}^{-1} \\ a_2 &= 5 \cdot 10^{-5} \mu\text{m}^2 \text{ keV}^{-2} \\ a_3 &= 2 \cdot 10^{-7} \mu\text{m}^3 \text{ keV}^{-3} \end{aligned}$$

provoked great controversies. Fig.3.9 compares the actual valid Q definition with the proposals of Morsttin et al. [1986], and ICRU-40. The first proposal increases the absolute Q values to maximal 50 for y greater than 175 keV/ μm . The latter one introduces a saturation of Q above $y=175$ keV/ μm and with decreasing lineal energies Q is continuously decreasing. This leads to different Q for photons of different energies and to decreasing the Q for very densely ionizing particles e.g. recoil heavy particles produced in tissue by 14 MeV neutrons. Introducing these modifications would require expensive changes in personal dosimetry systems. In addition, unfolding of quality functions for radiobiological experiments with heavy ions [Morsttin et al., 1989] did confirm the existence of statistically significant linear term in quality function which is missing in Eq.3.32.

4. EVALUATION AND INTERPRETATION OF ENERGY DEPOSITION FOR PHOTONS

In this chapter a method is presented which enables one to calculate photon-induced microdosimetric distributions in micrometer and nanometer targets. First, (Ch.4.1) a method of calculating of photon-induced energy deposition distributions in water and in TE gases is presented. The microdosimetric distributions calculated with this method are compared with measurements. Finally, a systematic review of microdosimetric distributions for different photon energies and different site diameters is given (Ch.4.2). The influence of photon energy, site diameter and type of physical interactions on the distribution structure, are also discussed.

4.1. METHOD OF CALCULATION OF MICRODOSIMETRIC DISTRIBUTIONS FOR PHOTONS

No evaluations were available which could assess energy deposition in nanometer sites and at the same time be verifiable in micrometer region, against the available measurements with tissue equivalent proportional counters. Calculations presented in this chapter fulfill these requirements. The method of calculation is similar to that used by [Goodhead & Brenner, 1983] but improved by scaling results in real microdosimetric quantities. In addition, it offers an insight into the physical structure of the distributions. A simplified diagram of these calculations is given in Fig.4.1. In the first step incident photon spectra, as known or gathered from literature, are used to calculate a secondary electron spectrum $\varphi(E)$. In the next step, electron tracks are simulated with energies randomly sampled from the electron spectrum, which are then used to score microdosimetric distributions. This method will be explained in more detail in the following subsections.

4.1.1. Calculation of secondary electron spectra in water

Calculations of secondary electron spectra $\varphi(E)$ in water were performed using PHOEL-2 code [Turner et al., 1980]. This is a Monte Carlo computer program which enables one to calculate initial energies of photoelectrons and Compton electrons generated by photons of a specified spectrum in an infinitely thick water phantom. Because pair production is not included in this program the energies of incident photons are limited to about 2 MeV.

The algorithm of the program is as follows. A photon of an energy randomly chosen from the photon spectrum interacts either via Compton scattering or via photoelectric effect. The probability of photoelectric effect is taken as the ratio of photoelectric attenuation, τ and total attenuation, μ , and with this probability the photoeffect is randomly selected. If photoelectric effect occurs and the energy, E , of the incident photon is greater than 532 keV, then a photoelectron with energy, T , $T=E-532$ and an Auger electron of energy 508 keV, are emitted (see Ch.2.3). If $E < 532$ eV, then a photoelectron of energy $T=E-12$ eV is produced from the L shell. When a Compton electron is produced, its energy E is randomly selected from the normalized electron energy spectrum calculated from Eq.2.8, and the interaction of the photon of energy $E'=E-E_c$ is again randomly selected to be either Compton scattering or photoeffect.

4. ... energy deposition for photons

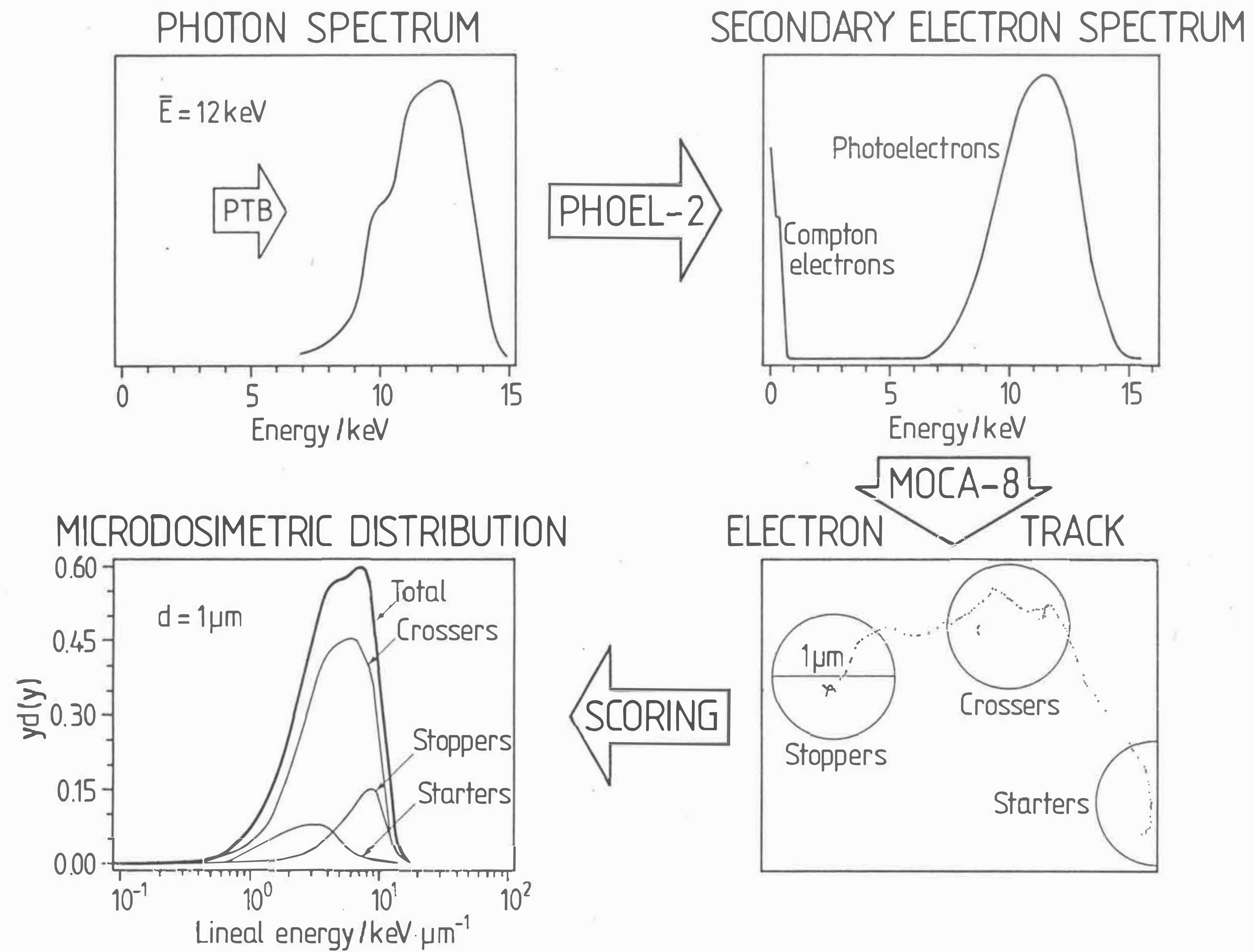


Fig.4.1 Schematic presentation of the method used to calculate microdosimetric distributions for photons. For more explanation see text.

An option in program allows the user to consider only single Compton scattering. This corresponds to a physical situation when the mean free path of the photon is much higher than the thickness of the biological sample and only the first scattering gives rise to energy deposition in the sample. This is the case, e.g., for irradiations of cell colonies plated on a thin mylar foil. The secondary electron spectra $\varphi(E)$ used in the following calculations were calculated with this single scattering option.

Fig.4.2.b demonstrates examples of single-collision secondary electron spectra $\varphi(E)$ induced in water by photon fields shown in Fig.4.2.a. One can distinguish low energy contributions from Compton electrons and photoelectric effects of energies almost corresponding to incident photons. The 508 eV Auger electrons are not shown in this figure.

4.1.2. Simulation of electron tracks in water vapour and scoring microdosimetric distributions.

In the next step, a set of electron tracks was calculated with the code MOCA-8 (see Ch.2.3.1). Usually about 1000 electron tracks were generated for photons of energies of several dozen keV. Energies of these electrons were randomly sampled from a single-collision electron spectrum $\varphi(E)$ calculated with Phoel-2 but modified by subtracting from the spectrum 508 eV Auger electrons. The reason for this subtraction was that emission of an Auger electron is correlated with emission of a photoelectron. Thus, in these calculations, as a photoelectron was created, an Auger electron of energy 508 eV was initiated from the same point of origin in a randomly chosen direction and both electron tracks were stored as an one track.

The scoring procedure was based on the sampling on individual transfer points Kellerer and Chmelevsky [1975b]. Distributions were scored separately for Compton and for photoelectrons. This was done by dividing the secondary electron spectrum $\varphi(E)$ into the Compton electron spectrum, $\varphi_C(E)$, and the photoelectron spectrum, $\varphi_P(E)$. Random selection of the electron energy to produce a track was performed by taking into account the relative frequencies of both types of events, R_C and R_P

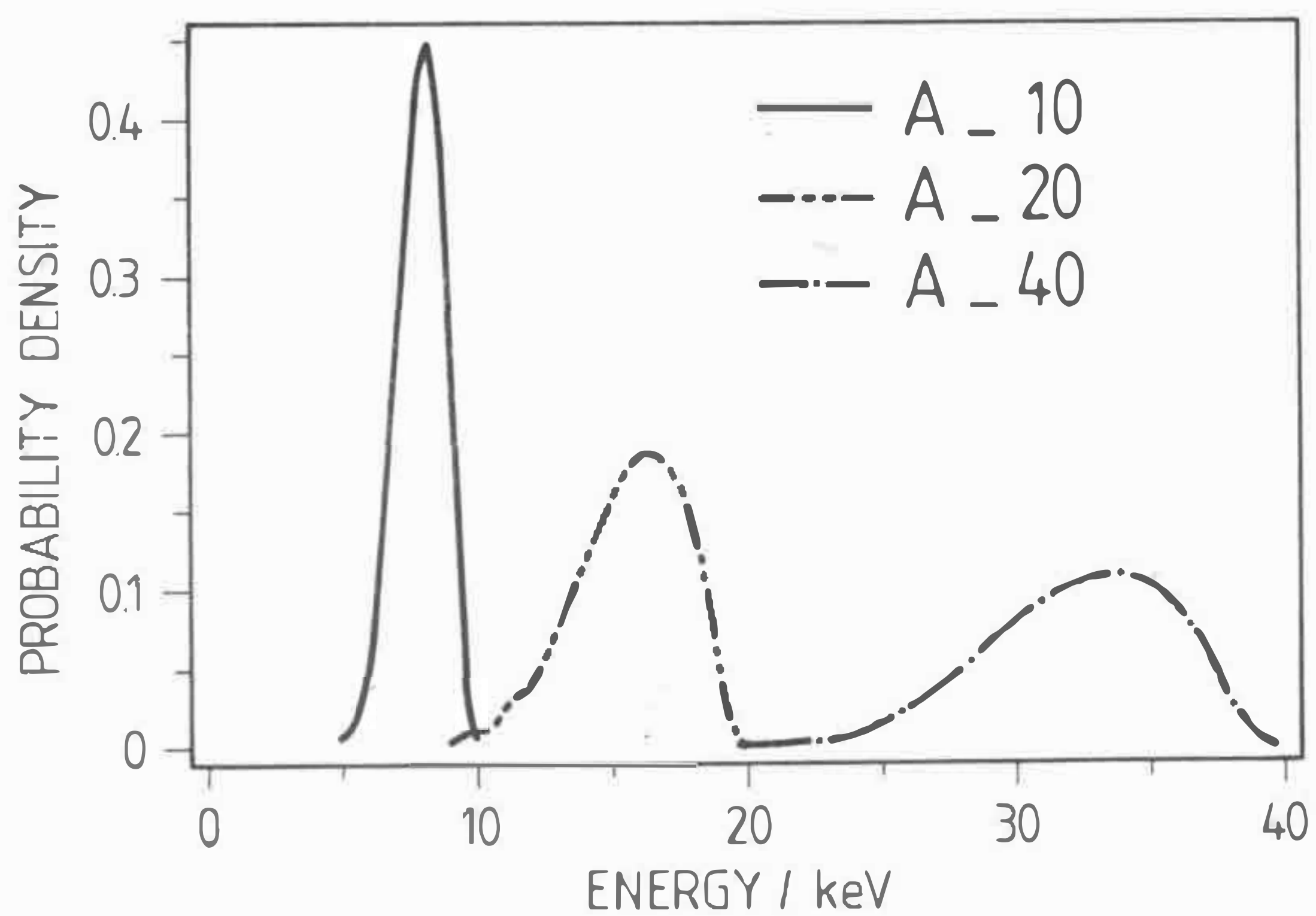
$$R_C = \frac{\int \varphi_C(E) dE}{\int \varphi(E) dE} \quad (4.1a)$$

$$R_P = \frac{\int \varphi_P(E) dE}{\int \varphi(E) dE} \quad (4.1b)$$

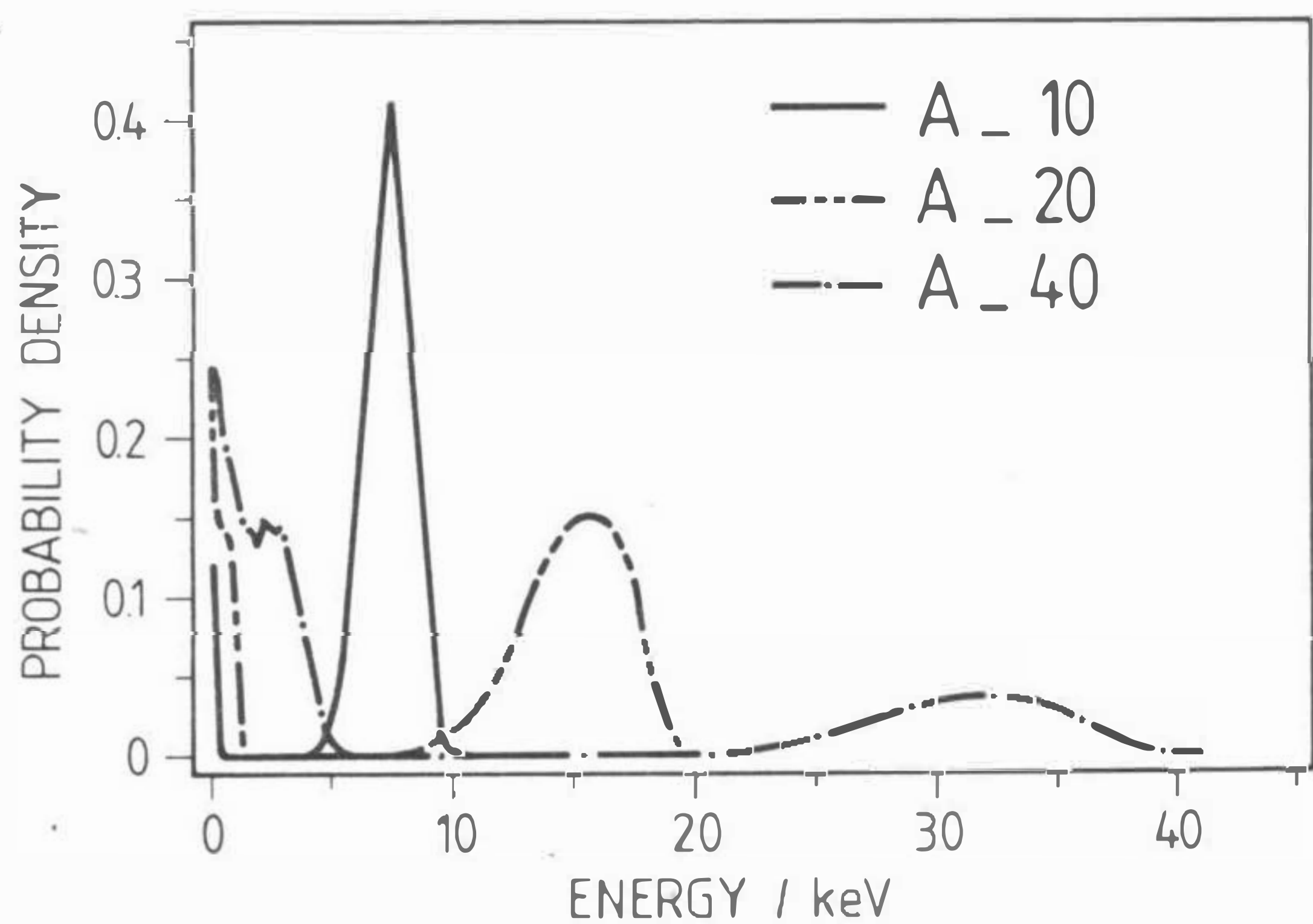
$$R_P + R_C = 1 \quad (4.1c)$$

Compton electron tracks and photoelectron tracks were used to separately scoring the dose distributions of lineal energy for Compton, $d_C(y)$, and photoeffect, $d_P(y)$.

Another classification of events was made simultaneously, by scoring microdosimetric distributions separately into starter, stopper, crosser and insider. Each position of a sampling sphere was compared with positions of the first and the last ionization in the track (see Fig.4.1 and Fig.3.5). An event was classified as an insider if both points were covered in the sampling sphere; as crosser if both were outside the sphere etc.

**Fig.4.2a**

Energetic spectra of X-rays produced with voltages 10, 20 and 40 kVp. The symbols A denote the class of strongly filtrated X-ray spectra which are used as reference radiations for calibrating dosimeters and are specified by International Organization of Standardization [ISO, 1979].

**Fig.4.2b**

Energy distributions of secondary electrons induced in water by X-rays spectra shown in Fig.4.2a. One can distinguish in the spectra the high energy electrons produced in photoeffect and the low energy Compton electrons.

4.1.3 Method of approximation of microdosimetric distributions for TE targets.

The above method of calculation of photon induced microdosimetric distributions is limited actually to distributions in water vapour because presently available Monte Carlo track structure codes are written only for that medium. Track simulations performed for cross sections relevant to the gas phase are later rescaled to the density of 1 g/cm³. On the other hand, measurements of microdosimetric distributions are almost exclusively performed with tissue equivalent proportional counters (see Ch.3.3). It is important to check how differences between the atomic composition of TE materials and of water influences photon-induced microdosimetric distributions.

Fractions of dose due to Compton and photoelectrons, F_C and F_P , can be calculated as

$$F_C = \frac{\int \varphi_C(E) E dE}{\int (\varphi_C(E) + \varphi_P(E)) E dE} \quad (4.2a)$$

$$F_P = 1 - F_C \quad (4.2b)$$

It is possible to approximate microdosimetric distributions in TE targets by a re-calculation of microdosimetric distributions in water. Total lineal energy distribution, $d(y)$, can be obtained as a sum of the normalized Compton, $d_C(y)$, and photoelectric, $d_P(y)$, lineal energy distributions weighted by the fraction of doses, F_C and F_P , due the respective types of events

$$d(y) = F_C d_C(y) + F_P d_P(y) \quad (4.3)$$

The normalized lineal energy distributions, $d_C(y)$ and $d_P(y)$, are fairly identical for water and TE gases because the normalized secondary electron spectra, $\varphi_C(E)$ and $\varphi_P(E)$ are rather insensitive for changing the considered media.

This conclusion for Compton electrons can be drawn from Eq.2.8. The energy of a secondary Compton electron, E , is a function of primary photon energy and is independent of medium composition. Also the photoelectron spectra in water and TE gases differ only slightly due to small differences in K-shell binding energies. The oxygen atoms in water (binding energy 0.51 keV) are substituted in a TE material by carbon and nitrogen atoms of binding energies 0.4 keV and 0.28 keV, respectively.

Substitution of water into a TE gas changes only the ratio of events (or dose, F_C/F_P) due to Compton and photoelectrons. Therefore, the distributions for a TE gas can be simply obtained by calculating new values of F_C and F_P using Phoel-2, without the need to repeat the time-consuming Monte Carlo calculations of $d(y)$.

4.2. RESULTS OF CALCULATIONS AND DISCUSSION

In this section, the method described in the previous paragraph is used to calculate photon induced microdosimetric distributions. These distributions are compared with measurements performed with the KFA counter (Ch.4.2.2) and with a wall-less TEPC (Ch.4.2.3). By separately presenting the results of calculations for Compton and photoelectrons as well as for crossers, insiders, starters and stoppers, the structure of distributions will be studied. In the last paragraph (Ch.4.2.4) calculated microdosimetric distributions for nanometer sites will be presented and discussed.

4.2.1. Calculation of fraction of dose due to Compton and photoelectrons in TE gases.

Fig.4.3.a presents the total attenuation coefficient, μ/ρ_0 , for the TE gases and for atomic water. The curve for H_2O was taken from Turner and co-workers [1980]. The curves for TE gases were calculated using attenuation cross sections for H, C, N and O from Hubbel [1969] and the atomic composition of TE gases, from ICRU 36 [1983]. The attenuation coefficients for Compton scattering are approximately equal for water and TE gases because these media have approximately the same average Z/A, which results in a similar electron concentration per unit mass. This equality is only slightly disturbed by the different hydrogen content : 11.1 % per weight in H_2O , and 10.3 % in TE gases. Photoelectric attenuation coefficients are lower for TE gases due to lower photoelectric attenuation coefficients of carbon and nitrogen as compared to oxygen.

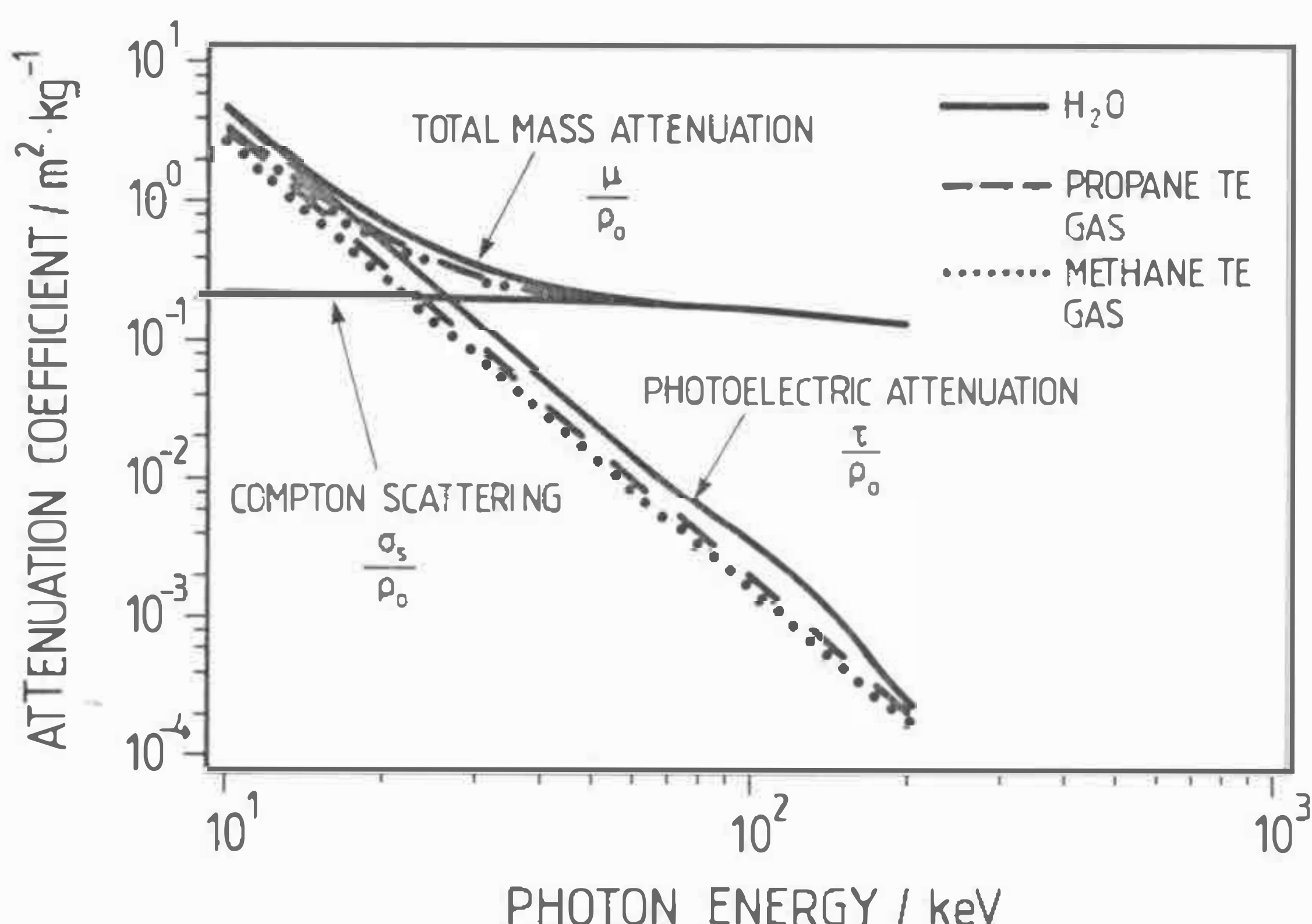


Fig.4.3a Total mass attenuation coefficients μ/ρ_0 for H_2O , propane TE gas and methane TE gas as a function of the photon energy.

Fig.4.3.b, which was derived from Fig.4.3.a., shows the ratio of photoelectric to total attenuation coefficients versus photon energy. For a given photon energy, Compton scattering occurs in TE gas with a significantly higher probability than in water. For instance, for 20 keV photons, 41% of the photons will be Compton-

scattered in propane TE gas, 38% in methane gas and 29% in H_2O . This higher contribution of Compton interactions will increase the contribution of Compton electrons in the total $d(y)$ distribution.

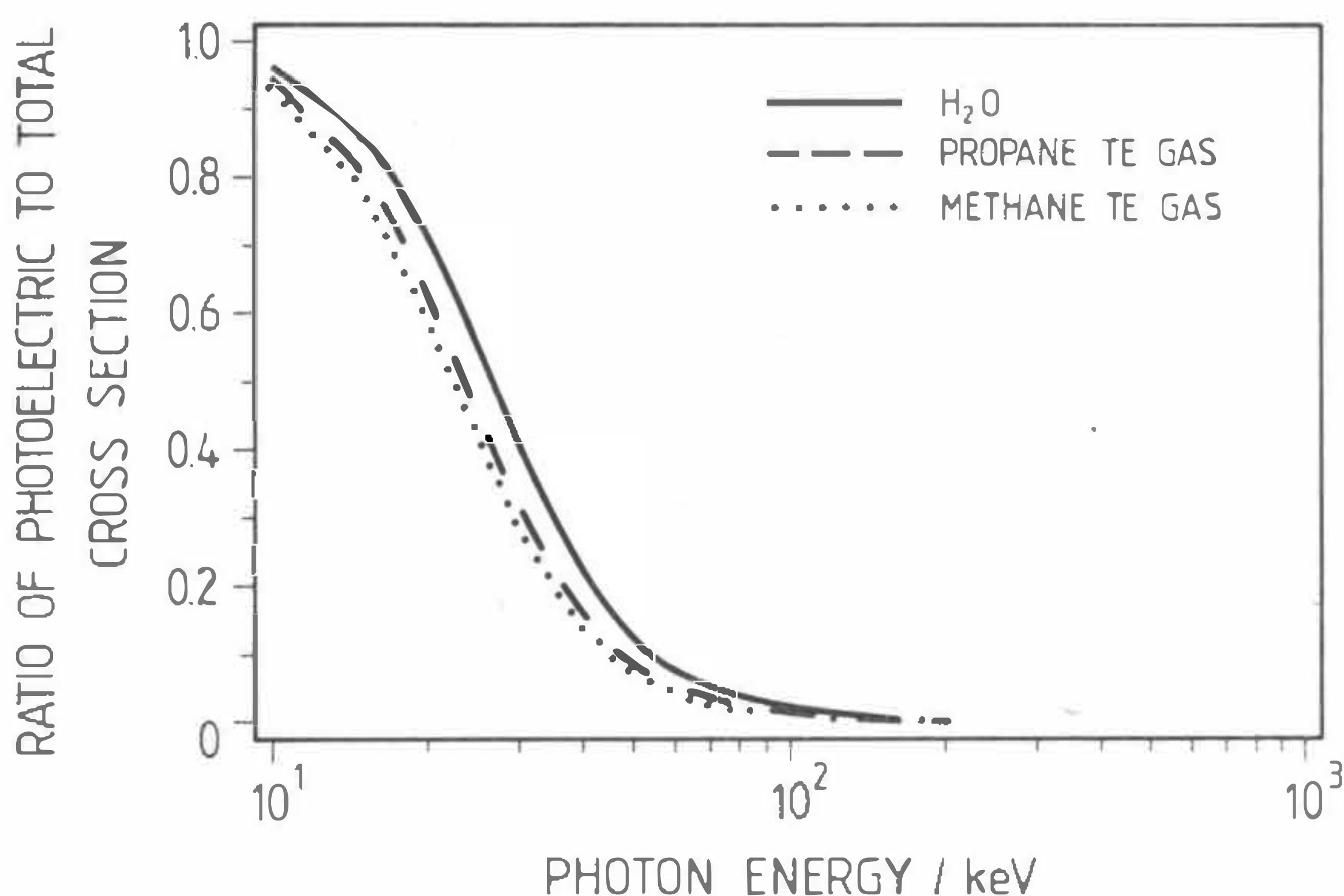


Fig.4.3b *Ratio of photoelectric to total attenuation coefficients τ/μ for H_2O , propane and methane TE gases as a function of the photon energy. Fig.4.3b was derived from the Fig.4.3a.*

Tab.4.1 summarizes information on Compton interactions in methane-based TE gas and in water of photons in the well-defined photon spectra used in experiments with the KFA counter. These results were derived from calculations of Compton electron spectra $\varphi_c(E)$ performed with Phoel-2 for cross sections from Fig.4.3.b.

It is seen in Tab.4.1 that the greatest absolute differences in the fraction of doses due to Compton effects occur for X-rays energies between 60 and 100 kVp, but they do not exceed 10% of the total dose. Outside this region, photon interactions with the TE gas are well-approximated by interactions with water (vapour).

Fig.4.4 presents microdosimetric distributions for one of the studied photon field denoted¹⁾ A_80. The bold line represents result of measurements with the KFA counter, the dash-dot line result of Monte Carlo calculations for water vapour and the dash-dot-dot line the distribution for the TE gas obtained from the distribution for water by using Eq.4.3 and Tab.4.1. This figure demonstrates the range of possible differences in energy deposition in TE and water targets. For photon energies above 100 keV and below 60 keV these differences will be smaller.

¹⁾ Symbols A denote the class of strongly filtrated X-ray spectra which are used as reference radiations for calibrating dosimeters and are specified by International Organization of Standardization [ISO, 1980]. The number "80" denotes the maximum energy (in keV) of photons occurring in the spectrum.

Tab. 4.1

Parameters of photon interactions with water vapour and with the methane-based TE gas used in the KFA counter.

ID	Average photons energy	Number of Compton electrons per 1 photon		Fraction of dose due to Compton el.		Frequency mean electron energy
		E keV	H ₂ O TE methan	F H ₂ O	TE methan	
A_10	9	0.028	0.043	.0005	.0008	0.13
A_15	12	0.076	0.107	.0021	.0030	0.28
A_20	17	0.166	0.224	.0065	.0095	0.49
A_30	25	0.412	0.504	.032	.046	1.08
A_40	33	0.634	0.720	.095	.134	1.86
A_60	47	0.884	0.887	.304	.394	3.69
A_80	66	0.929	0.952	.577	.676	6.38
A_100	83	0.963	0.977	.767	.844	9.93
A_120	100	0.978	0.987	.863	.915	13.7
A_150	118	0.984	0.991	.913	.945	18.2
A_200	161	0.996	0.998	.99	.99	31.2
A_300	248	1.000	1.000	1.00	1.00	60.1

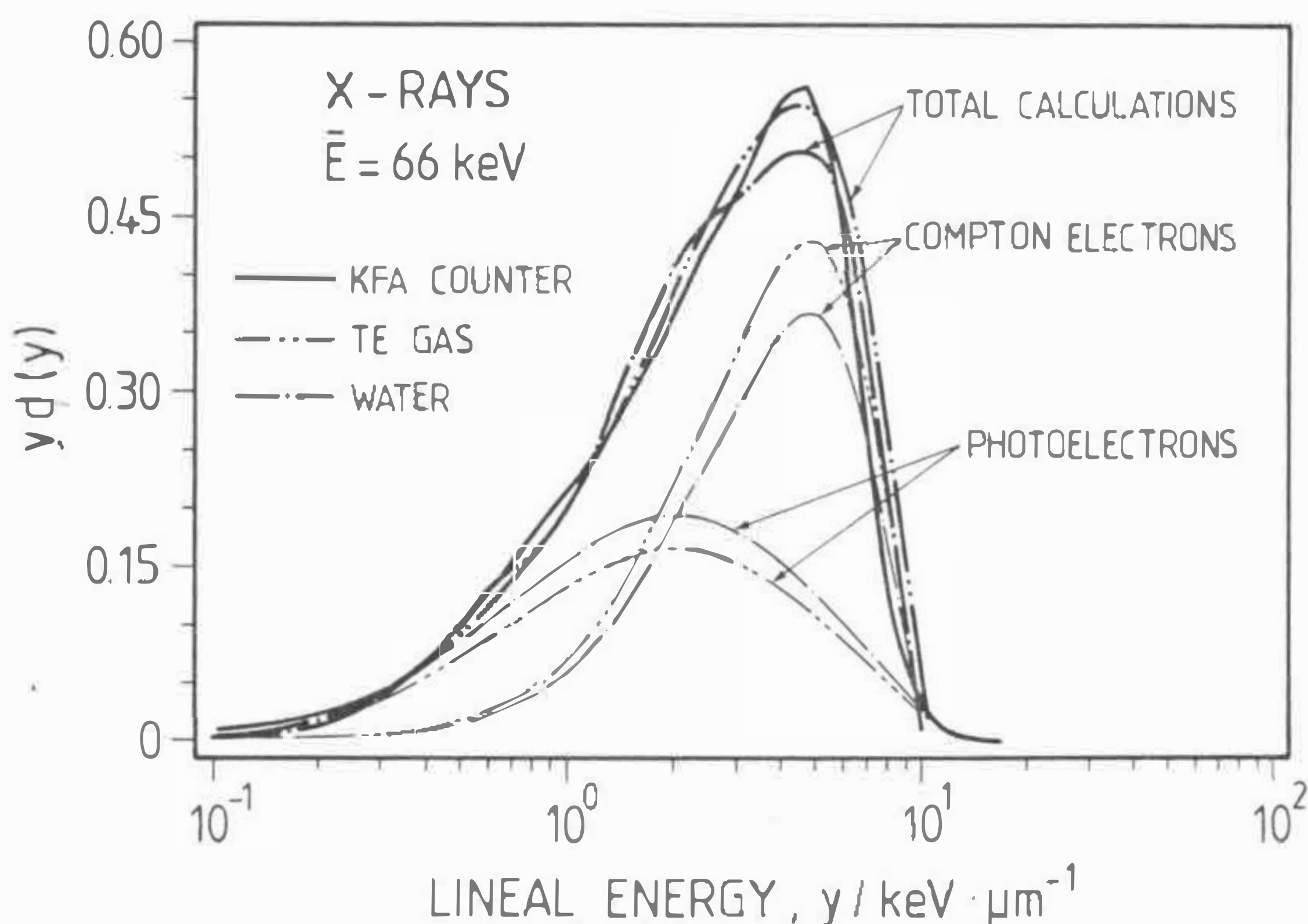


Fig.4.4 Comparison of measured [Schmitz, 1989] and calculated $y_d(y)$ distributions for A_80 X-rays ($E=66$ keV). The distributions for TE gas were obtained by normalizing distributions for water according to the relative contribution to the dose of Compton and photoelectrons (see Eq.4.3).

4.2.2. Comparison of calculated and measured with walled KFA TEPC microdosimetric distributions

The KFA counter is described in the Ch.3.3. One aspect, which should be taken into account in numerical simulations, is the existence of a counter wall which distorts the input photon spectrum. The question arises how the degradation of the primary photon spectrum in the counter wall influences the measured microdosimetric distributions. This was studied by Schmitz et al. [1989] who showed that for 10 to 300 kVp X-rays, the normalized microdosimetric distributions measured with 5, 15 and 20 mm polyethylene walls do not differ significantly as demonstrated in Fig.4.5. Therefore, in the following calculations the possible effects of distortion of input photon spectrum due to counter walls will be neglected.

Calculations were performed for spherical sites of 2 μm in diameter and for water vapour. It was shown in the previous paragraph that for photons of energies about 80 keV differences are the highest between the TE methane gas and water vapour.

Figs.4.6.a-b illustrate dose distributions of lineal energy for photons of average energies 9 keV (A_10) and 17 keV (A_20). For this photon energy range, photoeffect predominates and the contributions of Compton electrons to dose is only 0.05 and 0.6%. For A_10 the secondary electron spectrum contains photoelectrons of energies from 7.5 to 9.5 keV. Csda range in water of 9 keV electrons is of about 2 μm [Berger, 1973]. In this case, about 40 % of dose produced by photoelectrons arises from insiders i.e. photoelectrons completely stopped in the 2 μm target. For A_20 insiders practically do not occur while secondary electrons have a csda range from 5 to 8 μm . Dose is mostly deposited by crossers. The right-side asymmetry in the $d(y)$ distribution is produced by stoppers. It is characteristic of stoppers that they always contribute to the highest lineal energies because of the highest energy concentration at the end of the electron track.

Fig.4.7 presents the calculated (bold lines-TOTAL) and measured (dashed lines) microdosimetric distributions for photon spectra of average energies 33, 48 and 118 keV. In this energy range the predominating type of photon interactions with the medium changes: while photoeffect in water is the main interaction for 33 keV, at 118 keV the Compton electrons predominate. These three energies are therefore representative for explaining the role of Compton and photoelectrons in the shape of the microdosimetric distribution. For 33 keV photons, 90.5% of the dose in water is produced by photoelectrons. Compton electrons deposit dose around lineal energies of 2 keV/ μm and strongly contribute to the left-hand sided peak in the total distribution. For 48 keV photons, the average energy of Compton electrons increases, shifting the Compton peak to about 3.5 keV/ μm . This peak is made up by insiders and stoppers. Photoelectrons, i.e. electrons of about 48 keV mean energy, mostly cross the site, producing a broad distribution due to energy straggling. For photons of mean energy 118 keV, the fraction of dose due to photoeffect is only 8%, which in practice, does not affect the distribution shape. The frequency mean energy of the Compton electrons is in this case 20 keV. This is the reason why the shape of this $y_d(y)$ distribution is similar to the shape of distribution for A_20 photons (Fig.4.6).

In general, this comparison has shown that despite the many simplifications introduced, the presented calculations represent measured microdosimetric distributions quite well. With the help of these calculations it is possible to identify, the contributions of different types of physical interactions to photon-induced microdosimetric distributions. It is clear, however, that these calculations are not able to explain all aspects of measured distributions, e.g. the occurrence of a double peak in distribution A_40 in Fig.4.7.

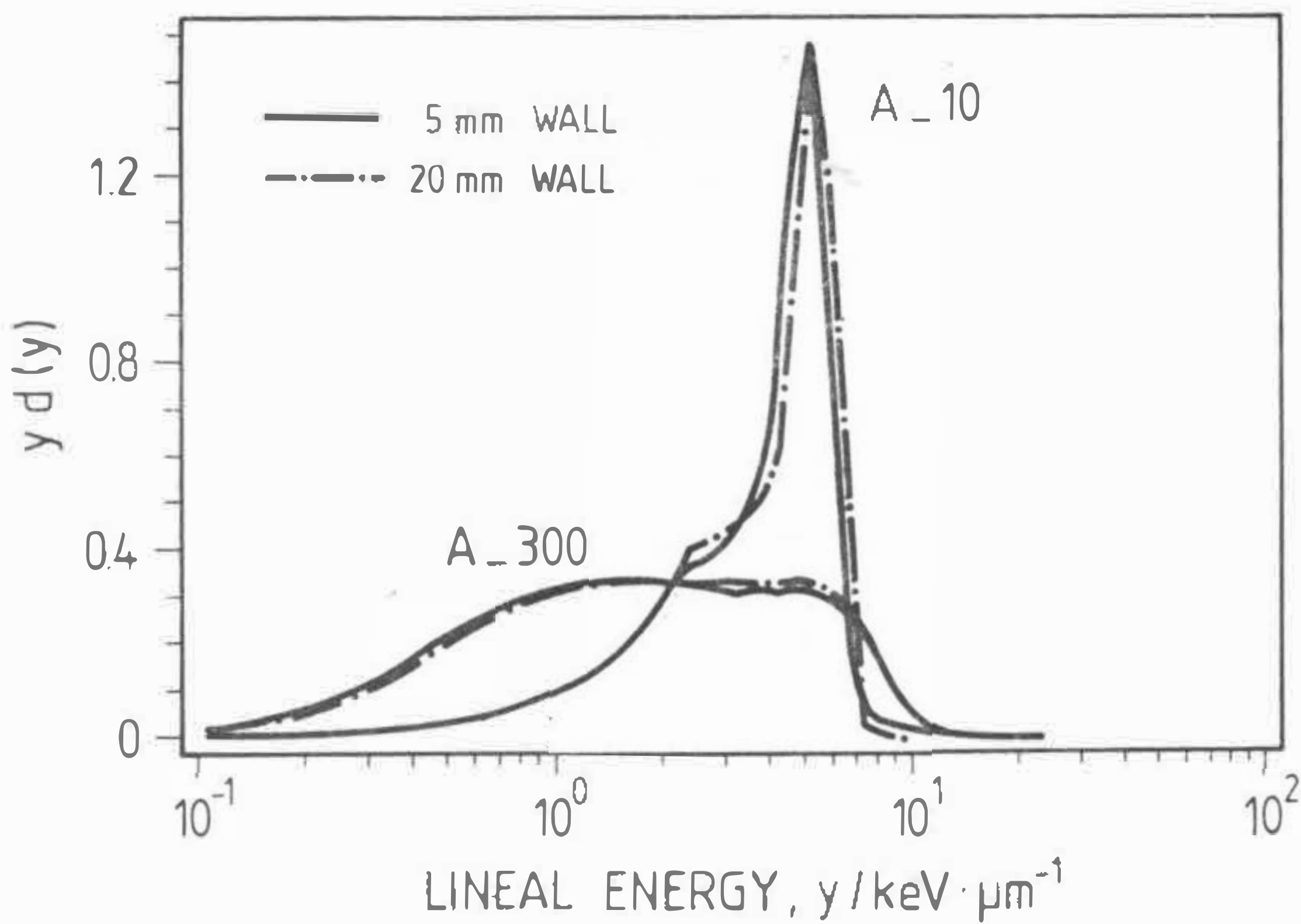


Fig.4.5

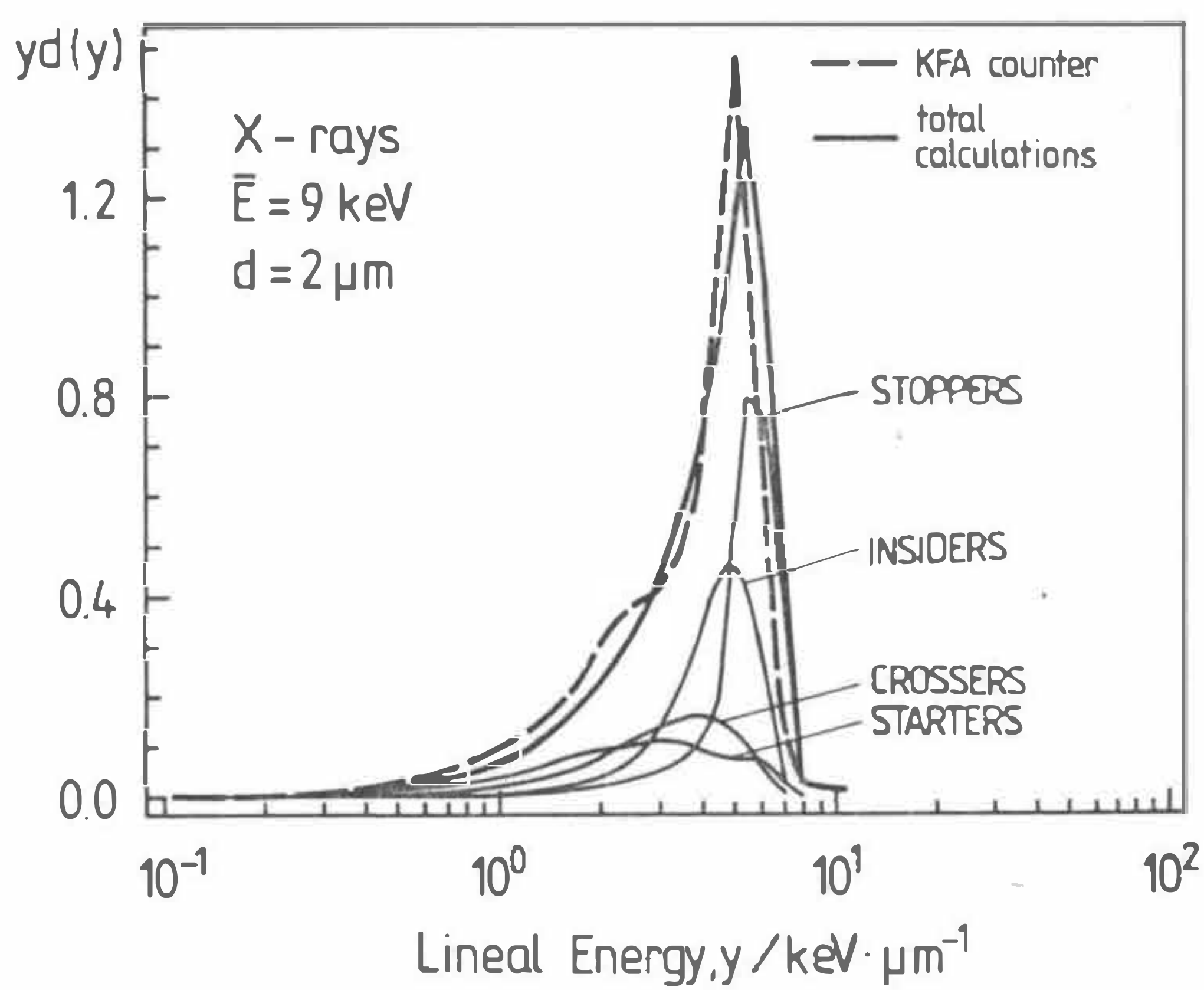
Dose lineal energy distributions measured with the KFA TEPC for two wall thickness (20 mm (broken line) and 5 mm (solid line) and for photon spectra A_10 and A_300. This figure demonstrates that the degradation of the input photon spectrum on the counter walls does not significantly changes photon induced microdosimetric distributions. The similar results were obtained for intermediate photon energies [Schmitz, 1989]

4.2.3 Comparison of calculated and measured with wall-less TEPC microdosimetric distributions

A large set of microdosimetric distributions for photons in the energy range from 12 to 1250 keV was measured by Kliauga and Dvorak [1978] with a wall-less proportional counter. A comparison with the measurements performed for 11.9 and 25.3 keV photons is particularly interesting because in the experiments the simulated diameter was varied from 0.25 to 8 μm .

Figs.4.8.a-b compare calculated and measured dose distributions of lineal energy for 11.7 and 25.3 keV narrow photon spectra and simulated diameters of 0.24, 0.48, 0.96, 1.9, 3.9 and 7.7 μm . Rounded-off values are used for denoting diameters in the figures and in text, e.g. 0.96 μm is referred to as 1 μm . For the considered photon energies the predominating type of photon interaction with water is photoelectric effect. The 11.5 keV secondary electrons produced by 12 keV photons have a c.s.d.a range in water of 3.3 μm and can be totally absorbed in a 4 and 8 μm sites. It is seen in Fig.4.8a where sharp peaks occur at about 4.5 keV/ μm ($d = 4 \mu\text{m}$) and 2.2 keV/ μm ($d = 8 \mu\text{m}$).

a)



b)

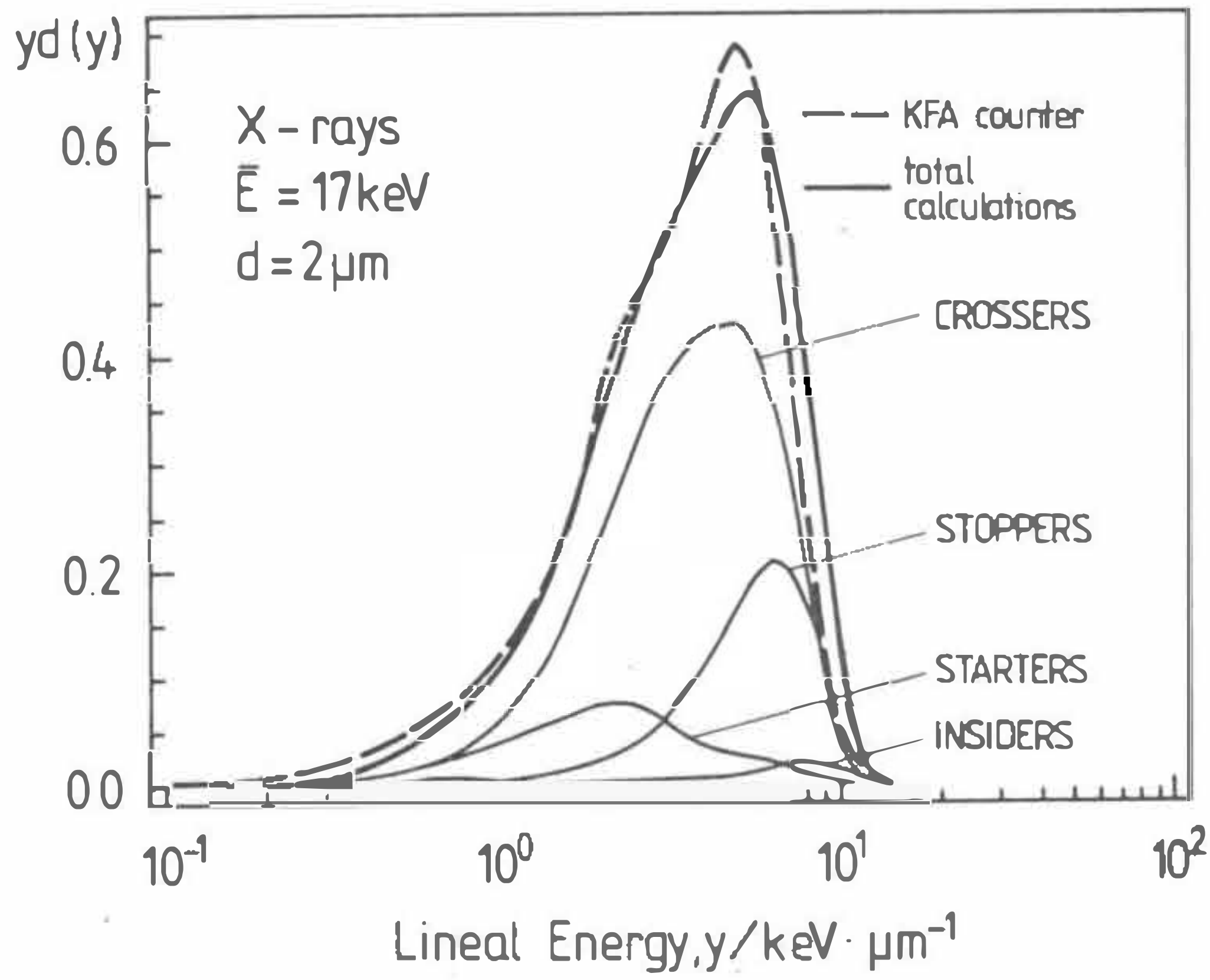
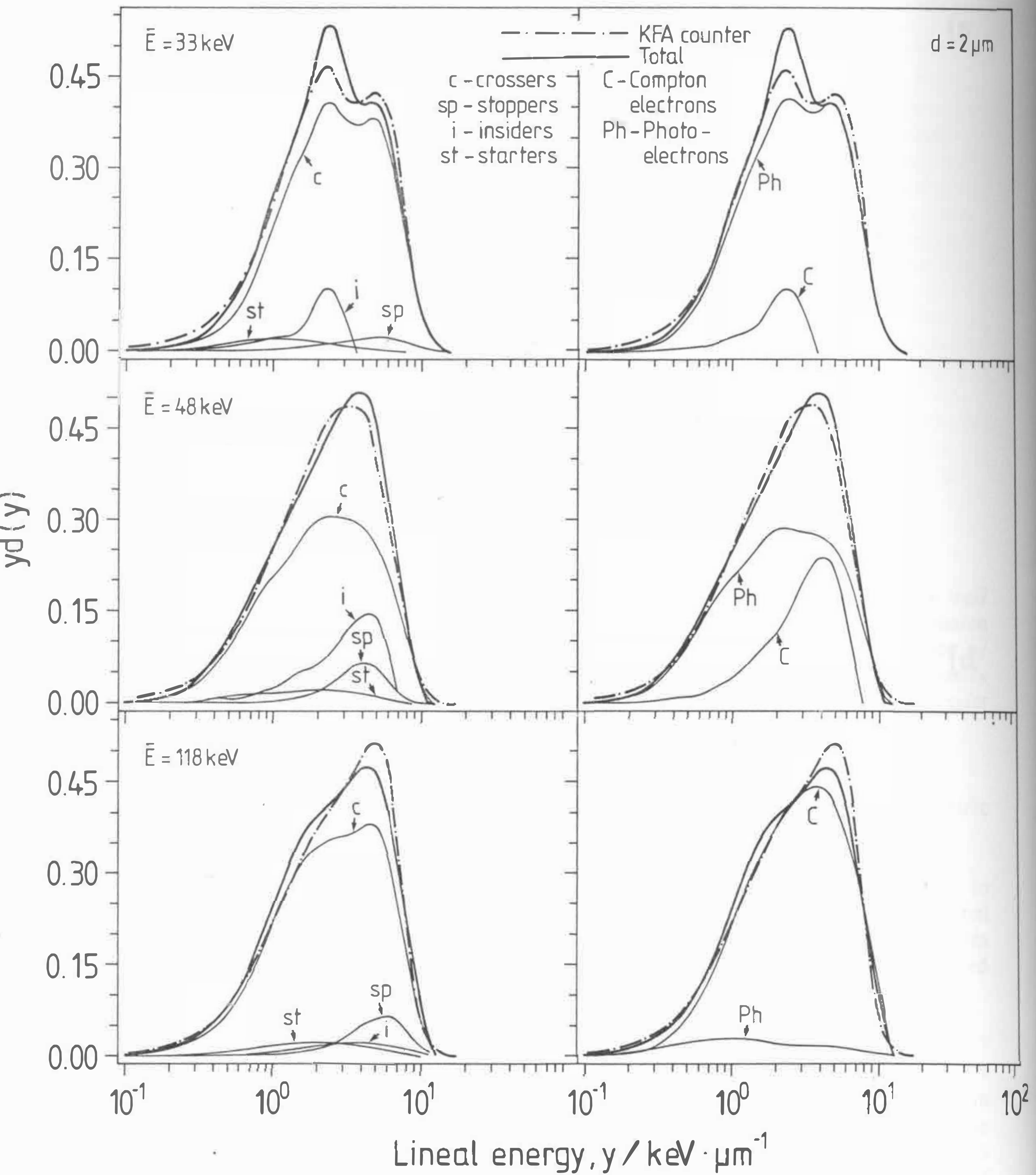


Fig.4.6

Comparison of $y_d(y)$ distributions measured with the KFA counter (dashed lines) [Schmitz, 1989] and calculated with the method described in the Ch.4.1 (solid lines). The bold line - the total $y_d(y)$ distribution; the thin lines - contributions from stoppers, starters, insiders and crossers. a) A_{10} ($\bar{E} = 9 \text{ keV}$) b) A_{20} ($\bar{E} = 17 \text{ KeV}$)

**Fig.4.7**

Comparison of measured [Schmitz, 1989] and calculated $y_d(y)$ distributions for X-rays: A_{40} ($\bar{E}=33 \text{ keV}$), A_{60} ($\bar{E}=48 \text{ keV}$) and A_{150} ($\bar{E}=118 \text{ keV}$). On the left side the contributions from crossers, stoppers, starters, insiders and on the right side contributions from photo- and Compton electrons.

No such effect is seen in Fig.4.8b because the $12.8 \mu\text{m}$ range of 25 keV electrons exceeds the maximum simulated diameter ($8 \mu\text{m}$). Here, only about 3% of the dose is delivered via the Compton effect. The dose-average energy of Compton electrons is 1.8 keV and these electrons are likely to be totally absorbed in spheres larger than $1 \mu\text{m}$. For $d = 8 \mu\text{m}$ these electrons give rise to lineal energies around $0.34 \text{ keV}/\mu\text{m}$. Indeed, a small peak around this value can be observed in the experimental and calculated distributions. For lower simulated diameters, energy deposition due to Compton electrons is hidden within the high "background" of photoelectrons.

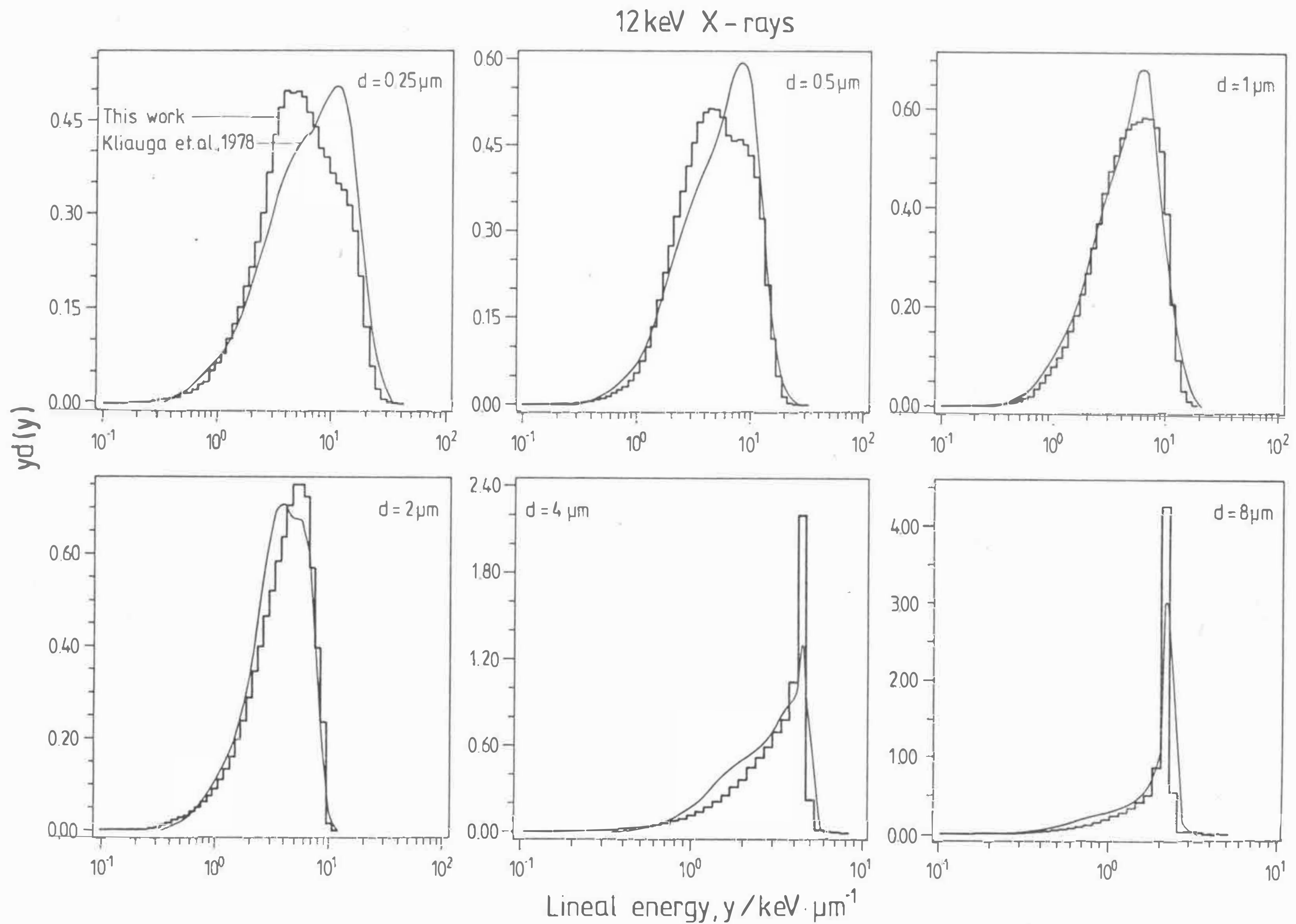
The general agreement between the calculated and measured microdosimetric distributions is good. Some differences between the calculations and experiment cannot be, however, unequivocally explained. When analyzing distributions for 8, 4 and 2 micrometers (Fig.4.8b) one can see indications of small peaks at 0.7, 1.5 and 3 keV/ μm . These peaks do not occur in the calculated distributions. The presence of these peaks indicates that the secondary electron spectrum obtained in the counter volume contains more low energetic electrons (of energy approximately 4 keV) than assumed in calculations. 4 keV electrons have a csda range of about $0.5 \mu\text{m}$ and still have a chance to be totally absorbed in a $0.5 \mu\text{m}$ site. Contributions of such events are clearly observed in the measured $d(y)$ distributions for 0.5 and $0.25 \mu\text{m}$. It is interesting to state here that no disagreements between calculations and the TEPC measurements are observed which could be specific to low simulated diameters.

4.2.4 Microdosimetric distributions for nanometer targets

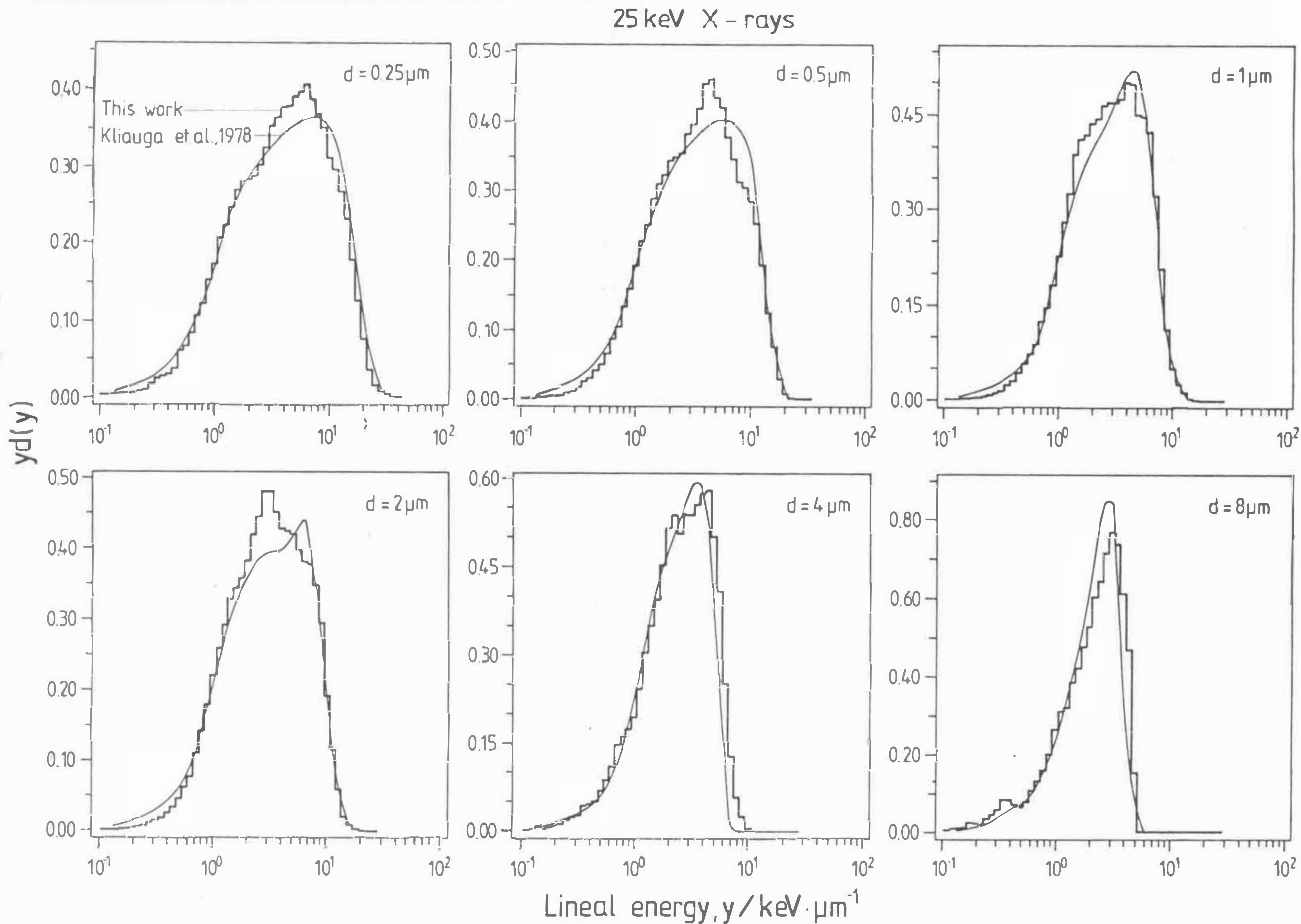
The present method of calculations of microdosimetric distributions leads to fairly good agreement with measurements. An advantage of the calculations is that it is possible to apply them to simulated diameters in the nanometer range, which at present is beyond the scope of experimental measurement.

It has been already shown in the previous section that the shape of the photon-induced microdosimetric distribution depends more on the relation between the range of secondary electrons and the site diameter than directly on the physical type of interactions taking place in the counter. If a sensitive site is large enough to completely absorb secondary electrons (insiders), then the counter works as a spectrometer. A "tail" at lower lineal energies arises from particles crossing the spherical site at impact parameters close to 1, and also from starters and stoppers.

This distribution structure can be observed on Figs.4.9.a-f. 1 keV photons usually produce two electrons in water (photo- and Auger electrons), each of about 0.5 keV energy and a range of about 20 nm. These electrons are likely to be totally stopped in spherical targets of 100 and 50 nm diameter and deposit respectively about 90% and 70% of dose as insiders. For 20 nm targets, total absorption can only take place when both electrons are emitted in about the same direction. Hence this type of events occurs with much lower probability. 5 keV photons (Fig.4.9b) produce electrons of about $0.7 \mu\text{m}$ range and these are likely to be absorbed in $2 \mu\text{m}$ and $1 \mu\text{m}$ sites giving rise to peaks at respectively 3.75 and $7.5 \text{ keV}/\mu\text{m}$. 50 keV photons (Fig.4.9e) induce photoelectric electrons, which are usually crossers and produce broad microdosimetric distributions. With decreasing site diameters the variance of the distribution increases and the right edges of the distributions are shifted towards higher lineal energies. It is interesting to state the similarity between 20 keV and 100 keV distributions. The reason for that is that similar secondary electron spectra are produced for 20 keV photons via photoeffect and for 100 keV via Compton scattering.

**Fig.4.8a**

Calculated and measured with spherical wall-less counter [Kliauga & Dvorak, 1978] $yd(y)$ distributions induced by photons of average energy of 11.9 keV.

**Fig.4.8b**

Calculated and measured with spherical wall-less counter [Kliauga & Dvorak, 1978] $y_d(y)$ distributions induced by photons of average energy of 25.3 keV.

Fig.4.10 presents $yd(y)$ distributions for 250 kVp X-rays, filtered with 1.5 mm Cu [Wachsmann & Drexler, 1976]. This figure was calculated by scoring both ionization and excitations events. The discrete nature of energy depositions at $d=3$ nm and low lineal energies below 10 keV/ μ m is produced due to energy deposition in the form of single ionizations or excitations and corresponds to the differential optical oscillator strength distribution in water vapour [Paretzke, 1987]. E.g., the small peak at 3.5 keV/ μ m arises from 7.5 eV excitations in the dissociation of the H_2O molecule. The peak around 6.5 keV/ μ m is produced due to ionizations from the $1b_1$ shell (12.6 eV) [Paretzke, 1987] and due to excitations.

At the scale of a few nanometers, the term "energy deposition in a site" is not very precise because of quantum mechanical uncertainties [ICRU 36, 1983]. Therefore at low diameters, instead of energy deposition, the number of ionizations in a site is sometimes used. Fig.4.11 presents distribution of the number of ionizations in 20 nm spherical sites due to soft and 250 kVp X-rays. The peak for 0.28 keV X-rays corresponds to total absorption of the secondary electron. The broadness of the peak represents physical fluctuations in the number of primary ionizations produced by electrons of a given energy. The ionization distributions are useful in the analysis of the high biological effectiveness of soft X-rays [Goodhead & Brenner, 1983].

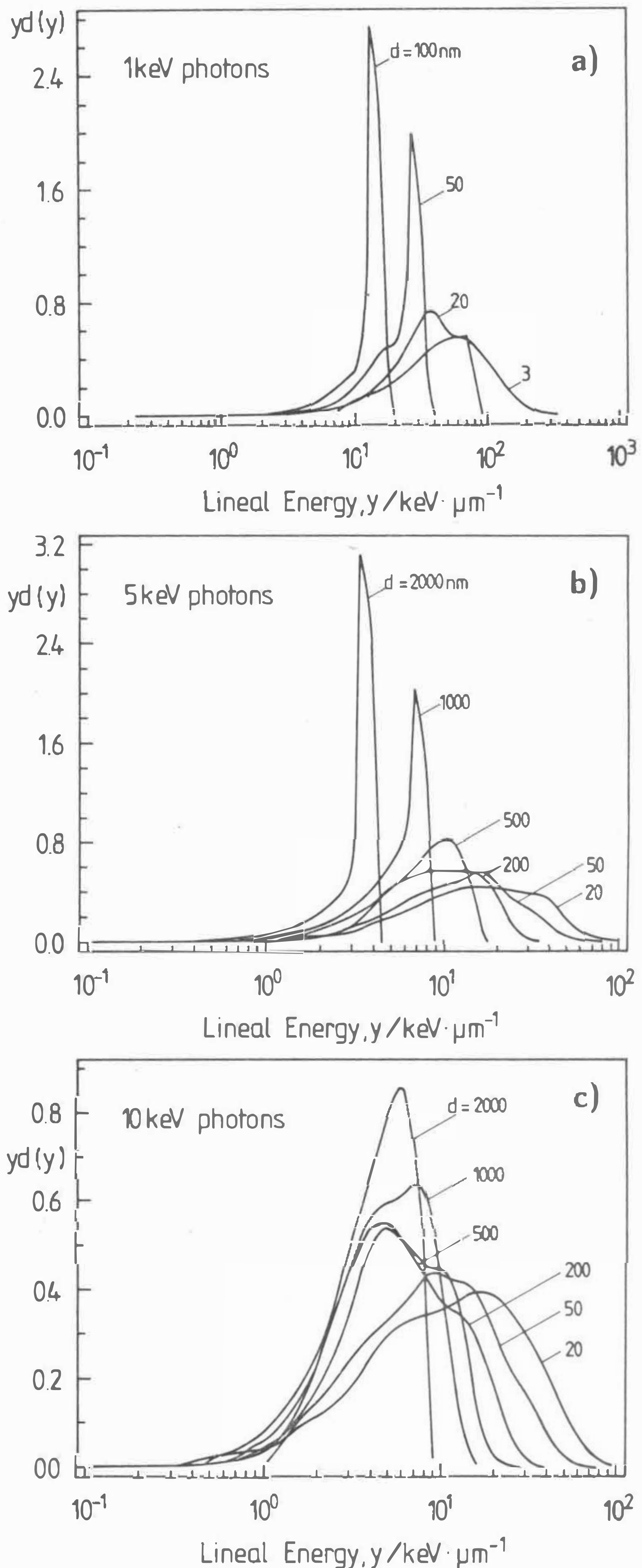
4.2.5. Limitations of the method

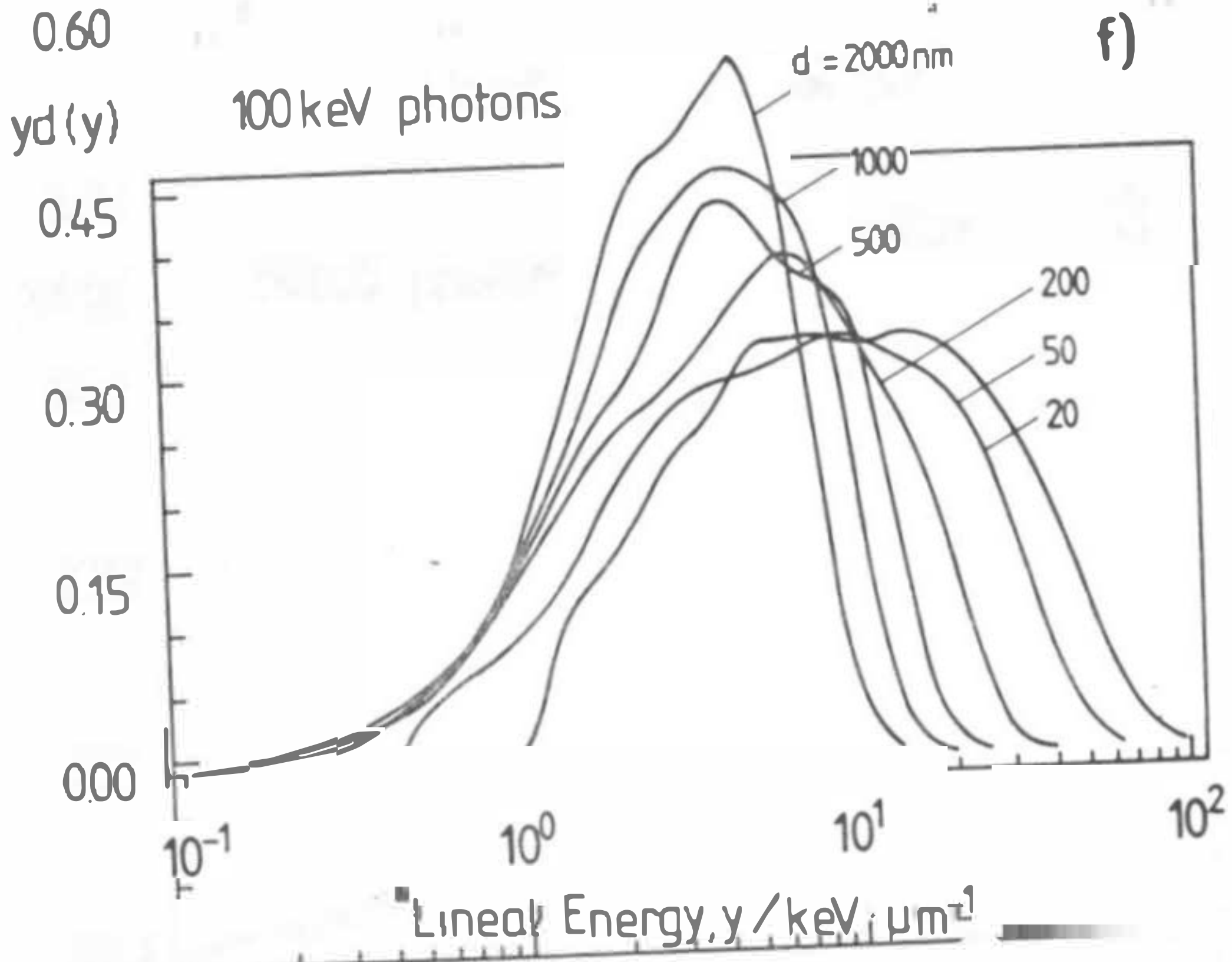
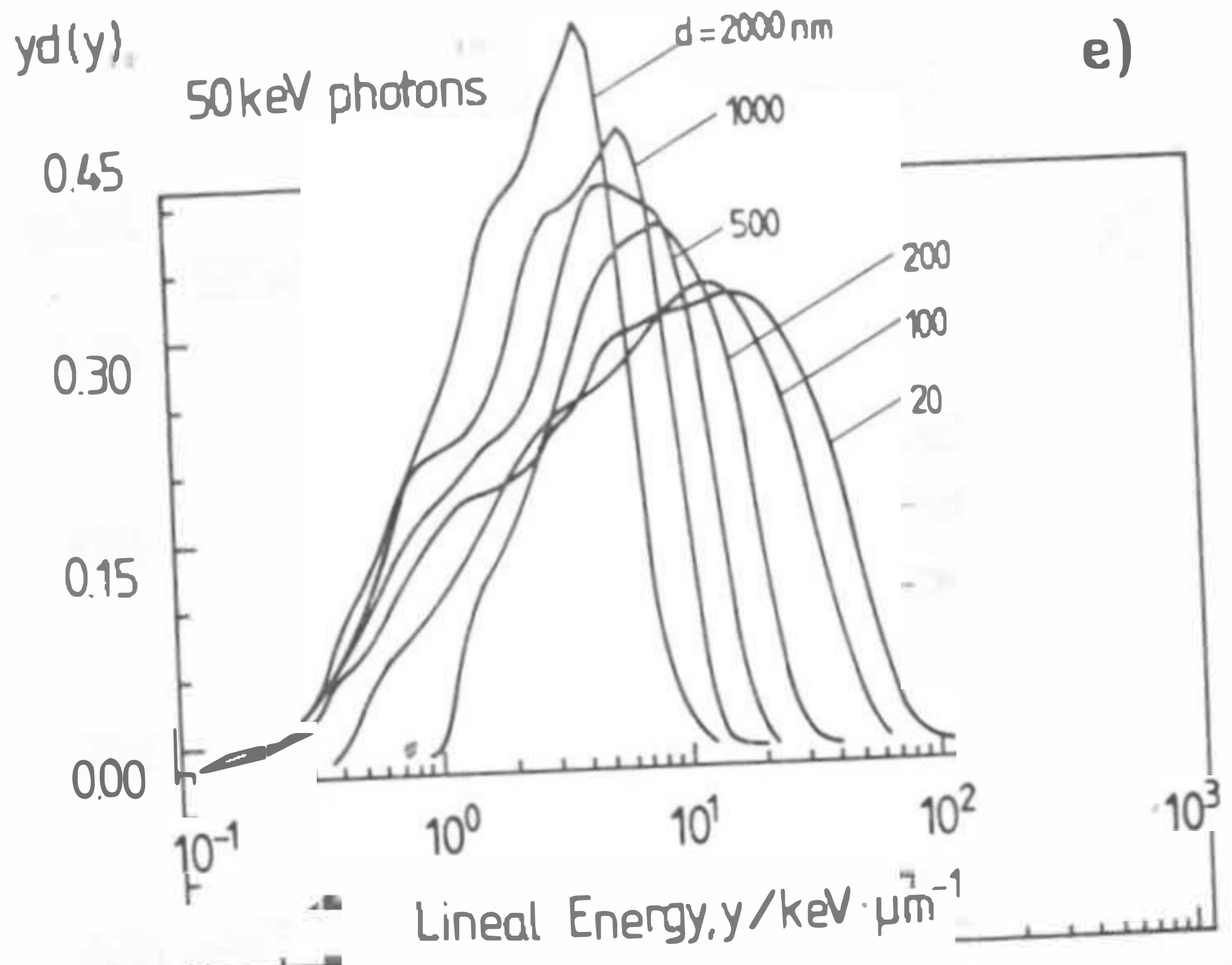
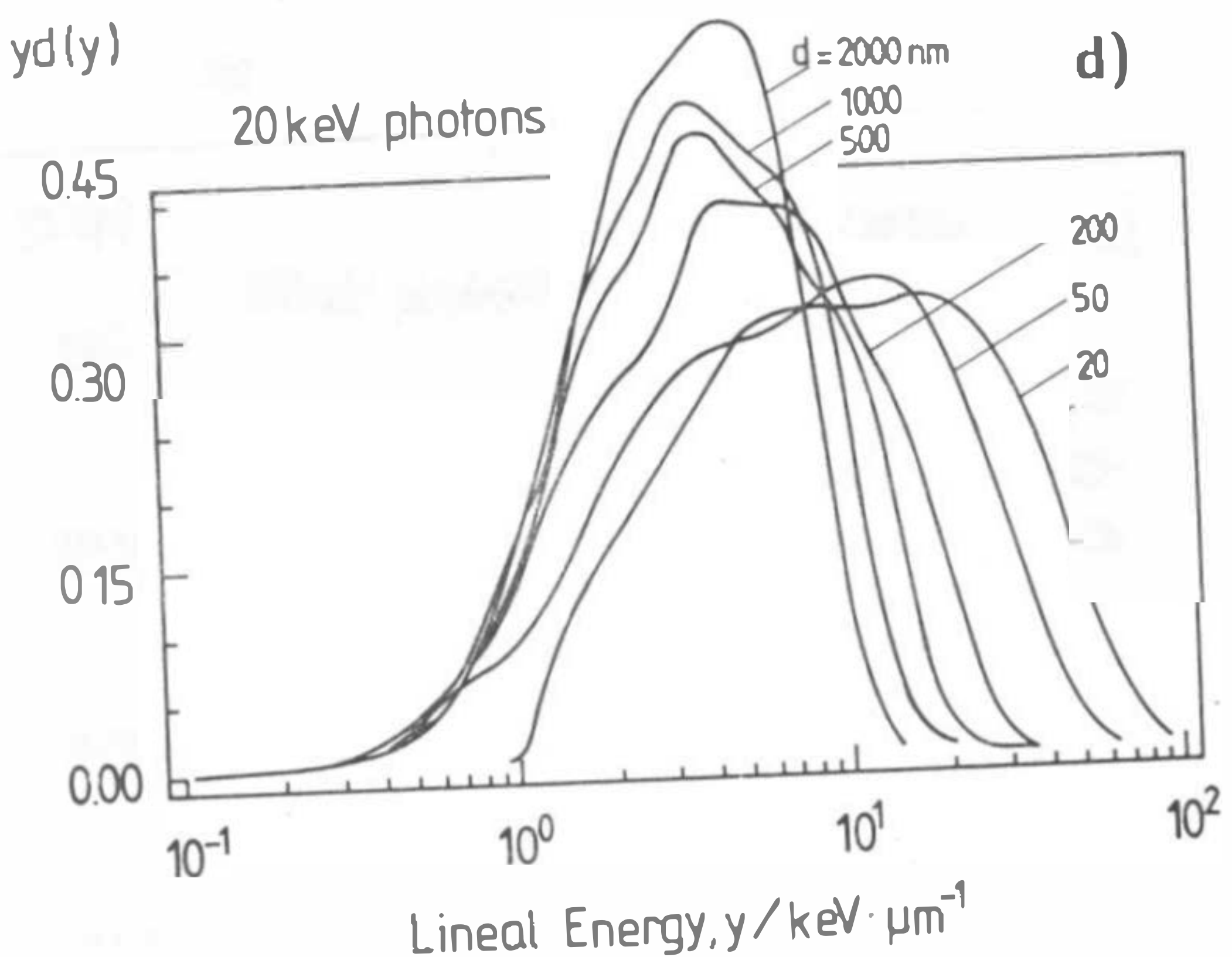
The above presented method of numerical simulations of photon-induced microdosimetric distributions has several limitations. The most important of them are:

- i) Electron track structure calculations are performed in this work with the code MOCA-8 which simulates electron tracks in water vapour for energies from 20 eV to 100 keV. In order to assess microdosimetric distributions for 300 kVp X-rays, MOCA-8 was extended to electron energy 162 keV, which is the Compton edge for 300 keV photons. This extension was made by scaling the mean free path of electrons by the electron stopping power taken from ICRU-36 [1983] but leaving other electron cross sections as tabulated for 100 keV electrons. This simplified approach can be used, e.g., for 250 kVp X-rays because only of 10 % of dose is deposited by electrons with energies above 100 keV. It cannot be, however, used to calculate tracks induced by gamma-rays from Ba-137 ($E=661$ keV) and Co-60 ($E=1250$ keV). A new version of MOCA program is under development with electron energy range to 1 MeV [Paretzke, 1987].
- ii) Track structure calculations are performed for water vapour whereas the measurements of microdosimetric distributions are always performed with tissue equivalent proportional counters. This was discussed in details in Ch.4.2.1.
- iii) In the present calculations, ideal radiation equilibrium between the targets and the surrounding medium is assumed. Targets are placed in an infinite, uniform medium which does not degrade the incident radiation and which has an identical structure and composition as the targets. This is not the case in practical measurements where counter walls not only disturb the incident radiation but produce a secondary particle spectrum different from that produced by the gas.
- iv) In cylindrical counters the chord length spectrum differs from the triangular chord-length spectrum of the sphere.

Fig.4.9

Calculated dose lineal energy distributions for a) 1 keV, b) 5 keV and c) 10 keV d) 20 keV e) 50 and 100 keV monoenergetic photons. Only ionization events were used in calculations being converted into lineal energy using $W=31$ eV.





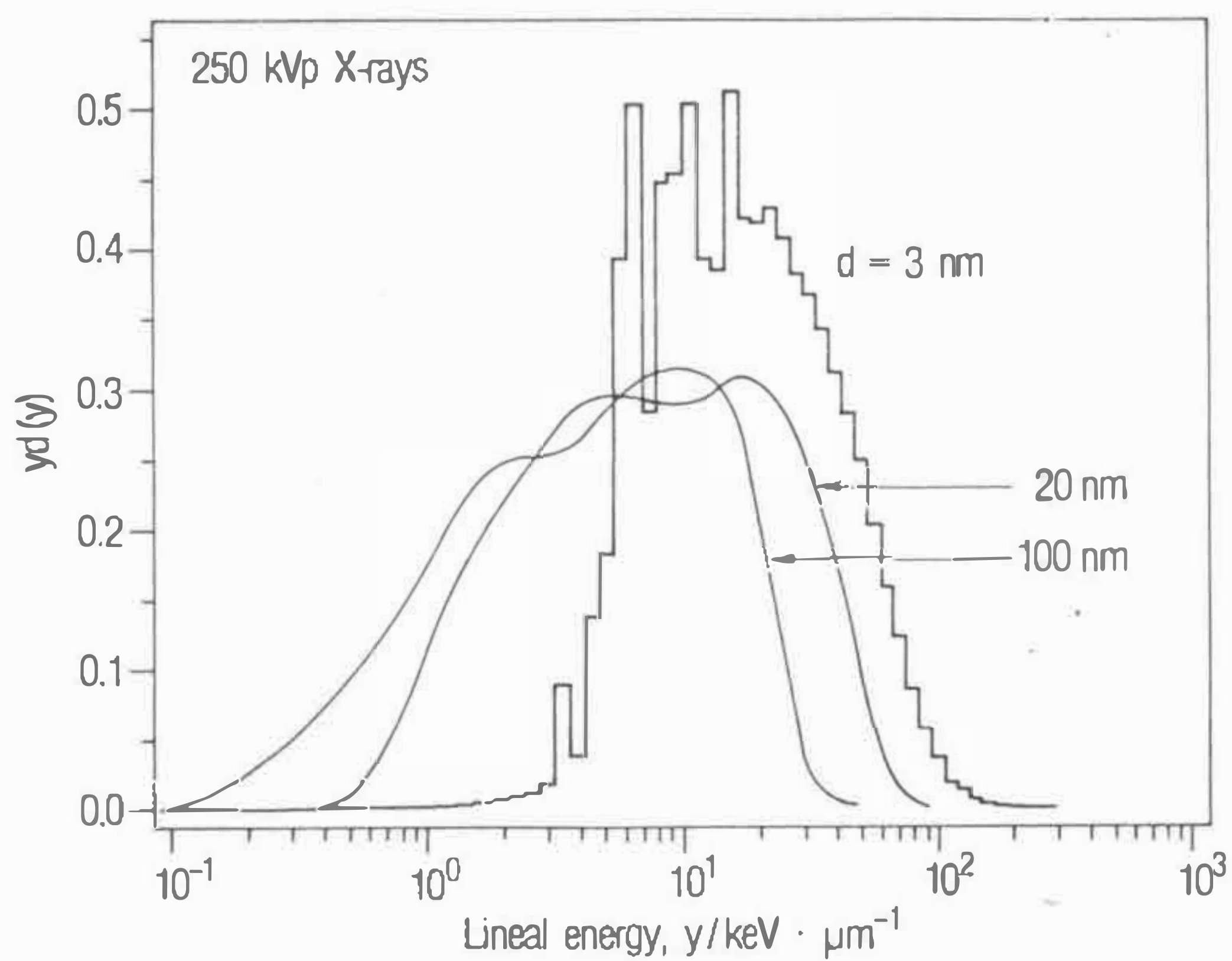


Fig.4.10

Calculated dose lineal energy distributions in 3, 20 and 100 nm sites for 1.5 mm Cu filtrated 250 kVp X-rays. Calculations were performed for water vapor. Both ionizations and excitations events were taken into account.

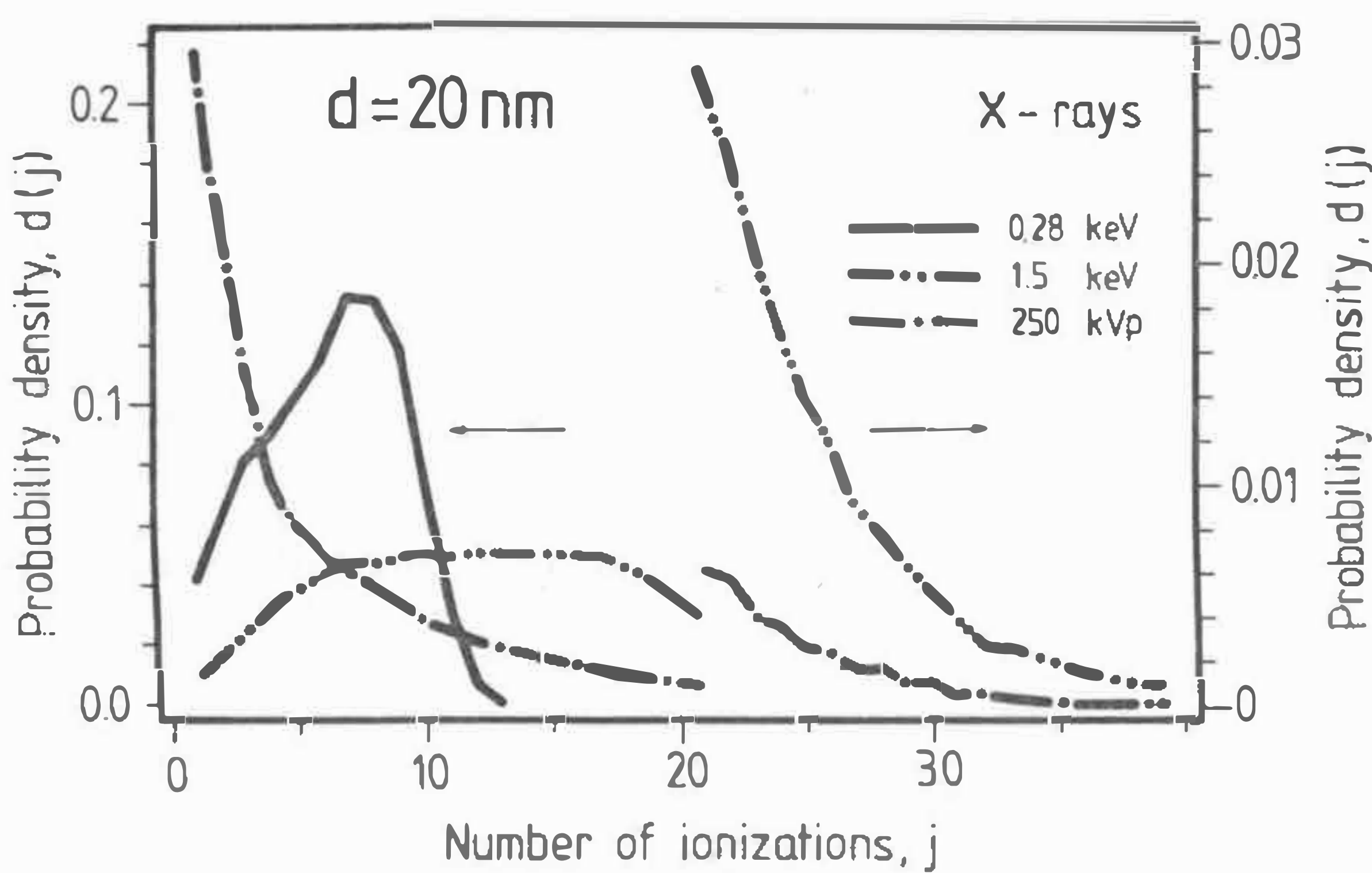


Fig.4.11

Calculated frequency ionization distributions in 20 nanometer spherical sites for soft and 250 kVp X-rays.

5. EVALUATION AND INTERPRETATION OF ENERGY DEPOSITION FOR IONS.

Ions are of particular importance in radiation biology, because they enable the investigation of radiation effectiveness in a wide range of LET and under well defined physical conditions. Therefore, results of experiments with ions are useful for testing radiobiological models.

The pattern of energy deposited by ions in matter consists of a region of very high energy deposition (track core) and a large region of lower ionization density, where ionizations are produced by delta-electrons ejected by an ion. This structure of an ion track is of great interest for radiobiology and therefore is considered in detail in microdosimetry.

In practice, only a few experimentally measured microdosimetric distributions for ions are available even for micrometer sites (see Ch.3.3.3). For sites of nanometer dimensions, numerical track-structure calculations are so far the only possibility. In this chapter Monte Carlo ion track structure simulations are applied to evaluate microdosimetric distributions. Then, a recipe is derived in order to approximate calculated microdosimetric distributions in targets of micrometer and nanometer dimensions by simple analytical functions.

Due to the lack of corresponding experiments the calculated microdosimetric distributions for ions cannot be, in practice, checked against the measured experimental distributions in sites. A certain test for applicability of the track structure calculations to investigate straggling of energy deposition is offered by comparison of calculated and measured radial dose distributions. This is done in the last part of this chapter.

5.1. PRINCIPLES OF ION ENERGY DEPOSITION IN A SENSITIVE SITE

5.1.1. Ion and delta-events microdosimetric distributions

It was proposed by Guenther and Shultz [1983] that energy deposition in the site due to ion action could be described by two types of microdosimetric distributions, related to different type of interactions with the sensitive volume.

The first distribution concerns energy deposition due to events produced by an ion crossing the target (ion event). Dose and frequency distributions of ionizations related to this type of events are denoted by $d^{(i)}(j)$ and $f^{(i)}(j)$, where j is the number of ionizations. The superscript (i) is to indicate that these distributions relate to ion events.

For ions passing outside the sensitive volume and depositing energy in the site only by delta electrons, the superscript (δ) is used. The functions $d^{(\delta)}(j)$ and $f^{(\delta)}(j)$ denote the dose and frequency distributions of ionizations caused by delta-ray events. $j^{(i)}$ and $j^{(\delta)}$ correspond to the first moments of ion- and delta-event frequency distributions. The ion-events are also called crossers [ICRU 36, 1983] or direct events [Kellerer, 1971] and delta-ray events are called "touchers", or indirect events.

The expression for total distribution of ionizations in the site is following [Guenther & Schultz, 1983]:

$$f_1(j) = (1 - \mu_F) f^{(i)}(j) + \mu_F f^{(\delta)}(j) \quad (5.1)$$

where the weighting factor is the fraction of delta-ray events in the sensitive site, μ_F . When μ_D is a fraction of dose in the targets due to delta-events, the relation between μ_D and μ_F is as follows [Guenther & Schultz, 1983]:

$$\mu_F = \mu_D \frac{\bar{j}_F}{\bar{j}^{(\delta)}} \quad (5.2a)$$

The mean number of ionization for the total spectrum, \bar{j}_F , can be obtained by weighting the mean number of ionizations for delta- and ion-events:

$$\frac{1}{\bar{j}_F} = (1 - \mu_D) \frac{1}{\bar{j}^{(i)}} + \mu_D \frac{1}{\bar{j}^{(\delta)}} \quad (5.2b)$$

5.1.2 Straggling of energy deposition in small targets

Guenther and Schultz [1983] used an analytical approach to approximate the $f^{(i)}(j)$ and $f^{(\delta)}(j)$ distributions. Calculations were performed for site diameters from 100 nm to 10 μm . No attempt was made to account for these factors which straggled energy deposition in the site.

In fact, if ions traverse a sensitive volume at random, the amount of energy deposited in that volume depends not only on the actual chord length of the ion in the volume. Energy deposited in the volume by these ions depends also on the energy transported by delta-rays out of the volume. Ions which do not traverse the sensitive volume may pass by close enough so that some energy is deposited in the volume by a delta-ray.

Thus, there are four different factors that contribute to the energy deposition of an individual ion into a sensitive volume:

- the variation of the actual chord length of the ion in the volume,
- the straggling of energy loss, i.e., the fluctuation of energy loss of the ion along this chord length,
- the energy transfer by delta rays out of the volume (efflux),
- the energy transfer by delta rays into the sensitive volume (influx).

In this work, sensitive volumes are assumed to be spheres. It is also assumed that an ion source is situated at infinite distance i.e. that ions move parallel to each other when the target is intersect. Hence, the chord length distribution for a sphere has a triangular shape [Rossi, 1968]. Energy straggling and delta-ray efflux are expressed by introducing a straggling function, which modifies the triangular chord length distribution. Events due to particles passing outside the sensitive volume (influx of delta-rays) are described by a separate function.

5.2. FORMULATION OF THE ANALYTICAL APPROACH

In the present work, microdosimetric distributions for ions are calculated for arbitrary relations between the locations of the site and the particle track. This approach corresponds to a situation in a radiobiological experiment where it is not possible to intersect a target with a given impact parameter or to find out this parameter a posteriori.

5.2.1 Ion events

If straggling of energy loss and delta-ray transport are disregarded, the number of ionizations could be set roughly proportional to the chord-length. This can formally be expressed as the product of $T(j) = A j$ and a step function, $S(j)$, which is equal to 1 between zero and j_m and equal to 0 for larger values j . The corresponding equation can be written as follows:

$$f^{(i)}(j) = S(j) A j = \begin{cases} A j & \text{for } j \leq j_m = \frac{3}{2} \bar{j}^{(i)} \\ 0 & \text{for } j > j_m \end{cases} \quad (5.3)$$

where $\bar{j}^{(i)}$ is the first moment of the distribution $f^{(i)}(j)$ and A is the normalization factor. j_m is the number of ionizations produced by particles passing the site diametrically. A specific example of such triangular distribution is shown in Fig.5.1a.

If j is integer, the normalization constant is equal to:

$$A = \frac{2}{\sum_{j=1}^{\infty} \frac{9}{4} j^2 + \sum_{j=1}^{\infty} \frac{3}{2} j} \quad (5.4a)$$

For $\bar{j}^{(i)} \gg 1$ (or for continuous variable e.g. lineal energy), A is approximately equal to

$$A = \frac{8}{9} \bar{j}^{(i)}^{-2} \quad (5.4b)$$

To introduce the fluctuations due to energy-loss straggling and delta-ray efflux, the step function $S(j)$ is replaced by a two parameter function $F(j)$ ¹⁾:

$$F(j) = \frac{1}{e^{B(j-C)} + 1} \quad (5.5)$$

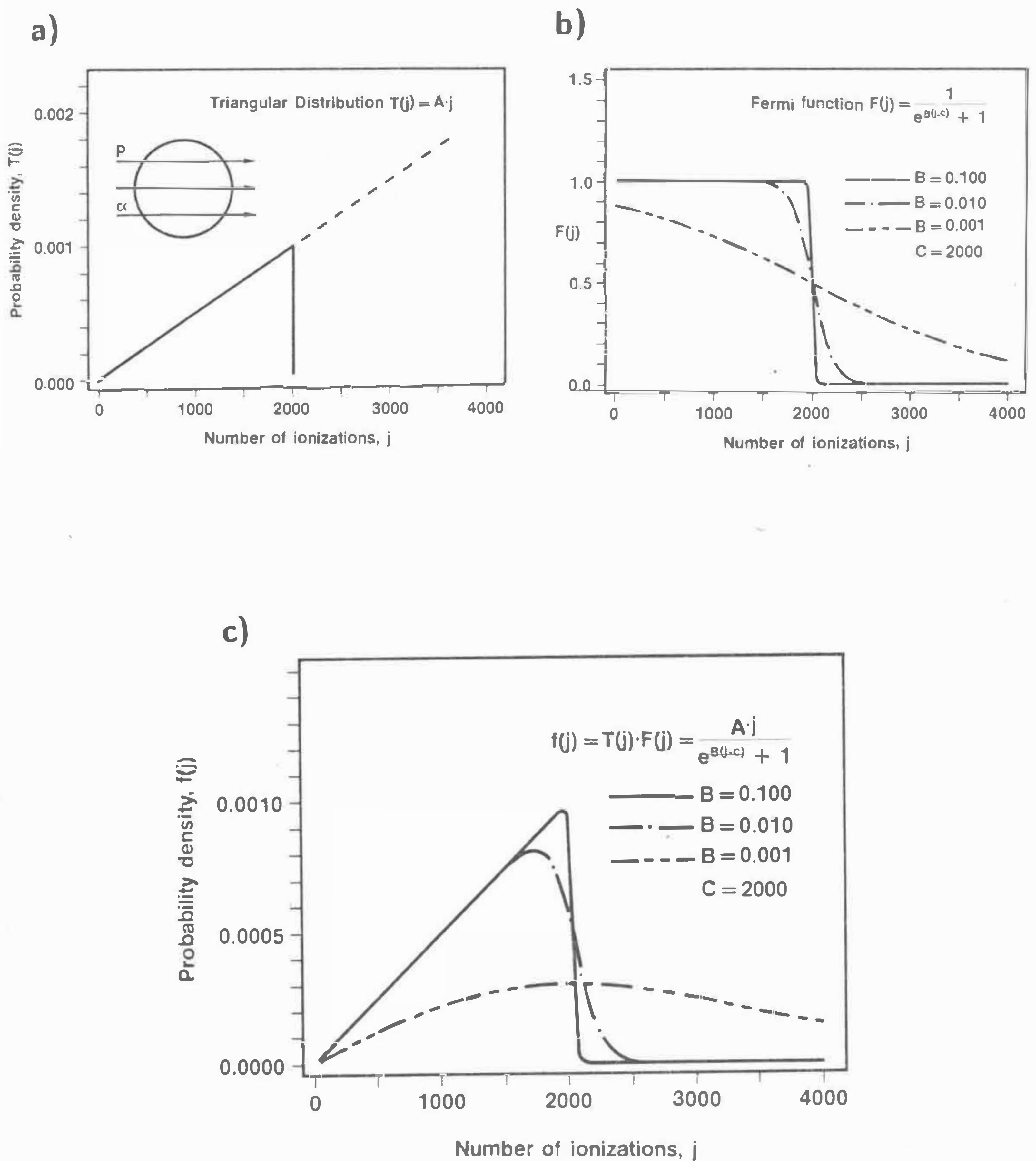


Fig.5.1

- a) The "idealized" shape of an ionization spectrum for ion-events as resulting from the chord length distribution. The maximum number of ionizations corresponds to the particles passing through the center of the sphere.
- b) Fermi function for 3 different B parameters. This function is to represent the process of energy-deposition straggling due to fluctuations in energy loss and transport of secondary electrons.
- c) The analytical description of energy-deposition by ions crossing the spherical site as made up from the functions of Figs. a and b.

Fig.5.1b presents an example of $F(j)$ for different values of parameter B . These parameters determine the width of the function; with increasing B (maintaining $C=2000$) the $F(j)$ function approaches a step function.

The single-event spectrum for ion-events is the product of the triangular function A_j and the straggling function $F(j)$:

$$f^{(i)}(j) = F(j) A_j = \frac{A_j}{e^{B(j-C)} + 1} , \quad j = 1, 2, \dots \quad (5.6)$$

The normalization parameter, A , is now equal to:

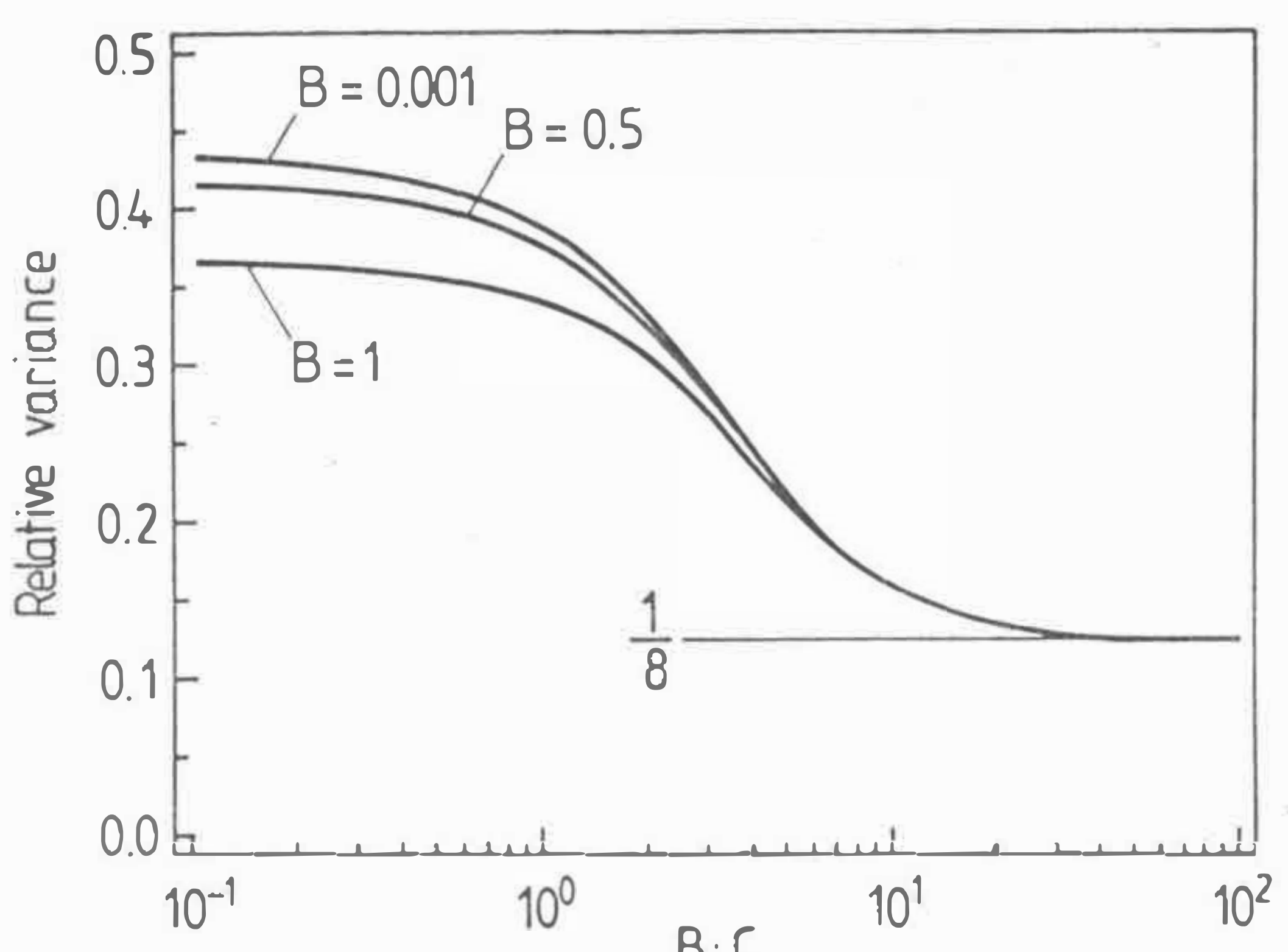
$$A = \frac{1}{\sum_{j=1}^{\infty} \frac{j}{e^{B(j-C)} + 1}} \quad (5.7)$$

Examples of $f^{(i)}(j)$ for $C=2000$ and different values of B are depicted in Fig.5.1c. For spectra with low straggling (large spheres and slow, densely ionizing ions), the parameter C approaches $1.5 j^{(1)}$, the maximum number of ionizations possible with a triangular distribution.

It is convenient to characterize distributions by their moments. The relative variance of a distribution is a measure of the shape (width) of the distribution. Fig.5.2 shows the relative variance of $f^{(i)}(j)$ as a function of $B \cdot C$ for 3 different values of B . For B smaller than 0.5 the variance is slightly dependent on B and only the product $B \cdot C$ determines the shape of the considered distribution. For ideally triangular distributions the relative variance is equal to $1/8$ [Kellerer, 1971]. This is the case for $B \cdot C$ larger than about 30. For smaller values of $B \cdot C$, the relative variance increases and this corresponds to distributions with larger straggling.

Fig.5.2

Relative variance of $f^{(i)}(j)$ given by Eq.5.6 versus $B \cdot C$. For arguments larger than about 30 the relative variance approaches $1/8$ - theoretical value for triangular distributions.



5.2.2. Delta-ray events

Particles passing outside the site deposit energy only by delta electrons. Histograms in Fig.5.3 demonstrate exemplary results of Monte Carlo calculations of frequency ionization distributions for 1.2 MeV alpha particle in 20 nm targets in water. The uppermost picture shows the delta-event distribution $f^{(\delta)}(j)$. It can be seen that this and other $f^{(\delta)}(j)$ Monte Carlo-calculated distributions (see also later Fig.5.7) - plotted on logarithmic scale - can be well fitted by a straight line.

Therefore, the function used to approximate $f^{(\delta)}(j)$ should fulfill the following requirements:

- be an exponential (or power) function
- be normalized to 1
- the first moment of this function be equal to $\bar{j}^{(\delta)}$.

For a continuous variable, x , these requirements are fulfilled by a simple exponential function $f(x) = (1/\bar{j}^{(\delta)}) \exp(-x/\bar{j}^{(\delta)})$. This relation does not however hold for integer j . Therefore the following function of integer j was found to approximate the delta-event distributions

$$f^{(\delta)}(j) = \frac{1}{(\bar{j}^{(\delta)} - 1)} \left[\frac{\bar{j}^{(\delta)} - 1}{\bar{j}^{(\delta)}} \right]^j \quad (5.8)$$

where j denotes the number of ionizations and $\bar{j}^{(\delta)}$ represents the frequency mean number of ionizations for delta-events. It can be shown that:

$$\sum_{j=1}^{\infty} f^{(\delta)}(j) = 1 \quad (5.9a)$$

and

$$\sum_{j=1}^{\infty} j f^{(\delta)}(j) = \bar{j}^{(\delta)} \quad (5.9b)$$

5.2.3. Total distribution of ionization $f_1(j)$

The general expression for the frequency distribution of ionizations in a spherical site irradiated by a parallel, broad beam of ions, $f_1(j)$, is made by weighting contributions from ion- and delta-ray events. With Eq.5.1, Eq.5.6 and Eq.5.8 one gets

$$f_1(j) = (1 - \mu_F) \frac{A j}{e^{B(j-C)} + 1} + \frac{\mu_F}{(\bar{j}^{(\delta)} - 1)} \left[\frac{\bar{j}^{(\delta)} - 1}{\bar{j}^{(\delta)}} \right]^j \quad (5.10)$$

In Eq.5.10, four parameters are needed to calculate the frequency distribution of ionizations: parameters B and C for the ion-events distribution and parameters $\bar{j}^{(\delta)}$ and μ_F for the mean size and the fraction of delta-ray events. The first two parameters, B and C , are obtained by fitting Eq.5.6 to ion-event frequency distributions derived from

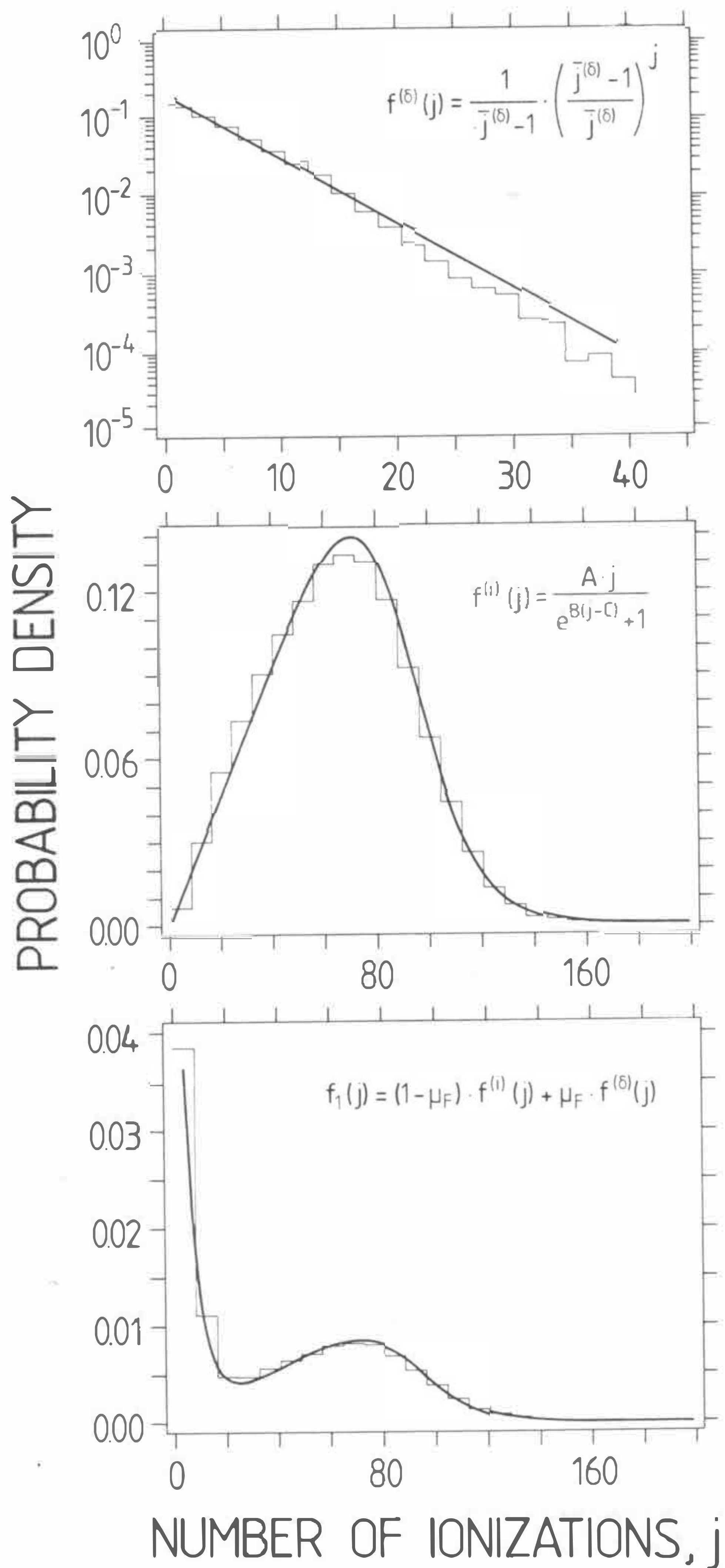


Fig.5.3

Frequency distributions of ionization for a) delta and b) ion events in 20 nm spherical site from 0.3 MeV/amu alpha particles. c) Total distribution for ion- and delta-events. Lines - model predictions; histograms - Monte Carlo calculations.

Monte Carlo calculations. The next parameter, $\bar{j}^{(\delta)}$, is just the first moment of $f^{(\delta)}(j)$ distribution.

The last parameter, μ_F , can easily be derived from the fraction of dose due to delta-events, μ_D , which is a constant for different ions having the same velocity (see next paragraph Ch.5.2.4).

Equations (5.10, 5.7 and 5.2) together with tables of parameters B, C, $\bar{j}^{(\delta)}$ and μ_D (see Appendix C) enable one to calculate ionization distributions for ions of arbitrary energy in arbitrary site diameters.

5.2.4 Method of scoring ionization distributions.

The technique of scoring of microdosimetric distributions is schematically depicted in Fig.5.4. When a track was produced and stored, a systematic search through all ionizations in the track was made. From the location of each ionization a sampling-sphere was randomly placed at a distance not greater than the sphere radius, r . This assured that the sampling sphere covered at least the coordinates of the ionization.

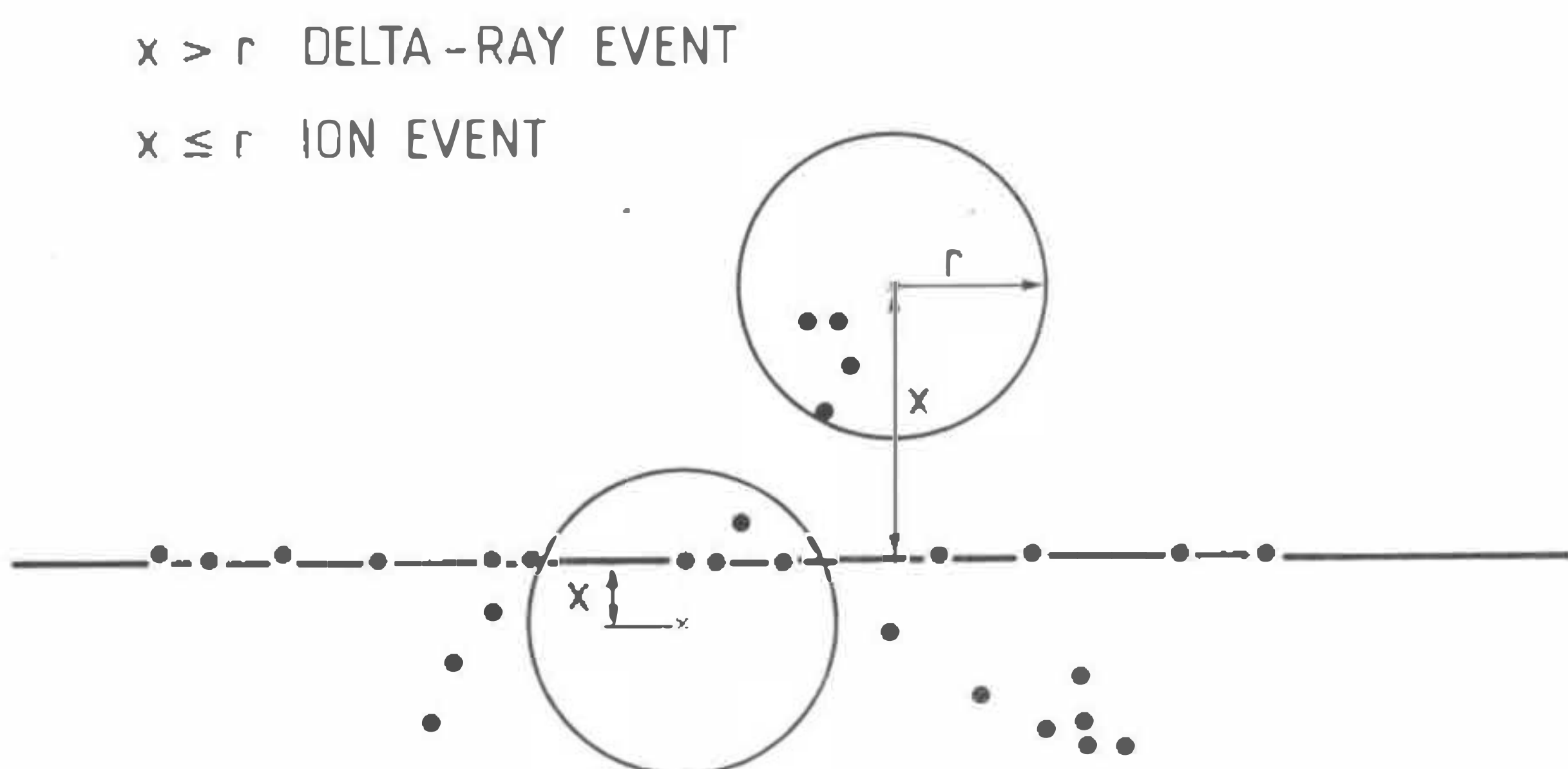


Fig.5.4

Schematic explanation of scoring technique used to calculate ion- and delta-events. The center of sampling sphere is randomly placed in the distance from the given ionization point not greater than the sphere radius, r . When the ion axis crosses the sampling sphere ($x \leq r$) then the event is classified as an ion-event, if not ($x > r$) as an delta-event.

If the distance from the track axis to the center of the sampling sphere was greater than r (track axis did not cross the sampling sphere), then such an event was classified as a

delta-event and stored in the delta-event distributions $d_{MC}^{(\delta)}(j)$; if not, it was classified as an ion-event and stored in the ion event distribution $d_{MC}^{(i)}(j)$. The scoring procedure presented above leads to dose distributions [Kellerer & Chmelevsky, 1975b] of ionizations, $d_{MC}^{(\delta)}(j)$ and $d_{MC}^{(i)}(j)$. μ_D can be calculated as

$$\mu_D = \frac{\sum_j d_{MC}^{(\delta)}(j)}{\sum_j d_{MC}^{(\delta)}(j) + \sum_j d_{MC}^{(i)}(j)} \quad (5.11)$$

where $d_{MC}^{(\delta)}(j)$ and $d_{MC}^{(i)}(j)$ denote here Monte Carlo calculated, non-normalized ion- and delta-events distributions.

5.3. RESULTS AND DISCUSSION

Tracks of protons and alpha particles in water vapour with a density of 1 g/cm³ were generated using the Monte-Carlo code Moca-14 (version January 1984) for 6 discrete energies from 0.3 to 10.0 MeV/amu. The details of the program are given in Ch.2.3. The size of tracks, used for scoring for each particular ion and energy point, was of about 10⁵ ionizations. The ionization distributions were scored for 10 different diameters (1-1000 nm).

All the calculations presented in this paper were performed for the so-called track segment regime, i.e., the particle was not slowed down as it underwent interactions. This limitation is introduced by the track structure code MOCA-14 which does not allow for slowing down. The magnitude of the systematic error, introduced by this approach, can be easily assessed: the slowest alpha particle considered (1.2 MeV) has a stopping power of about 216 keV/μm in ICRU tissue [ICRU 36, 1983] and after passing 1 μm of tissue is slowed down to an energy of about 1 MeV. A 1 MeV alpha particle has a stopping power of 230 keV/μm in ICRU tissue. Therefore, the real energy loss of a 1.2 MeV alpha particle within 1 μm, with the stopping power of 224 keV/μm (arithmetic mean of 216 and 230 keV/μm), would be about 4% higher than assumed in the track-segment calculations value of 216 keV/μm.

5.3.1. Parameters of analytical approach

Parameters B and C were fitted simultaneously using a least-square method. This was done by finding values of B and C for which the value of the following expression was at minimum

$$Q = \sum_{j=1} (f_{MC}^{(i)}(j) - f^{(i)}(j))^2 \quad (5.12)$$

$f_{MC}^{(i)}(j)$ is the Monte Carlo calculated frequency distribution of ionization and $f^{(i)}(j)$ is expressed by Eq.5.6, where the parameter A is given by Eq.5.7. Eq.5.6. is nonlinear with regard to parameters B, C. Thus, for minimizations of Eq.5.12 a nonlinear least-square fitting program NL2SOL was used [NL2SOL, 1983].

Results of this fit are given in Appendix C (Tabs.C.1a-b). Relative standard deviations of B did not usually exceed 2% (max. standard deviation of B is 2.1% for 0.3 MeV protons and $d=10$ nm) being typically less than 1.0%. Uncertainties of fitting C increase with decreasing site diameter and decreasing LET of an ion. For 0.3 MeV/amu alpha particles and $d=1000$ nm, the relative standard deviation of C is 0.067%, reaching 1% for 5 nm and 30% for 2 nm. For 5 MeV protons the relative standard deviations of C were 0.3% for $d=1000$ nm and 4.5% for $d=200$ nm.

When going to smaller diameters (e.g. 1 nm for 0.3 MeV alphas and 100 nm for 5 MeV protons) C becomes negative and this two-parameter fit becomes unstable. In that case various combinations of B, C can be found which give satisfactory fit. In this situation, however, the total distribution is dominated by the delta-ray influx (Eq.5.8) and the chosen value of C has a meaningless influence on the total distribution. Regions where C becomes negative delimit the applicability of the analytical recipe. For practical purposes a value of C=0 had been chosen for these cases.

The quality of the above-described fitting procedure can also be estimated by comparing values of $\bar{j}^{(i)}$ derived from Monte-Carlo calculations with the first moment of the function in Eq.5.6 (Fig.5.5). For high and medium $\bar{j}^{(i)}$ the fit is very good. Deviations (max. 21% for 5 MeV proton and $d=20$ nm) for low $\bar{j}^{(i)}$ show the difficulties in the region where C approaches 0.

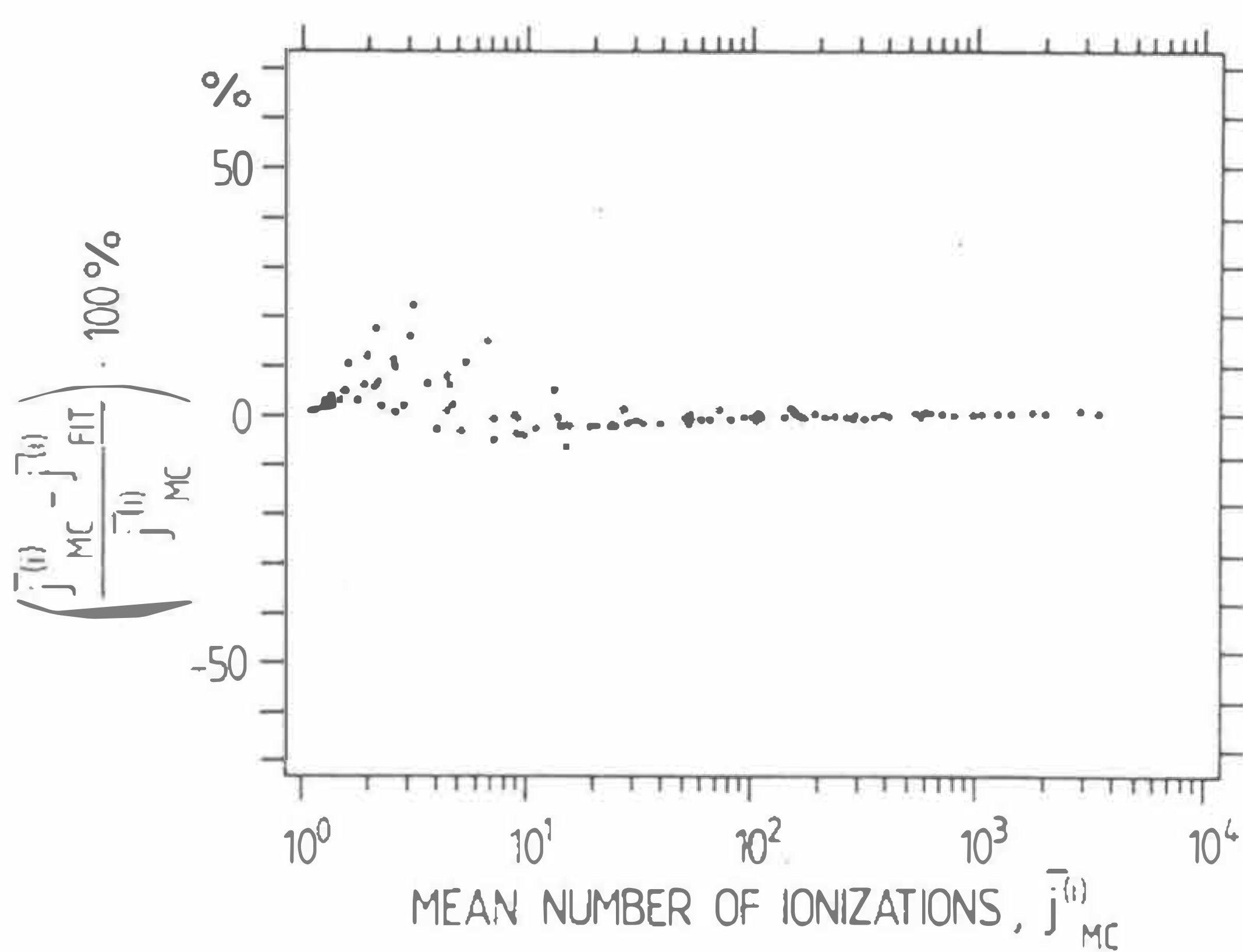


Fig.5.5 Relative deviation of the frequency mean number of ionizations for ion events. $\bar{j}_{fit}^{(i)}$ denotes the frequency mean number of ionizations for ion-events calculated from Eq.5.6 using data from Appendix C. $\bar{j}_{mc}^{(i)}$ denotes the frequency mean number of ionizations for ion events obtained from Monte Carlo calculations.

An important parameter of this analytical description of ion- and delta-event distributions, is the fraction of dose in the site due to delta-ray action, μ_D . The parameter μ_D depends on ion velocity and is almost independent of the charge of the investigated ions. This is because, in the considered energy range, the ion charge determines the density of emission of the secondary electrons and only slightly their energetic spectrum [Guenther & Schultz, 1983].

μ_D was first evaluated by Kellerer [1971] on the basis of radial dose distribution of ions, scaled in terms of radius-restricted Linear Energy Transfer, LET_r , taken from Baum [1969]. Fig.5.6 presents the values of μ_D , calculated from 1, 2 and 5 MeV/amu proton and alpha particle tracks (as described in the previous section) and compared with the calculations of Kellerer [1971] and Guenther [Guenther & Schultz, 1983]. Statistical uncertainties in evaluating μ_D were assessed by repeating calculations several times for different tracks in which 30000 ionizations were scored. μ_D varies from track to track, usually within about 1%, reaching 3% for 10 MeV ions. These error bars are not marked in Fig.5.6. because they are smaller than the marker size. The general agreement is good: for larger diameters the Monte Carlo results fit better the Kellerer calculations and below 100 nm they match well Guenther's curves.

The last parameter of the present recipe is the mean number of ionizations for delta-ray distributions, $j^{(\delta)}$. For high velocities of ions, ejected delta-rays are well separated from each other when compared to the small size of the target. Therefore, for low simulated diameters and energetic ions energy deposition to the target comes usually from a single delta-ray. The delta-ray spectrum is assumed to be identical for protons and alpha particles (disregarding the absolute number of delta-rays due to different charge). Therefore, $j^{(\delta)}$ is almost identical for protons and alpha particles for low simulated diameters and energies above 2 MeV/amu.

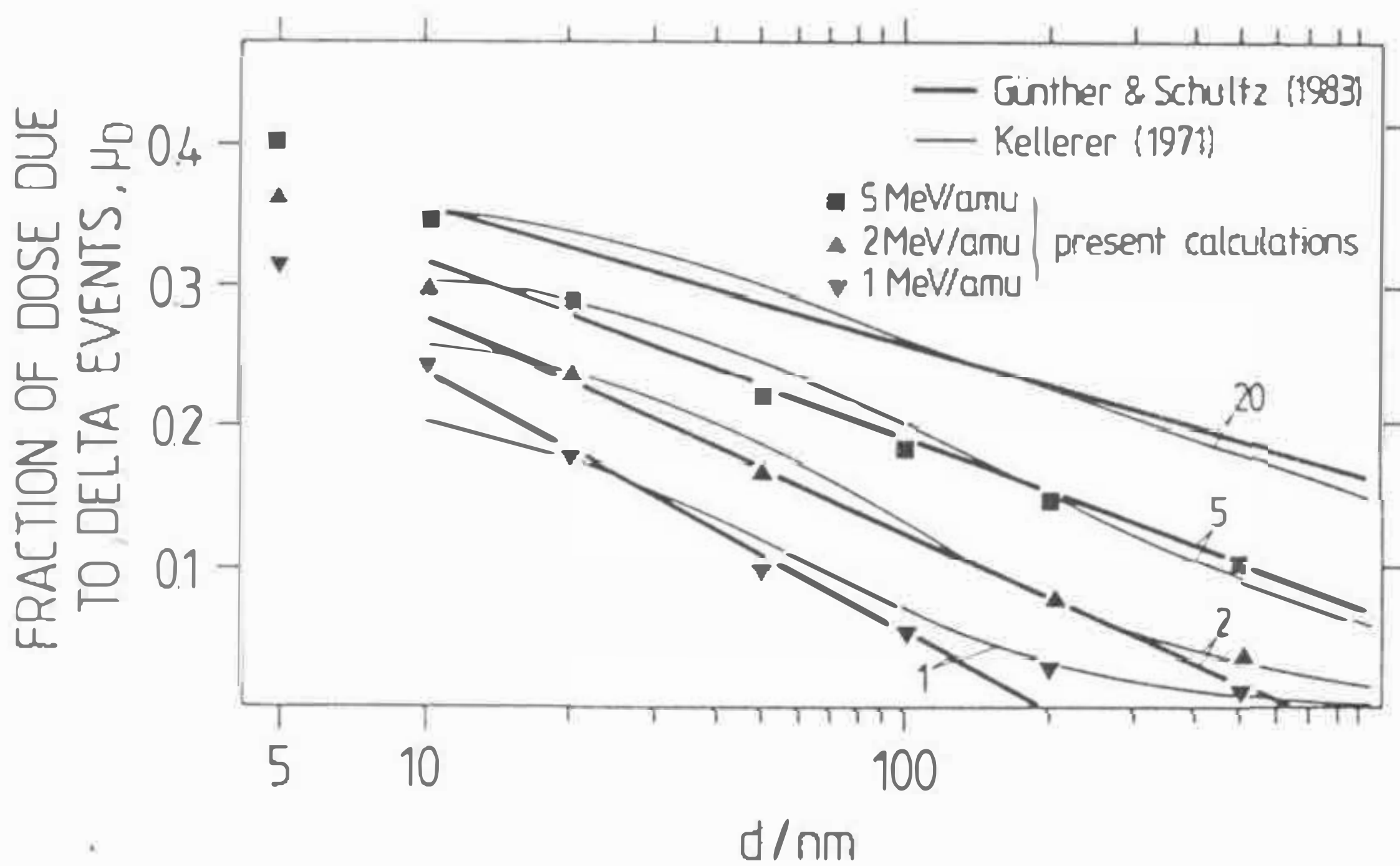


Fig.5.6

Fraction of dose due to delta events for 1, 2 and 5 MeV/amu ions. The thin lines as given by [Kellerer, 1971], thick from [Guenther & Schultz, 1983]; markers denote Monte Carlo calculations of the present work. The uncertainties of calculated values of μ_D are of 1-2% and are not depicted in the figure.

5.3.2. Microdosimetric distributions

In this paragraph energy deposition is considered in terms of ionizations. This is done for two reasons. Firstly, it facilitates the scoring procedure. Secondly, the term "energy deposition" as defined in ICRU 36 [1983] is not well defined in small volumes of the order of 1 nm due to quantum mechanical uncertainties and collective effects such as plasmons or phonons. Finally, there is evidence that just ionizations are of importance in produce biological lesions [Dertinger & Jung, 1969].

Therefore, in the present approach, only the ionizations events were scored for microdosimetric distributions. For each track, however, the total energy-deposition and the total number of ionizations were recorded to obtain the energy, w , for producing a pair of ions in water vapour. These results are shown in Tab.5.1. Since the delta-ray energy spectrum of protons and alpha particles of the same velocity, in the considered energy range, do not differ significantly, their differential w -values should be almost equal. In fact, the calculated differences between protons and alpha particles of the same velocity and for 100000 ionizations tracks were no larger than 0.06 eV.

Tab.5.1 *The average differential energy, w , required by protons to produce a one pair of ions in water vapour*

Energy/ MeV/amu	$w / \text{ip/eV}$
0.3	34.1
0.5	33.8
1.0	33.6
2.0	33.2
5.0	32.8
10.0	32.8

The following figures, Fig.5.7-Fig.5.9, show that the analytical function, with the fitting parameters B and C evaluated in this work and given in Appendix C.1, is a fair description of the real distributions. The Monte-Carlo calculations are shown in the form of histograms; the lines represent the fit.

Fig.5.7 presents the delta-event spectra obtained for 1, 10 and 100 nm sites. For fast ions and low site diameters, the Monte Carlo and analytically calculated distributions (Eq.5.8) match very well. For 1 MeV/amu particles, the shape of the spectra becomes more complex: events with low ionizations numbers occur with a higher probability than those calculated from Eq.5.8. This results in an underestimation of the delta-ray contribution to the total $f_1(j)$ spectrum for larger diameters. However, since the relative contribution of delta-events becomes very small for higher diameters and low ion energies, errors caused by this approximation are not significant.

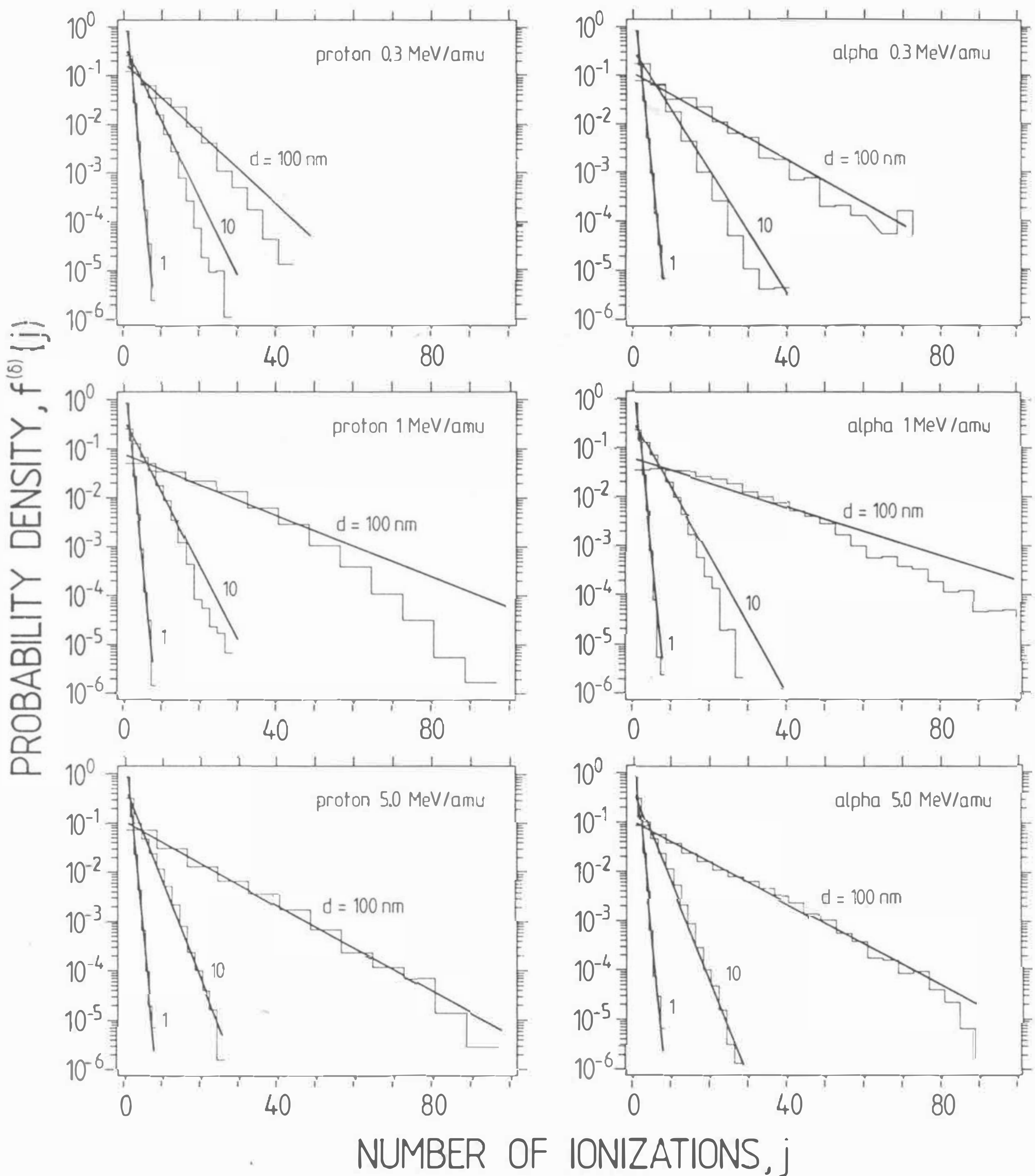


Fig.5.7

Delta-event frequency distributions of ionization for protons and alpha particles with energies 0.3, 1.0 and 5.0 MeV/amu. Lines - analytical approach (Eq.5.8); histograms - Monte Carlo calculations.

Fig.5.8 presents some examples of ion-event distributions, $f^{(i)}(y)$, scaled in terms of lineal energy. For each ion energy, the w -value from Tab.5.1 was used to convert number ionizations into energy. With decreasing site diameter (Fig.5.8a) and increasing ion energy (Fig.5.8b), the fluctuations of energy-deposition become larger and the spectra gradually lose their triangular shape. For diameters of a few nanometers, the distributions are represented by monotonically decreasing functions. Such changes in shape of the frequency distributions are easily understood when comparing the mean free path for primary ionization of ions with the dimension of the site. If these parameters are of the same order of magnitude, then single or double ionization events will most probably occur and the chord length spectrum no longer plays a significant role. The increase of straggling of energy-deposition by a 1.2 MeV alpha particle with decreasing site diameter is shown in Fig.5.9.

The code MOCA-14 enables one to calculate ion tracks in terms of ionizations and excitations. It is easily possible to adopt this approach to score energy deposited instead of ionizations. In Fig.5.10a and Fig.5.10b are presented the dose distributions of lineal energy for 0.3 MeV protons and for site dimensions of 1 and 20 nm. These distributions were calculated in two ways. The thin line represents the distribution obtained by taking into account ionizations and excitations. The bold line was calculated by scoring ionizations only and assuming a constant differential w -value¹⁾ $w=34.1$ eV. For target volumes of 20 nm, ionization and energy-deposition distributions do not differ significantly. This is not true for the 1 nanometer diameter site. This spectrum exhibits a complex structure reflecting dominant physical processes of energy deposition in water vapour.

5.3.3. Investigation of limits of MOCA-14

Microdosimetric distributions from ions are difficult to be experimentally determined. Thus no reasonable comparison can be done between measured and calculated with the present approach microdosimetric distributions. However, sufficient set of experimental data for ions exists for radial distribution of dose around ion tracks. The review of experiments and calculations of radial dose distributions is given in Appendix A.

Radial dose distribution and distribution of energy deposited in a site give complementary information of spatial pattern of ion energy deposition but they can be numerically derived basing on this same set of physical data. In this section calculated radial dose distributions are compared with measurements in order to investigate the limits of actual Monte Carlo track structure simulations, especially for ions with higher Z. The method of calculation of radial dose distributions from ion tracks is given in Appendix A.2

Figs.5.11 presents radial dose distributions calculated with the code Moca-14 (histograms), with the model of Katz [Waligórski et al., 1987] (lines) and measured experimentally [Wingate & Baum, 1976] (triangles). Both calculations were performed for water, whereas measurements were done in a TE gas and then recalculated to unit density. For 1 and 3 MeV protons the general agreement is very good. The calculations based on the Katz model are placed slightly above experimental points in the region between 1 and 10 nm (the "hump" region) and at the peripheries of the tracks. This is clearly visible for distributions from 1 and 3 MeV

¹⁾ The differential w -value is the average energy required to produce an ion-pair by a particle of specified energy.

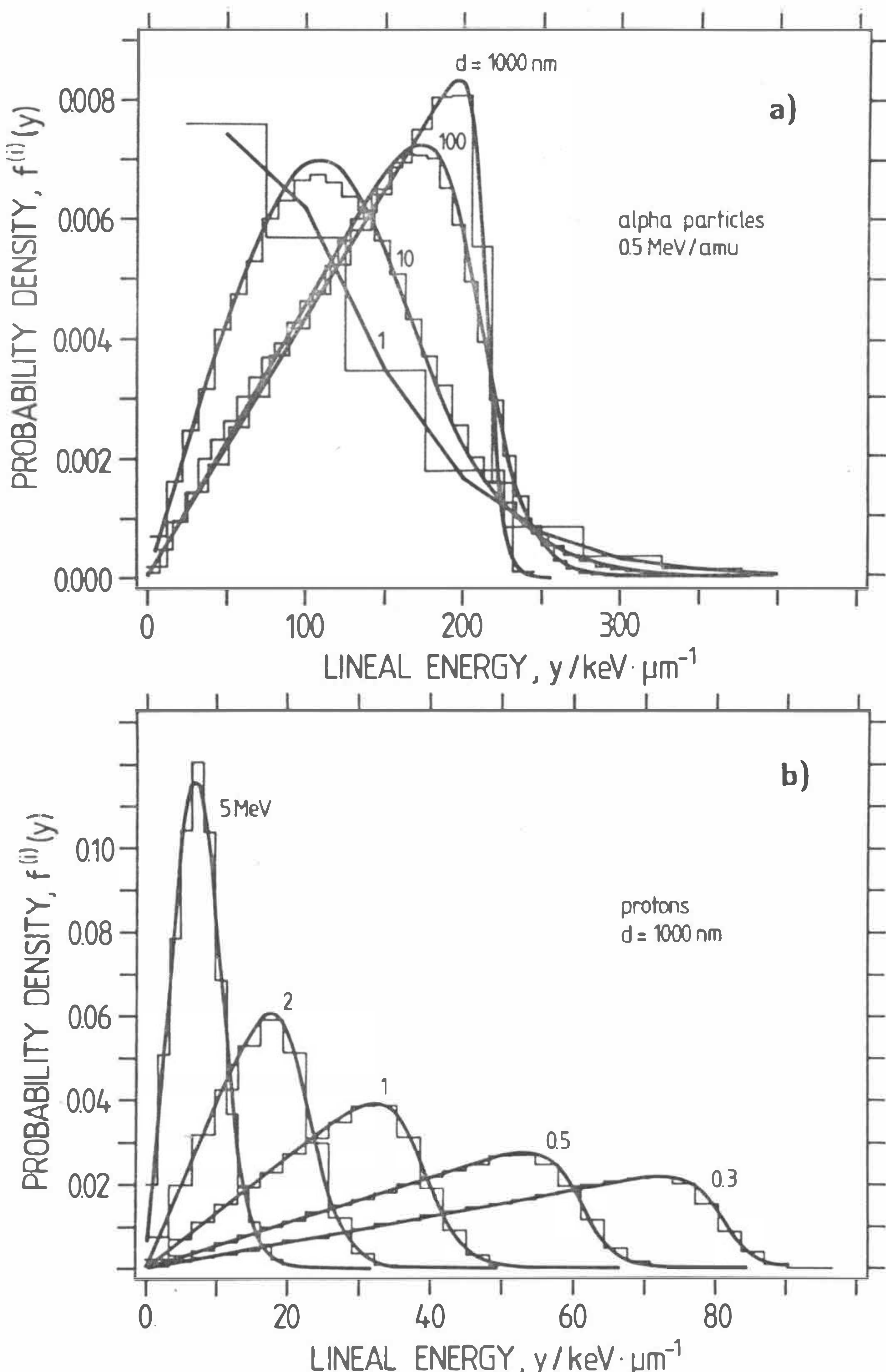


Fig.5.8

Ion-event frequency distributions scaled in terms of lineal energy for a) $E=0.5 \text{ MeV/amu}$ alpha particles and different site diameters and b) for the diameter of 1000 nm and different proton energies. Lines - analytical approach (Eq.5.6); histograms - Monte Carlo calculations.

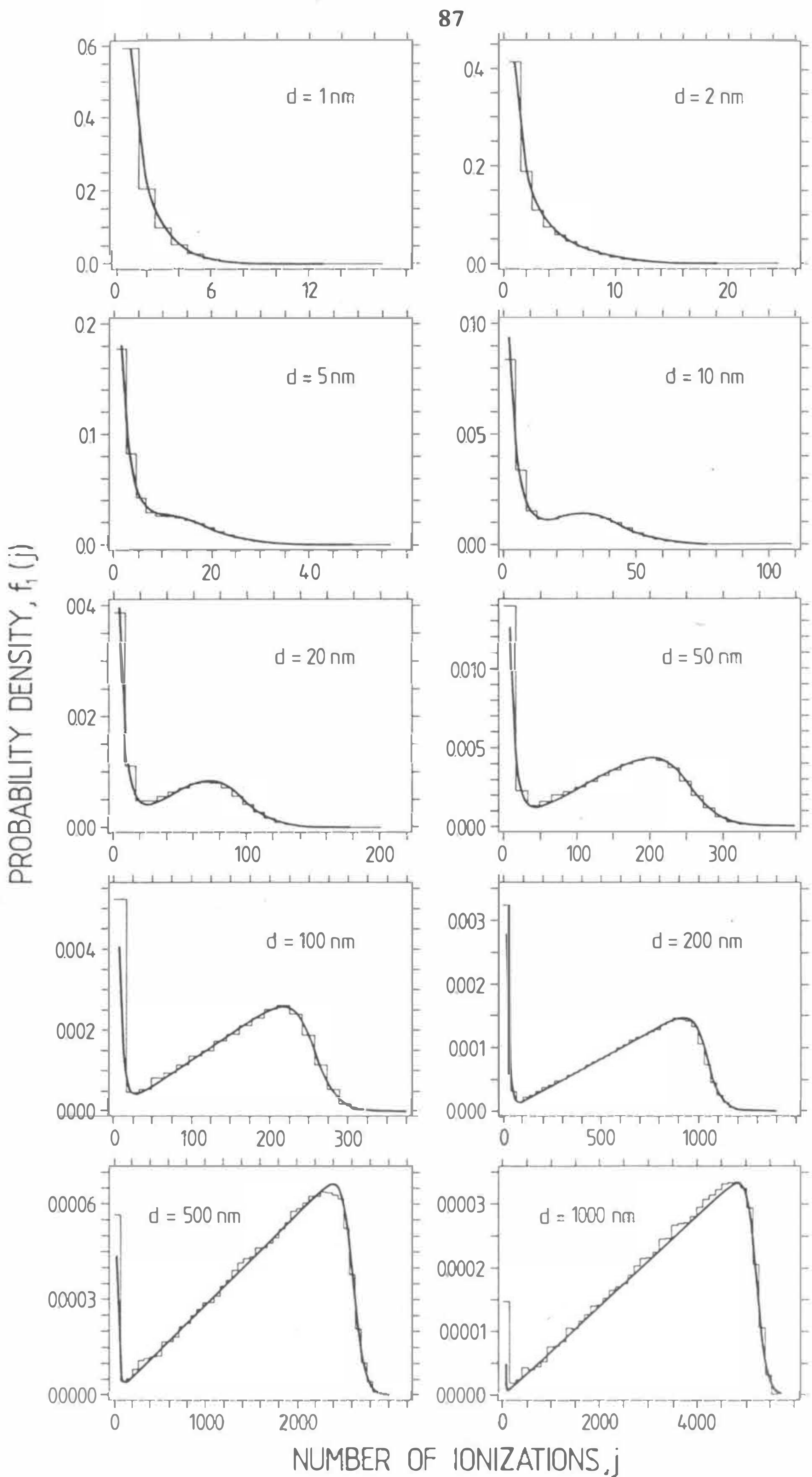
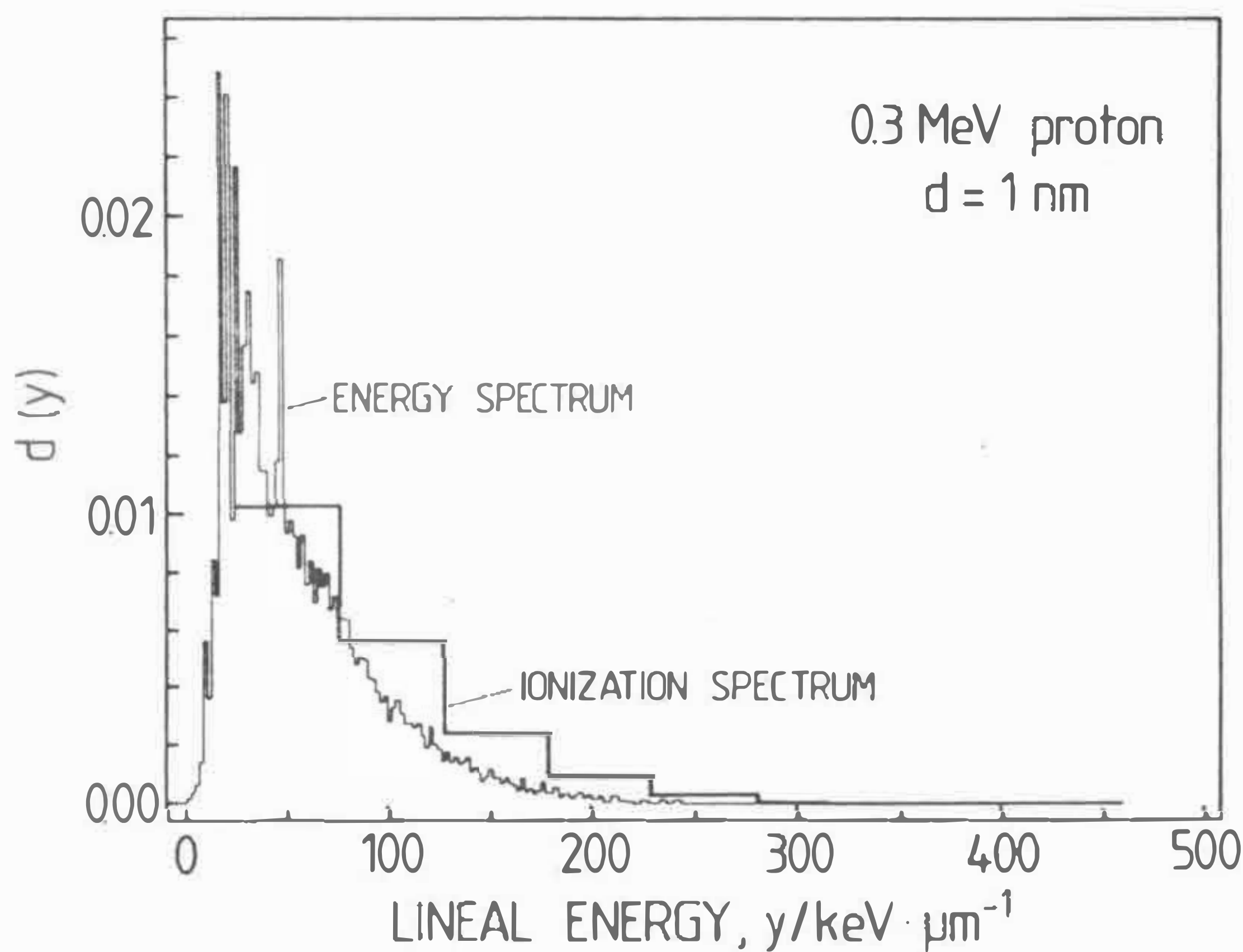


Fig.5.9

Frequency distributions of ionization for 0.3 MeV/amu alpha particles and different site diameters. Lines - analytical approach (Eq.5.6); histograms - Monte Carlo calculations.

a)



b)

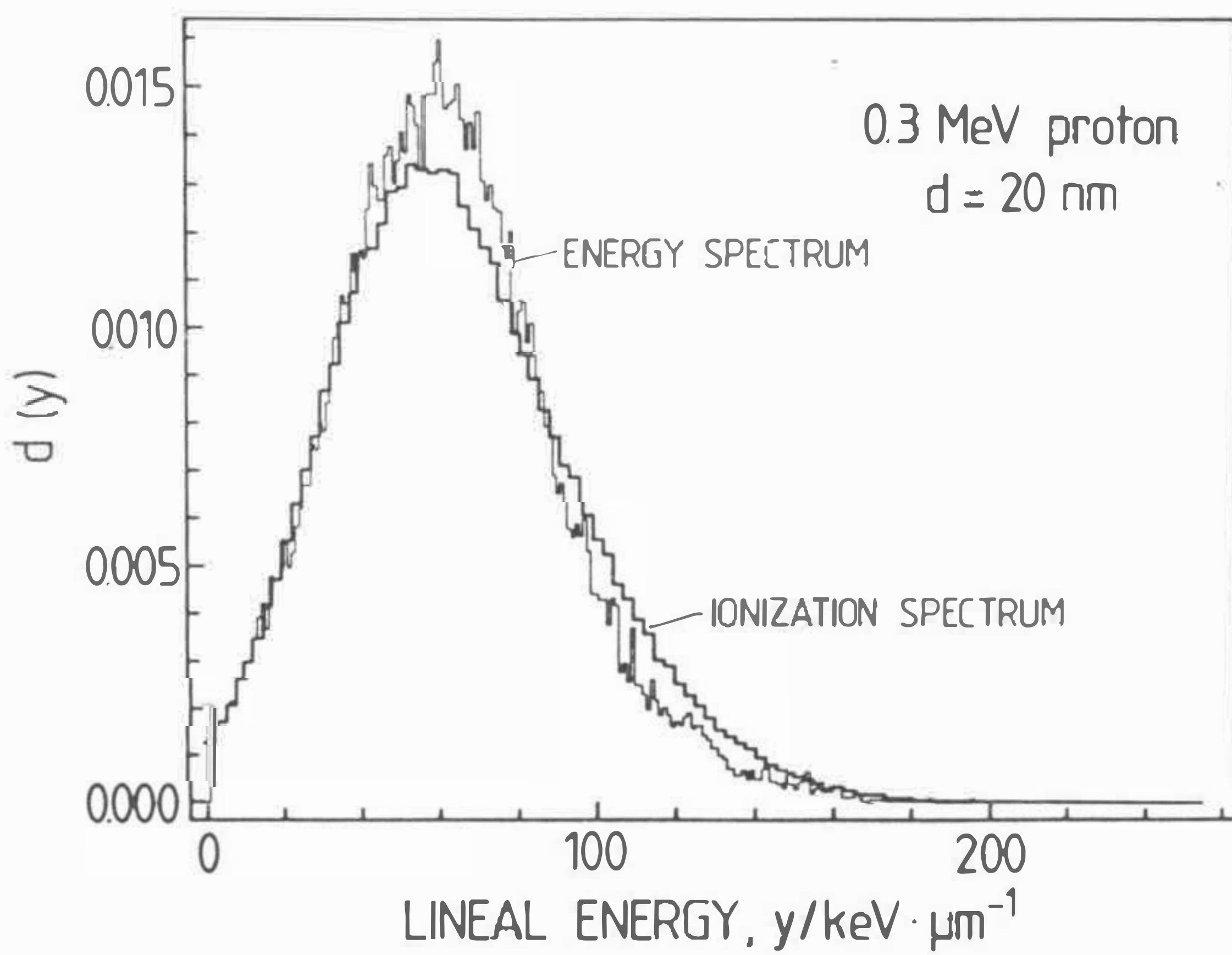


Fig.5.10

Calculated dose distributions of lineal energy for 0.3 MeV proton and site diameter a) 1 nm and b) 20 nm in water vapour. Thin lines show lineal energy spectra obtained from scoring ionizations and excitations. The thick line was obtained from scoring ionizations only and converting them into lineal energy spectrum with differential w-value 33.1 eV.

alpha particles. The "hump" was introduced to the calculations of Waligorski to better fit experimental data and to make the original Katz [Katz et al., 1971] formula consistent with the total stopping power of the ion i.e. the integral over radial dose to reproduce the total stopping power of the ion. The overestimation of dose in the periphery of tracks is a result of assuming normal ejection of delta electrons with regard to the ion path. The range of electrons, as calculated with both approaches, are approximately equal but the probability of reaching track peripheries by electrons ejected perpendicularly is higher than in the Monte Carlo calculations, where a realistic angular ejection distribution was used.

Fig.5.12 demonstrates radial dose distributions calculated using both approaches for 0.25, 1, 5 and 20 MeV protons. For the 20 MeV protons the Monte Carlo calculations overestimate the analytical model. The secondary spectrum of electrons produced by protons are calculated in the MOCA-14 from the semiempirical model of Wilson and co-workers [1985] which is based on measurements of corresponding spectra for protons of energies from 0.5 to 4.2 MeV. The authors did not recommend using their model for energies below 0.5 MeV [Miller et al, 1985] and above 10 MeV [Wilson, 1988].

The comparison of measured and calculated radial dose distributions for heavy ions with $Z \gg 1$ can serve as a test for the applicability of the effective charge concept in track structure calculations. The formula of Barkas [1953] for effective charge is incorporated in the MOCA-14 program in order to rescale the mean free path of the proton into a mean free path of the ion. Fig.5.13 compares the radial dose distributions measured in TE gases and calculated for water vapour using MOCA-14 and rescaled to unit density. For iodine and bromine ions of energies approximately 0.5 MeV/amu the agreement for radial distances greater than 2 nm is poor whereas for oxygen ions of energy 2.56 MeV/amu is already acceptable. Therefore, when applying the MOCA-14 programs to heavy ions with $Z \gg 1$ one should take into account that effective charge approximation should not be used below 0.5 MeV/amu. This conclusion was also drawn by Waligórska and co-workers [1987].

A tendency can be observed in Figs.5.11 and 5.13 that at low radial distances calculations overestimate measurements. One possible explanation of these discrepancies is that the measured number of ionizations is transformed into energy deposition using an average W -value whereas the calculations take into account both ionizations and excitations. At low radial distances between about 0.1 and 10 nm, energy is deposited by a large number of low-energy electrons. These slow electrons produce a smaller number of ionizations per unit dose than fast electrons of energies greater than 1 keV. Fig.5.14 shows the radial distribution of energy required to produce an ion pair, $w(r)$, calculated for 0.3, 1.0 and 20 MeV protons (see Appendix A). For radial distances greater than 10 nm $w(r)$ approaches a constant value of about 32 eV which corresponds to the W -value for fast electrons in water vapour. At the radial distance of 1 nm, $w(r)$ becomes dependent on proton energy, reaching 48 eV for 0.3 MeV, 51 eV for 1 MeV and 56 for 20 MeV protons. For comparison, the differential w -value for 1 MeV protons is equal to 33.5 eV. The conclusion can be drawn that the comparison between the measurements and calculations should be performed by scoring (in calculation procedure) ionizations only or multiplying the measured radial ionizations distributions by the distribution $w(r)$.

Radial dose distributions, calculated with the track structure code MOCA-14, are in good agreement with experiments for ion energies above 0.5 MeV/amu. For slower ions, the effective charge approximation used to rescale proton data to heavy ions data, causes underestimation of the calculated radial doses. For small radial distances, application of a more realistic, radius-dependent w -value converting ionizations into dose improves the correlation between measurements and calculations.

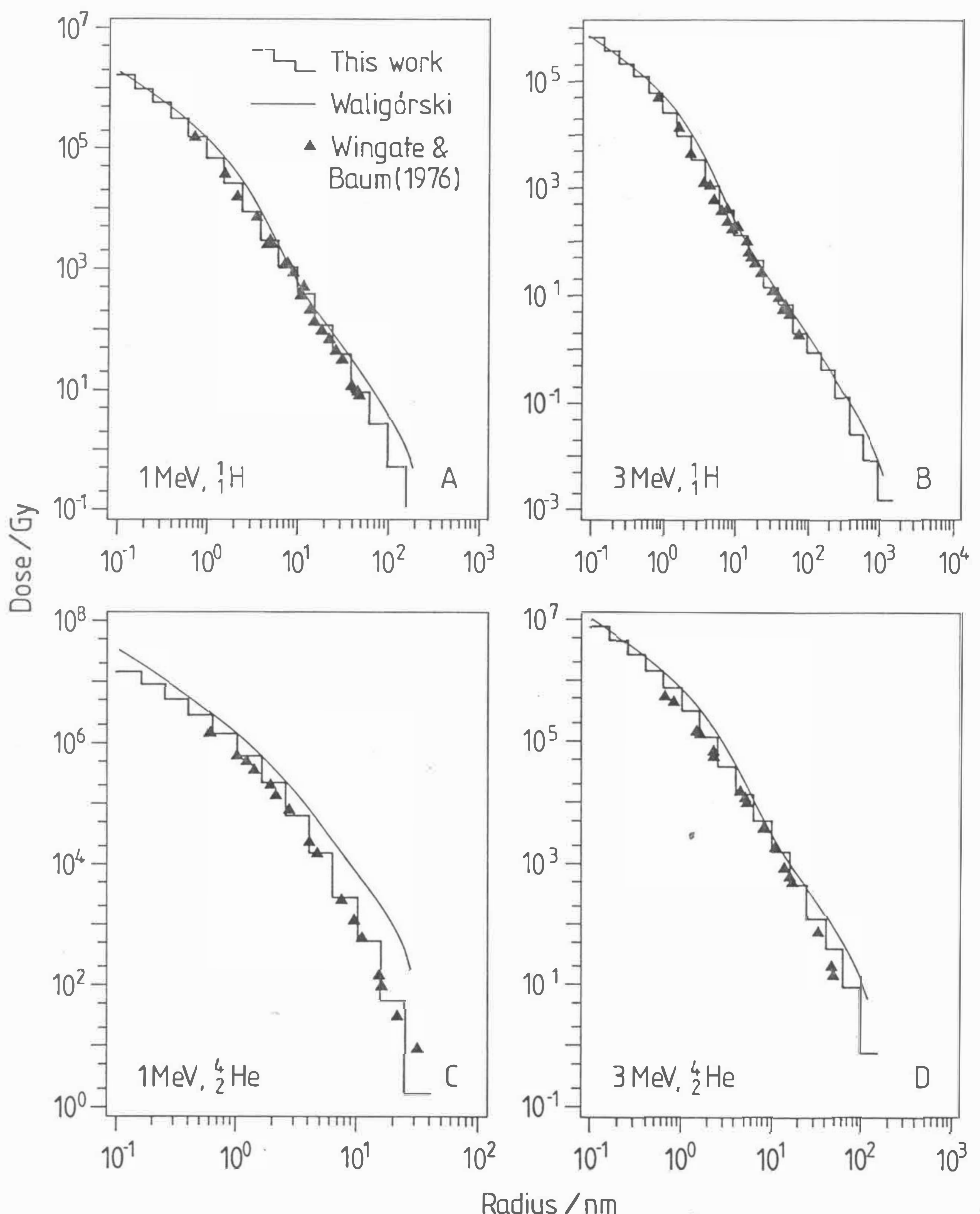


Fig.5.11

Comparison of radial dose distributions measured by [Wingate & Baum, 1976] in TE gas with track structure Monte Carlo calculations (this work) and calculations done with model of [Waligórski et al., 1987]. The radii should be interpreted as the results of scaling from the distances in dilute gases to unit density.

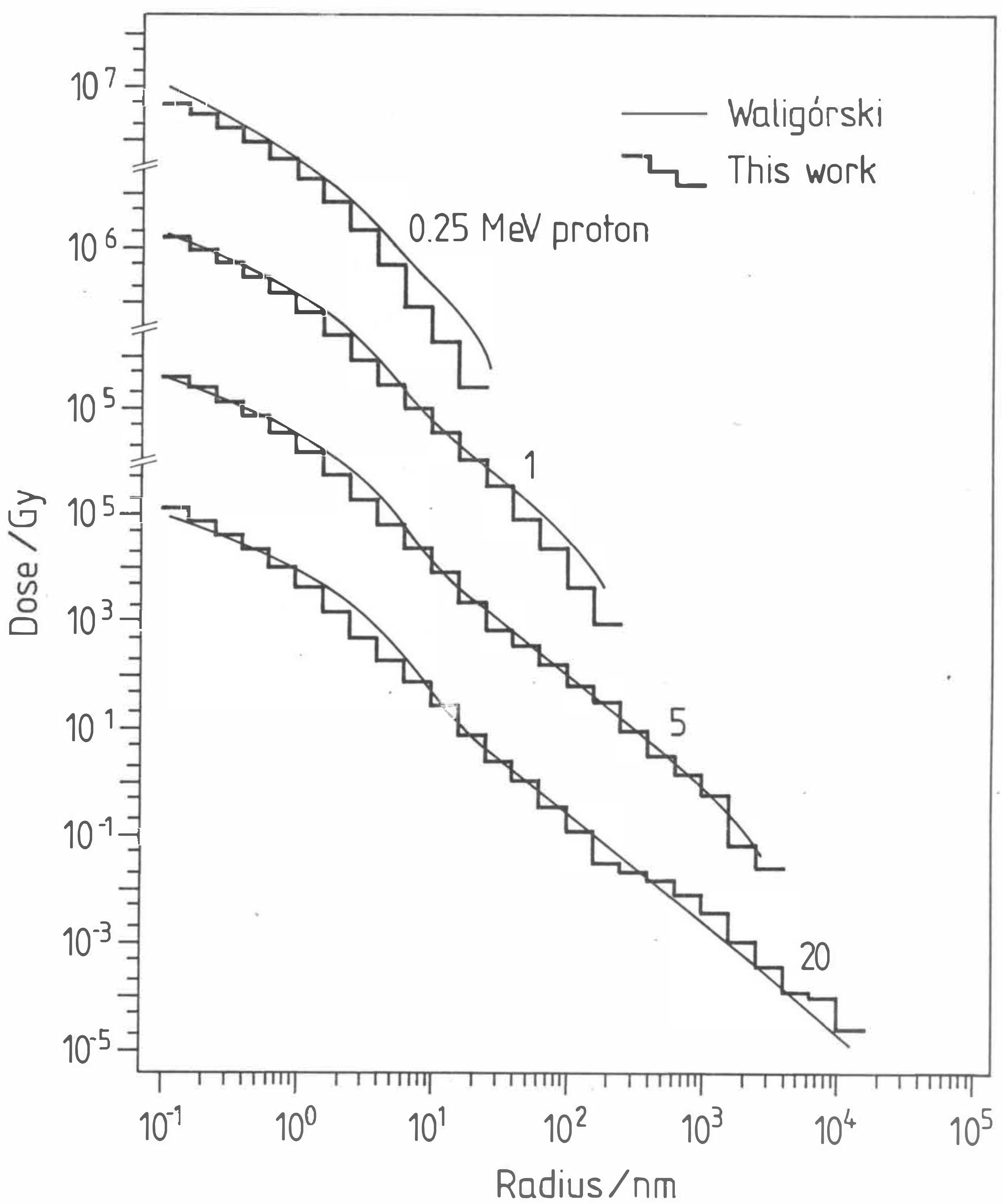


Fig.5.12 Comparison of radial dose distributions produced by 0.25, 1, 5 and 20 MeV protons. Histograms represent results of track structure calculations and lines are calculated with the model of [Waligórski et al., 1987]

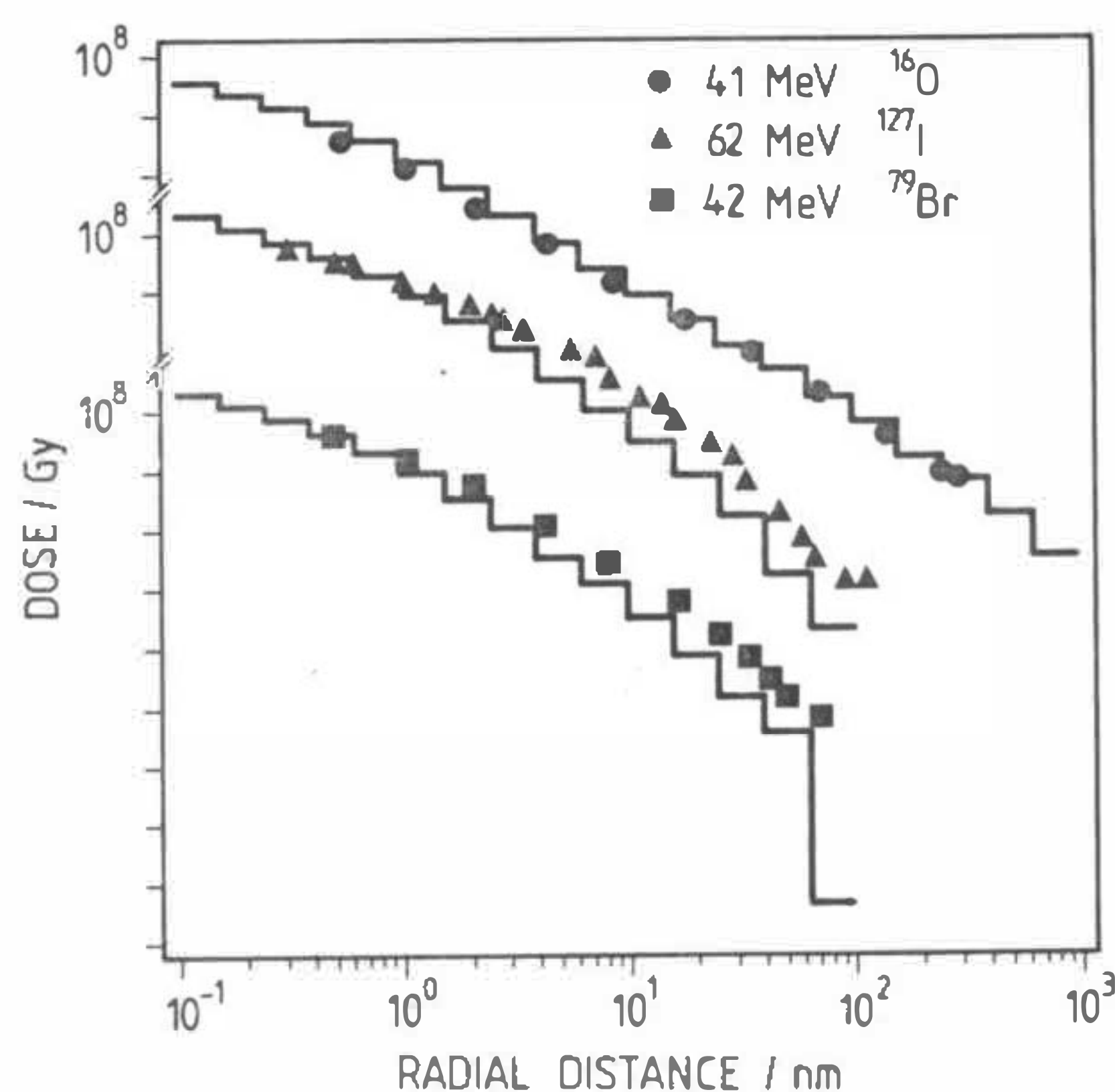


Fig.5.13 Radial dose distribution produced by heavy ions. Markers denote experiments of [Varma, 1977]- (41 MeV ^{16}O), [Baum, 1974] (62 MeV ^{127}I) and [Varma, 1977] (42 MeV ^{79}Br) and the histograms - Monte Carlo calculations.

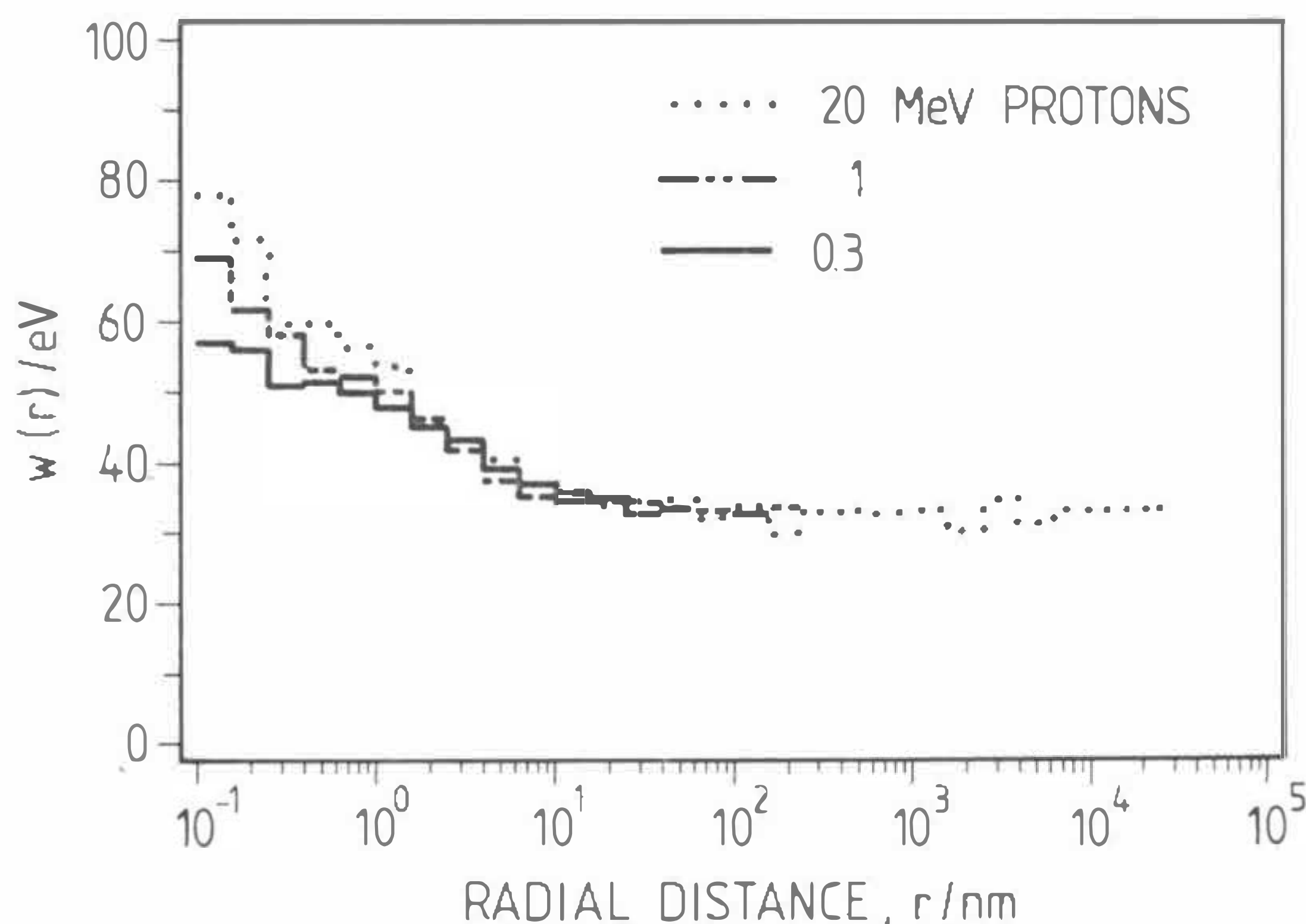


Fig.5.14 Calculated with MOCA-14 radial distributions of differential w -value, $w(r)$ i.e. energy required to produce an ion pair. Calculations were performed for 0.3, 1 and 20 MeV protons. The energy deposition on the ion axis ($r=0$) is not shown in the figure.

6. DETERMINATION OF BIOLOGICAL RESPONSE FUNCTIONS

The concept of biological response functions has been already introduced in Ch.3.6. The main assumption in this concept is that there exists a function which relates energy deposited in the target to the probability of the biological effect in the target. It is not possible to measure directly such a function. Results of typical radiobiological experiments are the mean values which reflect an average response of individual cells in a large population affected by a very different energy deposition events. It is, however, possible to unfold this function from experiments with several radiation modalities.

An input data set used to unfolding biological response functions consists from coefficients α which express initial slopes of dose-response curves and microdosimetric distributions, $f(y)$, specific for radiation modalities and size of targets. Initial slopes of dose-response curves were collected from literature or evaluated and are presented in the Appendix B. In the chapters 4 and 5 microdosimetric distributions were calculated for experiments with photons and ions. These distributions and initial slopes will be used now to unfold biological response functions.

6.1 METHOD OF CALCULATIONS

6.1.1. Choice of unfolding method

The choice of unfolding technique depends on the type of problem studied. In unfolding by a parametric representation, the type of the function taken to analyses determines the shape and the structure of the final solution. It was not the purpose of this work to specify *a priori* any particular model of radiation action and according to this model fit corresponding response functions. Discrete interval methods are more likely "model independent" and only codes working according to this principle were considered.

For the purpose of this work the algorithm of the computer code SAND-II was modified and applied to unfold biological response functions. This program was developed to unfold a set of integral equations resulting from neutron spectrum measurements with activation foils. The use of SAND-II was recommended after several tests and intercomparisons performed with other unfolding codes [Chiochio et al., 1970], [Draper, 1971], [Dierckx et al., 1972]. Particular problems in activation foil analysis are somewhat different from those in radiobiology, e.g. the shapes and the coverage of microdosimetric distributions are not necessarily similar to those represented by neutron cross sections. The SAND's algorithm has, however, a lot of advantages: is simple and easily to control, always gives positive solutions, is time-efficient and can be performed on small computers. The schematic algorithm of unfolding code SAND-II was presented in Ch.3.5.

6.1.2. Modifications of SAND-II

An important disadvantage of the SAND-II algorithm is its inability to evaluate uncertainties of the unfolded function. The algorithm itself (see Fig.3.8) does not take into account the uncertainties of input parameters. Biological effects are in most cases measured with significant standard deviations and these errors have to be represented in the evaluated response functions. In the present calculations the following method was

introduced in order to evaluate the influence of errors in biological input data on the unfolded response functions.

It is assumed that errors of initial slopes of dose-response curves are normally distributed. Mean values, α_i , and the corresponding standard deviations, σ_i , are known from fitting the dose-response curves. From these distributions (α_i , σ_i) a set of current α_{il} values is randomly selected and for this particular set of data unfolding is performed. This procedure is repeated L times ($L > 100$). For each lineal energy point j, the mean value of the response R_j and the standard deviation of that point, σ_{Rj} , are calculated:

$$R_j = (1/L) \sum_{1/1}^L R_{jl} \quad (6.1a)$$

$$R_j^2 = (1/L) \sum_{1/1}^L R_{jl}^2 \quad (6.1b)$$

$$\sigma_{Rj} = \left[\frac{LR_j^2 - (R_j)^2}{L-1} \right]^{1/2} \quad (6.1c)$$

An important question arises whether a function obtained with such an unfolding routine can be considered as a response function. The first simple criterion is as suggested in Eq.3.23a. The value of the parameter Q can be obtained in this case by using an average response function R_j to Eq.3.22. This approach, however, does not take into account uncertainties of input parameters α_i . To assess these influences the following procedure is suggested:

After each cycle of unfolding, l, performed with a given set of actual parameters α_{il} the ratio of experimental to calculated effect was computed:

$$r_{il} = \frac{\alpha_i}{\alpha_{il}} ; \quad i=1, \dots M \quad (6.2)$$

After repeating this calculations L times the mean value and the standard deviation σ_{ri} of the r_{il} ratios were calculated:

$$r_i = (1/L) \sum_{1/1}^L r_{il} \quad (6.3a)$$

$$r_i^2 = (1/L) \sum_{1/1}^L r_{il}^2 \quad (6.3b)$$

$$\sigma_{ri} = \left[\frac{L \cdot r_i^2 - (r_i)^2}{L-1} \right]^{\frac{1}{2}} \quad (6.3c)$$

Unfolding is considered to be successful if r_i for all i approaches one i.e. evaluated responses α_{ij} are equal to the experimental values α_i . To test statistically whether this is a case the following quantity is considered:

$$\chi^2 = \sum_{i=1}^N \frac{(r_i - 1)^2}{\sigma_{ri}^2} \quad (6.4)$$

This quantity, which expresses the measure of the deviation of the r_i from 1, is assumed to follow the χ^2 distribution. Next, a significance level is chosen and compared with the fractile χ^2_{N-1} for $N-1$ degrees of freedom. If

$$\chi^2 > \chi^2_{N-1} \quad (6.5)$$

the hypothesis that r_i approaches constant function equal 1 must be rejected.

6.1.3. Testing the program SAND-II

As stated in chapter 3, Eq.3.20 is usually undefined and does not have, in general, a unique solution. In such a case, a choice of the given solution depends on prior knowledge on the solution e.g. on a initial guess function and regularizations applied. However, the algorithm of SAND-II allows only for a positive response function $R(y)$ and that constraint causes that an exact solution cannot usually be found. Thus, only approximate solutions can be considered which are still dependent on prior knowledge about the solution. It is therefore important to test the properties of the SAND algorithm in order to correctly interpret the unfolded biological response functions.

The tests were performed for different structure of input microdosimetric distributions and for α coefficients calculated using several known (assumed) response functions. The technical details of the test performed are given in the Appendix D.

The most important conclusion drawn from these tests is that for reliable unfolding of a biological response function it is necessary to have a good coverage of the whole lineal energy range with microdosimetric distributions. For the lineal energies for which only single microdosimetric distribution is present or the probabilities are in a given region very small (e.g. on the borders of the considered lineal energy range) solutions are much dependent on assumed initial guess functions.

The other type of tests were done in order to investigate the influence of the uncertainties in the input biological data on final response function (see Appendix D). This type of test indicated that some oscillations observed in the unfolded biological response functions can have their origin in uncertainties of the biological input data.

6.2. RESULTS OF UNFOLDING AND DISCUSSION

6.2.1. Biological Response Functions for DNA double strand breaks and their implications for radiobiology.

Unfolding of Biological Response Functions for DNA dsb was performed for site diameters of 20 nm. The choice of the target diameter was somewhat arbitrary. 20 nm corresponds approximately to the diameter of the nucleosome fiber, which seems to be the basic structure formed by DNA throughout most of the time in the cell cycle [Finch & Klug, 1976].

The measured number of DNA double strand breaks is normalized to the mass of the irradiated DNA (see Appendix B). Thus, an absolute number of breaks per cell nucleus or per one ΦX -174 bacteriophage can be calculated by taking into account the mass of DNA in these targets. For hamster cells [Ritter et al., 1977] the DNA content was taken to be 10 pg ($6 \cdot 10^{12}$ Daltons) as measured by Todd [1975]. The mass of DNA in the ΦX -174 bacteriophage used in experiments of Christensen et al. [1972] was taken to be $3.56 \cdot 10^6$ Daltons [Kornberg, 1983]

Fig.6.1 presents unfolded biological response functions for experiments of Christensen et al. [1972] (bold line with dashed lines denoting 1 SD) and Ritter et al. [1977] (bold dashed-dotted line with dotted lines denoting 1 SD). The unfolding technique described in Ch.3.6 was used together with the stochastic modifications (Ch.6.1.1). Iterations were stopped when Q_1 (Eq.2.51a) was smaller than 0.001. The quality of unfolding was tested with the χ^2 test (Eq.6.5). For both functions, the calculated χ^2 are small with respect to $N=6$ degrees of freedom, being 0.5 for ΦX -174 and 0.13 for DNA in hamster cells. This gives high probabilities ($P=0.999$ and $P=0.9999$) with which the hypotheses cannot be rejected. The calculated maximum probability (cross section), σ_ϵ , for ΦX -174 is $5.58 \cdot 10^{-15} \text{ m}^2$, which corresponds to a diameter of about 80 nm. The "real" size of the replicative form of ΦX -174 DNA has dimensions of the same order of magnitude but is not precisely specified because of the irregular shape of the object. The maximum cross section, σ_ϵ , calculated for Chinese hamster cells was $1.38 \cdot 10^{-8} \text{ m}^2$ which is about 200 times higher than the geometrical cross section of the mammalian cell nucleus ($64 \mu\text{m}^2$). Therefore, an ion crossing the cell nucleus with lineal energy greater than $1000 \text{ keV}/\mu\text{m}$ can produce, at maximum, about 200 non-rejoining DNA breaks in the cell nucleus. For energy deposition around $100 \text{ keV}/\mu\text{m}$ the number of breaks is, on the average, about 20.

Once BRF is available it can be used to calculate the frequency of DNA dsb after irradiations with arbitrary radiation modalities. For these purposes the response function $R(y)$ for DNA breaks in Chinese hamster cells (Fig.6.1) was used as an universal response function. First, the microdosimetric distributions, corresponding to radiation modalities from different experiments, were calculated using parameters from Appendix C.2. Then, these distributions were folded with the $R(y)$ (Eq.3.22) in order to calculate the frequencies of DNA breaks. The ratio of the frequency of DNA breaks, α_n , induced by a given radiation and the frequency of breaks for 250 kVp X-rays, α_X , will be called here RBE_{DNA}

$$\text{RBE}_{\text{DNA}} = \frac{\alpha_n}{\alpha_X} \quad (6.6)$$

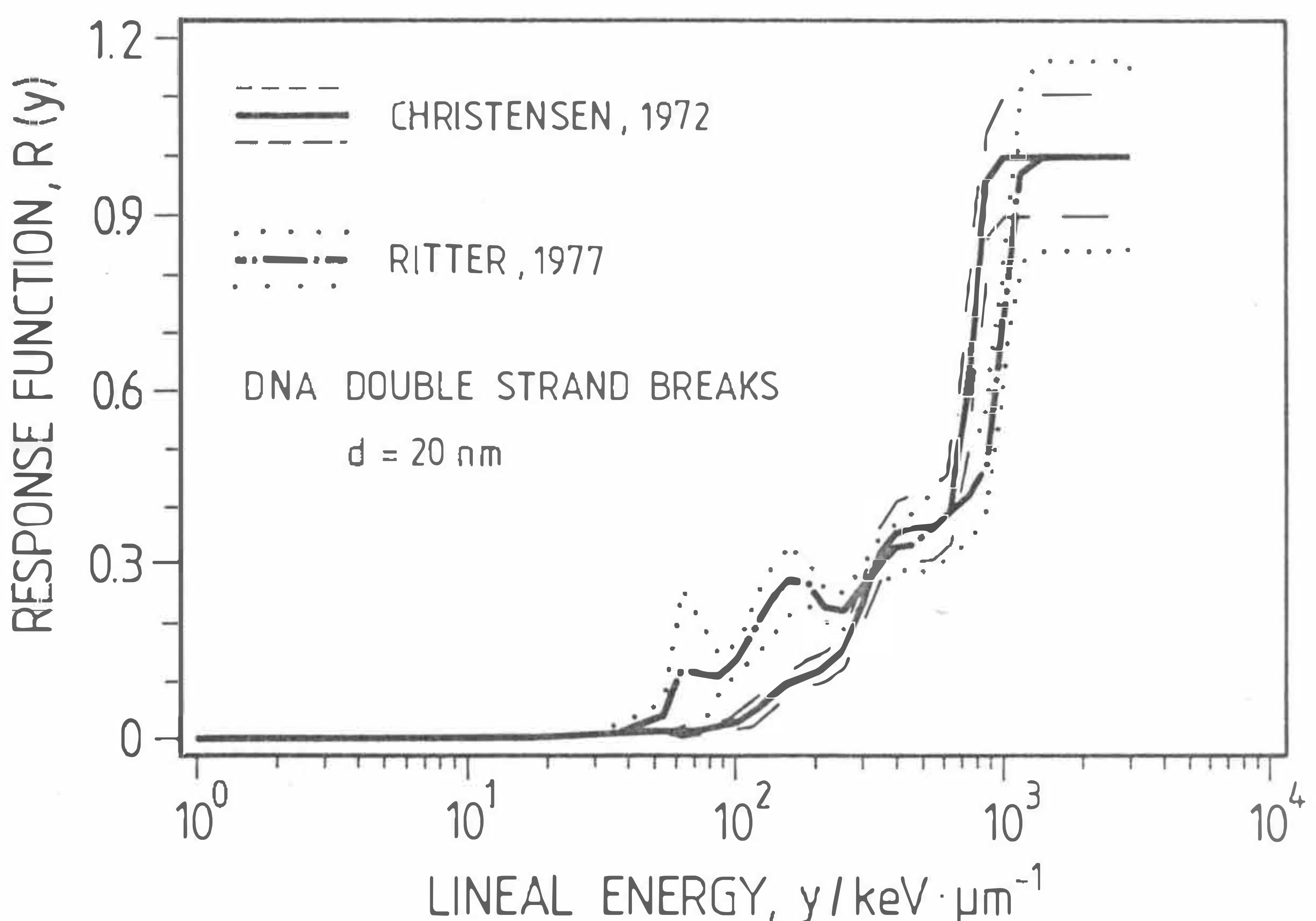
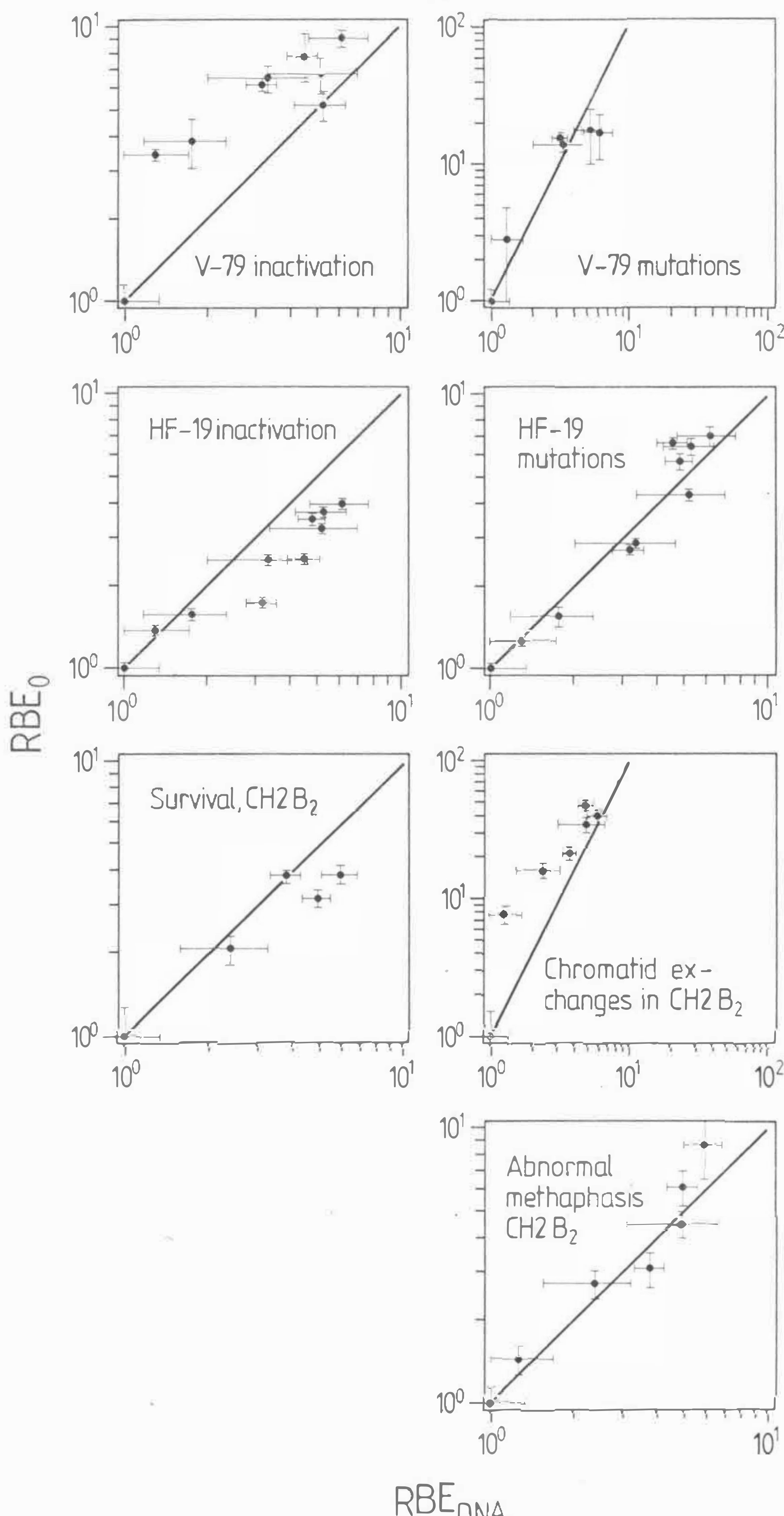


Fig.6.1 Biological response functions for DNA dsb unfolded for the experiments of [Christensen et al., 1972] and [Ritter et al., 1977]. Microdosimetric distributions for ions were calculated using Eq.5.10 and parameters from Appendix C (Tab.C.3.). The distribution for 250 kVp X-rays are recalculated from Fig.4.11. The initial slopes were taken from Appendix B. The dashed and dotted lines indicate the region of 1 SD of the response functions calculated with Eq.6.1c.

Figs.6.2 show the correlation between the relative efficiency in producing a given biological effect as cell killing, mutation etc. (RBE_0) and the efficiency in producing DNA breaks in these cells (RBE_{DNA}) by the same radiations. The analysis is performed for the set of cellular experiments of Skarsgard et al. [1967] and Cox et al. [1977a]. Lines representing direct proportionality (at 45°) and quadratic dependence (at 63°) between the relative efficiencies of DNA breaks and the investigated end-points are plotted to guide the eyes. The linear or quadratic dependence of cellular effects on frequency of DNA double-strand breaks can suggest the different basic mechanisms leading to biological effects on cellular level.

The closest correlation between the frequency of DNA double-strand breaks and the corresponding cellular effect can be observed for HF-19 mutations and abnormal metaphasis in CH₂B₂ cells. The maximum RBE_{DNA} is of about 6 what reflects the DNA breakage data applied to unfolding. This corresponds to the well-known experimental observation, that even for very densely ionizing radiation the RBE for

**Fig. 6.2**

Relative efficiency in inducing an effect on cellular level (RBE_0) versus efficiency in producing DNA breaks (RBE_{DNA}). The cellular data concerns experiments of [Skarsgard et al., 1967] and [Cox et al., 1977a]

production of DNA breaks is much smaller than RBE for most cellular end-points and for tissues, which for some end-points for neutrons exhibit an RBE greater than 100.

It is a well documented hypothesis that DNA breaks are the primary lesions leading to most of the biological alterations in living organisms. It should be, however, kept in mind that these lesions only initiate a long chain of biochemical processes, leading to very different effects in the variety of systems. Therefore it should not be surprising that the efficiency of radiation to produce DNA double strand breaks and the efficiency to produce a given effect are not the same, even if DNA is the primary lesion. Energy deposition in the site is an important but certainly not the only factor which determinates radiation quality. There is experimental evidence [Feinendegen, 1988] that in addition to direct action on the DNA, an indirect action due to low-LET radiations occurs, e.g. due to the production of long-range radicals.

Investigation of biological response in terms of energy deposited in the site does not always give reasonable results. Fig.6.3 presents the unfolded BRF for DNA dsb in yeast cells [Frankenberg et al., 1986]. Cells were irradiated with 0.3, 1.5 keV and Co-60 photons. In this analysis, instead of microdosimetric distributions for Co-60, which are unavailable for nanometer-size sites, the distribution for 250 kVp X-rays was used. The unfolded function exhibits a sharp peak around 8 to 10 ionizations ($20 \text{ keV}/\mu\text{m}$) which corresponds to lineal energies produced by 0.3 keV photons in 20 nm targets (See Fig.4.11). The response function is an integral probability function; with increasing energy deposited the probability of an effect cannot decrease. Therefore, energy deposition in the target alone cannot explain the high biological effectiveness of soft X-rays in producing DNA dsb in yeast cells.

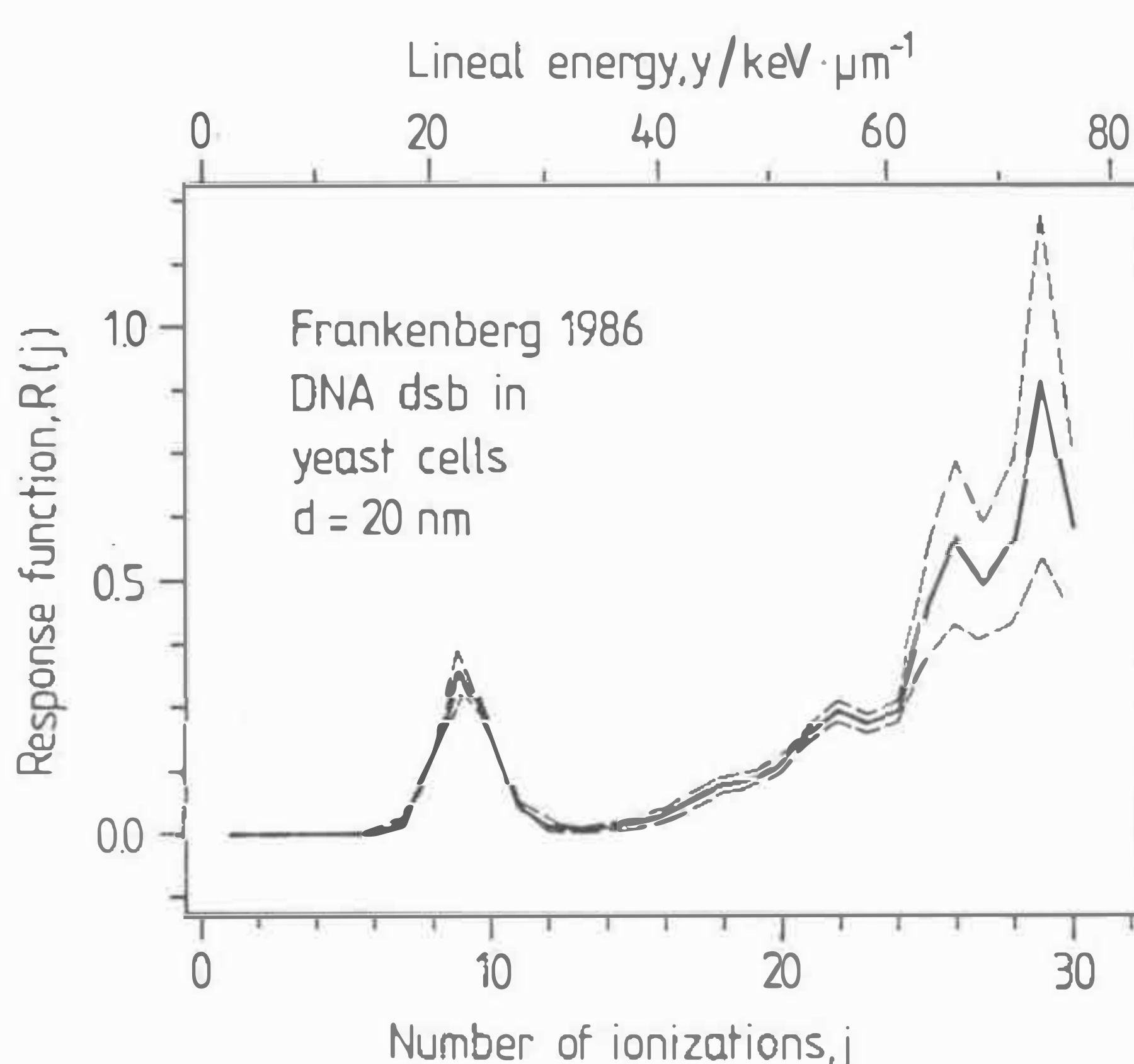


Fig.6.3

Preliminary results of unfolding biological response function for DNA dsb induced in yeast cells by soft X-rays [Frankenberg et al., 1986]. Due to lack of microdosimetric distributions for Co-60 gamma rays the distribution for 250 kVp X-rays was used. The dashed lines show the 1 SD of the unfolded function, calculated with Eq.6.1c.

6.2.2. Biological Response Functions for cellular effects and their implications for radiation protection.

Radiation-induced biological effects in cells, as mutations and chromosomal aberrations, are considered to be relevant for radiation protection. Calculations of BRF for these end-points are helpful (see Ch.3.6) in the formulation of a new concept of Quality Factor. The goal of this paragraph is to present some new results of calculation of response (or specific quality) functions and on this basis to verify some critical points in the ongoing discussion on radiation quality.

The site size used to unfold biological response functions for cellular effects is $1 \mu\text{m}$. The choice of target size is more pragmatic than based on theoretical premises. The mass of a unit density site of $1 \mu\text{m}$ corresponds to the mass of an average human chromosome but the more important practical considerations is that the diameter of $1 \mu\text{m}$ is the most frequently used simulated diameter in microdosimetric proportional counters available on the market. It is mainly for this reason that the proposals of new regulations of Quality Factor given in ICRU-40 are based on the site size of $1 \mu\text{m}$.

In fact, from the theoretical point of view, it would be better if a much smaller simulated diameter were used. For example, 24 keV neutrons produce recoil protons having a range of several dozen nanometers. The presence of insiders causes underestimation of lineal energy measured by a $1 \mu\text{m}$ counter because their range is much smaller than the mean chord length of $0.66 \mu\text{m}$. This in turn leads to underestimation of the Quality Factor because the counter measures short, densely ionizing tracks as they were long tracks produced by low-LET particles.

It was already mentioned in Ch.3.6 that two types of unfolding had contributed to the ongoing discussion on Quality Factor. Zaider and Brenner [1986, 1987] were solving Eq.3.27 using a least squares method (unparametric unfolding) and smoothed their results with a saturated polynomial of the third order covering the linear term in Eq.3.25. Their SQF function, calculated for chromosome aberrations in human lymphocytes, exhibited a plateau at y below $0.1 \text{ keV}/\mu\text{m}$. The results of this particular unfolding were used to justify the ICRU-40 proposal for a new Quality Function but the SQ function was finally taken without the linear term, a_1 . Morstyn et al. [1989] applied parametric unfolding with statistical analysis to study several cellular experiments, mostly with heavy ions. He did not confirm for all the Specific Quality Functions the lack of linear term in Eq.3.25.

Fig.6.4 compares the Specific Quality Functions unfolded using the SAND algorithm (thin lines) with results obtained by Morstyn et al. [1989] (bold lines) for mutations in human fibroblasts HF-19, mutations in V79 Chinese hamster cells and chromosome aberrations in CH2B₂ cells. In both approaches the same input data were used i.e. idealistic triangular spectra for heavy ions, 250 kVp X-ray distribution from Braby and Ellett [1972] and the initial slopes as compiled in Appendix B. The agreement is good for lineal energies above $20 \text{ keV}/\mu\text{m}$. For smaller lineal energies SQ functions unfolded with SAND-II become guess function dependent. Thin dotted lines denote response functions calculated with guess function having linear term of Eq.3.25 not equal to zero whereas full thin lines were calculated without the linear term ($a_1=0$). This dependence on guess functions is caused by a poor coverage of lineal energy range by microdosimetric distributions below $10-20 \text{ keV}/\mu\text{m}$. In fact, for lineal energies below $10 \text{ keV}/\mu\text{m}$ predominates the single one microdosimetric distributions for 250 kVp X-rays.

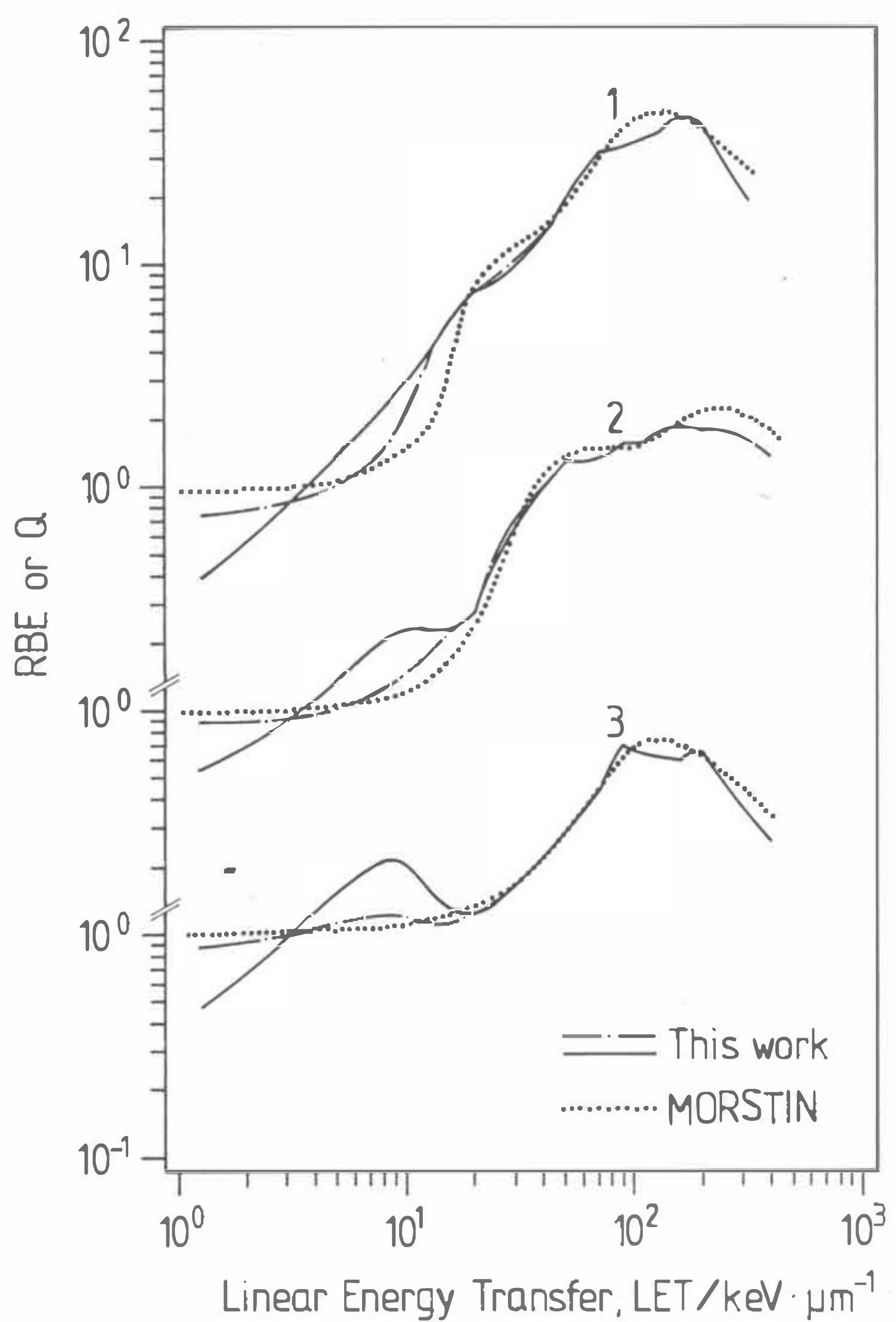


Fig.6.4

Quality Function for chromatid exchanges in CH2B₂ cells (1), V79 Chinese hamster cells (2) and mutations in human fibroblasts (3). The bold lines- [Morstин et al., 1989]; the thin lines- this work. The thin dotted line corresponds to calculations with an initial guess function without linear term in Eq.2.53 ($a_1=0$) and the thin continues line with the linear term. Quality Function is expressed in terms of LET.

Fig.6.5 compares specific quality functions as calculated for mutations of human fibroblasts (data from Cox et al. [1977a]). The broken line represents present calculations (SAND-II) and the bold line represents the results obtained by Zaider and Brenner [1986]. The agreement between the SAND-II and the least-square solution is quite satisfactory except for the lowest and highest lineal energies. The rapid decrease of response occurs for lineal energies above 500 keV/ μm for which only one microdosimetric distribution for argon ions is present.

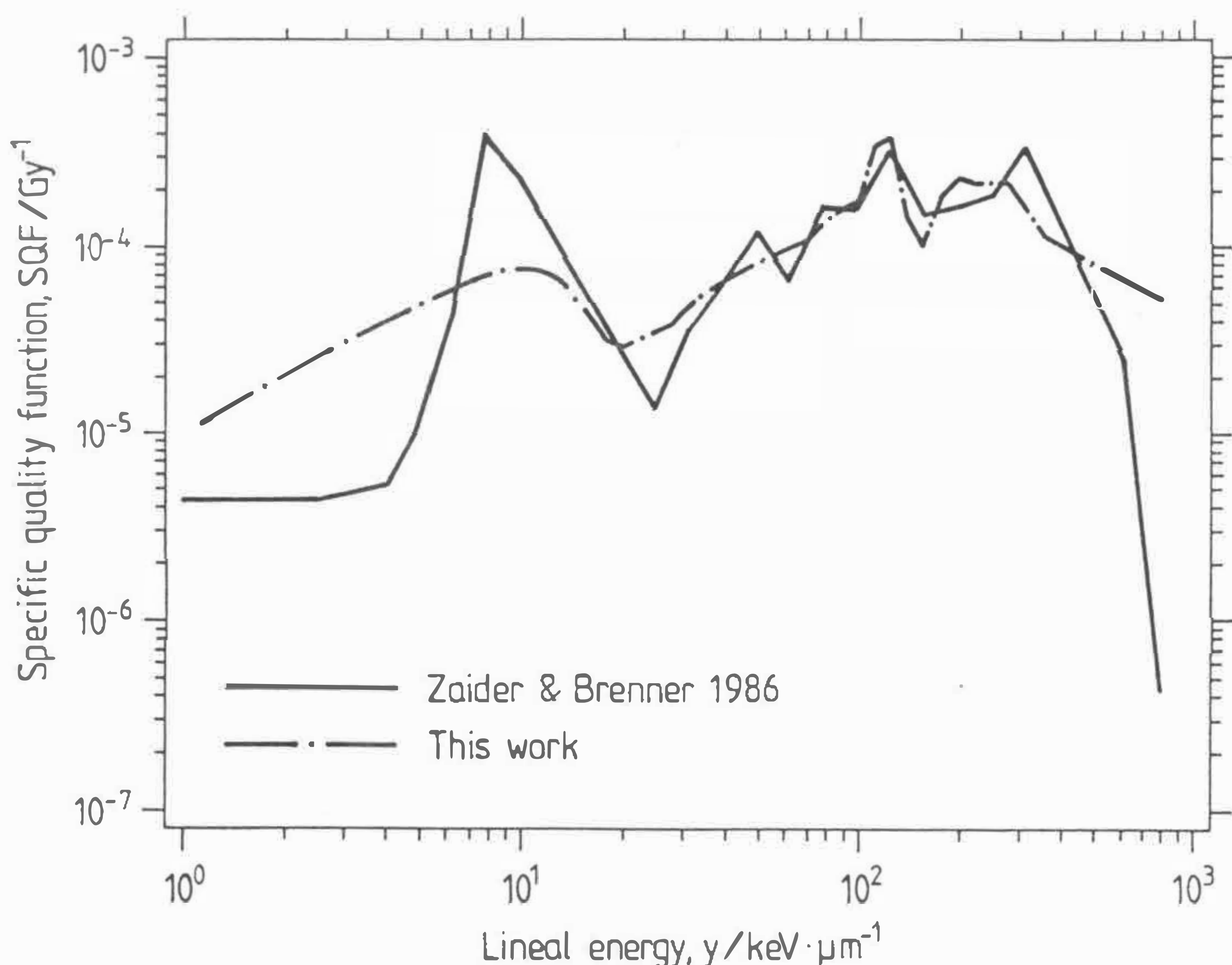


Fig.6.5

Specific Quality Functions for mutations in human fibroblasts HF-19. The bold line shows results of [Zaider & Brenner, 1986] and the dotted line unfolding done with SAND-II algorithm

Figs.6.6 present the unfolded quality functions for chromosome aberrations in human lymphocytes. The functions are normalized to the response of 250 kVp X-rays i.e. the microdosimetric distribution for X-rays folded with the presented quality functions give one. The set of initial slopes and microdosimetric distributions were taken from the work of Zaider and Brenner [1986]. Ten different radiations were used in the analysis (three low-LET, five neutrons and two alpha-particle) assuring good coverage of lineal energy range. For that reason the solutions in Fig.6.6a (heavy lines) do not strongly depend on the initial guesses (plotted with thin lines). The minimum in Quality Functions about 200 keV/ μm reflects the fact that the measured biological effectiveness for alpha-particles is

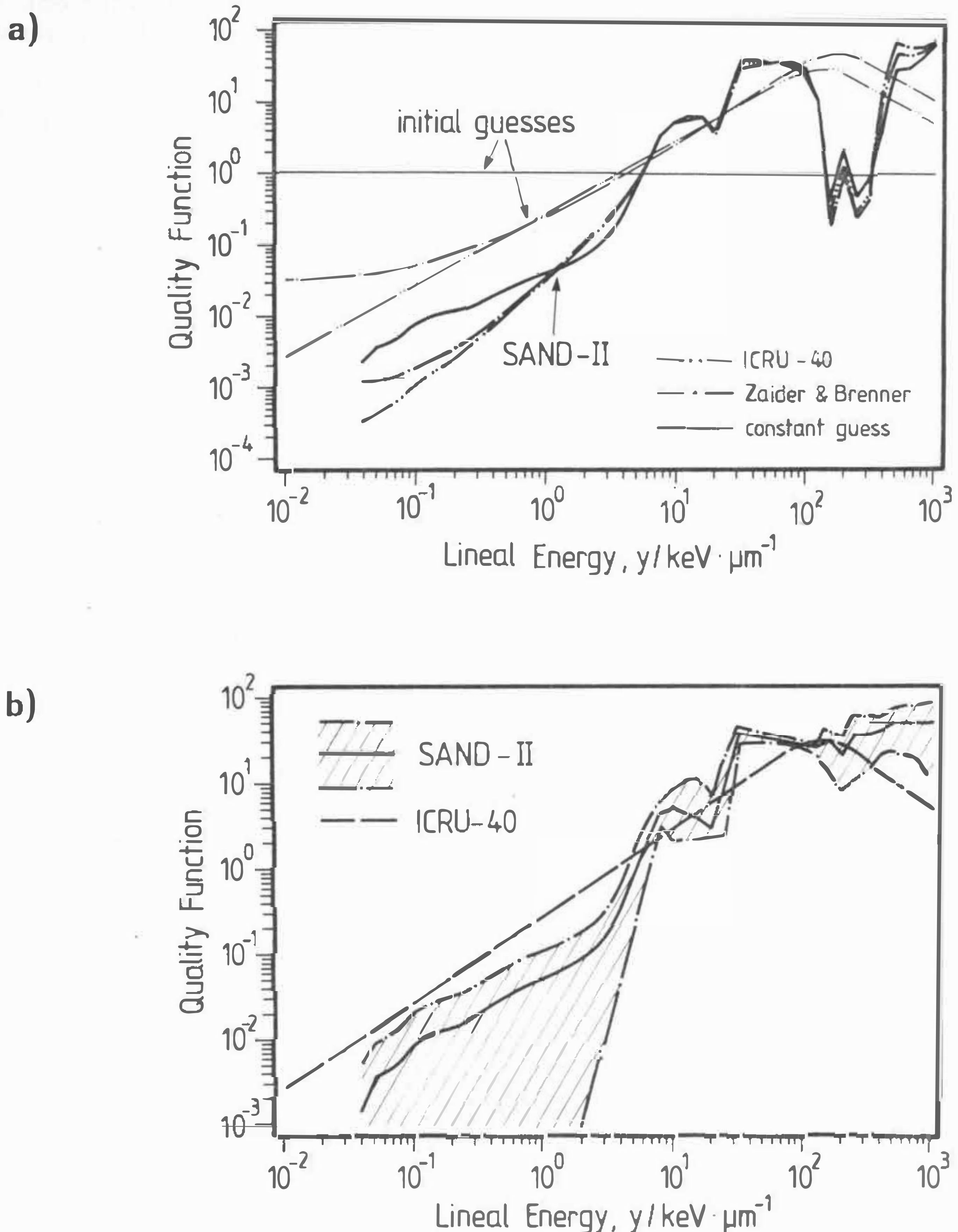


Fig.6.6

a) *Quality Functions for experiments with chromosome aberrations in human lymphocytes. The thin lines denote different initial guess functions; the bold - the corresponding unfolded Quality Functions.*

b) *Quality Function unfolded for the set of experiments as in Fig.6.6a but with excluded two experimental points for alpha-particles. The marked field denotes the region of 1 S.D.*

of a factor 3 smaller than the effectiveness of neutrons. When the alpha-particle data are excluded from the analysis then the minimum is not present any more (Fig.6.6b). For lineal energies above 200 keV/ μm no clear decrease of QF can be observed, as postulated by ICRU-40.

In conclusion, the unfolded SQF functions demonstrated in Figs.6.6a,b cannot be used to support the particular proposal of International Commission of Radiation Units and Measurements formulated in the ICRU-40 [1986] to change the existing definition of Quality Factor. Also, the analysis of experiments with heavy ions appear to offer no clear arguments for changing the present specification of the Quality Factor for low-LET radiations. This type of investigation serve rather more precise information about the region of the highest radiation quality i.e. around 100 keV/ μm . It would be, however, a good experimental practice to use, in future experiments with heavy ions, more than one low-LET radiation, such as soft X-rays, 250 kVp, Cs-137, Co-60, fast electrons, etc.

7. SUMMARY AND CONCLUSIONS

Energy of ionizing radiation is transferred to biological matter in discrete events. Due to the small dimensions of biological targets and due to the spatial pattern of these events, the energy deposited fluctuates considerably from target to target. Therefore, average macroscopic parameters used to describe radiation action and radiation quality as LET or dose are not relevant for describing radiation effects in, e.g., cells or DNA molecules.

Microdosimetry offers an alternative methodology to investigate radiation action. The distribution of energy deposition in small volumes is considered to be the primary factor which affects the induction of biological lesions. Such distributions of energy deposited can be measured or calculated. Measurements with proportional counters are however limited to site dimensions not much smaller than one micrometer. Therefore, numerical methods are presently the only method to assess microdosimetric distributions for nanometer sites. In this work such calculations were performed using Monte Carlo simulations of charge particle tracks.

A method has been developed which enables one to calculate microdosimetric distributions for photons. The method consists of two steps. First, a secondary electron spectrum induced in water by photons is calculated. Then, electron tracks are simulated and used to score microdosimetric distributions. The method allows an insight into the physical structure of the energy distribution, e.g. it is possible to identify contributions of Compton and photoelectrons to the total distribution. While calculations were performed for photon interactions in water, a simple recalculation allows one to apply them to distributions in TE gas. Microdosimetric distributions were calculated for photons of energies ranging from 0.3 keV to 300 keV and for targets of sizes in the range from a few nanometers to 2 μm . Results of these calculations compare favorably with distributions measured with wall-less and walled proportional counters. It was shown that for a given photon energy range and a given range of site diameters, the shape of the microdosimetric distribution is not directly related to the type of photon interaction in the counter but is principally determined by the relationship between the site diameter and the range of secondary electrons. Therefore, e.g., 20 keV photons (which induce mostly photoelectrons in water) and 100 keV photons (which induce mainly Compton electrons in water) produce very similar microdosimetric distributions. Photon induced microdosimetric distributions for nanometer targets were calculated for the first time and are now available for radiobiological modeling.

Energy deposition due to ion action was investigated with the Monte Carlo track structure program Moca-14 which simulates proton tracks in water vapour. Tracks of heavy ions are obtained by scaling the proton mean free path by an effective charge. In this work, dose distributions around the ion path were calculated and compared with measured radial dose distributions. This comparison has shown that the effective charge concept can be used to approximate track structure for heavy ions of energies greater than 0.5 MeV/amu. This limitation must be taken into account when analyzing radiobiological experiments with heavy ions. It was also demonstrated that the average value of energy required to produce an ion pair, W , should not be used to recalculate experimental ionization distributions into dose distributions at distances smaller than 10 nm from ion path. The energy required to produce an ion pair for such low radii is higher due to the presence of large numbers of low-energy electrons in the immediate vicinity of the ion's path. This energy depends on ion velocity.

Calculations of ion-induced microdosimetric distributions demonstrated that for small targets of some nanometers the straggling of energy deposition is considerable and the

chord-length approach should not be used to approximate microdosimetric distributions. Microdosimetric distributions due to the action of delta-electrons were calculated for the first time. It was shown that these frequency distributions of energy deposited in a target of some nanometers can be well approximated by simple exponential functions. Delta-electrons, which are ejected to the target by an ion passing outside the site, give a significant contribution to the dose in small targets. For example, delta-electrons contribute as much as 40% of dose from 10 MeV protons in 20 nm targets. Therefore, when calculations of DNA response are performed, realistic microdosimetric distributions, including delta-rays must be applied. An analytical recipe was developed which enables one to approximate such realistic microdosimetric distributions. Parameters of this recipe were calculated for protons and alpha particles, over the energy range 0.3-10 MeV/amu and diameters 1-1000 nm. The recipe will be useful in introducing straggling of energy deposition to microdosimetric neutron calculations, where energy in the target is deposited by a whole spectrum of secondary charged particles.

Results of radiobiological experiments are helpful in investigations to radiation quality. However, these experiments are performed for doses which are much higher than those relevant in radiation protection. Therefore, a radiobiological model has to be applied in order to extrapolate from high-dose data to the low-dose region. Most of the available models assume the existence of positive, non-zero initial slopes in the dose-response curves. A large set of initial slopes obtained in experiments with heavy ions and photons are collected and compiled in this work.

Calculated microdosimetric distributions and the initial slopes of dose-response curves were used to unfold Biological Response Functions, BRF. This is an alternative approach in describing radiation action on biological matter. Instead of explaining the underlying biophysical mechanisms, the BRF correlates energy deposition in a submicroscopic target and the biological effect. A Biological Response Function evaluated for DNA strand breaks in V79 Chinese hamster cells was used to calculate the number of DNA breaks in other radiobiological experiments with heavy ions and photons. It was shown that for some end-points (e.g. abnormal metaphasis in CH₂B₂ cells and mutations in human fibroblasts) exists direct proportionality between the frequency of DNA breaks and the frequency of effects on cellular level.

The unfolding of BRF performed for some cellular effects induced by heavy ions has shown that analysis based on such data leads to somewhat uncertain conclusions in the low-LET region because of poor coverage of microdosimetric distributions at low lineal energies. From that point of view, the ICRU 40 proposals for a new Quality Factors are questionable over the region of lineal energies below 3 keV/ μ m. From the point of view of radiation protection it would be more advantageous to keep the present QF regulations i.e. a constant value of the QF for photons. It is also recommended that in future experiments with heavy ions to study radiation quality, more than one low-LET radiation be applied.

APPENDIX A

A.1 Measurements and calculations of radial dose distributions.

Energy deposition around an ion track can be considered not only in a small target with which the ion interacts directly or indirectly. It is also of interest in radiobiology to gather information on the average dose around an ion track, i.e. to measure or calculate the distribution of average dose as a function of radial distance from the ion path.

A.1.1. Experiments

Radial dose distributions are usually measured with low pressure ionization chambers. In such an experiment, then ionization current produced by ejected delta-rays is measured as function of radial distance from the ion path. This current is then recalculated into dose using the value of average energy required to produce an ion pair, W. The advantage of radial dose measurements is that the radial dose can be determined even for small radial distances below 1 nm.

Baum and co-workers [1974] measured radial distributions of ionization around heavy ion tracks (38 MeV ^{16}O , 33 MeV ^{127}I , 62 MeV ^{127}I) using a variable-pressure ionization chamber containing a movable screen-walled probe chamber. Good agreement was found between measurements and calculations based on the continuous slowing down approximation [Paretzke, 1973]. At radial distances less than 1 nm the measured radial dose distributions were lower than those calculated. The authors attributed this discrepancy to the lack of charge equilibrium for the accelerated heavy ions.

The same chamber was used to measure radial dose distributions from 1 and 3 MeV protons and alpha particles of the same energies in hydrogen and a TE gas [Wingate & Baum, 1976]. These authors found agreement within 5% between the measurements for protons with calculations of Paretzke for intermediate radial distances i.e. at about 5-15 nm. For larger radial distances, calculations, based on measured spectra of secondary electrons [Toburen, 1971], [Toburen, 1972] and binary encounter theory [Garcia et al., 1968], overestimated the measured by a factor of 1.5-2. For low radial distances and for protons, calculations underestimated the measured values by about 5-25%. It was stated by the authors that the differences at radial distances around 1 nm were caused by applying a constant W-value to converge ionizations into dose, i.e. disregarding the possibility that W-value should increase for low-energy electrons which were stopped in the vicinity of the ion path.

In two experiments Varma et al. [1977], [1980] measured the radial dose around path of 41 MeV ^{16}O ions in N_2 and TE gases and 42 MeV bromine ions in TE gases. The experiments were compared with calculations performed using the continuous slowing down approximation (CSDA) and the Rutherford formula for ejection of secondary electrons. The percent deviation of experimental values from those calculated varied from -22% to 37% over the range of radial distances from 0.5 to 70 nm. In calculations, the emission of Auger electrons by incident ions as well as they radial dependence of the w-value, were not taken into account.

With a new accelerator facility (BEVALAC at Lawrence Berkeley Laboratory) it was possible to increase the energy of investigated ions to several hundred MeV/amu [Varma & Baum, 1980]. It was shown that for such high energies and large radial distances

reaching 1 mm, the radial dose distribution follows an inverse square radius dependence. The track structure calculations are not yet available for such high ion velocities.

A.1.2 Calculations

Two groups of method were developed to calculate radial dose distributions around ion tracks. To the first group belong calculations based on Monte Carlo track structure codes [Paretzke, 1988], [Hamm et al., 1985], [Zaider et al., 1983]. The other group consists of analytical models based on more simple assumptions [Butts & Katz, 1967], [Fain et al., 1974], [Baum, 1969], [Waligorski et al., 1987]. The advantage of these last methods is that they enable one to approximate energy deposition for ions and energies which are not available for more detailed Monte Carlo track structure calculations.

Katz and co-workers [Butts & Katz, 1967], [Katz et al., 1971] derived an expression for the radial distribution of dose around the path of the heavy ion on the basis of the Rutherford formula for delta-ray production assuming normal ejection of delta-rays and applying an effective charge formula [Barkas, 1953]. This expression was later improved in order to account for a "hump" in measured distributions in the region 1-10 nm [Waligórski et al., 1987]. The new expression fits well the measured radial distributions above 0.5 MeV/amu. Below this energy, deviations between calculations and experiment indicate the limit of validity of the effective charge formula. An additional reason for disagreement at radial distances lower than 10 nm is presumed to be the use of a constant W value for converting ionizations into energy, as discussed earlier.

Variations of W-values with radial distances from the trajectory of the particle were evaluated by Fain [Fain et al., 1974], showing no significant change with respect to the particle energy. These calculations were based on a theoretical model involving energy deposition through such basic processes as ionizations, excitations and vibration of medium molecules.

A.2 Method of calculation of radial dose distributions from simulated tracks.

Heavy ions tracks were generated by the code MOCA-14. The radial distribution of dose $D(r)$ was calculated by grouping energy deposition events which had occurred within the radial distances $(r, r+dr)$ and dividing the total energy deposition in this cylinder by the mass of this cylinder. In addition to energy deposition, the radial distributions of ionizations, $J(r)$, was scored. $J(r)$ is here defined as the number of ionizations per unit mass. Therefore, the radial distribution of energy required for producing an ion pair, $w(r)$, could be calculated as:

$$w(r) = \frac{D(r)}{J(r)} \quad (\text{A.2.1})$$

The average differential w value, which is usually used in experiments to convert ionizations into dose distributions, $D'(r)$, can be calculated as

$$w = \frac{\int w(r) J(r) r^2 dr}{\int J(r) r^2 dr} \quad (\text{A.2.2})$$

and

$$D'(r) = w J(r) \quad (\text{A.2.3})$$

APPENDIX B

B.1. Evaluation of initial slopes of dose-response curves.

An evaluation of initial slopes of dose-response curves is always based on somewhat arbitrary premises because no single radiobiological model can explain all aspects of radiation action and suggest an appropriate analytical expression to fit all experimental results [Guenther & Schultz, 1983]. Most dose-response curves can be fitted with a statistical accuracy similar to that experimentally obtainable by a variety of analytical expressions containing a number of free parameters. Such a fit is by itself not a proof of the validity of a model.

DNA double strand breaks

In Tab.B.1 are gathered the values of initial slopes of dose-effect relationships for DNA double-strand breaks, together with their estimated uncertainties at the level of one standard deviation. For DNA double-strand breaks most experiments exhibit linear relationships between dose and frequency of double-strand breaks [Guenther & Schultz, 1983]. All DNA experiments analyzed in this work are considered to follow this linear dose-effect relationship.

Christensen's data [1972] are read from Tab.1 and Fig.5 of the original paper. Error bars plotted by the authors on the original Fig.5 were calculated by repeating the experiment with a given radiation modality several times and taking the mean value and standard deviation of the mean frequency of DNA dsb. These error bars do not account for uncertainties of a single experiment, which were estimated by these authors to be within about 15% (one standard deviation). For three types of ions (Li, B, C) experiments were performed only once and standard deviations were set up in the Tab.B.1 arbitrarily at 15%. In the set of measurements with Co-⁶⁰ gamma-rays one result ($4.2 \cdot 10^{-14}$ breaks/Gy/Dalton for experiment I.D. No.10-FB) is in serious disagreement with others which vary between 0.9 and $1.7 \cdot 10^{-14}$ and was therefore not taken into account in the calculation of the mean and the standard deviation.

Mean values and standard deviations of relative efficiencies for non-rejoining break induction in Chinese hamster V79 cells were read from the Fig.1 of the work of Ritter et al. [1977] and normalized to the absolute number of non-rejoining breaks. This normalization was performed using the information that the absolute number of breaks for X-rays was $(2.67 \pm 0.14) \cdot 10^{-14}$ breaks/Gy/Dalton and the percentage of non-rejoining breaks $1.4 \pm 0.4\%$. The uncertainty of break-induction for X-rays (not plotted in Fig.2 of the original paper), was estimated as the sum of relative variances of the number of breaks and the percentage of non-rejoining breaks.

The average induction frequencies and corresponding standard deviations of DNA dsb in yeast cells come from Tab.1 of the work of Frankenberg and co-workers [1986]. Standard deviations calculated from fitting experimental points by regression analysis are relatively low, of the order of a few percent.

Cellular experiments

Cellular data are gathered in Tabs.B.2-5. Five groups of experiments were analyzed.

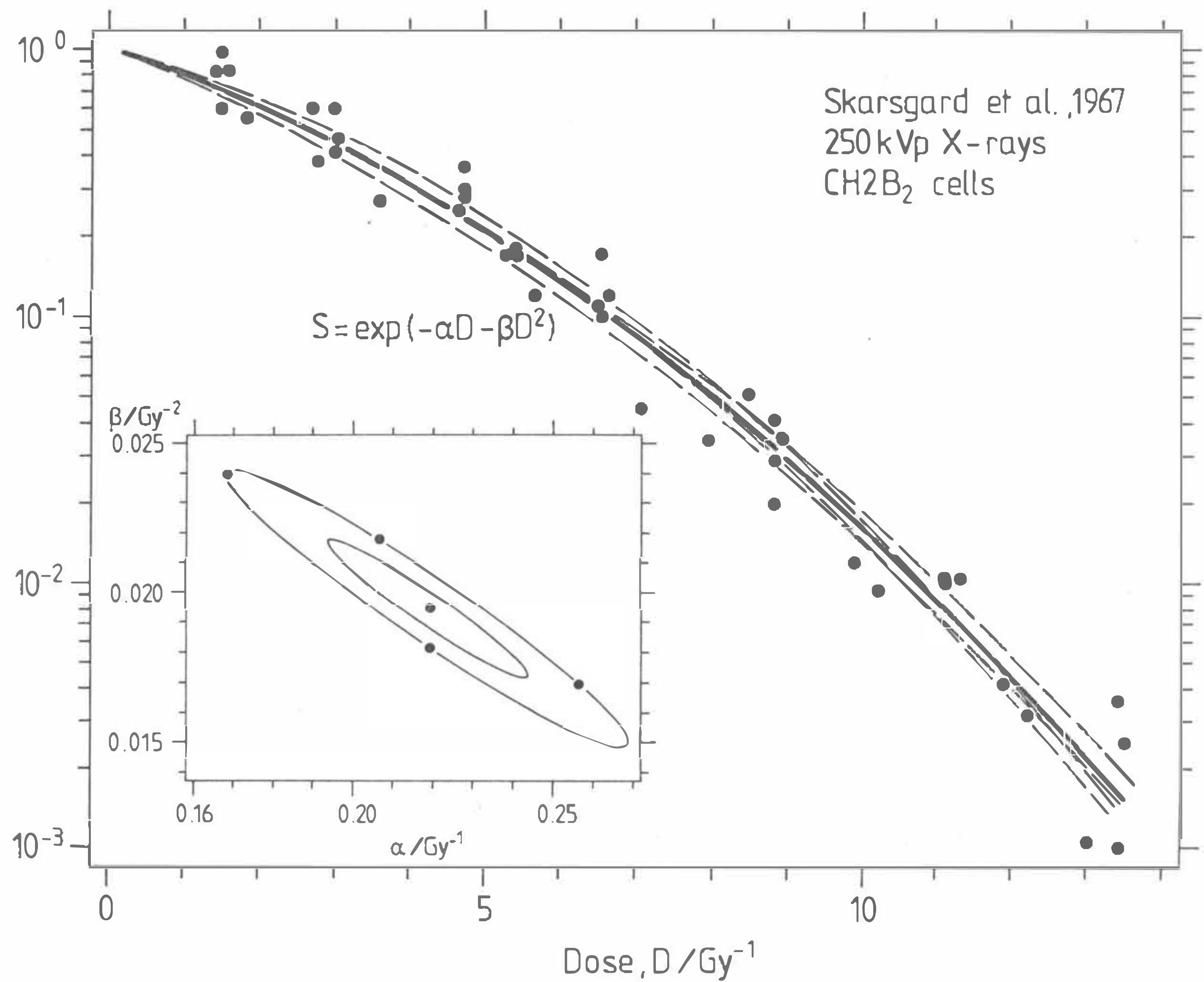
Cox and co-workers [1977a] performed extensive measurements of mutations and inactivations in human fibroblasts HF-19 and Chinese hamster cells V79 induced by ions of LET up to 470 keV/ μ m. Coefficients and their standard deviations, calculated from fitting the human fibroblasts data to linear and hamster data to linear-quadratic models are reported. The original survival curves were not published in the paper, which makes any check of the published coefficients impossible. Morstin [Morstin et. al, 1989] states, that the initial slope for X-rays for HF-19 cells could be questionable and the quoted uncertainties presumably be underestimated.

Todd [1967] reported results of experiments with T-1 human kidney cells (end-point: inhibition of colony formation) irradiated by 50 kVp X-rays and heavy ions in LET range from 6.5 to 1940 keV/ μ m. The alphas and their standard deviations shown in Tab.B.4 were derived from cross sections (Table.II in original paper) and RBE versus LET curve (Fig.6 in original). The same author [Todd, 1975] reported results of similar experiments for M3-1 Chinese hamster cells. Data presented in Tab.B.4 was obtained by fitting linear (for Ne-20, O-16, N-14 and B-11) and linear-quadratic dependencies (for other radiations) to published survival curves.

Data of Bird [Bird et al., 1980], which were fitted with a linear-quadratic expression, were taken directly from the original publication and are given in Table.B.5.

Skarsgard and co-workers [1967] performed experiments with CH2B₂ cells investigating their survival, abnormal metaphase and chromatid exchanges. In the original work α coefficients were not reported. Initial slopes for survival curves were fitted in this work with the linear-quadratic expression to the originally published data points using the NL2SOL computer code of the ZAM mathematical library [NL2SOL, 1983]. Fig.B.1. presents an example of such a fit performed for survival of 250 kVp X-rays with covariance ellipses shown for 67 and 95% confidence limits. The point in the center of ellipses corresponds to the best fit (bold curve), the other points plotted at 95% confidence band corresponds to the family of broken curves.

Data for chromatid exchanges, summarized in the Tab.B.2, was taken from [Brenner,1988] fitted with Eq.2.39 and, for comparison, from [Morstin et al., 1989] fitted by "saturated polynomials" which assure the highest statistical credibility of the fit. In this fitting technique, different degree of "saturated polynomials" with varying number of parameters were fitted and after each trial the actually achieved χ^2 value was calculated. The lowest achieved value of χ per degree of freedom was used as a selection criterion for the "best" α .

**Fig.B.1**

Example of fitting equation $S = \exp(-\alpha D - \beta D^2)$ to survival curve for CH2B₂ cells [Skarsgard et al., 1967] and 250 kVp X-rays. Dots show experimental points, the bold line the best fit. The value of α and β correspond to the position of central point in the ellipse of covariance. The broken lines were calculated for (α, β) points placed on the ellipse for 95% confidence.

Tab.B.1

Initial slopes of DNA double strand breaks evaluated from experiments with heavy ions and soft X-rays

Radiation	LET [keV·μm ⁻¹]	$\alpha \cdot 10^{-12}$ [Gy D ⁻¹]
<hr/>		
[Christensen et al, 1972], ΦX-174 virus,		
Co-60	0.3	1.3 ± 0.36
H	5.8	0.90 ± 0.10
He	34.3	2.08 ± 0.40
Li	78.5	2.47 ± 0.25
B	225	4.55 ± 0.46
C	332	5.59 ± 0.56
O	550	6.11 ± 0.86
Ar	2420	4.68 ± 0.47
<hr/>		
[Ritter et al., 1977], Chinase hamster V79 S171 cells		
X-rays	2	3.6 ± 0.5
H	9.4	3.35 ± 1.3
H	27	6.51 ± 2.1
Be-9	151	18.3 ± 1.7
C-12	332	12.7 ± 1.2
Ne-20	827	9.1 ± 1.2
Ar-40	1953	8.7 ± 1.1
<hr/>		
[Frankenberg et al., 1986], yeast cells		
Co-60	0.3	4.23 ± 0.8
0.28 keV X	-	15.99 ± 3.1
1.5 keV X	-	9.32 ± 1.8

Tab.B.2

Initial slopes of dose-response curves for cellular end-points in experiments of [Skarsgard et al, 1967].

Radiation	LET / keV·μm ⁻¹	α / Gy ⁻¹
<hr/>		
survival of CH2B ₂ cells, fit: this work		
250 kVp X-rays	2	0.219 ± 0.025
Li-7	44.3	0.454 ± 0.055
B-9	126.5	0.846 ± 0.051
C-12	189.	0.691 ± 0.056
O-16	351.	0.843 ± 0.046
<hr/>		
chromatid exchange, fit: [Morsttin et al., 1989]		
250 kVp X-rays	2	0.008 ± 0.003
He-4	19.1	0.061 ± 0.008
Li-7	44.3	0.128 ± 0.016
Li-7	72.7	0.275 ± 0.034
B-11	126.5	0.317 ± 0.038
C-12	189.	0.387 ± 0.029
O-16	351.	0.171 ± 0.018
<hr/>		
chromatid exchange, fit: [Brenner, 1988]		
250 kVp X-rays	2	0.014 ± 0.013
He-4	19.1	0.052 ± 0.017
Li-7	44.3	0.097 ± 0.017
Li-7	72.7	0.212 ± 0.022
B-11	126.5	0.288 ± 0.022
C-12	189.	0.325 ± 0.020
<hr/>		
abnormal metaphases, fit: [Morsttin et al., 1989]		
250 kVp X	2	0.114 ± 0.011
He-4	19.1	0.165 ± 0.016
Li-7	44.3	0.313 ± 0.034
Li-7	72.7	0.515 ± 0.055
B-11	126.5	1.000 ± 0.250
C-12	189.	0.700 ± 0.100
O-16	351.	0.350 ± 0.050

Tab. B.3

Initial slopes of dose-response curves for cellular end-points in experiments of [Cox et al., 1977a].

Radiation	LET keV· μm^{-1}	INACTIVATIONS				
		V-79		HF-19		
		α Gy $^{-1}$	α Gy $^{-1}$	α Gy $^{-1}$	α Gy $^{-1}$	
250 kVp	2	0.143	\pm	0.015	0.792 \pm	0.02
He-4	20	0.49	\pm	0.03	1.09 \pm	0.02
	28	0.55	\pm	0.05	1.25 \pm	0.05
	50	0.93	\pm	0.10	1.98 \pm	0.03
	70	0.96	\pm	0.14	2.57 \pm	0.05
	90	1.29	\pm	0.8	3.16 \pm	0.07
	110	0.74	\pm	0.9	2.96 \pm	0.10
B-11	160	-			2.79 \pm	0.14
	200	1.12	\pm	0.21	2.00 \pm	0.03
	470	0.88	\pm	0.04	1.38 \pm	0.03

Radiation	LET keV· μm^{-1}	MUTATIONS				
		V-79		HF-19		
		α Gy $^{-1} \cdot 10^{-4}$				
250 kVp	2	0.035	\pm	0.005	0.310 \pm	0.008
He-4	20	0.10	\pm	0.07	0.394 \pm	0.008
	28	-			0.485 \pm	0.039
	50	0.49	\pm	0.06	0.899 \pm	0.033
	70	-			1.35 \pm	0.06
	90	0.60	\pm	0.22	2.2 \pm	0.17
	110	0.62	\pm	0.27	2.01 \pm	0.14
B-11	160	-			1.78 \pm	0.12
	200	0.62	\pm	0.43	2.07 \pm	0.09
	470	0.54	\pm	0.05	0.85 \pm	0.03

Tab.B.4

Initial slopes of dose-response curves for cellular end-points in experiments of [Todd, 1975].

[Todd, 1975], survival of M3-1 Chinese hamster cells.

M3-1

Radiation	LET keV/ μm	α Gy^{-1}
50 kVp	2	0.34 \pm 0.07
H-2	6.5	0.42 \pm 0.13
He-4	25	0.61 \pm 0.12
Li-7	55	0.82 \pm 0.23
B-11	165	1.27 \pm 0.11
C-12	220	1.17 \pm 0.12
N-14	300	0.89 \pm 0.04
O-16	385	0.78 \pm 0.04
Ne-20	580	0.60 \pm 0.02
Ar-40	1940	-

Tab.B.5

Initial slopes of dose-response curves for cellular end-points in experiments of [Bird et al., 1980].

Radiation	LET keV/ μm	G1/S		late-S phase	
		α Gy^{-1}	α Gy^{-1}	α Gy^{-1}	α Gy^{-1}
250 kVp	2	0.22	\pm 0.04	0.087	\pm 0.02
H-1	10.2	0.399	\pm 0.069	0.122	\pm 0.018
H-2	20.4	0.497	\pm 0.088	0.208	\pm 0.042
H-2	31	0.773	\pm 0.146	0.272	\pm 0.051
	40	0.854	\pm 0.112	0.364	\pm 0.123
	67	1.165	\pm 0.232	-	
He-3	91	1.560	\pm 0.070	0.717	\pm 0.077
	127	1.466	\pm 0.027	0.822	\pm 0.045
	170	1.427	\pm 0.200	0.688	\pm 0.061

Appendix C

C.1. Exemplary calculation of a microdosimetric distribution using the developed analytical functions

An exemplary calculation of parameters for a site of 20 nm diameter and 0.3 MeV alpha particles is presented below. From Tab.C.1b one finds $B=0.0774$ and $C=87.4$. The sum in the denominator of Eq.5.7 quickly converges and $A=2.44E-4$. As the next step, the first moment of $f^{(i)}(j)$ (Eq.5.6) is calculated and found equal to $j^{(i)}=66.1$. Then one takes $\mu_D=0.053$ from Tab.C.2 and $j^{(\delta)}=5.7$ from Tab.C.1b, and calculates $j_F=42.3$ with the help of Eq.5.2b and $\mu_F=0.39$ with Eq.5.2a. This set of parameters enables one to calculate the distributions of ionizations as given by Eq.5.10. Figs.5.3a,b show the partial frequency ionization distributions calculated using these parameters and compared with distributions obtained from track structure calculations. Fig.5.3c indicates the manner in which the total spectrum $f_1(j)$ is constructed. In this particular case $\mu_F=0.39$, i.e., about 39% of events in the sensitive site are due to delta-rays produced by ions passing outside the site.

Tab.C.1a

PROTONS	0.3 MeV/amu	0.5 MeV/amu	1.0 Mev/amu	2.0 MeV/amu	5.0 MeV/amu	10 MeV/amu
1 nm	1.22	1.22	1.21	1.20	1.19	1.18
	.175E+1	.198E+1	.231E+1	.263E+1	.295E+1	.307E+1
	.000E+0	.000E+0	.000E+0	.000E+0	.000E+0	.000E+0
2 nm	1.50	1.50	1.48	1.44	1.42	1.38
	.115E+1	.138E+0	.172E+1	.205E+1	.239E+1	.256E+1
	.000E+0	.000E+0	.000E+0	.000E+0	.000E+0	.000E+1
5 nm	2.28	2.34	2.24	2.13	2.02	1.89
	.481E+0	.665E+0	.109E+1	.139E+1	.180E+1	.203E+1
	.000E+0	.000E+0	.000E+0	.000E+0	.000E+0	.000E+1
10 nm	3.3	3.5	3.4	3.1	2.8	2.50
	.221E+0	.310E+0	.537E+0	.902E+0	.139E+0	.170E+1
	.107E+1	.000E+0	.000E+0	.000E+0	.000E+0	.000E+1
20 nm	4.4	5.3	5.4	4.7	3.9	3.34
	.142E+0	.164E+0	.246E+0	.461E+0	.945E+0	.132E+1
	.190E+2	.840E+1	.000E+0	.000E+0	.000E+0	.000E+1
50 nm	5.5	8.1	10.	8.7	6.5	5.28
	.835E-1	.889E-1	.112E+0	.161E+0	.392E+0	.713E+0
	.677E+2	.441E+2	.182E+2	.000E+0	.000E+0	.000E+0
100 nm	6.5	9.7	14.	14.	11.	8.14
	.587E-1	.588E-1	.707E-1	.939E-1	.174E+0	.346E+0
	.149E+3	.105E+3	.564E+2	.213E+2	.000E+0	.000E+0
200 nm	6.8	11.	19.	23.	18.	13.7
	.443E-1	.420E-1	.455E-1	.592E-1	.917E-1	.154E+0
	.312E+3	.230E+3	.134E+3	.655E+2	.146E+0	.000E+0
500 nm	8.2	14.	24.	38.	39.	30.
	.284E-1	.270E-1	.272E-1	.313E-1	.508E+0	.614E+0
	.794E+3	.598E+3	.373E+3	.202E+3	.789E+2	22.1
1000 nm	12.	17.	26.	49.	66.	54.
	.191E-1	.182E-1	.189E-1	.208E-1	.308E-1	.349E-1
	.160E+4	.121E+4	.772E+3	.444E+3	.184E+3	79.1

Parameters $j^{(\delta)}$, B, C of the analytical recipe (see Ch.5) for protons in water vapour. The presentation of the parameters in a single rectangle is as follows:

 $j^{(\delta)}$

B

C

ALPHA PARTICLES	0.3 MeV/amu	0.5 MeV/amu	1.0 MeV/amu	2.0 MeV/amu	5.0 MeV/amu	10 MeV/amu
1 nm	1.23	1.23	1.22	1.21	1.19	1.18
	.888E+0	.106E+1	.139E+1	.177E+1	.228E+1	.260E+1
	.540E-1	.000E+0	.000E+0	.000E+0	.000E+0	.000E+0
2 nm	1.56	1.53	1.49	1.45	1.42	1.39
	.452E+0	.542E+0	.804E+0	.119E+1	.170E+1	.205E+1
	.159E+1	.000E+0	.000E+0	.000E+0	.000E+0	.000E+0
5 nm	2.58	2.49	2.34	2.15	2.02	1.90
	.226E+0	.259E+0	.319E+0	.506E+0	.984E+0	.139E+1
	.143E+2	.961E+1	.234E+1	.000E+0	.000E+0	.000E+0
10 nm	4.0	4.0	3.6	3.1	2.7	2.49
	.133E+0	.152E+0	.196E+0	.249E+0	.513E+0	.882E+0
	.380E+2	.276E+2	.147E+0	.293E+1	.000E+0	.000E+0
20 nm	5.7	6.3	5.9	4.9	3.9	3.3
	.778E-1	.888E-1	.115E+0	.154E+0	.234E+0	.451E+0
	.875E+2	.668E+2	.396E+2	.187E+2	.000E+0	.000E+0
50 nm	8.6	11.	12.	9.2	6.7	5.2
	.471E-1	.473E-1	.606E-1	.816E-1	.114E+0	.158E+0
	.246E+3	.194E+3	.123E+3	.671E+2	.216E+2	.000E+0
100 nm	10.	14.	18.	16.	11.	8.0
	.348E-1	.322E-1	.356E-1	.500E-1	.730E-1	.878E-1
	.509E+3	.412E+3	.268E+3	.152E+3	.614E+2	.199E+2
200 nm	13.	17.	25.	26.	19.	13.
	.256E-1	.222E-1	.230E-1	.308E-1	.449E-1	.510E-1
	.103E+4	.844E+3	.571E+3	.332E+3	.143E+3	.643E+2
500 nm	20.	22.	32.	45.	40.	29.
	.148E-1	.142E-1	.153E-1	.172E-1	.228E-1	.271E-1
	.259E+4	.214E+4	.148E+4	.893E+3	.400E+3	.215E+3
1000 nm	21.	22.	38.	60.	70.	54.
	.962E-2	.892E-2	.112E-1	.111E-1	.144E-1	.158E-1
	.520E+4	.428E+4	.299E+4	.185E+4	.856E+3	.471E+3

Tab.C.1b

Parameters $j^{(\delta)}$, B, C of the analytical recipe (see Ch.5) for alpha particles in water vapour. The presentation of the parameters in a single rectangle is as follows:

$$\begin{pmatrix} j^{(\delta)} \\ B \\ C \end{pmatrix}$$

DIAMETER	0.3 MeV/amu	0.5 MeV/amu	1.0 MeV/amu	2.0 MeV/amu	5.0 MeV/amu	10 MeV/amu
1 nm	.39	.42	.46	.49	.51	.59
2 nm	.31	.36	.41	.44	.48	.55
5 nm	.19	.25	.32	.36	.40	.50
10 nm	.11	.17	.24	.30	.34	.44
20 nm	.053	.099	.17	.24	.29	.39
50 nm	.016	.040	.097	.16	.22	.34
100 nm	.006	.016	.052	.12	.18	.29
200 nm	.002	.006	.025	.077	.14	.25
500 nm	.0005	.0017	.007	.035	.10	.21
1000 nm	.0001	.0005	.003	.016	.071	.17

Tab.C.2 Fraction of dose due to delta-events, μ_D , to the spherical targets of diameters from 1 to 1000 nm. Results obtained from Monte Carlo track structure calculations in water vapour with the code MOCA-14.

Tab.C.3

Parameters of the analytical recipe (see Ch.5) which enable to calculate ionization distributions in 20 nm spherical targets for ions used in several radiobiological experiments.

Radiation	B	C	μ_D	$j^{(\delta)}$
[Skarsgard et al., 1967]				
He-4	.444	0.0	.37	3.22
Li-7(58 MeV)	.195	2.80	.38	3.19
Li-7(30 MeV)	.151	20.1	.26	4.38
B-11	.116	39.7	.26	4.19
C-12	.0995	65.3	.30	3.91
O-16	.0741	128.	.29	3.85
[Christensen et al., 1972]				
H	1.10	0.0	.373	3.30
He	0.214	0.0	.320	3.83
Li	0.157	25.6	.273	3.92
B	0.0851	86.7	.265	4.19
C	0.0729	126.	.306	4.39
O	0.0565	231.	.241	4.64
Ar	0.0261	1120.	.150	9.42
[Ritter et al., 1977]				
H	0.740	0.0	.286	3.87
H	0.247	0.0	.186	5.22
Be-9	0.110	54.3	.276	4.29
C-12	0.0706	133.	.284	4.46
Ne-20	0.0418	342.	.255	4.96
Ar-40	0.0285	852.	.223	6.31
[Cox et al., 1977a]				
He-4 20	0.369	0.0	.343	3.45
28	0.271	0.0	.331	3.57
50	0.180	11.2	.243	4.28
70	0.146	21.8	.199	5.11
90	0.129	33.5	.180	5.68
B-11 110	0.124	34.7	.310	3.51
160	0.111	58.2	.320	3.78
200	0.102	77.9	.281	4.51
N-14 470	0.0555	191.5	.254	4.68
[Todd , 1975]				
H-2	1.09	0.0	.340	3.45
He-4	0.304	0.0	.306	3.70
Li-7	0.159	12.2	.299	3.78
B-11	0.105	58.2	.302	3.93
C-12	0.0900	87.6	.300	4.11
N-14	0.0783	119.	.313	3.96
O-16	0.0683	156.	.274	4.46
Ne-20	0.0572	239.	.267	4.87
Ar-40	0.0349	789.	.223	5.82

Appendix D

Testing the program SAND-II

As stated in Ch.3, Eq.3.20 is usually undefined and does not have, in general, a unique solution. Many different solutions can be found and these solutions are dependent on guess functions and regularizations applied. It is therefore important to test the properties of the SAND-II code in order to correctly interpret the unfolded response functions.

Two different sets of microdosimetric distributions were used in tests. Fig.D.1a shows $yf(y)$ distributions for $d = 1 \mu\text{m}$ induced by heavy ions (idealistic triangular distributions) and by 250 kVp X-rays measured by Ellet and Braby [1972]. These radiation modalities were used in experiment of Skarsgard [Skarsgard et al., 1967]. A characteristic feature of these microdosimetric distributions is that the low lineal energy region is covered only by a single distribution from 250 kVp X-rays. Another set of distributions was calculated for a site diameter of 20 nm, for the experiment of Todd [1975] (Fig.D.1b). For such a low site diameter a large number of events in the site are produced by delta-electrons. All distributions demonstrate a similar shape at low lineal energies.

Two type of tests were performed.

a) guess function and a response function:

A known, ideal response function R_i with a threshold (Figs.D.2a) and without a threshold (Fig.D.2b), were used to calculate effects α_i^0 using Eq.3.22 and microdosimetric distributions from Figs.D.1a,b. The sets of α_i^0 were next used to unfold response functions with the program SAND-II (without stochastic modifications).

Iterations were started from 3 different initial guess functions (marked with broken line): a constant guess function (1), a saturated exponential function, with (2) and without a threshold (3). In the lineal energy range between 10 and 200 keV/ μm , which is well covered by microdosimetric distributions, the deconvoluted functions (bold line) matches the ideal response quite well. For lineal energies below 10 keV/ μm , the deconvoluted functions follow the shape of the initial guess and do not fit to ideal response. This follows from the fact that in the considered lineal energy range these deconvoluted functions are determined by a single microdosimetric distribution. Therefore in the expression for the correction factor (See Fig.3.8) only one weighting factor w_{ij} does not vanish, namely:

$$f_j^0 = \ln r_i \quad (\text{D.1})$$

and the new response function R_j^1 is now calculated as

$$R_j^1 = R_j^0 r_i \quad (\text{D.2})$$

As all bins of the unfolded response function R_j below 10 keV are always modified with a common factor r_i , the shape of the unfolded response function merely follows the shape of the initial guess. Of course, this conclusion is valid also for the highest part of the linear energy range.

A similar situation occurs when microdosimetric distribution have similar amplitude for a given bin j . Then

$$w_{1j} \approx w_{2j} \approx \dots \approx w_{mj} \quad (D.3)$$

which gives

$$f_j^0 = \ln r_i \quad (D.4)$$

and finally

$$R_j^1 = R_j^0 r_i \quad (D.5)$$

This is a case for the distributions evaluated for 20 nm sites and lineal energies partly below 10 keV/ μ m.

The conclusion to be drawn from this test is that for reliable unfolding of a biological response function it is necessary to perform experiments with such radiation modalities which produce microdosimetric distributions adequately covering the interesting lineal energy range and not similar in shape.

It is worth mentioning that these requirements of input data are also valid for other unfolding methods, e.g. for the least squares methods with matrix inversion. Setting similar microdosimetric distributions leads in that case to ill-conditions for an inverted matrix.

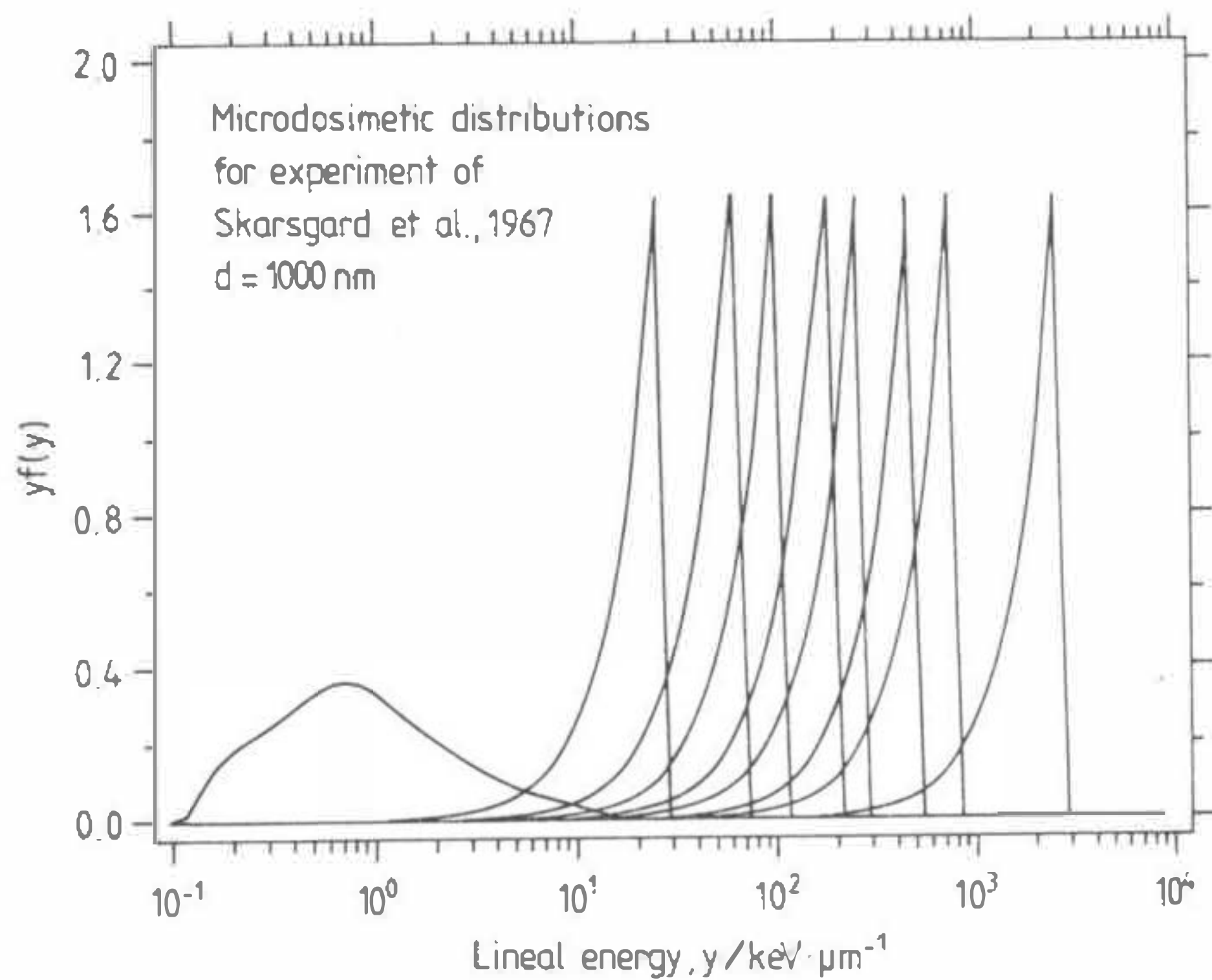
b) deviations from ideal response

This test was performed in order to verify how uncertainties in biological input data influence the solution. An ideal response function was assumed and the corresponding set of initial slopes, α , calculated using Eq.3.22 and microdosimetric distributions from Fig.D.1b. These α were next randomly deviated according to normal error distribution with standard deviations of 0, 10 and 20%. and used to unfold a response function.

Fig.D.3 presents results of these unfolding. For non-deviated initial slopes, α , and a relatively close guess, the deconvoluted function well matches the ideal response. This is, however, not the case for functions unfolded from slightly deviated input parameters. In case of curve B, the amplitude of deviations between then unfolded and the ideal functions is as much as 50% and is much higher than the amplitude of deviations between the ideal and deviated parameters.

This type of test indicates that some oscillations observed in the unfolded biological response functions can have their origin in uncertainties in the biological input data.

a)



b)

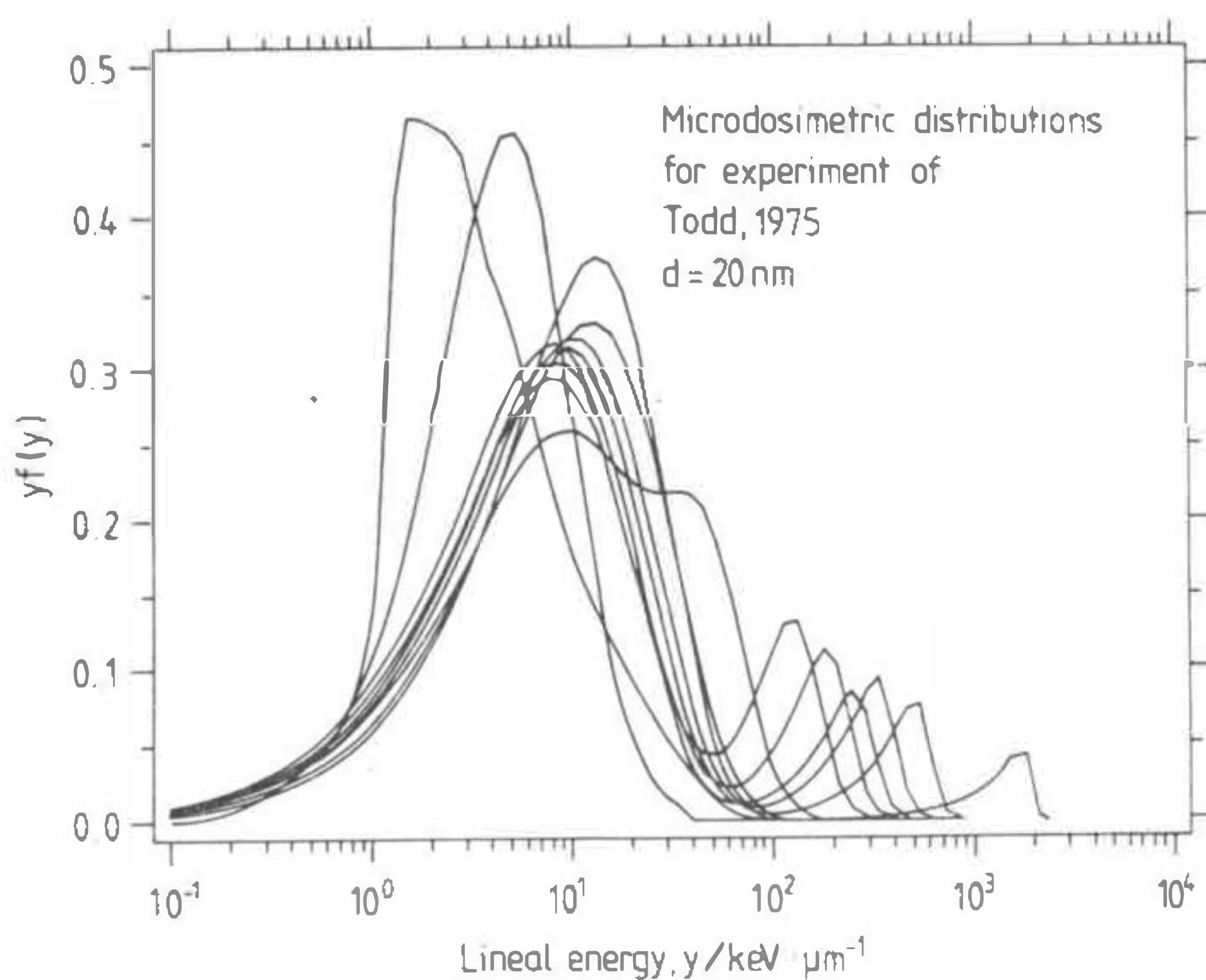
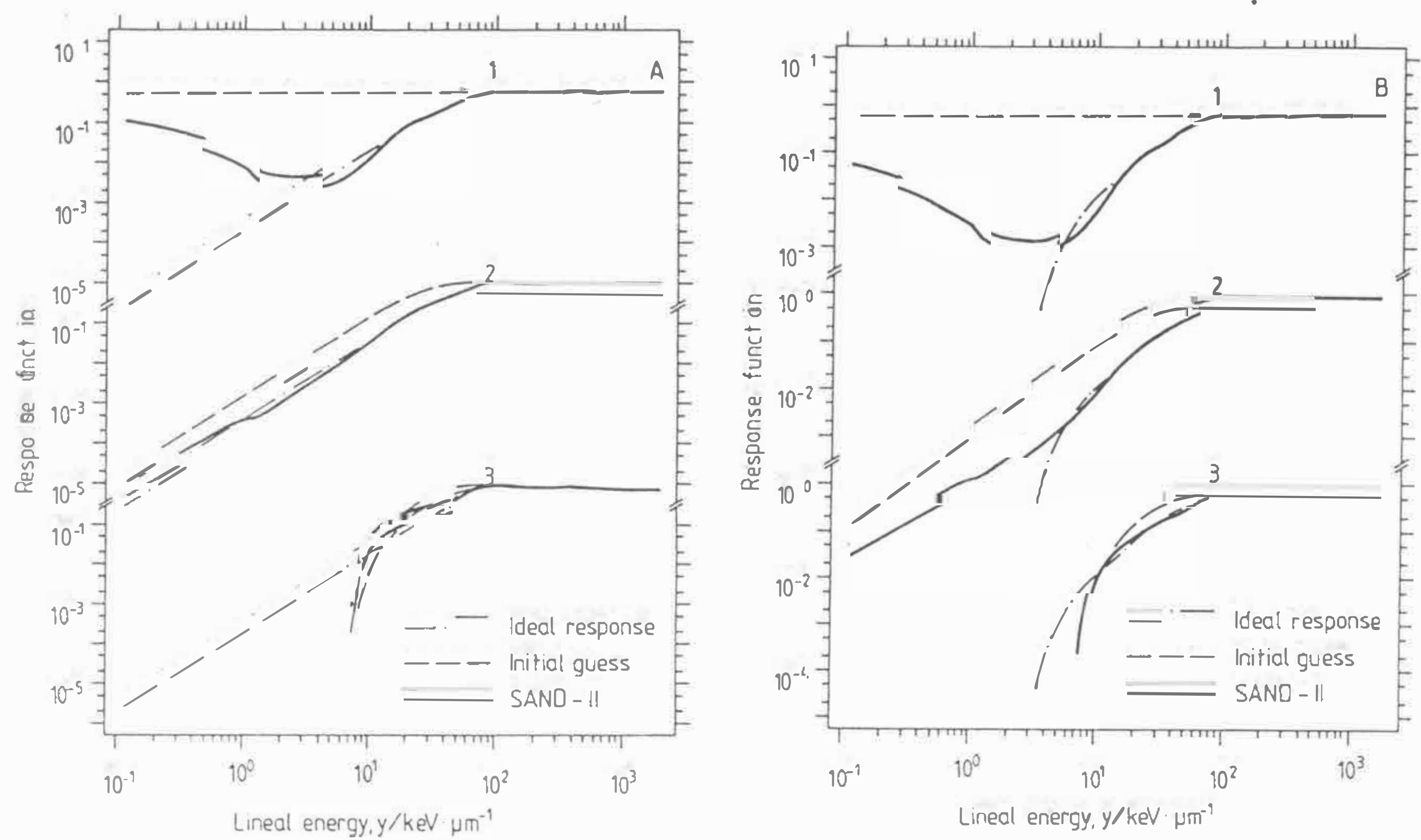


Fig.D.1 Microdosimetric distributions $yf(y)$ for radiation modalities used in experiments of:

a) [Skarsgard et al., 1967], assumed site diameter $d = 1 \mu\text{m}$, idealistic triangular spectra for ions, distribution for 250 X-rays from [Braby & Ellett, 1971])

b) [Todd, 1975], assumed site diameter $d = 20 \text{ nm}$, microdosimetric distributions calculated using track structure calculations. For lineal energies below about $2.25 \text{ keV}/\mu\text{m}$ (which corresponds to the 1 ionization in 20 nm site) the calculated distributions for ions were extrapolated using Eq. 5.10.

**Fig.D.2a**

Results of testing the SAND-II unfolding algorithm. Ideal response functions (dotted line) without (A) and with the threshold (B) (see next page) were assumed and used to calculate α coefficients with Eq.3.22 applying microdosimetric distributions from Fig.D.1a. In the second step these α coefficients and the same microdosimetric distributions $yf(y)$ were used to unfold, with different initial guess functions (dashed lines), corresponding response functions (bold lines).

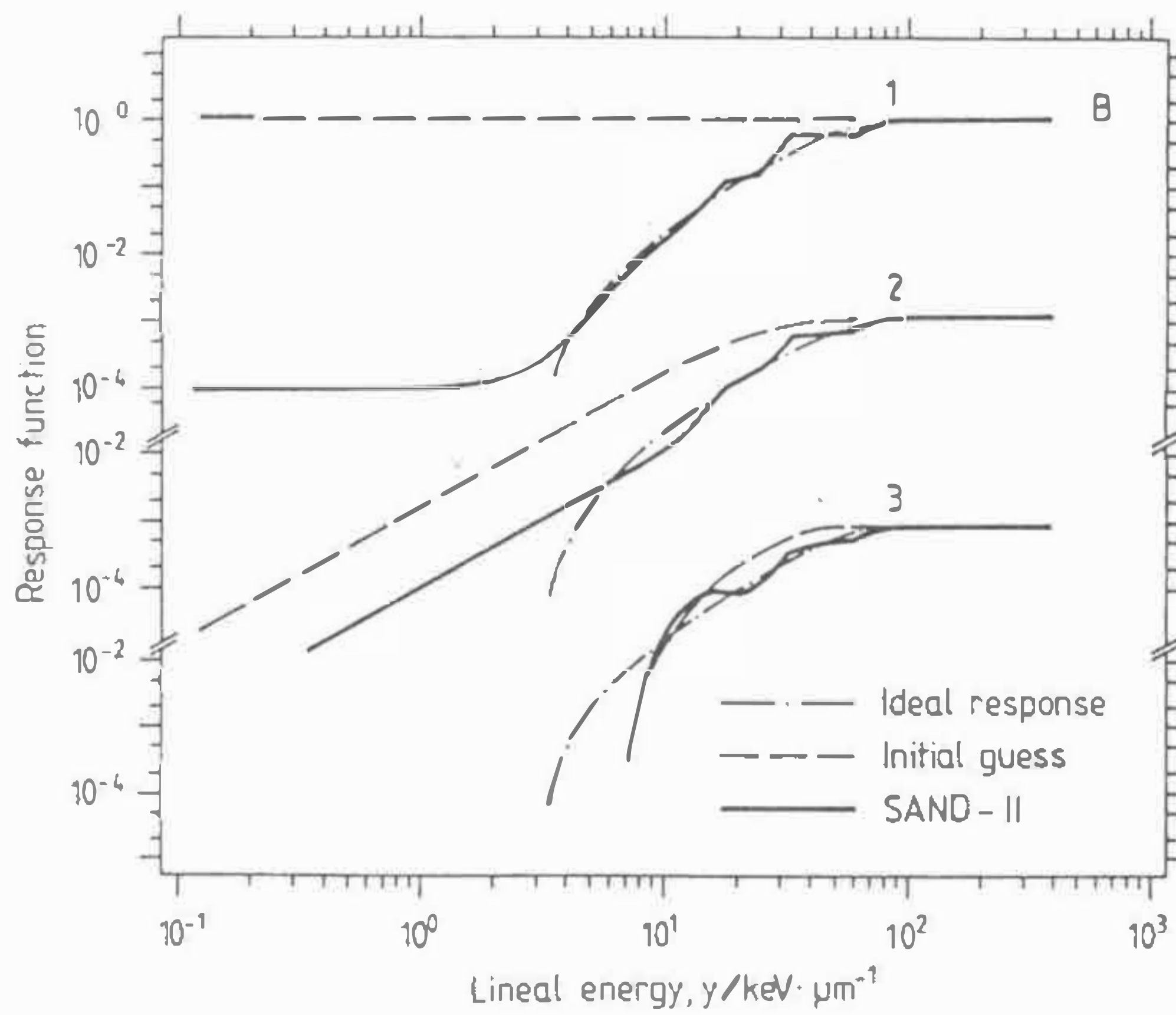
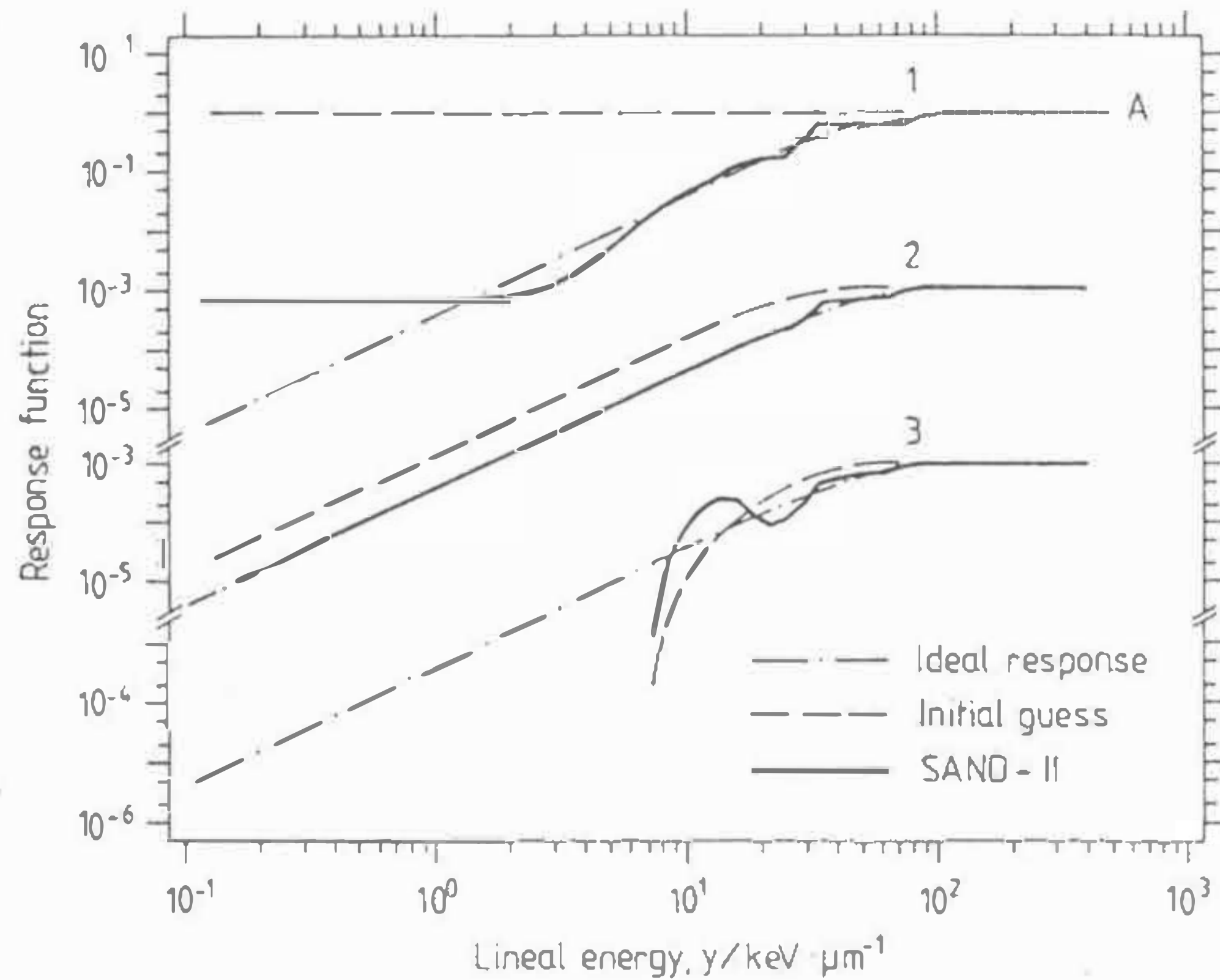
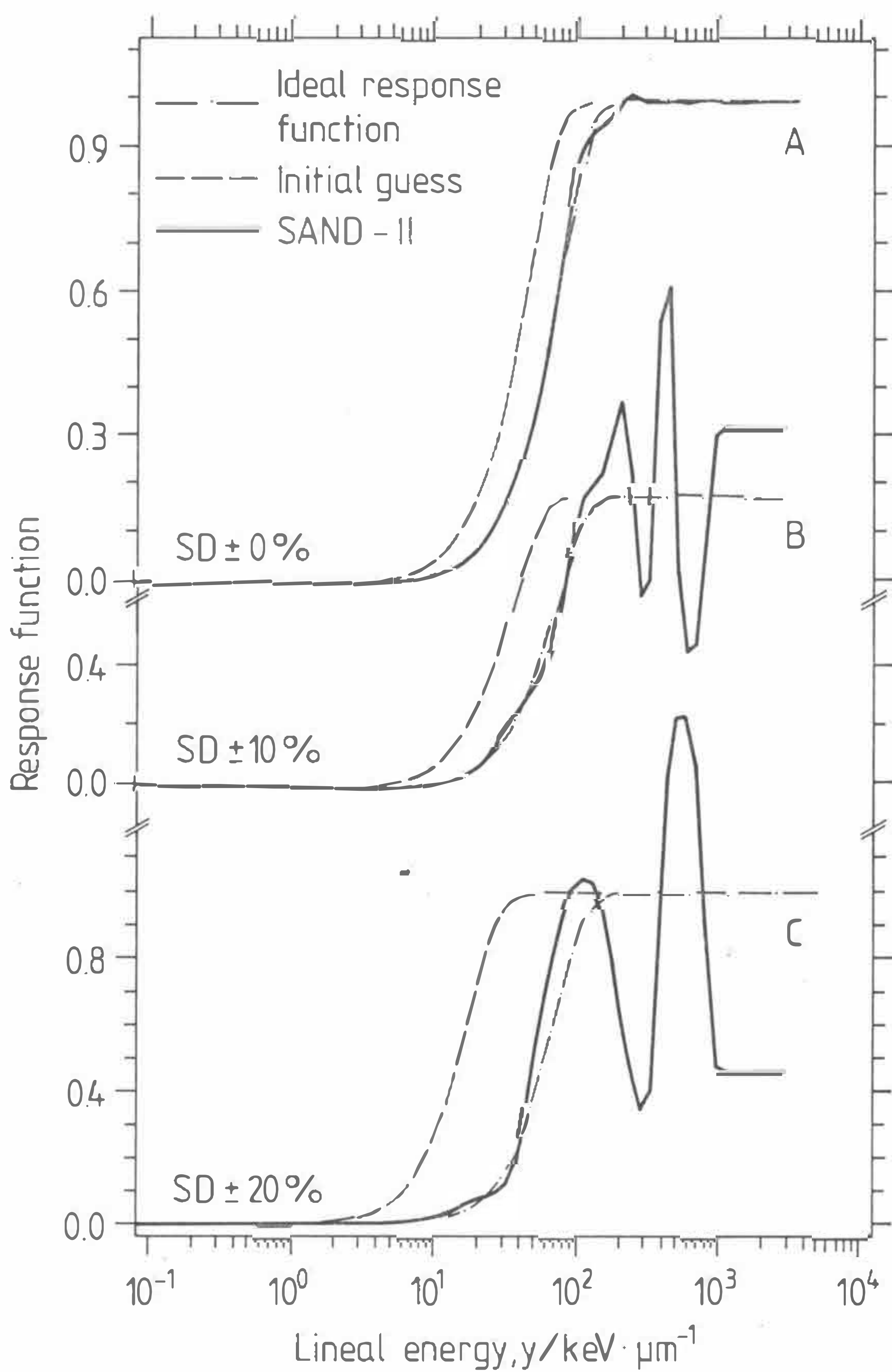


Fig.D.2b

Results of testing the SAND-II unfolding algorithm. Ideal response functions (dotted line) without (A) and with the threshold (B) (see next page) were assumed and used to calculate α coefficients with Eq.3.22 applying microdosimetric distributions from Fig.D.1b. In the second step these α coefficients and the same microdosimetric distributions $yf(y)$ were used to unfold, with different initial guess functions (dashed lines), corresponding response functions (bold lines).

**Fig.D.3**

Results of testing the SAND-II unfolding algorithm. α parameters, calculated with the assumed ideal response function (dotted lines), were randomly deviated assuming normal distribution of error and relative standard deviations 0%, 10% and 20%. These perturbated set of parameters were used to unfold response functions with the SAND-II algorithm (bold lines).

REFERENCES

- Appleyard, R.K. (1949) *Relative yields of ions produced by alpha particles in air and water vapor.* Nature **164**, pp.838
- Attix, F.H. (1986) *Introduction to radiological physics and radiation dosimetry.* John Wiley & Sons, Inc. New York.
- Barendsen, G.W., Beusker, T.L.J., Vergroesen, A.J. and Budke, L. (1960) *Effects od different ionizing radiations on human cells i tissue culture. II. Biological experiments.* Radiat. Res. **13**, 841-849.
- Barendsen, G.W., Walter, H.M.D., Fowler, J.F. and Bewley, D.K. (1963) *Effects of different ionizing radiations on human cells in tissue culture. II Experiments with cyclotron-accelerated alpha particles and deuterons.* Radiat. Res. **18**, 106-119
- Barkas, W.H. (1963) *Nuclear Research Emulsion.* Vol. I (London, New York: Academic Press Inc.), p. 371
- Baum, J.W., (1969) *Comparison of distance- and energy restricted linear energy transfer for heavy particles with 0.25 to 1000 MeV/amu.* In Microdosimetry, Proceedings of 2nd Symposium on Microdosimetry (H.G. Ebert, ed.) pp.653-666, Euratom, Brussels
- Baum, J.W., Varma, M.N., Wingate, C.L. and Kuehner, A.V. (1974) *Nanometer dosimetry of heavy ions tracks, LET_r .* In Proc. 4th Symposium on Microdosimetry (edited by Booz, J., Ebert, H.G. and Waker, A.) Commission of the European Communities, Luxemburg.
- Bednarek, B., Olko, P. and Booz, J. (1988) *Double peak-effect in microdosimetric proportional counters and its interpretation.* Nucl. Instr. Meth. **A274**, 349-358.
- Berger, M.J., (1973) *Improved Point Kernels for Electron and Beta-Ray Dosimetry.* Report NBSIR 73-107
- Berger, M. J. (1985) *Energy Loss Straggling of Protons in Water Vapour.* Radiat. Prot. Dosim. **13**, No.1-4, pp.87-90
- Bethe, H.A. (1933) *Quantenmechanic der Ein- und Zwei-Elektronen Probleme.* In "Handbuch der Physik" (H.Geiger and K.Scheel, eds.) 2nd ed., Vol.24, Part II, p.273, Springer, Berlin.
- Bichsel, H. (1968) *Charge Particle Interactions.* In "Radiation Dosimetry" (Attix, F.H. and Roesch, W.C., eds.) Academic Press, New York.
- Bird, R.P., Rohring, N., Colvett, R.D., Geard, C.R., and Marino, S.A. (1980) *Inactivation of synchronized Chinese hamster V79 cells with charged-particle track segments.* Radiat. Res. **82**, 277-289
- Booz, J. and Feinendegen, L.E. (1987) *Applications of Microdosimetry.* Proc. of the 8th ICRR, Edinburgh, July 1987 (ed. Fielden E. M. et al.), Vol.2 , pp. 331- 337.
- Booz, J. and Feinendegen, L.E. (1988) *A microdosimetric understanding of low-dose radiation effects.* Int. J. Radiat. Biol. **53**, 13- 21

Booz, J., Fidorra, J. and Feinendegen, L.E. (1981) *Quality Factor of Mixed-Radiation Neutron Gamma-Rays: Comparison of the Radiation-Component Method and of the y_D Method*. In Proc. of the 7th Symp. of Microdosimetry (Ed. by J. Booz, H.G. Ebert and H.D. Hartfiel), Commission of the European Communities, pp. 607-621

Booz, J., Paretzke, H.G., Pomplun, E. and Olko, P. (1987) *Auger-electron cascades, charge potential and microdosimetry of iodine-125*. Radiat. Environ. Biophys. **26**, 151-162

Bond, V.P. and Varma, M.N. (1982) *A stochastic, weighted hit size theory of cellular radiobiological action*. In Proc. 8th Symp. on Microdosimetry (Juelich, FRG, Sept. 1982), pp.423-438. EUR-8395, CEC, Luxemburg, 1983.

Bonura, T., Town, C.D., Smith, K.C. and Kaplan, H.S. (1975) *The influence of oxygen on the yield of DNA double strand breaks in X-irradiated Escherichia coli K-12*. Radiat. Res. **63**, 567-577

Brenner, D.J. (1988) *On the probability of interaction between elementary radiation-induced chromosomal injuries*. Radiat. Environ. Biophys. **27**, 189-199

Brenner, D.J. and Zaider, M. (1984) *The Application of Track Calculations to Radiobiology II. Calculations of Microdosimetric Quantities*. Radiat. Res. **98**, 14-25

Brice, D. K. (1972) *Three-parameter formula for the electronic stopping cross section at non-relativistic velocities*. Phys. Rev. **A 6**, pp. 1791-1805

Butts, J.J. and Katz, R. (1967) *Theory of RBE for heavy ion bombardment of dry enzymes and viruses*. Radiat. Res. **30**, 855-871

Carter, L. L. and Cashwell, E. D. (1975) Particle-transport simulation with the Monte Carlo method. ERDA Technical Information Center, Oak Ridge, Tennessee, TID-26607

Caswell, R.S., Coyne, J.J. (1978) *Energy Deposition Spectra for neutrons based on recent cross section evaluation*. Proc. 6th. Symp. Microd. Report No. EUR 6064, Eds. Booz, J., and Ebert, H.G., (Harwood Publishers, London)

Chadwick and Leenhouts (1981) *The molecular theory of radiation biology*. Springer-Verlag, Berlin Heidelberg New York ISBN 3-540-10297-3

Charlton, D.E., Goodhead, D.T., Wilson, W.E. and Paretzke, H.G. (1985) *The deposition of energy in small cylindrical targets by high LET radiations*. Radiat. Prot. Dosim. **13**, No. 1-4, 123-125

Chiocchio, O., Dierckx, R. and Maracci, G. (1970) *Measurements of fast reactor type neutron spectra by foil activation techniques*. Nucl. Instr. Meth. **91**, 45-56

Chmelevsky, D., Kellerer, A.M, (1977) *Computations of Microdosimetric Distributions for Small Sites*. Radiat. Environ. Biophys. **14**, 123-136

Christensen, R.C., Tobias, C.A., Taylor, W.D. (1972) *Heavy-ion-induced single-and double-strand breaks in $\Phi X\text{-}174$ replicative form DNA*. Int. J. Radiat. Biol. **22**, 457-477

Coppola, M. and Booz, J. (1973) *Influence of energy straggling on the shape of neutron produced single event spectra*. Biophysik **9**, 225

Coppola, M. and Booz, J. (1975) *Neutron scattering and energy deposition spectra* Radiat. Environ. Biophys. **12**, 157

Cross, W.G and Ing, H. (1985) *Neutron Spectroscopy In: The dosimetry of ionizing radiation*, Vol.II, pp.91-167 (Kase, K.R., Bjaerngard, B.E. and Attix, F.H., eds.) Academic Press, INC.

Cox, R., Thacker, J., Goodhead, D.T. and Munson, R.J. (1977a) *Mutation and inactivation of mammalian cells by various ionizing radiations* Nature **267**, 425-427

Cox, R., Thacker, J. and Goodhead, D.T. (1977b) *Inactivation and mutation of cultured mammalian cells by aluminium characteristic ultrasoft X-rays. II. Dose-responses of Chinese hamster and human diploid cells to aluminium X-rays and radiations of different LET*. Int. J. Radiat. Biol., **31**, 561-576.

Davies, D.R. and Evans, H.J. (1966) *The role of genetic damage in radiation-induced cell lethality*. In: Advances in Radiation Biology (Augenstein, L.G., Mason, R. and Zelle, M., eds.) Vol.2, pp.243-353, Academic Press New York, London

Davisson, C.M. and Evans, R.D. (1952) *Gamma-ray absorption coefficients*. Rev. Mod. Phys. **24**, 79.

Deering, R. A. and Race, R. (1962) *Heavy Ion Irradiation of HeLa Cells* Radiat. Res. **17**, 774-786

Dertinger, H. and Jung, H. (1969) *Directe und indirecte Strahlenwirkung*. pp.78-98. In: Molekulare Strahlenbiologie. Springer Verlag, Berlin

Dierckx, R., Nimis, M.L., Sangiust, V. and Terrani, M. (1972) *Unfolding methods in neutron spectra measurements by foil activation technique*. Nucl. Instr. Meth. **105**, 1-4

Draper, E.L. (1971) *Integral reaction rate determinations - Part I: Tailored reactor spectrum preparation and measurement*. Nucl. Sci. Eng. **46**, 22-30

Dugle, D.L., Gillespie, C.J. and Chapman, J.D. (1976) Proc. Nat. Acad. SCi. USA, **73**, p.809

Eisberg, R. and Resnick, R. (1974) *Quantum Physics of Atoms. Molecules. Solids. Nuclei and Particles*. John Wiley & Sons, New York.

Edwards, A.A. and Lloyd, D.C. (1980a) *On the prediction of dose-rate effects for dicentric production in human lymphocytes by X- and gamma-rays*. Int. J. Radiat. Biol. **37**, 89-92

Edwards, A.A. , Purrot, R.J., Prosser, J.S. and Lloyd, D.C. (1980b) *The induction of chromosome aberrations in human lymphocytes by alpha-radiation*. Int. J. Radiat. Biol. **38**, 83-91

Ellet, W.H. and Braby, L.A. (1972) *The microdosimetry of 250 kVp and 65-kVp X-rays, Co-60 gamma-rays. and tritium particles*. Radiat. Res. **51**, 229-243

Evans, R.D. (1955) *The Atomic Nucleus*. Mc-Graw-Hill Book Company, New York

Fain, J., Monnin, M. and Montret, M. (1974) *Spatial energy distribution around heavy-ion path*. Radiat. Res. 57, 379-389

Feinendegen, L.E., Booz, J., Bond, V.P., Sondhaus, C.A. (1985) *Microdosimetric Approach to the Analysis of Cell Responses at the Low Dose and Dose Rate*. Radiat. Prot. Dosim. 13, No.1-4, 259-265

Feinendegen, L.E., Bond, V.P., Booz, J. and Mühlensiepen (1988) *Biochemical and cellular mechanisms of low-dose effects*. Int. J. Radiat. Biol. 53, No.1, 23-27

Finch, J.T. and Klug, A. (1976) *Solenoid model for superstructure in chromatin*. Proc. Natl. Acad. Sci. USA 73, 1897-1901.

Frankenberg, D., Goodhead, D.T., Frankenberg-Schwager, M., Harbich, R., Bance, D.A. and Wilkinson, R.E. (1986) *Effectiveness of 1.5 keV aluminium K and 0.3 keV carbon K characteristic X-rays at inducing DNA double-strand breaks in yeast cells*. Int. J. Radiat. Biol. 50, No.4, 727-741

Garcia, J.D. (1968) *Ejected Electron Distributions* Phys. Rev. 177, No.1, 223-229

Glass, W.A. and Braby, L.A. (1969) *A wall less detector for measuring energy deposition spectra* Radiat. Res. 49, 477.

Glass, W.A. and Gross, W. (1972) *Wall-less detectors in microdosimetry* p.221 in: Topics in Radiation Dosimetry, Radiation Dosimetry Supplement 1, Attix, F.J., Ed. (Academic Press, New York)

Goodhead, D.T. and Thacker, J. (1977) *Inactivation and mutation of cultured mammalian cells by aluminium characteristic ultrasoft X-rays. I. Properties of aluminium X-rays and preliminary experiments with Chinese hamster cells*. Int. J. Radiat. Biol. 31, No.6, 451-559

Goodhead, D.T. and Brenner, D.J. (1983) *Estimation of a single property of low-LET radiations which correlates with biological effectiveness*. Phys. Med. Biol. 28, 485-492

Goodhead, D.T. (1987) *Relationship of microdosimetric techniques to applications in biological systems*. In: *The dosimetry of ionizing radiation. Vol.II*, (Kase, K.R., Bjärngard, B.E., Attix, F.H., eds.) Academic Press, Orlando, Florida

Gross, W., Biavati, B.J. and Rosi, H.H. (1970) *Microdosimetry of directly ionizing particles with wall-less proportional counters*. Proc. Symp. Microdosimetry, 3rd, Stresa, Italy p.873

Gross, W. and Rodgers, R.C. (1972) *Heavy ion event spectra*. Proc. 3rd Symp. Microdosimetry, Report No. EUR 4810, Ebert, H.G., Ed. (Commission of the European Communities, Luxemburg)

Guenter, K. and Schultz, W. (1983) *Biophysical Theory of Radiation Action - A Treatise on Relative Biological Effectiveness* (Akademie-Verlag Berlin)

Hamm, R.N., Turner, J.E., Ritchie, R.H. (1984) *Calculated Ionization Distributions in Small Volumes in Liquid Water Irradiated by Protons*. Radiat. Res. 97, 16-24

Hamm, R.N., Turner, J.E., Wright, H.A. (1985) *Statistical fluctuations in heavy charged particle tracks*. Radiat. Prot. Dosim. 13, 83-86

Hamm, R.N., Turner, J.E., Ritchie, R.H. and Wright, H.A. (1985) *Calculation of Heavy-Ion Tracks in Liquid Water*. Radiat. Res. Suppl. 8:104, S-20-S-26

Hubbel, J.H. (1969) *Photon cross sections, attenuation coefficients, and energy absorption coefficients from 10 keV to 100 GeV*. Report NSRDS-NBS29, U.S. National Bureau of Standards.

Hubbel, J.H. (1982). *Photon mass attenuation and energy-absorption coefficient from 1 keV to 20 MeV*. Int. J. Appl. Rad. Isot. 33, 1269.

Hum, J.L. (1984) *The analysis of Auger electrons released following the decay of radioisotopes and photoelectric interactions and their contribution to energy deposition*. Thesis, KFA Report Jü1-1932.

ICRP (1966) Recommendations of the International Commision on Radiological Protection 1965, ICRP Publ. 9, Pergamon, Oxford

ICRP (1977) *Recommendations of the International Commission on Radiological Protection*, ICRP Publ. 26. *Annals of the ICRP* 1(3), 1-51, Pergamon, Oxford.

ICRP (1985) *Statement from the 1985 Paris Meeting of the ICRP*. ICRP-85/G-03

ICRU (1970) Report 16 *Linear Energy Transfer*, International Commission on Radiation Units and Mesurements, Betheda, Maryland.

ICRU (1980) Report 33 *Radiation Quantities and Units*, International Commission on Radiation Units and Measurements, Betheda, Maryland.

ICRU Report 36, (1983) *Microdosimetry*, International Commission on Radiation Units and Mesurements, Betheda, Maryland.

ICRU Raport 40 (1986) *The Quality Factor in Radiation Protection*. International Commission on Radiation Units and Measurements, Bethesda, Maryland

ISO (1980) International Organization for Standardization (ISO). X and Gamma Reference Radiations for Calibrating Dosimeters and Dose Ratemeters for Determining Their Response as Function of Energy, ISO Stand. 4037- 1979. ISO, Geneva.

Katz, R., Ackerson, B., Homayoonfar, M. and Sharma, S.C. (1971) *Inactivations of cells by heavy ions bombardment*, Radiat. Res. 47, 402

Katz, R. and Sharma, S.C. (1973) *Response of cells to fast neutrons, stopped pions and heavy ions beams*, Nucl. Instr. and Methods 111, 93-116

Kellerer, A.M. (1968) *Mikrodosimetrie. Grundlagen einer Theorie der Strahlenqualität*. GSF-Report B-1, November 1968.

Kellerer, A.M. (1971) *An Assessment of Wall Effects in Microdosimetric Measurements*. Radiat. Res. 47, 377-386

Kellerer, A.M. and Chmelevsky, D. (1975a) *Criteria for the applicability of LET*, Radiat. Res. 63, 226

Kellerer, A.M. and Chmelevsky, D. (1975b) *Concepts of Microdosimetry. II. Probability Distributions of the Microdosimetric Variables*. Radiat. Environ. Biophys. 12, 321-335.

Kellerer, A.M. and Hahn, K. (1988) Considerations on the Revision of the Quality Factor. Radiat. Res. 114, 480-488

Kellerer, A.M. and Rossi, H.H (1972) *The theory of Dual Radiation Action* Cur. Top. Radiat. Res. Quart. 8, 85-158

Kliauga, P. and Dvorak, R. (1978) *Microdosimetric Measurements of Ionization by Monoenergetic Photons*. Radiat. Res. 73, 1-20

Kliauga, P. and Rossi, H.H. (1976) *Microdosimetric distributions as a function of radial distance from heavy ion tracks*. Symp. of Microdosimetry, 5th, Pallanza (Italy), eds. Booz, J., Ebert, H.G. and Smith, B.G.R. (Luxemburg: Euroatom), p.127-140

Kliauga, P. (1989) *Measurements of single event energy deposition spectra at 5 nm to 250 nm simulated site sizes*. Submitted to Radiat. Prot. Dosim.

Klein, O. and Nishina, Y. (1929) Z. Physik, 52, 853.

Kornberg, A. (1983) *DNA Replication*. W.H. Freeman and Comp., San Francisco

Kraft, G., Kraft-Weyrather, W., Ritter, S., Scholtz, M. and Stanton, J. (1988) *Cellular and subcellular effect of heavy ions: a comparison of the induction of strand breaks and chromosomal aberration with the incidence of inactivation and mutation*. GSI Raport GSI-88-52.

Lea, D. E. (1956) *Action of Radiations on Living Cells*. Cambridge, University Press

Lederer, C.M. and Shirley, V.S. (1979) *Table of isotopes*, 7th ed., Wiley-Interscience, New York.

Leuthold, G. and Burger, G. (1985) *Structure and microdosimetric classification of computer simulated ion tracks*. Radiat. Prot. Dosim. 13, No.1-4, 37-40

McElroy, W.N., Berg, S., Crockett, T. and Hawkins, R.G. (1967) *A computer automated iterative method for neutron flux spectra determination by soil activation*. AFWL-TR-67-41, U.S. Air Force Weapons Laboratory

Meeting, N.F., Rossi, H.H., Braby, L.A., Kliauga, P.J., Howard, J., Zaider, M., Schimmerling, W., Wong, M. and Rapkin, M. (1988) *Microdosimetry near the trajectory of high-energy heavy ions*. Radiat. Res. 116, 183-195

Menzel, H.G. and Booz, J. (1976) *Measurement of radial energy deposition spectra for protons and deuterons in tissue-equivalent gas*. In proc. 5th Symposium on Microdosimetry (Edited by Booz, J., Ebert, F. G. and Smith, B. G. R.) Commission of the European Communities, Luxemburg

Miller, J.H., Wilson, W.E. and Manson, S.T. (1985) *Secondary electron spectra: a semiempirical model*. Radiat. Prot. Dosim. 13, No. 1-4, 27-30

Morstin, K., Bond, V.P., Baum, J.W. (1989) *A probabilistic approach to obtain Hit-Size Effectiveness Functions which relate microdosimetry and radiobiology.* To appear in: Radiat. Res.

Morstin, K., Kawecka, B., Booz, J. (1985) *Combined Primary and Secondary Particle Transport Calculations of Microdosimetric Distributions in Tissues and Tissue Substitutes.* Radiat. Prot. Dosim. 13, 103-110

NCRP (1954) *Permissible dose from external sources of ionizing radiation.* Raport 17, NBS Handbook 59 (US Govt. Printing Office, Washington, DC)

NL2SOL (1983) *Programmpaket zur Behandlung nichtlinearer least squares Probleme. Kurzinformation.* KFA-ZAM-0022-MATH

Oda, N. and Iwanami, S. (1984) *Microdosimetric Distributions for Nanometer-Size Targets in Water Irradiated with Co-60 Gamma Rays: Frequency Distributions of Effective Primary Events by Individual Tracks of Electrons.* Radiat. Res. 98, 1-13

Olko, P., Booz, J., Paretzke, H.G. and Wilson, W.E. (1989) *Energy deposition in the nanometre sites based on the track structure calculations.* Proceedings of an advisory group meeting organized by the International Atomic Energy Agency, Vienna, 13-16 July 1988, IAEA-TECDOC-506.

Olko, P., Schmitz, Th., Morstin, K., Dydejczyk, A. and Booz, J. (1989) *Microdosimetric distributions for photons.* To appear in Radiat. Protec. Dosim.

Olko, P. and Booz, J. (1989) *Energy Deposition in Spherical Sites Due to Protons and Alpha Particles.* To appear in: Radiat. Environ. Biophys.

Opal, C.B., Beaty, E.C. and Peterson, D. (1972) W.K. At. Data 4, 209

Orlic, M. (1989) *Microdosimetric semiconductor counter.* To be published in Radiat. Protec. Dosim.

Paretzke, H.G. (1973) *Comparison of track structure calculations with experimental results.* In: Proc. of 4th Symp. on Microdosimetry (Ed. Booz, J., Ebert, H.G., Eickel, R. and Waker, A.), Commission of the European Communities, pp.141-165

Paretzke, H.G. (1987) *Radiation Track Structure Theory.* In: Kinetics of Nonhomogeneous Processes, pp. 89-170, Edited by G.R. Freeman, John Wiley & Sons, New York

Paretzke, H.G. (1988) Private information

Paretzke, H. G. and Berger, M. (1978) *Stopping Power and Energy Degradation for Electrons in Water Vapor.* In 6th Symposium on Microdosimetry (ed. Booz, J. and Ebert, H. G), Harwood, Holland, pp.749-758,

Patton, W. F., Hurst, G. S. and Bortner, T. E. (1957) *Measurement of the Average Energy Lost by a 5 MeV Alpha Particle in Producing an Ion Pair in Water Vapor.* Report ORNL-2352, Oak Ridge National Laboratory, Oak Ridge, TN

Pohlit, W. and Heyder, I.R. (1981) Radiat. Res. 87, p.613

Pszona, S. (1976) *A track ion counter*. Proc. Symp. Microdosim., 5th, Verbania Pallanza, Italy, 1975 pp. 1107-1121. Comm. Eur. Communities EUR, EUR-5452

Radford, I.R. and Hodgson, G.S. (1985) *¹²⁵I-induced DNA double strand breaks: use in calibration of the neutral filter elution technique and comparison with X-ray induced breaks*. Int. J. Radiat. Biol., 48(4), 555-566.

Radford, I.R. (1986) *Evidence for a general relationship between the induced level of DNA double-strand breakage and cell-killing after X-irradiation of mammalian cells*. Int. J. Radiat. Biol., 49(4), 611-620.

Ritter, M.A., Cleaver, J.E. and Tobias, C.A. (1977) *High-LET radiations induce a large proportion of non-rejoining DNA breaks*. Nature 266, 653-655

Rossi, H.H. and Rosenzweig, W. (1955) *A device for the measurements of dose as a function of specific ionization*. Radiology 64, 404.

Rossi, H.H. (1959) *Specification of radiation quality*. Radiat. Res. 10, 522.

Rossi, H.H. (1968) *Microscopic Energy Distributions in Irradiated Matter*. In Radiation Dosimetry (F. H. Attix, W. C. Roesch, and E. Tochilin, eds.), Vol.1: 43-92, Academic Press, New York

Routti, J.T. and Sandberg, J.V. (1985) *Unfolding activation and multisphere detector data*. Radiat. Prot. Dosim. 10, No.1-4, 103-110

Schmitz, Th. (1988) Private Communication

Schmitz, Th. (1989) Private Communication

Schmitz, Th., Smit, Th., Morstyn, K., Müller, K.D. and Booz, J., (1985) *Construction and First Application of a TEPC Dose-Equivalent Meter for Area Monitoring*. Radiat. Prot. Dosim. 13, 335-339.

Schmitz, Th., Kramer, H. M., Booz, J. (1989) *Assessment of the Photon Response of a TEPC as a Contribution to Implementing Operational Quantities for Dose Equivalent in Radiation Protection*, to appear in Radiat. Prot. Dosim.

Skarsgard, L.D., Kihlam, B.A., Parker, L., Pujara, C.M. and Richardson, S. (1967) *Survival, chromosome abnormalities, and recovery in heavy ion- and x-irradiated mammalian cells* Radiat. Res. Suppl. 7, 208-221

Sullivan, A.H. and Zielczyński, M. (1976) *Microdosimetry using ionization recombination*. in Proceedings of the 5th Symposium on Microdosimetry, Report No. EUR 5052, (Booz, J., Ebert, H.G. and Smith, B.G.R., eds.), Harwood Academic Publishers, London.

Swinehart, J.L. and Cerutti, P.A. (1975) *Gamma-ray induced thymine damage in the DNA in coli-phage $\Phi X 174$ and in E.coli* Int. J. Radiat. Biol., 27, 83-94

Toburen, L.H. (1971) *Distributions in energy and angle of electrons ejected from molecular nitrogen by 0.3 to 1.7 MeV protons*. Phys. Rev. A 3, 216-228

Toburen, L.H. (1972) *Energy transfer to electrons in fast proton collisions* Radiat. Res. 50, 6-19

Todd, P. (1967) *Heavy-Ion Irradiation of Cultured Human Cells.* Radiat. Res. Supplement 7, 196-207

Todd, P. (1975) *Heavy Ion Irradiation of Human and Chinese Hamster Cells in Vitro.* Radiat. Res. 61, 288-297

Turner, J.E., Hamm, R.N., Wright, H.A., Modolo, J.T., and Sardi, G.M.A.A. (1980) *Monte Carlo calculations of initial energies of Compton electrons and photoelectrons in water irradiated by photons with energies up to 2 MeV.* Health Phys. 39, 49-55.

Turner, J.E., Paretzke, H.G., Hamm, R.N., Wright, H.A. and Ritchie, R.H. (1982) *Comparative Study of Electron Energy Deposition and Yields in Water in the Liquid and Vapor Phases.* Radiat. Res. 92, 47-60

UNSCEAR (1988) United Nations Scientific Committee on the Effects of Atomic Radiation. Raport to the general assembly.

Varma, M. N., Baum, J. W. and Kuehner, A. V. (1977) *Radial dose, LET and W for ¹⁶O ions in N₂ and tissue-equivalent gases.* Radiat. Res. 70, pp. 511-518

Varma, M. N., Baum, J. W. and Kuehner, A. V. (1980) *Stopping power and radial dose distribution for 42 MeV bromine ions.* Phys. Med. Biol. 25, pp. 651-656.

Varma, M.N. and Bond, V.P. (1982) *Empirical evaluation of a cell critical volume dose vs. cell response function for pink mutations in Tradescantia.* In Proc. 8th Symp. on Microdosimetry (Juelich, FRG, Sept. 1982), pp. 439-450, EUR-8395, CEC, Luxemburg, 1983.

Varma, M.N. and Zaider, M. (1989) *The radial dose distribution as a microdosimetric tool.* Submitted to Radiat. Prot. Dosim.

Vavilov, P.V. (1957) *Ionization losses of high-energy heavy particles.* Sov. Phys. JETP 5, 749.

Wachsmann, F. and Drexler, G. (1976) *Graphs and Tables for Use in Radiology.* ISBN 3-540-07809-6 Springer-Verlag Berlin, Heidelberg, New York

Waligórska, M.P.R., Hamm, R.N. and Katz, R. (1987) *The radial distribution of dose around the path of a heavy ion in liquid water.* Int. J. Radiat. Appl. Instrum., Part D, 309-319

Watson, J.D. and Crick, F.H.C. (1953) *A structure for deoxiribose nucleic acid.* Nature 171, pp.737-738

Wilson, W.E. (1978) *Analytical expression for cross section data.* In: Pacific Northwest Laboratory Annual Report for 1977, Part 4, pp. 2.7-2.9 Battelle, Pacific Northwest Laboratories, Richland, VA

Wilson, W.E. (1988) Private information

Wilson, W. E. and Miller, J. H. (1984) *An algorithm for secondary electron emission from water vapor by high velocity ions.* PNL-SA-11768

Wilson, W.E., Miller, J.H. and Paretzke, H.G. (1988) *Microdosimetric aspects of 0.3 to 20 MeV proton tracks.* *J. Crossers. Radiat. Res.* **115**, p.389

Wilson, W.E. and Paretzke, H.G. (1980) *Calculation of Ionization Frequency in Small Sites.* Radiat. Res. **81**, 326-335

Wilson, W.E. and Paretzke, H.G. (1981) *Calculation of Distributions for Energy Imparted and Ionization by Fast Protons in Nanometer Sites.* Radiat. Res. **87**, 521-527

Wingate, C. L. and Baum, J. W. (1976) *Measured radial distributions of dose and LET for alpha and proton beam in hydrogen and tissue-equivalent gas.* Radiat. Res. **95**, 231-247

Zaider, M., Brenner, D. J. and Wilson, W. E., (1983) *The Applications of Track Calculations to Radiobiology I. Monte-Carlo Simulation of Proton Tracks.* Radiat. Res. **95**, 231-247

Zaider, M. and Brenner, D.J. (1985) *On microdosimetric definition of quality factors.* Radiat. Res. **103**, 302-376

Zaider, M. and Brenner, D.J. (1986) *Evaluation of a Specific Quality Function for Mutation Induction in Human Fibroblasts.* Radiat. Prot. Dosim. **15**, No.2, 79-82

ACKNOWLEDGEMENTS

I would greatly like to thank Dr. J. Booz from the Institute für Medizin, Kernforschungsanlage Jülich for inviting me to work with him, introducing me into the domain of microdosimetry and for persistent help, support and encouragement during my work in his group. His personal engagement and scientific discussions stimulated this work.

I would like to express my gratitude to Prof. L.E. Feinendegen, director of the Institute of Medicine KFA Jülich for allowing me to perform this work in his Institute, for stimulating discussions and his interest in the progress of this work.

I am especially indebted to my supervisor, Dr. T. Niewiadomski from the Institute of Nuclear Physics, Kraków, for introducing me into radiation protection and for his continues help and interest during all stages of this work.

I like to express my best thanks to my colleagues from the Laboratory of Microdosimetry, especially to Thomas Schmitz, for their continues help and a fantastic atmosphere in our group.

I am much indebted to me colleagues, Dr. K. Morstin and Dr. M. Waligórski, for fruitful discussions and critical comments on the manuscript.

I like to thank Dr. Paretzke for supporting me with his computer programs MOCA-8, MOCA-14, Dr. Schmidt for the program RBEFIT (SAND) and Dr. P. Pihot for co-operation in modifying the SAND-II.

I thank the KFA council for financial support during my stay in the KFA Jülich.

Finally a warm thanks for the continual support to my wife Elzbieta and my children Aleksandra and Wiktor.